

Dissertation
submitted to the
Combined Faculties of the Natural Sciences and Mathematics
of the Ruperto-Carola-University of Heidelberg. Germany
for the degree of
Doctor of Natural Sciences

Put forward by
Tobias Marius Schmidt
born in: Wuppertal, Germany
Oral examination: 5th of February, 2019

Universität Heidelberg

Doctoral Thesis

**Constraints on Quasar Emission Properties from
the He II and H I Transverse Proximity Effect**

Tobias M. Schmidt

Max Planck Institute for Astronomy
University of California, Santa Barbara

Scientific advisor: Prof. Dr. Joseph F. Hennawi

Referees:

Prof. Dr. Joseph F. Hennawi

Prof. Dr. Cornelis P. Dullemond

Abstract

Bright quasars are powerful sources of ionizing radiation and have profound impact on the Inter-galactic Medium. In particular, they create regions with enhanced ionization and therefore reduced Lyman α forest absorption in their surroundings. Observing this so-called *transverse proximity effect* along background sightlines provides a view of the foreground quasar from different vantage points, and hence at different lookback times compared to the line-of-sight toward Earth. One can thus constrain the emission history (lifetime, age) and emission geometry (obscuration, opening angle) of the foreground quasar based purely on geometric and light travel time arguments. Both quantities are so far poorly constrained by observations but fundamental for the understanding of Active Galactic Nuclei.

To investigate the He II transverse proximity effect, we conducted an optical spectroscopic foreground quasar survey around 22 *HST*/COS sightlines, leading to a sample of 20 foreground quasars. We find statistical evidence for the He II transverse proximity effect and infer a constraint on the quasar lifetime of > 25 Myr. From a detailed modeling, based on cosmological hydrodynamical simulations and a dedicated photoionization model including quasar obscuration and finite quasar lifetime, we derive joint constraints on age and obscuration of individual objects, indicating that one quasar is old and unobscured ($t_{\text{age}} \approx 25$ Myr, $\Omega_{\text{obsc}} < 30\%$) while three other are either young ($t_{\text{age}} < 10$ Myr) or highly obscured ($\Omega_{\text{obsc}} > 70\%$). However, the models also reveal that the large scatter intrinsic to the He II Ly α forest prohibits further progress in the field.

I therefore developed a novel method that uses large numbers of H I Ly α forest spectra to map the 3D light echo of individual quasars. An end-to-end test confirms that such tomographic observations can constrain the age of hyperluminous quasars to better than 20%, requiring only 1–2 nights on existing 8–10 m facilities. The method bears potential to also constrain the quasar emission geometry and the full lightcurve over the past 100 Myr, rendering it a viable tool to investigate quasar properties.

Zusammenfassung

Quasare erzeugen große Mengen ionisierende Strahlung und haben weitreichenden Einfluss auf das Intergalaktische Medium. Insbesondere erzeugen sie Regionen mit erhöhter Ionisation und folglich reduzierter Lyman α Absorption. Die Beobachtung dieses sogenannten *transversalen proximity Effektes* entlang von Hintergrundlichtlinien erlaubt einen Blick auf den Vordergrundquasar aus einem anderen Blickwinkel und dementsprechend zu einem anderen Beobachtungszeitpunkt, verglichen mit der direkten Sicht auf den Vordergrundquasar. Dies erlaubt es, basierend auf rein geometrischen und Lichtlaufzeitargumenten, die Emissionsgeometrie (Abschattung durch Staub, Öffnungswinkel) und Emissionshistorie (Alter, Dauer der Aktivitätsphasen) des Vordergrundquasars zu bestimmen. Beide Aspekte sind bisher unzureichend bestimmt, jedoch essentiell für das Verständnis von Aktiven Galaktischen Kernen.

Zur Studie des transversalen He II proximity Effektes führten wir eine optische, spektroskopische Durchmusterung nach Vordergrundquasaren in der Umgebung von 22 mit *HST/COS* beobachteten He II Sichtlinien durch, wodurch nun 20 relevante Vordergrundquasare bekannt sind. Eine statistische Analyse zeigte das Vorhandensein des transversalen proximity Effektes und die Mindestdauer der Quasaraktivitätsphase konnte auf > 25 Mio. Jahre bestimmt werden. Durch eine detaillierte Modellierung, basierend auf kosmologischen hydrodynamischen Simulationen, verbunden mit einem Photoionisationsmodell das Effekte anisotroper Emission und endlicher Quasarlebenszeit berücksichtigt, konnte der Abschattungsgrad und das Alter von ausgewählten Vordergrundquasaren gemeinsam bestimmt werden. Es zeigte sich, dass ein Quasar alt und nur gering abgeschattet ist ($t_{\text{age}} \approx 25$ Myr, $\Omega_{\text{obsc}} < 30\%$), wohingegen drei weitere entweder sehr jung ($t_{\text{age}} < 10$ Myr) oder stark abgeschattet ($\Omega_{\text{obsc}} > 70\%$) sind. Außerdem zeigten die Simulationen, dass weiterreichende Erkenntnisse aufgrund der starken Varianz in der He II Ly α Absorption nur schwer möglich sein werden.

Ich habe daher eine neuartige Methode entwickelt, die mittels zahlreicher H I Ly α Absorptionsspektren die Lichtechos einzelner Quasare dreidimensional kartieren kann. Simulationen dieses tomographischen Verfahrens zeigen, dass sich das Alter von extrem leuchtkräftigen Quasaren mit 1–2 Nächten Beobachtungszeit an existierenden 8–10 m Teleskopen auf besser als 20% bestimmen lässt. Darüber hinaus ergibt sich die Möglichkeit, die Emissionsgeometrie von Quasaren detailliert zu untersuchen und die vollständige Lichtkurve auf Zeitskalen bis zu 100 Myr zu bestimmen.

Contents

1	Introduction	13
1.1	Active Galactic Nuclei	13
1.1.1	Early History of Quasars	13
1.1.2	The AGN Zoo	15
1.1.3	AGN Unification	20
1.1.4	Lifetime of Quasars	25
1.2	The Large Scale Structure of the Universe	26
1.2.1	The Intergalactic Medium	27
1.2.2	The Lyman α Forest	27
1.2.3	The Ly α forest as precision probe of the IGM	29
1.2.4	The Helium Lyα Forest	31
1.3	The Quasar Proximity Effect	32
1.3.1	The Line-of-sight Proximity Effect	33
1.3.2	The Transverse Proximity Effect	34
1.4	Outline of the Thesis	37
2	Systematic Search for the He II TPE	39
2.1	Description of the Survey	40
2.1.1	He II Sightlines	41
2.1.2	Deep Survey on 8 m class Telescopes	42
2.1.3	Wide Survey on 4 m Class Telescopes	45
2.1.4	Selection from SDSS and BOSS	46
2.1.5	Systemic Quasar Redshifts	46
2.1.6	Estimate of the He II Photoionization Rate	47
2.1.7	Final Quasar Sample	48
2.2	The Transverse Proximity Effect in Individual Sightlines	49
2.2.1	HS 1700+6416	49
2.2.2	Q 0302–003	53
2.2.3	Foreground Quasars with the Highest Observed Photoionization Rates	54
2.3	Statistical Data Analysis	55

CONTENTS

2.3.1	Average He II Transmission near Foreground Quasars	55
2.3.2	Monte Carlo Significance Estimate	57
2.3.3	Dependence on $\Gamma_{\text{QSO}}^{\text{HeII}}$	59
2.3.4	Redshift Evolution	60
2.3.5	Constraining the Quasar Lifetime with the Transverse Proximity Effect	61
2.4	Quantifying the Effect for Individual Quasars	63
2.5	Discussion	66
2.5.1	Interpretation and Limitations of our Lifetime Constraint	66
2.5.2	Absence of Transmission Spikes for Large Photoionization Rate Enhancements	67
2.5.3	Toy Model for the Ionization Rate along the Sightline	68
2.6	Summary and Conclusions	70
3	Modeling of the He II TPE	73
3.1	Data Sample	74
3.2	Models / Simulations	76
3.2.1	NYX Cosmological Hydrodynamical Simulations	76
3.2.2	Ionization State for Hydrogen and Helium	77
3.2.3	Computing Synthetic Spectra	78
3.2.4	H I and He II UV Background	78
3.2.5	Modeling Foreground Quasar Emission and Ionization Rates	82
3.2.6	Example of the Simulated Data	84
3.2.7	Average Transmission Profiles	86
3.3	Comparison to Data and Inference of Parameters	88
3.3.1	Likelihood Computation	88
3.3.2	Priors	91
3.3.3	Posterior Probabilities	91
3.4	Results	91
3.5	Discussion	94
3.5.1	Generalization to Quasar Population Properties and Constraints of Additional Parameter	96
3.5.2	Non-Lightbulb Quasar Lightcurves and Non-Equilibrium Effects	96
3.6	Summary	97
4	Mapping Quasar Light Echoes in 3D	99
4.1	Observational Setup	101
4.1.1	Quasar Luminosities	102
4.1.2	Field-of-View	102
4.1.3	Spectral Resolution	104

4.1.4	Required S/N and Exposure Times	104
4.1.5	Background Sightline Density	105
4.1.6	Summary of Observational Parameters	106
4.2	Models / Simulations	107
4.2.1	NYX Cosmological Hydrodynamical Simulations	107
4.2.2	Background Photoionization Rates	108
4.2.3	Foreground Quasar Photoionization Rates	108
4.2.4	Ionization State of Hydrogen	111
4.2.5	Computing Synthetic Spectra	112
4.2.6	Error Forward Model	112
4.3	Simulated Observations of Quasar Light Echoes	113
4.3.1	IGM Transmission Statistics	116
4.4	Inferring Parameters from Quasar Light Echoes	117
4.4.1	Transmission Probability Distribution Functions	118
4.4.2	Likelihood Computation	118
4.5	Results	121
4.5.1	Simulation Grid	121
4.5.2	Example Posteriors	122
4.5.3	Dependence on t_{age}	123
4.5.4	Dependence on z_{QSO}	124
4.5.5	Dependence on S/N	125
4.5.6	Dependence on Spectral Resolution	126
4.5.7	Dependence on Sightline Density	127
4.5.8	Dependence on Field-of-View	128
4.5.9	Dependence on Quasar Luminosity	129
4.5.10	Impact of Continuum Uncertainties	130
4.6	Conclusion	131
5	Concluding Remarks and Outlook	133

Chapter 1

Introduction

This Chapter is in some parts based on the introduction sections of publications by T. Schmidt, i.e. Schmidt et al. (2017a,b, 2018a,b). Some illustrative figures are taken from other publications and references are given accordingly in the captions.

The topic of this thesis is the *quasar proximity effect* which describes enhanced ionization in the intergalactic medium caused by the ionizing radiation of a nearby quasar. Although this might be a cryptic description at the current point, it highlights that this thesis has overlap with the research field of quasars and Active Galactic Nuclei (AGN) on one side and with studies of the Intergalactic Medium (IGM) and the Lyman α ($\text{Ly}\alpha$) forest on the other side. I will in the following give some background information on either topic and describe how the quasar proximity effect connects both fields. In particular, I will try to build some intuition for how quasars influence the ionization state of the IGM and at the same time observations of the IGM can be used to learn about quasar properties.

1.1 Active Galactic Nuclei

Quasars are the most luminous non-transient sources in the Universe and powered by the accretion of matter onto a supermassive black hole (SMBH). In the following, a short description of their initial discovery, their fundamental properties and the various different possible appearances and ways to observe quasar and related objects within the family of Active Galactic Nuclei (AGN) will be given.

1.1.1 Early History of Quasars

The initial discovery of quasars took place by detecting emission in the radio regime, the first *new* spectral window that opened up in the early 1950s. However, little could be learned without identifying optical counterparts. This required a precise location of the radio sources, only possible with either lunar occultations (e.g. Hazard et al. 1963) or interferometric observation (e.g. Matthews & Sandage 1963). An important early interferometric survey was the *Third Cambridge Catalogue of Radio Sources* (3C, Edge et al. 1959) at 159 MHz, which observed 471 objects. For many sources, the optical counterparts appeared star-like, leading to the designation as *quasi stellar radio source* or *quasar*. Insight into the nature of these objects was only achieved when Maarten Schmidt obtained deep optical spectra of the object 3C 273 and identified a set of broad (50 Å wide) emission lines as Balmer lines of hydrogen,

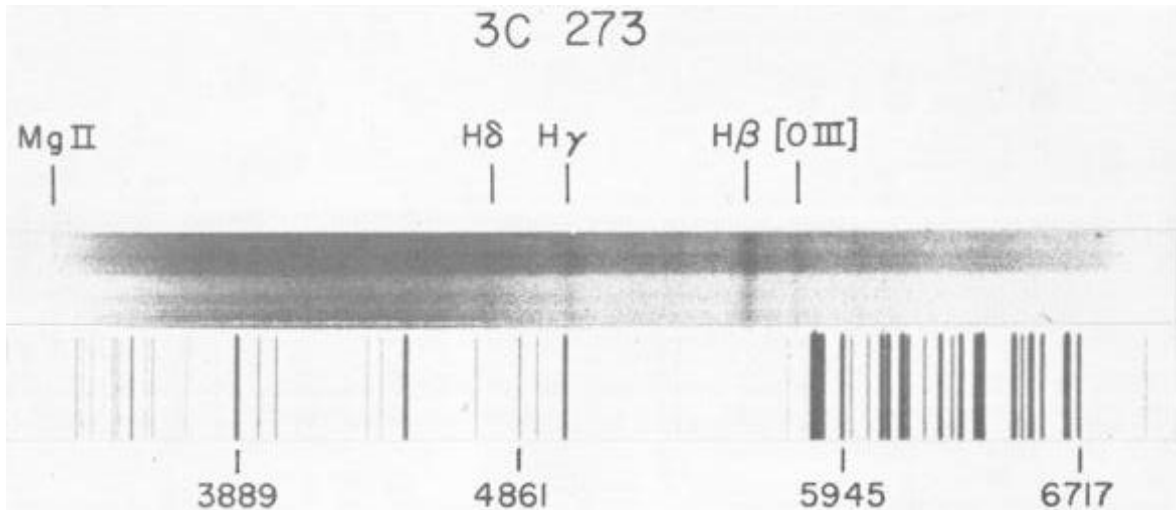


Figure 1.1: Discovery spectrum of the first quasar 3C 273 taken from [Greenstein & Schmidt \(1964\)](#). The top part displays an inverted spectrum of the object, clearly showing broad and strong emission lines of hydrogen and a narrow [O III] line from doubly ionized oxygen. These lines are shifted to 116% of their laboratory wavelength, indicating an origin at cosmological distances. Original caption: Spectrum of the quasi-stellar object 3C 273B, 400 Å/mm original, 103a-F, January 23. The comparison spectrum is H + He + Ne. Exposure over the upper half of the slit was three times that over the lower half. Redshifted emission lines of H and [O III] are indicated; also the barely visible line of Mg II, confirmed on denser exposures.

however at 116% of their laboratory wavelength ([Schmidt 1963](#)). The spectrum and the lines identified are shown in [Figure 1.1](#). The observed wavelength shift was identified with a cosmological redshift of $z = 0.16$, placing the object at a distance of $\simeq 500$ Mpc. Other explanations, e.g. a star with high gravitational redshift, were quickly ruled out, in particular due to the simultaneous observation of the forbidden [O III] transition. Right after Schmidt's discovery, emission lines in other quasars could be identified as well, in particular 3C 48 for which an even higher redshift of $z = 0.37$ was measured ([Greenstein 1963](#)).

These discoveries revealed that quasars are indeed extragalactic objects at cosmological distances and therefore have to be intrinsically extremely luminous. Already [Schmidt \(1963\)](#) concluded that 3C 273 with an apparent r -band magnitude of $m_r = 12.8$ mag has to be about 100× as luminous as a classical galaxy and similarly [Greenstein \(1963\)](#) stated that 3C 48 is 'possibly as bright as -26.3 mag, 10–30 times brighter than the brightest giant elliptical hitherto recognized'.

Since quasars appeared point-like, the emitting region had to be small, e.g. < 1 kpc for 3C 273 ([Schmidt 1963](#)). The observation of quasar variability on timescales of weeks and shorter (e.g. [Smith & Hoeffleit 1963](#)) implied that the emitting region had to be even smaller and cannot exceed 0.15 pc ([Matthews & Sandage 1963](#)), arguing that the light crossing time across the emitting region can not be substantially larger than the timescale on which substantial variability is observed.

It became clear that such enormous luminosities in such a confined region of space can not be powered by nuclear fusion. Therefore, the only plausible explanation for such high power outputs is the accretion of matter onto a black hole ([Salpeter 1964](#); [Zel'dovich 1964](#); [Lynden-Bell 1969](#)). While nuclear fusion, e.g. from hydrogen to helium, which is the dominant power source of all main-sequence stars, transform less than 1% of the rest mass into energy, accretion onto a black hole can be far more efficient.

Matter that is falling onto a black hole can form an accretion disc in which the gravitational energy is transformed via viscous friction into heat and finally radiated away. In this process,

1.1. ACTIVE GALACTIC NUCLEI

matter can spiral down to the innermost stable circular orbit (ISCO) which is for a non-spinning Schwarzschild black hole of mass M_{\bullet} located at a radius

$$r_{\text{ISCO}} = 6 \frac{G M_{\bullet}}{c^2} \approx 6 \text{ AU} \times \left(\frac{M_{\bullet}}{10^8 M_{\odot}} \right) \quad (1.1)$$

with G denoting the gravitational constant and c the speed of light. When arriving at the ISCO and finally plunging into the black hole, a certain fraction of the rest mass M of the infalling matter has been radiated away, according to

$$E = \eta M c^2. \quad (1.2)$$

The radiative efficiency η depends on the spin of the black hole. For non-rotating black hole, $\eta = 5.7\%$. If a black hole is spinning in prograde direction, the ISCO is smaller, the material can drop deeper into the potential well and the efficiency can exceed 30% (Thorne 1974). Since the accretion process would rapidly spin-up a non-rotating black hole, an average efficiency of $\eta = 10\%$ is often adopted, making accretion an order of magnitude more efficient than nuclear fusion.

The first comprehensive description of this accretion process was published by Shakura & Sunyaev (1973), presenting a theoretical explanation for the nature of X-ray binaries. However, quasar can in many ways be understood as a scaled-up version of X-ray binaries, where the central black hole has million or billion solar masses (therefore called supermassive black holes) instead of about one solar mass in the case of stellar X-ray binaries. In consequence, the luminosity of quasars might be higher by a similar amount.

The model of Shakura & Sunyaev (1973) primarily depends on the accretion rate \dot{M} which together with the radiative efficiency η , which itself depends mostly on the spin of the black hole, determines the luminosity of the object. The mass of the black hole has no influence on the luminosity but changes the structure of the disc since the radius of the ISCO depends on M_{\bullet} . A crucial factor for the accretion process is the viscosity in the disc which is required to transport angular momentum from the inner parts of the disc to the outskirts. However, Shakura & Sunyaev (1973) showed that for a large range in possible viscosities the structure of the accretion disc is not significantly changed. Also mentioned here should be the so called *Eddington Limit* which poses an upper limit for the luminosity of an accreting black hole. If the outward directed radiation pressure on the accreting gas exceeds the gravitational pull, no further material can be accreted. The maximal Eddington luminosity is therefore

$$L_{\text{Edd}} = \frac{4\pi G M_{\bullet} c m_{\text{p}}}{\sigma_{\text{Th}}} \approx 33\,000 \frac{M_{\bullet}}{M_{\odot}} L_{\odot} \quad (1.3)$$

in which m_{p} denotes the atomic mass of the gas (here hydrogen) and σ the scattering cross-section of the gas. Here one usually adopts the Thomson cross section σ_{Th} for scattering on free electrons, appropriate for a fully ionized gas. Assuming the validity of this Eddington limit already indicates that the black holes at the centers of quasars must have masses far in excess of tens of millions of solar masses.

1.1.2 The AGN Zoo

Very quickly after the first discovery, it was observed that quasars have a very broad and flat spectral energy distribution (SED), much broader than the approximate blackbody spectrum emitted by stars and galaxies (Oke 1963). It is now clear that accretion of matter onto a SMBH can lead to emission at all observable wavelengths, from the radio regime over the

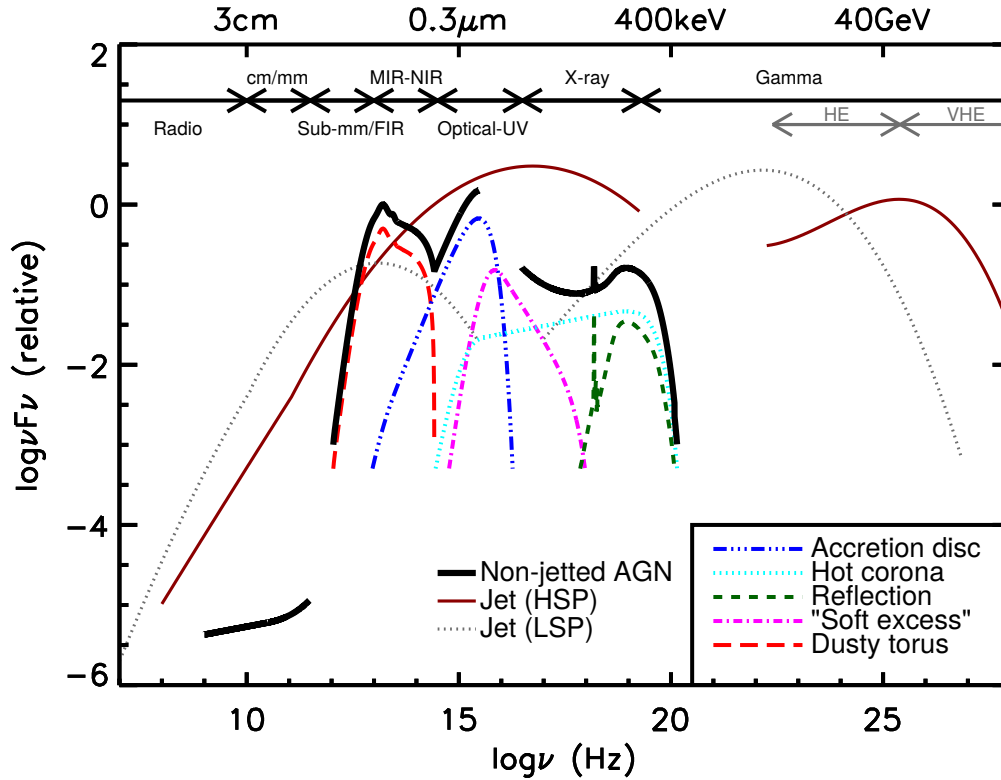


Figure 1.2: Schematic visualization of a quasar SED, taken from Padovani et al. (2017). In the optical and UV regime, the SED is dominated by the emission of the accretion disc, called the *big blue bump*. In the mid-IR, the emission stems from large amounts of hot dust with temperatures around 1000 K. Emission in the X-rays is dominated by a hot corona surrounding the accretion disc. The wavelength ranges between the far UV and soft X-rays are nearly unobservable. Therefore, the knowledge about this parts of the SED is limited. Quasars can have relativistic jets which can lead to substantial emission in the radio regime and if the jet is directed towards Earth also in the γ -rays and TeV regime.

infrared, the optical and UV regime, the X-rays and far into the γ -ray regime, which is illustrated in Figure 1.2. However, this does not mean that accreting SMBHs have a unique appearance across all spectral range. In fact, a rich diversity of object types and observational phenomena are related to more or less the same physical processes.

Since the research on quasars and the whole family of related objects was in the past – and still is – driven mostly by observations and empirical classification, a large *zoo* of different objects exists. Observations in different spectral ranges and with different observational techniques have lead to a complex variety of designations and a rather confusing nomenclature. The same object might have totally different classifications depending on the spectral range in which it is observed. Also, two objects might show the same properties in one spectral regime but have totally different appearances in other spectral ranges. To complicate matters further, the emission in at least some spectral regimes is most-likely highly anisotropic. The same object can therefore have totally different appearances when observed under different orientations and be classified as different types of objects.

Common to all of these object types and classifications is only that they are powered by accretion of matter onto a SMBH at the center of galaxies. For this process the term *Active Galactic Nuclei* (AGN) has been established. Although sometimes used slightly different in the literature, within this thesis, the term *AGN* denotes any kind of object from the whole family of sources that are powered by accretion onto a SMBH. A very brief and in some

aspects simplified overview over the *zoo of active galactic nuclei* is given below. The focus lies mainly on the wavelength regimes relevant for this project, namely the optical and UV. For a more detailed review including all spectral ranges see [Padovani et al. \(2017\)](#).

Radio

As mentioned before, the initial discovery of quasars was related to their radio emission. The emission is of non-thermal origin, showing a power-law behavior related to synchrotron emission of charged particles gyrating at relativistic speeds in magnetic fields. Interferometric observations are often capable to spatially resolve the radio emission. Here, two general types of sources exist, i.e. compact core dominated radio sources and lobe dominated sources ([Fanaroff & Riley 1974](#)). The latter ones show usually two gigantic radio lobes that can extend out to > 100 kpc scales. Often, highly collimated jets can be observed that are launched in the center of the host galaxy and extend outwards into the medium surrounding the galaxy where they are slowed down, shock and power the emission of the gigantic radio lobes. In the cases of core-dominated sources, the jet does not propagate far and the majority of the emission stems from the base of the jet.

If the optical counterpart of the radio source is compact (unresolved) and luminous, the object is classified as *quasi stellar radio source* (quasar) or *radio-loud Quasi Stellar Object* (QSO). In case one observes in optical wavebands at the location of the radio source a classical galaxy, in most cases a giant elliptical, the term *radio galaxy* is used. The first discovered and most-prominent object of this type is Cygnus A ([Baade & Minkowski 1954](#)).

When selecting quasars or QSOs in optical bands and then checking for their radio properties, it turns out that only a moderate fraction of the sources ($\simeq 10 - 20\%$, [Kellermann et al. 1989](#)) emit a substantial fraction of their total luminosity in the radio regime. These objects are called *radio loud*. The rest is classified as *radio quiet*. Since the emission of radio waves is often related to the presence of ultrarelativistic jets, there have been attempts to classify sources instead as *jetted* and *non-jetted* AGN ([Padovani et al. 2017](#); [Padovani 2017](#)).

Optical, Ultraviolet and Near Infrared

Today, the largest fraction of the known quasar sample has been discovered in optical wavebands. In particular the Sloan Digital Sky Survey (SDSS) delivered optical spectra of roughly half a million objects ([Pâris et al. 2018](#)). Contrary to the original meaning of the term *quasar*, a detection of the objects in the radio regime is nowadays no requirement anymore. In fact, most (90%) of the optically selected quasars are *radio-quiet*. More appropriate in this case would be the term *Quasi Stellar Object* or QSO, which makes no statement about the radio properties. However, the terms *quasar* and *QSO* are usually, and also within this thesis, used interchangeably.

In the optical and UV regime, quasar emission is dominated by a bright and blue continuum. It can be approximated with a power-law of the form $f_\lambda \propto \lambda^{-1.7}$ between 1000 \AA and 10000 \AA ([Selsing et al. 2016](#)). However, quasar spectra deviate substantially from a pure power law (see [Figure 1.3](#)) which leads to some ambiguity in the spectral slope. These very blue continua in the optical regime make quasars quite distinct from most stars or galaxies, as already noted by [Sandage et al. \(1965\)](#). At least in the local Universe, quasars can therefore be efficiently identified in optical multi-color photometry by their excess in the blues filters.

The optical and UV continuum emission is mostly thermal and comes from the accretion disc and is sometimes described as the *big blue bump* of the quasar SED (see [Figure 1.2](#)). The basic spectral properties of the emission can be derived from by accretion theory ([Lynden-Bell](#)

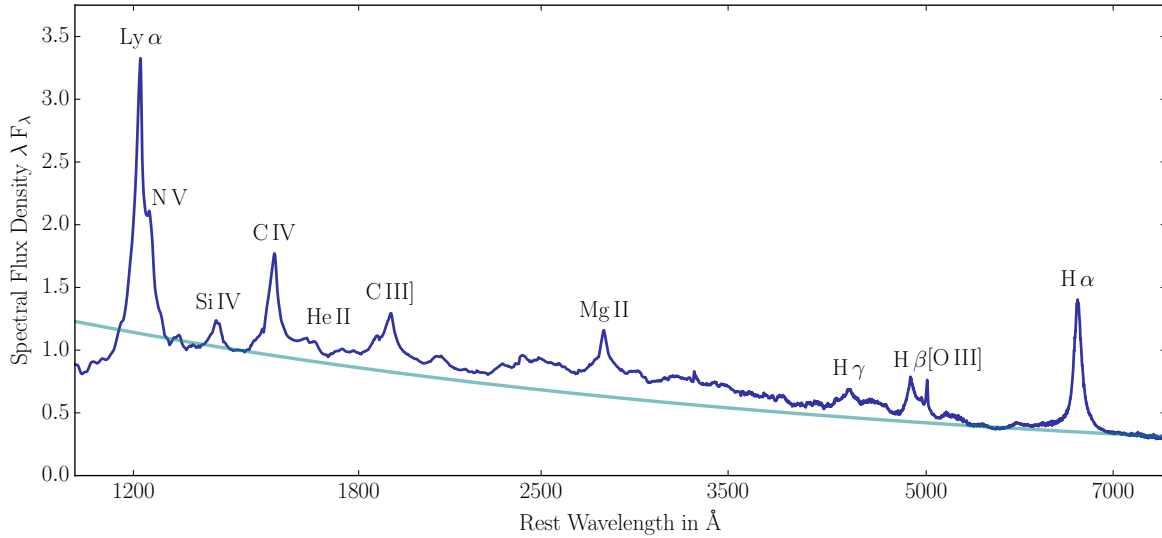


Figure 1.3: Quasar spectrum in the UV, optical and near-IR regime, based on the [Selsing et al. \(2016\)](#) quasar composite. The shown composite is representative for the typical appearance of quasar spectra. Note that for better visualization the wavelength axis is scaled logarithmically and the flux density plotted in terms of λF_λ , identical to νF_ν . The quasar continuum can be approximated by a power law, here of the form $F_\lambda \propto \lambda^{-1.7}$. In addition, quasars exhibit characteristic broad emission lines (see labels), of which many are extremely broad ($\Delta v \gg 1000 \text{ km s}^{-1}$), related to the high velocities of the emitting gas clouds close to the SMBH.

1969; Thorne 1974; Page & Thorne 1974; Shields 1978; Malkan 1983; Laor & Netzer 1989). However, the radiation is significantly reprocessed, making an accurate modeling challenging. The spectra of accretion discs have a cut-off towards short wavelengths, related to the peak temperature of the disc which itself depends on the innermost stable orbit around the black hole. For stellar mass black holes, e.g. in X-ray binaries, this cut-off lies in the X-ray regime and the disc directly contributes to the observed X-ray emission. For supermassive black holes, the peak temperature of the accretion disc is much lower and the cut-off moves in the regime between the far UV and the soft X-rays. Unfortunately, this spectral range between $\simeq 10 \text{ eV}$ and 200 eV is nearly unobservable due to the H I absorption in the interstellar medium of the Milky Way and a comparison of the theory to observations not possible.

In addition to the continuum, quasars show broad ($\Delta v \gg 1000 \text{ km s}^{-1}$) emission lines of e.g. H I, most prominently the Balmer series in the optical and the Lyman series in the UV, but also high-ionization metal lines like N V, Si IV, C IV, C III], or Mg II (see Figure 1.3 for an example spectrum). The emission comes from photoionized gas close to the black hole which is illuminated by the intense UV radiation from the accretion disc. The large widths of the lines, up to 10000 km s^{-1} , are attributed to the high velocities at which the gas is moving. Assuming Keplerian motion, this corresponds to distances of $\simeq 1000 r_S$ Schwarzschild radii from the black hole. The diverse and asymmetric shapes of the broad emission lines, in particular of the C IV line, reflect the complexity of the processes taking place in the emitting region.

In addition to the broad lines, there are narrow emission lines of forbidden, non-resonant transitions, most importantly [O III]. Since these emissions lines can only be produced in low-density environments and have widths of a few 100 km s^{-1} , they probably originate from photoionized gas at much larger distances from the black hole than the broad lines.

Apart from quasars, there are also so-called *Seyfert galaxies*. Originally discovered by [Seyfert \(1943\)](#), they were the first objects in the AGN family to be discovered. Seyfert galaxies are classical (spiral) galaxies that show unusual high-ionization emission lines in their

spectra. They can be subdivided in two types (Khachikian & Weedman 1974): Seyfert Type I galaxies exhibit very broad $> 1000 \text{ km s}^{-1}$ emission lines and a unusually bright and compact nucleus that emits a blue continuum emission. Seyfert Type II galaxies show emission lines of the same high-ionization species as seen in Type I, but the lines are much narrower and these galaxies do not exhibit a bright core. The same narrow lines are often also present in Type I, superimposed on the broad lines, which suggests some commonality between Type I and Type II Seyfert galaxies.

The central cores of Seyfert I galaxies have spectral characteristics very similar to those of quasars. They can therefore be seen as a low-luminosity version of a quasar. The classical dividing line between Seyfert I galaxies and quasars is a luminosity of $M_B = -22.3 \text{ mag}$, but more generally, a quasar dominates and completely outshines the stellar emission of its host galaxy while in a Seyfert galaxy the central AGN has a luminosity low enough that the galaxy around it is well visible.

Mid Infrared

Quite early, it was discovered that the spectra of quasars rises from the I band towards the K band (Johnson 1964; Low & Johnson 1965). This makes the SED even more dissimilar from stars or classical galaxies. Nowadays, this IR emission is attributed to the presence of large amounts of hot dust in AGN. The dust absorbs a substantial fraction of the optical and UV emission of the accretion disc and re-radiates it in the mid IR between $1 \mu\text{m}$ and a few tens of μm (see Figure 1.2). This leads to the so called *IR bump* in the SED of AGN, which can comprise comparable amounts of energy as the *big blue bump*. It is assumed that the dust extends inwards down to the radius at which it sublimates, corresponding to temperatures of up to 2000 K.

While many spectral characteristic in the radio, optical or X-ray regime might or might not be present, depending on the type of AGN, the strong mid-IR emission seems to be a *virtually universal* (Rieke 1978) characteristic for every type of AGN. Only very few AGN seem to be free of hot dust (e.g. Whysong & Antonucci 2004; Perlman et al. 2007; Jiang et al. 2010). The mid-IR emission is also a phenomenon rather unique for AGN. While luminous IR galaxies also have large amounts of dust, heated by massive star burst, this dust is colder ($T < 50 \text{ K}$ Magnelli et al. 2012) and does not reach the high temperatures seen in AGN.

Therefore, AGN can be very efficiently selected using mid-IR photometry (Stern et al. 2005, 2012; Assef et al. 2013). In particular the all-sky survey conducted by the *Wide-field Infrared Survey Explorer* (*WISE*, Wright et al. 2010) at $3.6 \mu\text{m}$ and $4.5 \mu\text{m}$ is sensitive to the characteristic mid-IR features of AGN and widely used to discover AGN, also within this study (see § 2.1.3).

X-Ray

The production of X-rays is another nearly universal feature of AGN activity (see e.g. Gilfanov & Merloni 2014, for a review) and therefore a rather reliable way to select AGN (Lusso et al. 2013; Marchesi et al. 2016). In fact, nearly all (luminous) extragalactic X-ray sources are AGN. The X-rays are produced by inverse Compton up-scattering of UV photons in a hot *corona* above the accretion disc. However, neither the exact geometry nor the details of the process are well understood.

The advantage of X-ray observations is, that they can penetrate through rather thick columns of gas or dust. Therefore, many optically obscured AGN can still be observed in the X-ray

CHAPTER 1. INTRODUCTION

regime. However, at extremely high column densities of $N_{\text{H}} \gtrsim 1/\sigma_{\text{Th}} = 1.5 \times 10^{24} \text{ cm}^{-2}$ ¹, the gas becomes *Compton thick*, meaning that the scattering of X-rays on free electrons makes the gas opaque. The number of AGN that escape detection in the X-ray regime due to the high column densities of intervening gas is debated, which poses a substantial limitation for compiling a complete census of AGN.

γ and TeV

AGN can produce electro-magnetic radiation up to the highest observable energies in the γ and TeV range (Padovani et al. 2017). This requires the presence of a ultrarelativistic jet that is closely aligned with the line of sight towards the observer. Objects of this type are called *Blazars* or for lower luminosity objects *BL Lacertae object*. The spectrum of these sources is a relatively flat power law without noticeable emission lines, making a redshift determination difficult. Since the jets are highly collimated and have a narrow opening angle, these objects are rare.

1.1.3 AGN Unification

Over the years, similarities and relations between the different object types within the AGN zoo were discovered. This led to concepts that explain a variety of observations with a rather simple model. These theories also suggests that many—or maybe even all—objects in the AGN family are governed by the same underlying mechanisms and are therefore intrinsically more or less identical. This is therefore called *AGN unification* and described in the following.

Striking evidence for the proposed unification model comes from the spectroscopic observations of Seyfert II galaxies in polarized light as presented in Antonucci (1984), Antonucci & Miller (1985) and Miller et al. (1991). For Type II sources that only exhibit narrow emission lines (e.g. NGC 1068), broad lines are visible when only referring to the polarized light. This indicates that there is no intrinsic difference between Seyfert Type I and Type II galaxies and that the broad lines as well as the optical and UV continuum are present in both types of objects. The only difference is that in Type IIs the direct sight onto the gas emitting the broad lines is blocked by an optically thick disc and does usually not reach the observer. When observing in polarized light however, one is sensitive to light that has been scattered and can via this *detour* still reach the observer. The scattering material are most-likely free electrons, as suggested by the low dependence of the polarization degree on wavelength, located above and below the obscuring disc. They provide an *electron-scattered image* of the central region of the AGN. The total amount of this scattered light is rather small, typically a few percent, but by analyzing the polarization properties of the radiation, the majority of direct and therefore unpolarized emission can be suppressed, allowing the detection of the scattered and therefore polarized light of the broad lines. Since the polarization direction is perpendicular to the jet axis as inferred from radio images, the picture emerges that the disc is located in the equatorial plane while the jets are launched in the polar directions. These observations have provided strong evidence that the different appearances of Seyfert I and Seyfert II galaxies are not related to an actual physical difference but purely an orientation effect. As suggested by Antonucci & Miller (1985), a Seyfert II galaxy is an AGN seen from the side or *edge on*. If one would observe the same object more from the polar direction, it would appear as a Seyfert I galaxy.

¹The opacity stems from free electrons, but since the gas is assumed to be fully ionized and mostly composed of hydrogen, this column density is for easier comparison to other observations usually expressed as hydrogen column density

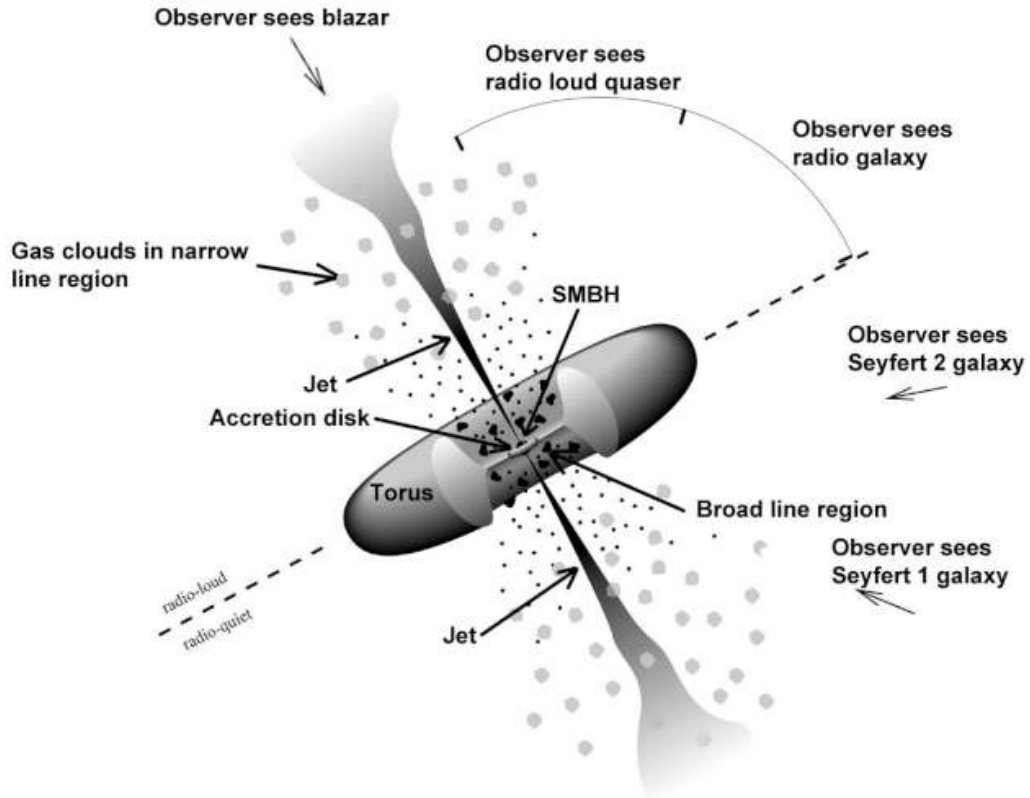


Figure 1.4: Illustration of the AGN unification model, showing the different components of the AGN and indicating the various types of objects an observer sees depending on his orientation with respect to the AGN. Note that the illustration is not to scale. Graphic taken from <https://fermi.gsfc.nasa.gov/science/eteu/agn/> but the original version of the figure was first published by Urry & Padovani (1995).

The narrow emission lines show a low degree of polarization in Type I and Type II. Their light apparently reaches the observer on a direct path (Antonucci & Miller 1985). This leads to the conclusion that the gas emitting the narrow emission lines has to be further away from the black hole, in a region that is not obscured.

Within the years, the initial ideas presented by Antonucci & Miller (1985) developed into a full *unified scheme of AGNs* that can explain the basic properties of nearly all members of the AGN zoo and relate their diverse appearances to just differences in luminosity, orientation with respect to the observer and the presence or absence of strong relativistic jets. While early ideas reach back to Greenstein & Schmidt (1964), substantial progress was only made in the mid 1980s and 1990s (see Antonucci 1993; Urry & Padovani 1995; Netzer 2015).

The model, which is illustrated in Figure 1.4, contains the following components:

- **Black Hole** sits in the center of the AGN and has a mass between $10^6 M_{\odot}$ and $10^{10} M_{\odot}$. It accretes matter at rates up to a few $M_{\odot} \text{ y}^{-1}$ in luminous objects. All scales given in the following depend on the mass of the black hole and/or on the luminosity and therefore accretion rate of the black hole.
- **Accretion Disc** is directly responsible for the emission of the optical and UV continuum (big blue bump). It extends inside to the ISCO at $\approx 6 r_{\text{S}}$ or 6 AU (for $M_{\bullet} = 10^8 M_{\odot}$) where the hottest temperatures occur. The peak temperature and therefore the high-frequency cutoff of the accretion disc spectrum depends on the mass of the black hole.

CHAPTER 1. INTRODUCTION

The accretion disc is probably surrounded by a hot corona which is responsible for the X-ray emission, produced by inverse Compton scattering of UV photons (e.g. Haardt & Maraschi 1993).

- **Broad Line Region** is the source of the broad lines and consists of photoionized gas that is illuminated by the UV continuum of the accretion disc. Velocities in the broad line region reach up to 10000 km s^{-1} , leading to the large width of the broad lines. The broad line region is located at distances of about 1000 AU to 10000 AU from the central black hole. It has been speculated that the broad line region is just the natural extension of the torus inside the dust sublimation radius. However, the exact geometry and structure of the broad line region is unclear.
- **Dusty Torus** is a geometrically thick structure outside the dust sublimation radius at parsec scales. It therefore contains large amounts of dust, making it opaque at optical and UV wavelength and leading to the obscuration of the accretion disc and the broad line region in Type IIs. The torus is also responsible for the mid-IR emission. The absorbed energy heats the dust to high temperatures $\simeq 1000 \text{ K}$ which is then re-radiated in the mid-IR around $1 - 30 \mu\text{m}$. This concept goes beyond the model proposed in Antonucci & Miller (1985), where the IR emitting dust was treated independently from the obscuring disc. However, there are several arguments that mid-IR emission and obscuration of the accretion disc are caused by the same dusty structure. First, dust has a large absorption cross section in the optical and UV regime. In addition, the strong mid-IR emission is observed in every AGN and also in unobscured Seyfert Is and quasars. This suggests that large quantities of dust are present in these objects but located in a way that they do not obscure the sight onto the accretion disc and the broad line region. The dust therefore shares all properties of the obscuring disc proposed in Antonucci & Miller (1985) and it makes sense to associate these two components with each other. Also, the strong mid-IR emission has to be powered in some way. Absorption of $\simeq 50\%$ of the UV continuum is a straight forward explanation to produce the observed SED (see Figure 1.2). Assuming a torus geometry is just the simplest possible shape one can assume since the structure has to be geometrically thick to shield the central accretion disc towards a substantial part of the full sphere and can not extend inwards of the dust sublimation radius. However there is still much debate about the exact geometry and structure of the torus. It was been argued that the torus might be just the flared outer and dusty part of the accretion disc. There is also debate about the distribution of the dust in the torus, e.g. if the dust is clumpy (e.g. Nenkova et al. 2002) or evenly distributed (Dullemond & van Bemmelen 2005).
- **Narrow Line Region** is the source of the narrow emission lines and located outside the torus at distances up to 1 kpc. Therefore, it is not obscured by the dust and seen in Type Is as well as Type IIs. The gas is photoionized, has a low density ($< 10^9 \text{ cm}^{-3}$), allowing the presence of forbidden emission lines like [O III].
- **Relativistic Jet**, if present, is launched towards the polar axis and if the line of sight towards the observer is aligned with the polar axis of the AGN, the observer sees a blazar. The radiation in this case is produced by high energetic charged particle accelerated in the jet and subject to strong relativistic beaming. This leads to a rather flat spectrum across all wavelength ranges. Jet are also responsible for the radio emission in radio loud AGN and power the large radio lobes. However, $\approx 90\%$ of the AGN are radio quiet and in this cases no evidence for (strong) jets is observed. The reason for *radio loudness* is unclear.

This AGN structure as it is illustrated in Figure 1.4 can be observed under three distinct groups of viewing angles:

1.1. ACTIVE GALACTIC NUCLEI

If an observer is located along the polar axis of the AGN and looks straight into the jet, the AGN will appear as blazar, BL Lac object or *Flat Spectrum Radio Quasar*. Since the opening angle of the jets is small ($\lesssim 15^\circ$, Urry & Padovani 1995; Giommi et al. 2013) such a configuration is rare and these objects appear in low numbers.

If the observer sees the AGN at moderate inclination, i.e. from outside the jet ($\gtrsim 15^\circ$) but still not edge-on ($\lesssim 60^\circ$), he has a direct and unobstructed sight onto the innermost parts of the AGN, in particular the accretion disc and the broad line region. The blue optical and UV continuum is therefore visible as well as the broad emission lines and the X-ray emission, leading to the classification of the object as quasar or Seyfert Type I galaxy.

If observed at rather high inclination ($\gtrsim 60^\circ$, nearly edge-on), the dusty torus blocks the direct sight onto the accretion disc and the broad line region. The object will appear as Seyfert II galaxy or *obscured quasar*, the high-luminosity analog of a Seyfert II. X-ray emission is still detected as long as the column density is low enough ($N_{\text{H}} \lesssim 10^{23} \text{ cm}^{-2}$) to not render the AGN *Compton thick*. In case the object has a jet and is radio-loud, one might observe a radio galaxy, probably exhibiting large radio lobes.

All orientations given above are stated with respect to the axis of the AGN. This does not necessarily correlate with the orientation of the host galaxy. The presence of jets and strong emission in the radio regime has to be seen as a sort of *add-on* to the properties in the other spectral ranges that independently might be there or might not (Antonucci 1993). There are correlations of radio loudness with properties of the host galaxy, e.g. morphology (radio galaxies are often cD galaxies) or the host also mass. It is also sometimes assumed that radio loud AGN host extremely massive SMBH that accrete at a very low fraction of the Eddington luminosity. However, the true cause for radio loudness is so far unknown, to some degree related to the difficulty of uniformly selecting AGN across different spectral ranges.

It has to be noted that the unified scheme as outlined above is intended to bring structure in the zoo of AGN but merely a cartoon and not capable to explain all AGN phenomena in detail (see already Antonucci 1993). Also, the geometry and spatial arrangement of the components is approximate, as well as their relative sizes. Alternative schemes have been proposed as well to e.g. explain the nature of the so called *broad absorption lines* seen in the optical spectra of $\approx 10\%$ of the quasars (Elvis 2000). The uncertainty about the structure of AGN and the details of the ongoing physical processes is related to the compactness of the sources. Resolving spacial scales of $\lesssim 1 \text{ pc}$ at cosmological distances of $\gtrsim 100 \text{ Mpc}$ is extremely challenging. For a few of the closest Seyfert galaxies, resolved observations of the warm and hot dust could be obtained using the VLT Interferometer (e.g. Hönig & Kishimoto 2017). Attempts to resolve the broad line region have been unsuccessful for a long time (e.g. Stern et al. 2015). However, the recent interferometric spectro-astrometric observations of 3C 273 by the GRAVITY Collaboration et al. (2018) achieve a precision of $\approx 10 \mu\text{arcsec}$, sufficient to gain spatial information about the broad line region. These observations show clear evidence that the gas in the broad line region exhibits ordered motion, consistent with rotation in a thick disc and confirm the *standard picture* described by e.g. Antonucci (1993); Urry & Padovani (1995).

One key property of the unification scheme is the amount of obscuration. In the described model, the UV continuum is emitted in two wide cones towards the polar axes of the AGN but blocked by the torus in the equatorial plane. However, the thickness of the dusty torus and therefore the fraction of the unit sphere around the AGN towards which the AGN is obscured Ω_{obsc} is poorly constrained. Alternatively, the amount of obscuration can also be parametrized by the (half-)opening angle of the emission cones α . Determining the shape of these ionizing cones would give insights into the structure of AGN, without the need to resolve these scales.

CHAPTER 1. INTRODUCTION

For a few nearby Seyfert galaxies, [O III] narrow band images show extended, highly anisotropic narrow line regions which shapes roughly resemble the form of two cones (Pogge 1988; Tadhunter & Tsvetanov 1989; Wilson et al. 1993). However, this is no direct measure of the opening angle of the emission since the shape of the extended narrow line region could be governed by the distribution of the illuminated gas.

Within the AGN unification framework and assuming that all AGN are identical, the fraction of obscured objects (i.e. Type II quasars) f_{obsc} is directly related to the fraction of the sky (solid angle) towards which each individual quasar is obscured Ω_{obsc} . Determining this fraction would therefore give key insights into the covering fraction of the torus and therefore the inner arrangement of the AGN. To conduct such a measurement, one requires observations in a spectral range where the AGN emission is (mostly) isotropic, e.g the mid-IR or the X-ray regime, and determine the number of objects which are luminous in the optical or UV regime as well.

Current studies report obscured fractions in the range $f_{\text{obsc}} \sim 30\% - 70\%$ (Simpson 2005; Brusa et al. 2010; Assef et al. 2013; Lusso et al. 2013; Buchner et al. 2015; Marchesi et al. 2016), but with substantial uncertainties. Also, it has been argued that not all AGN are actually identical, but that instead the obscured fraction decreases strongly with luminosity (e.g. Simpson 1998; Hönig & Beckert 2007; Assef et al. 2013). This can be understood in the context of the so-called *receding torus* model (Lawrence 1991) in which the intense radiation from very luminous AGN destroys or removes most of the dust. However, in contradiction to this, there have been studies that found no evidence for a luminosity dependence (e.g. Lusso et al. 2013). Also, some models favor a quite different geometry for the dust distribution or a different mechanism for the obscuration (e.g. Elvis 2000; Elitzur & Shlosman 2006; Keating et al. 2012). In particular, VLTI observations by Hönig & Kishimoto (2017) suggest that the hot dust observed in the near-IR is predominantly located along the polar axis of the AGN while the colder dust responsible for the mid-IR emission is in the equatorial plane. Buchner & Bauer (2017) attribute at least some of the obscuration to the host galaxy instead of a parsec scale torus. Other studies report observations incompatible with the idea of unification, e.g. Villarreal et al. (2017) who claim substantial differences in the supernova rate in Type I and Type II AGN or DiPompeo et al. (2017) who report different clustering properties for obscured and unobscured quasars. These intrinsic differences in the host galaxy properties of Type Is and Type IIs – if confirmed – is incompatible with the concept that obscuration is just a matter of orientation with respect to the line of sight and might point towards a rather different mechanism for the Type I / Type II dichotomy. One concept quite different was put forward by e.g. Hopkins et al. (2007). Here, Type I and II quasars are different evolutionary stages of the same object. After a galaxy merger, which is supposed to trigger a massive star burst and feed material to the the SMBH, the AGN first runs through a phase in which it is fully obscured and only after a *blowout* gets rid of the dust and appears as an unobscured quasar.

These examples show, that the geometry of the obscuring material and the UV emission of quasars is still highly uncertain. AGN unification models (Antonucci 1993; Urry & Padovani 1995; Netzer 2015) have been highly successful in explaining the emission properties of AGN with a relatively simple model and relate the observed dichotomy between Type I and Type II quasars (broad emission lines and bright UV continuum vs. only narrow lines) to the presence of a dusty torus and its orientation with respect to the observer. While this picture is widely accepted, the ultimate confirmation is still missing since each quasar can only be seen from a single vantage point. One possible strategy to circumvent this problem and to infer the three dimensional emission geometry of individual quasars is the *quasar proximity effect* (§ 1.3), which is the topic of this thesis.

1.1.4 Lifetime of Quasars

Another important property of AGN is the duration of their activity phases. While every massive galaxy is expected to host a SMBH, most of them remain in a quiescent stage and only a small fraction appear as luminous quasars at any given time. On the other hand, it is assumed that each galaxy at least once went through a luminous quasar phase and by this process grew its SMBH to its current mass. On short timescales, e.g. years to decades, quasars show sustained activity with variability of a few tenths of a magnitude (e.g. Sesar et al. 2007; MacLeod et al. 2010, 2012), but on longer timescales quasar lightcurves are virtually unconstrained by observations (e.g. Martini 2004). The processes which trigger quasar activity are presently unknown and models deliver a diversity of explanations for the sources of nuclear activity (e.g. Springel et al. 2005b; Hopkins et al. 2007; Novak et al. 2011; Cisternas et al. 2011). Inferring the duration of quasar activity phases would be crucial to gain insights into the physical processes that feed matter to the black holes and drive AGN activity.

In addition, due to their high luminosity, quasars have a profound impact on their environment on various scales. Quasar feedback for instance is usually invoked in galaxy formation simulations (Di Matteo et al. 2005; Hopkins et al. 2008a,b) to regulate the growth of massive galaxies and to match the galaxy luminosity function at the high-mass end. Also, quasars are the dominant source of hard ionizing photons ($E \gg 1 \text{ Ry}$) in the Universe and it has been proposed that *quasar flickering* could have a substantial impact on the ionization state of metals in the circumgalactic medium (Oppenheimer et al. 2018; Segers et al. 2017). On even larger scales, quasars dominate the metagalactic UV background at $z \lesssim 3.5$ (Faucher-Giguère et al. 2009; Haardt & Madau 2012; Khaire & Srianand 2018; Kulkarni et al. 2018a), which maintains the photoionization of the intergalactic medium (IGM) and drives the reionization of HeII (a more detailed description of this is given in §1.2.4). Therefore, quasars are directly responsible for the thermal and ionizing state of the IGM. A reliable constraint on the emission history of quasars would therefore be of interest for many fields in astronomy.

However, observations have so far not converged on a conclusive picture (see e.g. Martini 2004 for a review) and theoretical investigations lack predictive power (e.g. Springel et al. 2005b; Hopkins et al. 2007; Novak et al. 2011). In addition, different techniques are sensitive to different time scales, in terms of duration, but also regarding the kind of activity, which makes it difficult to compare different studies.

An upper limit for the duration of the luminous quasar phase around 10^9 yr comes from demographic arguments and the evolution of the AGN population, i.e. the rise and fall of the quasar luminosity function (see e.g. Kulkarni et al. 2018a).

Clustering measurements of quasars can estimate the host halo mass of quasars and by comparison to models of cosmic structure formation determine the fraction of halos that host a quasar. This measurement of the *duty cycle* can be converted in a quasar lifetime constraint t_{dc} , arguing that if *now* a certain fraction of halos with a given mass hosts a quasar, each of these halos itself should host a quasar for the same fraction of the Hubble time. Studies of this kind suggest values for t_{dc} between 10^7 yr and 10^9 yr (Adelberger & Steidel 2005; Croom et al. 2005; Shen et al. 2009; White et al. 2012; Conroy & White 2013; La Plante & Trac 2016). However, t_{dc} is only a measure for the integrated time a galaxy shows luminous quasar activity but does not constrain the duration of individual phases. It can not be distinguished if the time t_{dc} is spent in one long quasar phase or in a large number of short bursts. Also, duty cycle measurements have large uncertainties due to the unknown way quasars populate dark matter halos.

As already proposed by Soltan (1982), AGN activity leads to the growth of SMBHs and the current population of (quiescent) SMBHs in the centers of galaxies should relate to the past

CHAPTER 1. INTRODUCTION

accretion history and therefore total radiation emitted by quasars over cosmic history. Studies focusing on this mass assembly of SMBHs are sensitive to the total black hole growth time which might also include non-luminous or obscured phases. Constraints from such studies (e.g. Yu & Tremaine 2002; Shankar et al. 2009; Kelly et al. 2010) are between 30 and 150 Myr.

These methods mentioned above are of statistical nature and estimate population-averaged properties. Other methods focus on individual quasars and use the presence of a tracer that is sensitive to the quasar luminosity at some time in the past. They therefore measure for how long a quasar has been active (usually in terms of emitting ionizing UV photons) prior to the observation. This is denoted within this thesis as *quasar age* or t_{age} . For simplicity, and since more detailed measurements are often impossible, it is in this context usually assumed that quasars emit only a single burst in which they *turn on*, shine with constant luminosity for some time and *turn off* again. The duration of the activity in this *lightbulb model* is described as the *quasar lifetime* or t_{Q} (see e.g. Figure 4.8 in § 4.2.3 for a visualization and more detailed discussion). A measurement of t_{age} clearly constrains the quasar lifetime, but it has to be stressed that both quantities are distinct and $t_{\text{age}} \leq t_{\text{Q}}$. The assumption of a lightbulb model is clearly a simplification and realistic quasar lightcurves are certainly more complex. The ultimate goal has therefore to be a measurement of the full quasar lightcurve. This has so far not been possible but in § 5 we will describe how the work presented in this thesis could lead to such a measurement.

Currently, constraints for sustained activity over at least 10^6 yr comes e.g. from the presence of enormous Ly α nebulae around luminous quasars (Cantalupo et al. 2014; Hennawi et al. 2015). On slightly larger scales geometric constraints of $t_{\text{age}} \lesssim 8$ Myr might be derived from fluorescent Ly α emission of galaxies caused by the UV radiation of a nearby quasar as claimed by Cantalupo et al. (2012), Trainor & Steidel (2013) or Borisova et al. (2016). Even higher quasar ages around 10^7 yr are reported by Gonçalves et al. (2008) based on metal absorption systems in the vicinity of quasars. In contrast to this, Schawinski et al. (2015) claim a rather short quasar lifetime between 10^4 and 10^5 yr. All these studies have in common that they are based on only few quasars, have a rather limited range of timescales to which they are sensitive and suffer from various kinds of systematic uncertainties.

The most promising way to characterize quasar emission histories is related to their impact on the surrounding intergalactic medium (IGM). Since quasars are powerful sources of ionizing radiation, they create so called *proximity zones* in the IGM, megaparsec sized regions with enhanced photoionization. These regions contain detailed information about the past quasar emission. In the following, we will explain this effect in detail, describe how the studies of the Ly α forest in the spectra of background sources can be used to determine the ionization state of the IGM and give an overview of the existing lifetime constraints derived from the quasar proximity effect.

1.2 The Large Scale Structure of the Universe

Right after the *Big Bang*, the Universe was in a hot, dense and homogeneous state. At redshift of $z \approx 1100$, the Universe had cooled to temperatures below ≈ 3000 K, leading to the recombination of protons and electrons to neutral gas, nearly exclusively hydrogen and helium. This absence of free charges made the Universe transparent for photons below the ionization energy of hydrogen ($13.6 \text{ eV} = 1 \text{ Ry}$), resulting in the release of the Cosmic Microwave Background (CMB), which therefore could propagate freely and is nowadays observed as nearly perfectly isotropic and uniform blackbody spectrum with a temperature of $T_{\text{CMB}} = 2.7 \text{ K}$ (Alpher & Herman 1948; Penzias & Wilson 1965; Mather et al. 1994; Planck Collaboration et al. 2018). At the time of the CMB release, approximately 380 000 yr after the Big Bang, density fluctu-

1.2. THE LARGE SCALE STRUCTURE OF THE UNIVERSE

ations in the Universe were extremely small, of the order $\frac{\Delta\rho}{\rho} \approx 10^{-5}$ for baryons (Smoot et al. 1992). Since then, these density fluctuations did grow, primarily driven by the gravity of the Cold Dark Matter (CDM), and have led to the formation of collapsed structure, i.e. halos hosting galaxies and galaxy clusters (e.g. Press & Schechter 1974; Peebles 1980; Blumenthal et al. 1984).

This formation of cosmic structure is nowadays very well understood within the Λ -Cold Dark Matter paradigm (Λ CDM). Here, cold dark matter drives the hierarchical collapse of matter into cosmic sheets, filaments and halos, resulting in the structure called the *cosmic web*. The space between the filaments is occupied by underdense regions, so called *voids* (e.g. White & Rees 1978; Bond et al. 1996).

Breakthrough of this concept occurred in the early 2000s with the first massive (e.g. 100 Mpc box size) numerical cosmological simulations (e.g. Springel et al. 2005a). While these initial *collisionless* simulations did only track dark matter particles and their gravity, they were still able to reproduce observations quite accurately on large scales e.g. the distribution of galaxies (Springel et al. 2006). The reason for this is that on large scales, much larger than the halo size of galaxies, baryons trace dark matter to high accuracy. Nowadays, state-of-the-art cosmological hydrodynamical simulations also include baryons and their complicated physical effects, e.g. heating and cooling processes, shocks, ionization and chemical composition, as well as the formation of stars and galaxies (Vogelsberger et al. 2014; Lukić et al. 2015; Schaye et al. 2015; Bolton et al. 2017).

1.2.1 The Intergalactic Medium

A particular rich field for the study of the large scale structure of the Universe is the Intergalactic Medium (IGM). At high redshift ($z \gtrsim 3$), most of the baryons in the Universe are not located in collapsed structures like galaxies or galaxy clusters. Instead, they are situated in the IGM which fills the vast space between galaxies and has a very low density of $n_{\text{H}} \simeq 10^{-6} \text{ cm}^{-3}$. Its chemical composition is primordial, i.e. consisting nearly exclusively of hydrogen (70 %) and helium (30 %) (e.g. Coc et al. 2015). Since the IGM occupies low cosmic overdensities of $\frac{\Delta\rho}{\rho} \lesssim 10$ and is governed by relatively simple physics, it can to reasonable precision be described by e.g. a perturbation approach for the growth of cosmic structure (Zel'dovich 1970, but see also White 2014) and analytic descriptions for the thermal state (Hui & Gnedin 1997). For the same reason, the IGM can, in contrast to e.g. galaxy formation, rather easily be reproduced in cosmological hydrodynamical simulations, which now achieve percent level accuracy in the relevant observables like the power spectrum (Lukić et al. 2015). However, the densities in the IGM are usually far too low to observe the gas in emission. Instead, a highly efficient and very successful method is to take spectra of distant bright background sources and study the absorption imprinted by the IGM onto the continuum emission of the background source.

1.2.2 The Lyman α Forest

The discovery of quasars at high redshift allowed for the first time to observe the rest-frame UV continuum of quasars. Confronted with the spectrum of 3C 9 at $z = 2.01$ taken by Schmidt (1965), Gunn & Peterson (1965) very quickly realized that the observation of substantial transmission at wavelength shorter than the quasars Ly α emission line had tremendous implication for the ionization state of the IGM and therefore for the Universe as a whole.

They pointed out (but see also Scheuer 1965) that the Ly α line of neutral hydrogen in the intergalactic medium between Earth and the quasar should lead to substantial absorption. From the spectrum they estimated an average transmission at $\lambda_{\text{rest}} < 1216 \text{ \AA}$ of $\simeq 60\%$,

CHAPTER 1. INTRODUCTION

which corresponds to an HI density of $n_{\text{HI}} \approx 6 \times 10^{-11} \text{ cm}^{-3}$. From this measurement, Gunn & Peterson (1965) concluded that only a tiny fraction of 2×10^{-7} of the cosmic mass can be in the form of neutral hydrogen. Although at that time the cosmological models and the density distribution in the intergalactic medium were highly uncertain and the transmission measurement itself approximate, it was clear that only a vanishingly small fraction of the IGM can be neutral gas and the Universe had to be most-likely highly ionized. Gunn & Peterson (1965) speculated that the IGM could be kept ionized by collisional ionization or photoionization and therefore spread the initial idea for the now accepted concept of a metagalactic UV background that keeps the Universe in a highly ionized state. This also implied that there had to be an *Epoch of Reionization* (EoR) during which the Universe, which had become mostly neutral when matter and radiation decoupled (at $z \approx 1100$) and the CMB was released, was re-ionized again. Nowadays, it is assumed that this EoR occurred (at least for the hydrogen in the Universe) between redshifts of $z \approx 6$ and $z \approx 10$ (Planck Collaboration et al. 2018; Davies et al. 2018; Mason et al. 2018).

Subsequent observations (see e.g. a review by Rauch 1998 for more details) revealed that the intergalactic HI absorption is not homogeneous but actually composed of a large number of individual absorption lines. However, these lines are narrow (a few tens of km s^{-1}), requiring high spectral resolution to resolve them. Baldwin et al. (1974) confirmed that these absorption lines are actually caused (as expected) by neutral hydrogen. The evidence comes from the simultaneous observing of Ly α and Ly β lines related to the same absorption systems.

For the whole complex of individually narrow Ly α absorption lines in quasar spectra that together cause a substantial reduction in transmission, e.g. an absorption of 40% in the 3C 9 spectra, Weymann et al. (1981) formed the term *Lyman α forest*. An example for this is given in Figure 1.5. It shows why one might associate the numerous IGM absorption lines visible in high-resolution quasar spectra with the individual trees in a forest.

The nowadays still accepted picture of the Ly α forest was presented by Sargent et al. (1980), but see also reviews by Rauch (1998), (Meiksin 2009) and McQuinn (2016). Despite the quite clear interpretation by Gunn & Peterson (1965), there had lasted some debate about the degree to which the absorption lines seen in quasar spectra are caused by the intervening IGM or might be associated with the background quasar itself. Sargent et al. (1980) presented convincing evidence that nearly all hydrogen Ly α lines have to be of cosmological origin, while the population of metal absorption lines present as well have to be associated with the quasars. Due to their cosmological origin, each HI Ly α line is located at a different redshift and therefore observed at a different wavelength in the spectrum. Sargent et al. (1980) also determined the basic properties of the gas clouds responsible for the Ly α forest absorption. In particular, they confirmed that the gas is in photoionization equilibrium with the metagalactic UV background, having a neutral fraction of $X_{\text{HI}} = \frac{n_{\text{HI}}}{n_{\text{H}}} \simeq 10^{-5}$ and densities of $n_{\text{H}} \simeq 10^{-4} \text{ cm}^{-3}$. They also determined the average IGM temperature to $T_{\text{IGM}} \simeq 3 \times 10^4 \text{ K}$, characteristic for photoionized gas. However, these quantities can depend quite strongly on redshift.

A breakthrough for IGM studies occurred in the late 1990s with the introduction of a new generation of powerful high-resolution echelle spectrographs on 8–10 m class telescopes, most importantly the *High Resolution Echelle Spectrometer* (HiRes, Vogt et al. 1994) at the Keck I telescope on Mounakea, Hawaii and later the *Ultraviolet and Visual Echelle Spectrograph* (UVES, Dekker et al. 2000) at the ESO VLT observatory in Chile. While before, with 4-m-class telescopes, high-quality high-resolution spectra could only be obtained for the brightest quasars and still required tremendous integration times, these new instruments allowed to observe large numbers of quasars at high resolution, e.g. $R = \frac{\lambda}{\Delta\lambda} > 50\,000$, corresponding to $\Delta v < 6 \text{ km s}^{-1}$, and high signal-to-noise, up to $S/N > 100$. Such high spectral resolution is required to resolve individual Ly α forest lines which have minimum widths related to their

1.2. THE LARGE SCALE STRUCTURE OF THE UNIVERSE

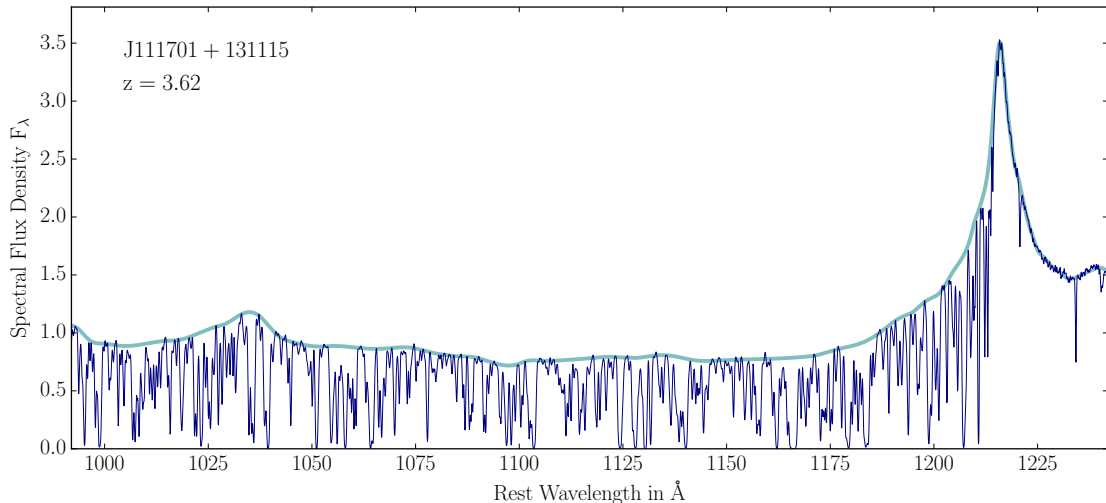


Figure 1.5: Illustration of the HI Ly α forest in the spectrum of a $z \approx 3.5$ quasar. Bluewards of the broad Ly α emission line of the quasar at $\lambda_{\text{rest}} \approx 1216 \text{ \AA}$, the spectrum exhibits a large number of relatively narrow absorption lines. These are caused by intervening neutral hydrogen in the IGM along the sightline. Due to the different redshifts of these absorbers, their Ly α absorption lines appear at different observed wavelengths. The full ensemble of absorption lines is described as the Ly α forest. For wavelength $\lambda_{\text{rest}} < 1025 \text{ \AA}$, also Ly β absorption lines are present in the spectrum. This part is therefore called Ly β forest and usually – to avoid confusion – discarded when analyzing the Ly α forest. The shown spectrum of J111701–131115 as well as the continuum estimate shown in green are taken from the public *XQ-100* survey (López et al. 2016).

thermal broadening, e.g. $\approx 16 \text{ km s}^{-1}$ at 6000 K (see e.g. Hiss et al. 2018). Today, hundreds of high-quality, high-resolution quasar spectra are available at redshifts $2 < z < 5.5$ (e.g. O’Meara et al. 2015, 2017; Walther et al. 2018a,b; Boera et al. 2018).

A quite complementary but equally important approach was taken by the Sloan Digital Sky Survey (SDSS, York et al. 2000) and its Baryon Oscillation Spectroscopic Survey (BOSS, Eisenstein et al. 2011; Dawson et al. 2013). While this survey was conducted on a relatively small telescope (2.5 m) and delivered spectra of low resolution ($R \approx 2000$) and often low S/N, it delivered completely unprecedented quantities of data. The use of multi-object spectrographs fed by optical fibers allowed to take spectra of up to 1000 objects simultaneously. In consequence, SDSS has now delivered spectra of over half a million quasar (Pâris et al. 2018) of which many cover the Ly α forest and allow statistical analysis of the IGM, i.e. the search for baryon acoustic oscillations at $z \simeq 2$ (e.g. Busca et al. 2013).

At lower redshifts, where the Ly α transition is not observable from ground, one requires space-based UV telescopes, in particular the Hubble Space Telescope (*HST*) to study the Ly α forest. Although the *HST* offers only a quite modest aperture of 2.5 m diameter, extensive studies of the low-redshift IGM have been conducted using the Space Telescope Imaging Spectrograph (STIS, Woodgate et al. 1998) and in recent times the highly sensitive *Cosmic Origins Spectrograph* (COS, Green et al. 2012).

1.2.3 The Ly α forest as precision probe of the IGM

The Ly α forest contains a wealth of information about the physical state of the gas in the IGM, in particular temperature and ionization state, and has become a precision probe of the large-scale structure of the Universe at basically all redshifts.

Key element for studies of the IGM is the detailed comparison of observations to accurate numerical simulations. Fortunately, simulating the IGM and therefore the Ly α forest is rather

CHAPTER 1. INTRODUCTION

simple, compared to other astrophysical processes. Until recently, many studies relied on so called *collisionless* simulations. These only include dark matter and provide information just about the cosmic (dark matter) density and the velocity structure within the simulation box. Hydrodynamical simulations distinguish between dark matter and baryon density and track the temperature of the gas as well. This requires a treatment of baryonic physics, i.e gas pressure, shocks, heating and cooling processes. Other quantities might be included as well. To calculate mock Ly α forest spectra, one has to post-process the simulation outputs. For this essential process, I will give a brief *recipe*. For more details see e.g. §3.2 or Rahmati et al. (2013).

First step in the post-processing is to determine the ionization state of the gas. In the simplest case, one assumes a homogeneous UV background (e.g. Faucher-Giguère et al. 2009; Haardt & Madau 2012), appropriate for a fully reionized universe. Ionization equilibrium of the gas (in this case for hydrogen) is then expressed by

$$n_{\text{HI}} \Gamma_{\text{tot}}^{\text{HI}} = \alpha_{\text{A}}^{\text{HII}} n_{e^-} n_{\text{HII}} \quad (1.4)$$

in which $\Gamma_{\text{tot}}^{\text{HI}}$ is the ionization rate of the UV background, $\alpha_{\text{A}}^{\text{HII}}$ the recombination coefficient and n_{e^-} , n_{HI} and n_{HII} the number densities of electrons, neutral and ionized hydrogen. The recombination coefficient $\alpha_{\text{A}}^{\text{HII}}$ has a slight temperature dependence. For a fully ionized Universe, $n_{e^-} \approx n_{\text{HII}} \approx n_{\text{H}}$ and Equation 1.4 simplifies to

$$\tau_{\text{HI}} \propto n_{\text{HI}} = \frac{\alpha_{\text{A}}^{\text{HII}}}{\Gamma_{\text{tot}}^{\text{HI}}} n_{\text{H}}^2. \quad (1.5)$$

Therefore, knowing the UV background and the cosmic hydrogen density n_{H} , which is on large scales proportional to the matter density, directly yields the HI density. Integrating these along a column and multiplying with the Ly α cross-section yields the optical depth τ_{HI} . Usually, a cosmological simulation delivers the matter or baryon density and the calculation above is executed for each pixel. The optical depths of each pixel are then assigned to individual absorption lines of an appropriate form, e.g Voigt profiles with amplitudes corresponding to the optical depth and positions and widths matched to velocities (or redshift) and temperatures, which are taken from the simulations as well. Alternatively, one can assume that all absorption happens locally which is known as the *fluctuating Gunn-Peterson approximation* (Gunn & Peterson 1965).

Following this *recipe*, one can with relatively few input parameters create mock Ly α forest spectra, nearly from *first principles*. If dark-matter-only simulations are used, the choice of a cosmology, UV background and an IGM temperature structure is in principle sufficient to create at least approximately correct mock spectra (see Sorini et al. 2016). To achieve percent-level accuracy in the used IGM statistics, e.g. the Ly α flux power spectrum, baryonic physics has to be included which complicates things, but the problem remains tractable (e.g. Lukić et al. 2015; Walther et al. 2018b). During the epoch of reionization, the assumption of a homogenous UV background is not justified. Here, one has to refer to semi-analytical models for the fluctuations in the UV background (Oñorbe et al. 2018) or simulations actually including radiative transfer calculations (Keating et al. 2018; Kulkarni et al. 2018b). It also has to be stated that, although numerical cosmological simulations are conceptually relatively simple, they can become extremely expensive in terms of computation time.

To compare observed spectra to simulations, one usually computes a summary statistic. Commonly used statistics of the Ly α forest are e.g the mean flux, averaged over scales ranging from a few Mpc to > 100 Mpc (Faucher-Giguère et al. 2008a; Becker et al. 2013, 2015), the Ly α flux probability distribution function (PDF, Bolton et al. 2008; Rorai et al. 2017a), the power

1.2. THE LARGE SCALE STRUCTURE OF THE UNIVERSE

spectrum (Walther et al. 2018a,b; Boera et al. 2018) or methods like wavelet analysis (Lidz et al. 2010) or the *curvature method* (Becker et al. 2011; Boera et al. 2014). Alternatively, individual absorption lines are fitted and their properties compared, e.g. the *b-N distribution* (Schaye et al. 2000; Rorai et al. 2018; Hiss et al. 2018).

Numerous studies, like the ones mentioned above, have used or developed these methods. Most of them were focusing on the thermal state of the IGM, i.e its temperature structure or the *pressure smoothing scale* (Rorai et al. 2017b). Other studies did measure the amplitude of the UV background (Becker & Bolton 2013) or constrained cosmological parameter like the scale of the baryonic acoustic oscillations (Busca et al. 2013), the neutrino mass (Palanque-DeLabrouille et al. 2013) or the presence of warm dark matter (Viel et al. 2013).

1.2.4 The Helium Ly α Forest

In addition to the hydrogen Ly α forest, there is also a helium Ly α forest. Singly ionized helium (He II) is a hydrogen-like ion and thus shows the same transitions (e.g. Lyman and Blamer series), however, at frequencies $4\times$ higher than the hydrogen equivalents. The He II Ly α forest therefore extends over the wavelength range $256 \text{ \AA} < \lambda_{\text{rest}} < 304 \text{ \AA}$ and in consequence can not be observed from the ground. Observations of the UV spectral regime can be conducted from space, but most instruments operate efficiently only for wavelengths $\gtrsim 1150 \text{ \AA}$ since the commonly used MgF optical coating shows extremely poor transmission at shorter wavelength. In addition, the neutral hydrogen in the interstellar medium of the Milky Way absorbs all hydrogen ionizing photons and makes extragalactic observations between 912 \AA and the soft X-ray regime at $\simeq 0.2 \text{ keV}$ impossible. Therefore, observations of the He II Ly α forest are only possible at redshifts $z \gtrsim 2.6$ but still require space telescopes specialized for the far-UV regime, like *HST/COS*.

Another problem for the study of the He II Ly α forest can occur from neutral hydrogen along the line of sight towards a background quasar. Intervening hydrogen Lyman limit systems absorb wavelengths $\lambda < 912 \text{ \AA}$, very similar to the interstellar medium of the Milky Way. Therefore, observations of the He II Ly α forest are only possible along sightlines that exhibit no hydrogen Lyman limit systems. This is a relatively rare case and in consequence only a small number of *helium transparent* quasar sightlines exist, limiting the full sample of science-grade He II spectra to only ≈ 25 objects.

Despite these difficulties, the He II Ly α forest is an important field of research. Since He II requires much higher ionization energies than hydrogen, it is a complementary probe for the UV background and the reionization of the Universe. According to the currently accepted picture (Miralda-Escudé 2003; Haardt & Madau 2012; Planck Collaboration et al. 2018; Davies et al. 2018; Mason et al. 2018), hydrogen was reionized at redshifts $z \simeq 8$ by the UV photons emitted from stars. However, their spectra were not hard enough to supply sufficient numbers of photons with energies $> 4Ry = 54 \text{ eV}$, required to doubly ionize helium. Such high-energetic photons could only be provided in sufficient quantities by quasars. Therefore, He II reionization was delayed until the quasar era, culminating in the completion of helium reionization at $z \approx 2.7$ (Madau & Meiksin 1994; Reimers et al. 1997; Miralda-Escudé et al. 2000; McQuinn 2009; Faucher-Giguère et al. 2009; Worseck et al. 2011; Haardt & Madau 2012; Compostella et al. 2013, 2014; Worseck et al. 2016, 2018). Since no other type of sources contributes significantly to the reionization of helium, detailed information about quasar emission and their contribution to the metagalactic UV background can be inferred from the process of helium reionization.

Since quasars are bright but rare sources, it is expected that He II reionization is a very patchy process. The general picture is that quasars create ionized bubbles around them which expand with time, and eventually overlap to form the relatively homogeneous UV background that

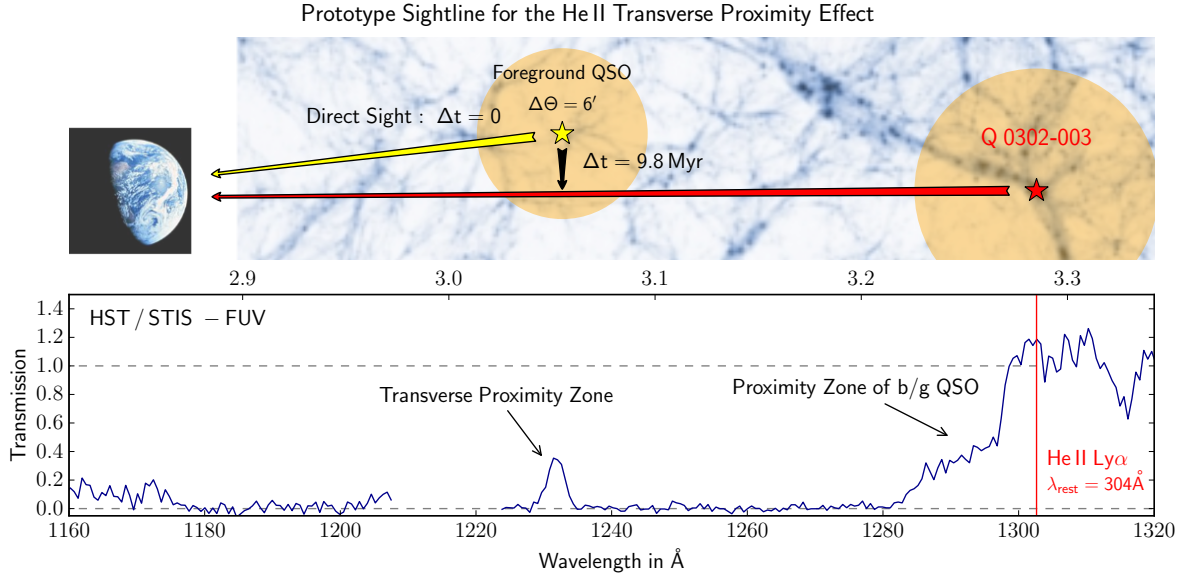


Figure 1.6: This illustration demonstrates the basic concept of the He II transverse proximity effect, showing the example of the Q 0302–003 prototype sightline. The bottom panel presents the *HST*/STIS FUV spectra from [Heap et al. \(2000\)](#), exhibiting an extended line of sight proximity effect close to the background sightline and a strong transmission peak at $z = 3.05$, caused by the proximity region of a close-by foreground quasar ([Jakobsen et al. 2003](#)). This constellation allows to derive a geometrical constraint on the age of the foreground quasar, based on the transverse light crossing time.

keeps the IGM in photoionization equilibrium up to the present day ([Bolton et al. 2006](#); [Furlanetto & Oh 2008](#); [McQuinn 2009](#); [Furlanetto & Dixon 2010](#); [Furlanetto & Lidz 2011](#); [Haardt & Madau 2012](#); [Meiksin & Tittley 2012](#); [Compostella et al. 2013, 2014](#)). At $z > 2.7$, before this process is completed, the morphology of He II reionization encodes information about the emission properties of quasars. For example, the shape and sizes of the ionization bubbles are sensitive to the amount of obscuration and the lifetime of quasars. The correlation of He II Ly α forest spectra with the location of quasar positions therefore offers a unique opportunity to gain insights into the emission properties of quasars. A detailed description of this *quasar proximity effect* is given below.

1.3 The Quasar Proximity Effect

The influence of quasars on their surrounding IGM can be detected in absorption spectra as statistically lower IGM Ly α forest absorption in the vicinity of the quasars. Due to their large amount of ionizing photons, quasars create so called *proximity zones* in the IGM, megaparsec sized regions with enhanced photoionization and therefore reduced Ly α absorption. This quasar proximity effect exists for H I as well as for He II and is a highly promising way to characterize quasar emission properties, in particular their emission history (age, lifetime) and emission geometry (obscuration, opening angle).

This *quasar proximity effect* is in general a three dimensional effect. However, it is usually observed in single Ly α forest absorption spectra. These probe the IGM along one-dimensional sightlines and depending on the geometry of these sightlines, different terms for the effect have been established. In particular, one distinguishes between *line-of-sight proximity effect* and *transverse proximity effect*. However, despite being observed in different ways and probing slightly different quasar properties, there is no fundamental difference and the quasar prox-

imity effect should always be understood as a three-dimensional or actually four-dimensional process when including the time dependence, independently of the observational technique.

1.3.1 The Line-of-sight Proximity Effect

The *line-of-sight proximity effect* describes reduced Ly α forest absorption in quasar spectra close to the quasar position, i.e. at the high-redshift end of the Ly α forest. Here, only one quasar is involved which acts as a background light source for the absorption spectroscopy and is also responsible for the enhanced ionization. This line-of-sight proximity effect is regularly observed in the H I Ly α forest (Carswell et al. 1982; Bajtlik et al. 1988; Scott et al. 2000; Dall’Aglio et al. 2008; Calverley et al. 2011), but also many He II sightlines exhibit a line-of-sight proximity effect (Reimers et al. 1997; Hogan et al. 1997; Anderson et al. 1999; Heap et al. 2000; Smette et al. 2002; Shull et al. 2010; Syphers & Shull 2013, 2014; Zheng et al. 2015). An example for the He II line-of-sight proximity effect is shown in Figure 1.6. Here, the far-UV spectrum of the He II Ly α forest exhibits nearly everywhere saturated absorption, so called Gunn-Peterson troughs (Gunn & Peterson 1965). However, in the vicinity of the background quasar, in the wavelength range $1280 \text{ \AA} < \lambda_{\text{obs}} < 1300 \text{ \AA}$, the He II transmission rises significantly and reaches nearly 100 % at the background quasar position. This enhanced transmission is caused by the strong He II ionizing flux of the Q 0302–003 background quasar.

The effective optical depth τ_{eff} in the Ly α forest scales inversely proportional to the total ionization rate as

$$\tau_{\text{eff}}(r) = \tau_{\text{eff}}(x \approx \infty) \times \frac{\Gamma_{\text{UVB}}}{\Gamma_{\text{UVB}} + \Gamma_{\text{QSO}}(r)} \quad (1.6)$$

where Γ_{UVB} denotes the UV background photoionization rate and $\Gamma_{\text{QSO}}(r)$ the ionization rate of the quasar at distance r , which scales approximately as $\propto r^{-2}$.

The proximity effect should not be understood as a Strömberg sphere. At least in most relevant cases, the IGM is highly ionized (even in the case of saturated Ly α forest absorption) and optically thin to ionizing radiation. The apparent *size* of the proximity zone is not determined by the position of an ionization front. Instead, the proximity region smoothly blends into the average Ly α forest where the ionizing radiation becomes insignificant compared to the metagalactic UV background. The decrease of $\Gamma_{\text{QSO}}(r)$ with increasing distance from the quasar is usually related to simple $\propto 1/r^2$ geometrical *dilution* and not by actual absorption of ionizing photons. Only in the case of very high redshifts ($z \gtrsim 6.5$ for H I or maybe $z \gtrsim 3.5$ for He II) can the IGM be significantly neutral and absorption of ionizing photons by the IGM actually relevant.

The line-of-sight proximity effect can be used to measure the strength of the UV background (see e.g. Calverley et al. 2011). For this, one has to estimate the amount of ionizing photons emitted by the quasar (Γ_{QSO}) based on its directly observable luminosity (e.g optical or UV continuum at $\lambda_{\text{rest}} > 1216 \text{ \AA}$) and compare the Ly α forest absorption τ_{eff} observed close to the quasar and far away from it ($r \approx \infty$). Alternatively, if the strength of the UV background is well known, one can infer the strength of the quasars ionizing radiation.

The line-of-sight proximity effect can also be used to constrain the quasar lifetime. Since it is observed *along the light cone*, one can not directly probe the quasar luminosity at past times. Of course, the ionizing radiation from the quasar requires time to reach a certain position along the sightline and this time span is longer if the distance from the quasar to that position is larger. However, this is exactly canceled out since the light which probes the absorption at that position requires less time to travel from there to the observer if this position is further away from the quasar. The total path length from the quasar to a certain

CHAPTER 1. INTRODUCTION

point on the sightline and from the to the observer is always the same. For an observer on Earth, a change e.g of the quasar ionizing flux therefore appears to affect all positions along the sightline simultaneously. Despite this, radiative transfer effects result in some limited sensitivity to the quasar emission history.

If a quasar suddenly changes its luminosity, e.g. turns on or off in the most extreme case, the gas in the IGM requires time to adjust to the new ionization equilibrium. As described e.g. in Khrykin et al. (2016), the transition from the old ionized fraction X_{old} to the new one X_{new} will follow approximately the form

$$X(t) = X_{\text{old}} e^{-t/t_{\text{eq}}} + X_{\text{new}} (1 - e^{-t/t_{\text{eq}}}), \quad (1.7)$$

i.e. it converges exponentially to the new state. The characteristic equilibration timescale t_{eq} depends on the recombination and photoionization timescale as $t_{\text{eq}} = (t_{\text{phot}}^{-1} + t_{\text{recom}}^{-1})^{-1}$. The recombination timescale is the inverse of the recombination rate (see § 3.5.2 for a formal definition) and thus rather long, of the order of Gyr. Therefore, the equilibration timescale is nearly always dominated by the photoionization timescale and photoionization and equilibration timescale can be used interchangeably. The photoionization timescale itself is the inverse of the total photoionization rate $t_{\text{phot}} = \Gamma_{\text{tot}}^{-1}$.

The presence of a line-of-sight proximity effect in quasar spectra consistent with the equilibrium expectation (Equation 1.6) therefore constrains quasar to shine for at least the equilibration timescale. However, for H I and $z < 5$, the equilibration timescale, dominated by the photoionization of the UV background of $\Gamma_{\text{UVB}}^{\text{HI}} \simeq 10^{-12} \text{ s}^{-1}$ (Becker & Bolton 2013), is less than $t_{\text{eq}} \simeq 10^4 \text{ yr}$ and provides only a weak lower limit on the quasar lifetime.

Despite this, there have been reports that for a few individual quasars the size of the proximity zone deviates from what one expects for the equilibrium case, leading to the claim that these quasars might be younger than $t_{\text{age}} \lesssim 10^4 \text{ yr}$ (Eilers et al. 2017). At higher redshift, during the epoch of reionization, t_{eq} is longer and a substantially neutral IGM can further delay the buildup of proximity zones, facilitating sensitivity to longer quasar ages (Davies et al. 2018). Alternatively, one can analyze the He II Ly α forest for which the photoionization rate is $\approx 1000\times$ lower (Worseck et al. 2018) and therefore the equilibration time is longer by the same amount. The He II line-of-sight proximity effect can therefore constrain quasar ages up to several Myr (Khrykin et al. 2016, 2018).

1.3.2 The Transverse Proximity Effect

Apart from the line-of-sight proximity effect, there is also the *transverse proximity effect* which comes into effect for close quasar pairs. Here, a background sightline passes close to a foreground quasar and thus probes the Ly α forest absorption in the vicinity of the foreground quasar. The foreground quasar with its ionizing radiation might create a proximity zone in its surrounding, a region in which the IGM is more ionized than usual. If the background sightline passes through this ionization bubble, it will show reduced Ly α absorption or even a *transmission spike* at the position of the foreground quasar. This is visualized in Figure 1.6, where the He II sightline towards the background quasar Q 0302–003 shows a very prominent transmission spike at redshift $z = 3.05$. This is related to a foreground quasar located at the same redshift and $\approx 6'$ or 3 Mpc (proper distance) separated from the background sightline.

The big advantage of this configuration is that the IGM absorption along the background sightline is sensitive to the luminosity of the foreground quasar at times earlier than the times we observe the quasar today and therefore directly probes the quasar emission history.

For the line-of-sight proximity effect, as outlines in § 1.3.1, the total path length from the quasar to a point on the sightline and from there to Earth is always constant and identical

1.3. THE QUASAR PROXIMITY EFFECT

with the distance to the quasar. Therefore, the Ly α forest absorption at all locations along the sightline is sensitive to the quasar luminosity at the same lookback time.

This is different for the transverse proximity effect. Here, the pathlength from the foreground quasar to a point on the background sightline and from there to Earth is always longer than the direct path from the foreground quasar to Earth. Therefore, the foreground quasars radiation that causes the enhanced IGM transmission at the background sightline has to be emitted earlier than the light we receive directly from the foreground quasar. This time difference, in the following be denoted as Δt , is crucial for our analysis. Following this, the transverse proximity effect offers a *look into the past* of the foreground quasar and is ideal to constrain its emission history.

If the distance from the foreground quasar along the line of sight is denoted as R_{\parallel} (with the negative axis pointing towards the observer) and the transverse distance as R_{\perp} , the time difference Δt between the direct sight towards the foreground quasar and the time probed by some Ly α absorption observed along a background sightline at position $(R_{\parallel} | R_{\perp})$ can be approximated as

$$\Delta t \approx \frac{1}{c} \left(\sqrt{R_{\perp}^2 + R_{\parallel}^2} + R_{\parallel} \right). \quad (1.8)$$

Here, R_{\parallel} and R_{\perp} are measured in proper length and the effects of cosmic expansion are neglected. A more detailed description is given later, e.g in §3.2.5 and §4.2.3, but some fundamental properties can be seen right away.

For $R_{\perp} = 0$, Equation 1.8 converges towards the case relevant for line-of-sight proximity effect and correctly yields $\Delta t = 0$, since R_{\parallel} is defined to be negative in front of the foreground quasar. For an absorber exactly behind the foreground quasar, the observed time difference is twice the distance from the quasar to the absorber. If an absorber is located exactly perpendicular to the line-of-sight, therefore at the same redshift than the foreground quasar and at $R_{\parallel} = 0$, the additional time is exactly the transverse light crossing time $\Delta t = c^{-1} R_{\perp}$. This case is also indicated in Figure 1.6. Curves of constant time difference Δt are parabolas with the quasar at the focal point and for a fixed R_{\perp} , Δt increases monotonically with R_{\parallel} .

Due to this time difference, the observation of a transverse proximity effect along a background sightline can directly constrain the age of the foreground quasar and allows robust estimates purely based on geometric arguments and the light travel time from the foreground quasar to the background sightline. This has been described in more detail e.g. by Dobrzycki & Bechtold (1991); Adelberger (2004); Furlanetto & Lidz (2011).

Since the He II UV background at $z \simeq 3$ is still rather low ($\approx 10^{-15} \text{ s}^{-1}$, Worseck et al. 2018), the ionizing flux of an individual luminous quasars can dominate over the UV background and cause a measurable proximity effect out to distances of tens of Mpc (see e.g. Figure 2.18). Similar scales can be reached for H I when considering ultraluminous quasars ($M_{1450} \approx -29$ mag, see Figure 4.2 and 4.3). Therefore, the transverse proximity effect can, at least in principle, constrain quasar ages up to 100 Myr.

Apart from the different emission time, the background sightline also probes the foreground quasars radiation from a different viewing angle compared to our vantage point from Earth and is therefore sensitive to the quasar emission geometry. In particular, it allows to test quasar unification model (Antonucci 1993; Urry & Padovani 1995; Netzer 2015) which predict that each quasar is obscured towards a substantial fraction of the sky by a dusty torus (see §1.1.3). Given that we observe a quasar as classical Type I quasar, we know that it has to be unobscured towards our vantage point. The presence of a proximity effect along a background sightline can now tell if the quasar emits as well towards this background sightline or might be obscured in that direction. Although observations along a single background sightline will not fully determine the emission geometry, probabilistic constraints of the amount of obscuration are possible (see Chapter 3). More detailed information on the quasar emission

CHAPTER 1. INTRODUCTION

geometry could be gained if several background sightlines are available that pass by the same foreground quasar (see Chapter 4).

Therefore, the transverse proximity effect offers great potential to constrain quasar emission properties and has been the topic of many studies. However, thus far, the H I transverse proximity effect did not delivered conclusive results (e.g. Liske & Williger 2001; Schirber et al. 2004; Croft 2004; Hennawi et al. 2006; Hennawi & Prochaska 2007; Kirkman & Tytler 2008; Lau et al. 2016). One reason for the difficulty of detecting the effect is the high mean IGM transmission at the typical redshift of $z \approx 3$. Therefore, the transmission enhancement caused by the foreground quasar is relatively small and difficult to detect (see e.g § 4.3.1). Also, quasars are hosted in cosmic overdensities which show enhanced absorption that counteracts the enhanced photoionization. Alternatively, quasar could actually be obscuration in the (approximate) transverse direction and therefor do not cause a strong transverse proximity effect.

Studying the proximity effects in helium is for several reasons advantageous over probing the same effect in hydrogen. At $z \lesssim 5$, the Universe is transparent to 1 Ry photons, resulting in a high and quasi-homogeneous UV background (e.g. Miralda-Escudé et al. 2000; Meiksin & White 2004; Bolton & Haehnelt 2007; Worseck et al. 2014). A single quasar therefore causes a significant increase over the background only within a relatively small zone of influence and the in general high H I Ly α forest transmission makes it difficult to recognize a region with even further enhanced transmission. At $z > 2.7$, before He II reionization is complete, helium offers a much larger contrast since the UV background is low and single quasars can produce a stronger enhancement over the background, resulting in a much larger region where the total ionization rate is dominated by the quasar. This extends far beyond the region in which the quasar host halo causes a substantial enhancement of the cosmic density field (Khrykin et al. 2016). At $z \approx 3$, He II spectra often show saturated Ly α absorptions with effective optical depths $\tau_{\text{eff}} \approx 5$ (Worseck et al. 2016). However, the helium in the IGM is already reionized with singly ionized fractions of $\approx 2\%$ (Khrykin et al. 2016, 2017). Under these conditions, a relatively modes enhancement of the He II ionization rate by a foreground quasar can cause a large increase in the he II transmission.

The first convincing evidence for a transverse proximity effect was therefore found in the He II sightline towards Q 0302–003 that exhibits a transmission spike at $z = 3.05$ (Heap et al. 2000) and a foreground quasar at practically the same redshift (Jakobsen et al. 2003). This prominent example represents the prototype case for the He II transverse proximity effect. From the required transverse light crossing time in this association, one can infer a geometrical limit of the quasar age of $t_{\text{age}} \gtrsim 10$ Myr (see Figure 1.6). In the same sightline Worseck & Wisotzki (2006) compared He II and H I spectra and computed the *hardness* of the radiation field, based on the relative absorption strength of the two ions, sensitive to ionization at 1 Ry and 4 Ry. They detect the proximity effect for at least one other foreground quasar which sets a lower lifetime limit of 17 Myr. Syphers & Shull (2014) claim a transverse proximity effect for another quasar 34 Mly away from the Q 0302–003 sightline, but this case is degenerate with the proximity effect of Q 0302–003 itself. In the limited sample of He II spectra and foreground quasars, Furlanetto & Lidz (2011) see indications against very long ($t_Q > 10^8$ yr) and very short ($t_Q < 3 \times 10^6$ yr) quasar lifetimes by simply counting He II transmission spikes under the assumption that they are associated with foreground quasars.

These examples show the potential of the He II transverse proximity effect in constraining the quasar lifetime. However, until 2009, only a handful of He II sightlines were known and no second unambiguous He II transverse proximity effect like to one in the Q 0302–003 sightline discovered.

1.4 Outline of the Thesis

The aim of the work presented in this thesis is to constrain quasar emission properties, in particular their lifetime and the amount of obscuration, from the analysis of the transverse proximity effect. Chapter 2 and 3 focus on the He II transverse proximity effect while in Chapter 4, I will present a novel method to map quasar light echoes in three dimensions based on the H I proximity effect.

The three main chapters of this thesis have all been (or will be) published as separate publications (Schmidt et al. 2017a, 2018a,b). Despite causing some redundancy, they will in this thesis be presented as mostly independent entities and with little changes compared to the form in which they were published initially. In particular, they are included here with their original conclusion section. In this way, this thesis also illustrates the development of knowledge and understanding of the transverse proximity effect throughout the five years of this Ph.D. project. The three chapters also highlight the development in methodology, in particular with respect to the statistical tools used for the analysis.

Our initial interest was focused on the He II transverse proximity effect. The installation of the Cosmic Origins Spectrograph (COS) on board the *Hubble Space Telescope (HST)* in 2009 initiated a new era of far UV astronomy. This resulted in the discovery of ≈ 20 new He II sightlines, substantially expanding the sample and for the first allowing a statistical analysis of the He II Ly α forest. The aim of the first project was therefore to complement this He II dataset with an optical spectroscopic survey, finding foreground quasars around these helium sightlines and conduct the first systematic analysis of the He II transverse proximity effect. This survey and the results are presented in Chapter 2. They include statistical evidence for the presence of the He II transverse proximity effect and a heuristic constraint on the quasar lifetime.

However, the outcome of the survey raised many new questions and the lack of transmission spikes associated with the newly discovered foreground quasars was puzzling. In the second project, presented in Chapter 3, I therefore performed a thorough theoretical investigation of the He II transverse proximity effect. In particular, I developed dedicated simulations of the He II Ly α forest transmission, based on cosmological hydrodynamical simulations and a purpose-developed photoionization model that includes the effect of finite quasar lifetime and quasar obscuration. This allowed for the first time to predict the appearance of the He II transverse proximity effect and to infer joint constraints on age and obscuration for a few individual foreground quasars.

However, the modeling of the He II transverse proximity effect also revealed its limitations and it became clear that further progress on this topic will probably require the capabilities of a future generation of space-based UV telescopes. These insights ultimately led to the development of a novel method that will map quasar light echoes in three dimensions. It will be based on a technique described as H I Ly α forest tomography and utilize existing and future ground-based optical telescopes. In Chapter 4, I line out the requirements and observational framework required for this new method, create realistic mock data from simulations, develop a statistical analysis pipeline and will finally show that detailed constraints on the age of individual quasar age can be inferred. In addition, I will present an extensive parameter study which is used to determine the optimal observing strategy.

This new method looks very promising and will hopefully deliver results soon. In Chapter 5, I will therefore conclude with a set of final remarks on the projects related to the He II transverse proximity effect and give an outlook on the future developments and applications of the new tomographic mapping technique developed in Chapter 4.

Chapter 2

A Systematic Search for the He II Transverse Proximity Effect

This Chapter is based on work published in Schmidt et al. (2017a). The He II spectra as well as the description of the He II data reduction in § 2.1.1 were supplied by G. Worseck and are published in Worseck et al. (2016, 2018). Deep imaging, mostly with LBT/LBC, for $\approx 2/3$ of the quasar fields and $\approx 1/3$ of the VIMOS spectroscopy was obtained ahead of the start of this Ph.D. project by N. Crighton, G. Worseck and J. Hennawi. Magellan/Megacam imaging for SDSS J1237+0126 was supplied by R. Simcoe. The *XDQSOz* catalog (DiPompeo et al. 2015) used for quasar selection was supplied by M. DiPompeo. All other parts are based on research conducted by author T. Schmidt, under supervision of J. Hennawi and G. Worseck at MPIA.

As lined out in § 1.3, the quasar transverse proximity effect is an ideal tool to investigate the emission properties of quasars and in particular constrain their lifetime. However, studies focusing on the H I transverse proximity effect did not lead to a conclusive detection (see § 1.3.2). This is to some degree related to the high IGM transmission in the H I Ly α forest at redshifts $z \simeq 3$, which results in a low contrast between the average IGM and a possible transverse proximity zone, making a detection of the effect difficult.

The first convincing evidence for the presence of a transverse proximity effect was therefore found in the He II sightline towards Q 0302–003. The *HST*/STIS spectrum of the background quasar (Heap et al. 2000, shown previously in Figure 1.6 but also in Figure 2.5 and 2.6) shows over most parts saturated He II Ly α absorption. However, it exhibits a prominent transmission spike at $z = 3.05$. Jakobsen et al. (2003) discovered a foreground quasar at the same redshift, located $\approx 6'$ away from the background sightline and established the picture that this foreground quasar is responsible for the He II transmission spike in the background sightline. From the required transverse light crossing time in this association, one can infer a geometrical limit of the quasar lifetime of $t_{\text{age}} \gtrsim 10$ Myr. Although this estimate is only based on a single object, it demonstrates the feasibility of deriving lifetime constraints using the He II transverse proximity effect.

Unfortunately, this prototype association remained the only convincing case for the transverse proximity effect. Despite substantial efforts (e.g. Worseck & Wisotzki 2006) no further association of a He II transmission spike with a foreground quasar was discovered. One limitation was the low number of suitable He II sightlines. The installation of the Cosmic Origins Spectrograph (COS, Green et al. 2012) on *HST* with unprecedented far-UV (FUV) sensitivity offered for the first time the opportunity for an extended survey of He II transparent quasars.

CHAPTER 2. SYSTEMATIC SEARCH FOR THE HE II TPE

Dedicated searches with *HST*/COS, assisted by the photometric all-sky UV survey of the *Galaxy Evolution Explorer* (*GALEX*), have led to the discovery of $\simeq 20$ new He II sightlines (Worseck & Prochaska 2011; Worseck et al. 2011; Syphers et al. 2012; Zheng et al. 2015; Worseck et al. 2016, 2018). This also called for a complementary foreground quasar survey, facilitating a detailed search for the transverse proximity effect in the newly observed He II sightlines.

The goal of this project is therefore to conduct a dedicated optical spectroscopic survey around 22 available He II sightlines to discover foreground quasars and to perform a systematic search for the He II transverse proximity effect. This then allows for the first time to statistically quantify the He II transverse proximity effect and to derive a constraint on the lifetime of quasars.

The optical survey, including the target selection, data reduction and analysis is described in § 2.1. In § 2.2 a few individual foreground quasars and their impact on the corresponding He II background sightlines are discussed. It follows in § 2.3 our statistical search for the presence of a He II transverse proximity effect in the average He II sightline from which we derive a statistical constrain on the quasar lifetime. In § 2.4 we investigate the object-to-object variation of the transverse proximity effect within our sample. We discuss the implications of our findings in § 2.5 and summarize in § 2.6.

Throughout this chapter we use a flat Λ CDM cosmology with $H_0 = 70 \text{ km s}^{-1} \text{ Mpc}^{-1}$, $\Omega_m = 0.3$ and $\Omega_\Lambda = 0.7$ which is broadly consistent with the Planck Collaboration et al. (2018) results. We use depending on the situation proper distances or comoving distances and denote the corresponding units as pMpc and cMpc, respectively. We denote the quasar lifetime with t_Q which assumes a *lightbulb* model for the quasar lightcurve and describes the full length of the emission period. The age of quasars, i.e. the time difference between *turn on* and time when the radiation that is now received on Earth was emitted, is denoted with t_{age} . Magnitudes are given in the AB system (Oke & Gunn 1983).

2.1 Description of the Survey

As part of a comprehensive effort to study He II reionization, we conducted an extensive imaging and spectroscopic survey to identify foreground quasars around 22 He II-transparent quasar sightlines for which science-grade *HST*/COS spectra are available. The survey consisted of a deep narrow survey covering the immediate vicinity of the He II sightline ($\Delta\theta \leq 10'$) down to a magnitude of $r \leq 24.0$ mag based on deep imaging and multi-object spectroscopic follow-up on 8 m-class telescopes, as well as a wider survey targeting individual quasars on 4 m telescopes. Finding quasars that have a separation from the He II sightline of more than $\approx 10'$ is in particular important to constrain long quasar lifetime. At redshift $z \approx 3$, an angular separation of $10'$ corresponds to a physical distance of only 4.7 pMpc or a light crossing time of 15 Myr. Therefore, to be sensitive to quasar ages longer than that, we also conducted the wider but shallower survey on 4 m class telescopes extending out to $\Delta\theta \approx 90'$.

The sample from our own surveys was complemented by quasars from the Sloan Digital Sky Survey (SDSS, York et al. 2000) and the Baryon Oscillation Spectroscopic Survey (BOSS, Eisenstein et al. 2011; Dawson et al. 2013), specifically from the twelfth data release (DR12, Alam et al. 2015) spectroscopic quasar catalog (Pâris et al. 2017). In the context of our study, SDSS and BOSS cover a similar parameter space (magnitude $r \lesssim 21$ mag) as our wide survey. However, the SDSS quasar selection is substantially incomplete at $z \approx 3$ (Fan 1999; Richards et al. 2002a, 2006; Worseck & Prochaska 2011). This makes it necessary to conduct our own wide survey and find the quasars not identified by SDSS.

Table 2.1. Overview of the FUV spectra used for this work.

Quasar	Instrument	R	Program	PI	References
PC 0058+0215	COS G140L	2000	11742	Worseck	9
HE2QS J0233–0149	COS G140L	2000	13013	Worseck	10, 11
Q 0302–003	COS G130M	18000	12033	Green	7, 10, 11
SDSS J0818+4908	COS G140L	2000	11742	Worseck	9
HS 0911+4809	COS G140L	2000	12178	Anderson	3, 5, 9
HE2QS J0916+2408	COS G140L	2000	13013	Worseck	10, 11
SDSS J0924+4852	COS G140L	2000	11742	Worseck	4, 9
SDSS J0936+2927	COS G140L	2000	11742	Worseck	9
HS 1024+1849	COS G140L	2000	12178	Anderson	5,9
SDSS J1101+1053	COS G140L	2000	11742	Worseck	4, 9
HS 1157+3143	STIS G140L	1000	9350	Reimers	1, 9
SDSS J1237+0126	COS G140L	2000	11742	Worseck	9
SDSS J1253+6817	COS G140L	2000	12249	Zheng	3, 8, 9
SDSS J1319+5202	COS G140L	2000	12249	Zheng	8, 9
Q 1602+576	COS G140L	2000	12178	Anderson	5, 9
HE2QS J1630+0435	COS G140L	2000	13013	Worseck	10, 11
HS 1700+6416	COS G140L	2000	11528	Green	6, 9
SDSS J1711+6052	COS G140L	2000	12249	Zheng	8, 9
HE2QS J2149–0859	COS G140L	2000	13013	Worseck	10, 11
HE2QS J2157+2330	COS G140L	2000	13013	Worseck	10, 11
SDSS J2346–0016	COS G140L	2000	12249	Zheng	3, 8, 9
HE 2347–4342	COS G140L	2000	11528	Green	2, 9

Note. — References: 1) Reimers et al. 2005; 2) Shull et al. 2010; 3) Syphers et al. 2011; 4) Worseck et al. 2011; 5) Syphers et al. 2012; 6) Syphers & Shull 2013; 7) Syphers & Shull 2014; 8) Zheng et al. 2015; 9) Worseck et al. 2016; 10) Schmidt et al. 2017a; 11) Worseck et al. 2018

2.1.1 He II Sightlines

Our foreground quasar survey targeted fields around 22 He II-transparent quasars observed with *HST*/COS or *HST*/STIS (Table 2.1). Worseck et al. (2016, 2018) describe the homogeneous data reduction and analysis of these spectra, including a much improved *HST*/COS background subtraction (dark current, quasi-diffuse sky emission, scattered light) and suppression of geocoronal contamination compared to the default CALCOS pipeline reductions from the *HST* archive. This improved reduction ensures that weak excess He II transmission due to the transverse proximity effects is not affected by zero-level calibration errors. Almost all spectra (20/22) have been taken with the *HST*/COS G140L grating ($R = \lambda/\Delta\lambda \sim 2000$ at 1150 Å, $\simeq 0.24$ Å per Nyquist-binned pixel). Their signal-to-noise ratio per binned pixel at He II Ly α of the background quasar varies between 2 and 15, mostly depending on whether the sightline was known before to be He II-transparent (Shull et al. 2010; Syphers & Shull 2013, 2014; Zheng et al. 2015), or had been discovered in recent *HST*/COS surveys (Worseck et al. 2011; Syphers et al. 2012; Worseck et al. 2016). The sightline to HS 1157+3143 was observed with the *HST*/STIS G140L grating ($R \sim 1000$, 0.6 Å pixel $^{-1}$; Reimers et al. 2005). For the Q 0302–003 sightline we used the higher-quality *HST*/COS G130M data ($R \approx 18,000$, $\simeq 0.03$ Å per Nyquist-binned pixel; Syphers & Shull 2014) instead of the *HST*/STIS data presented in Worseck et al. (2016). We checked our reduction by comparing the measured He II effective optical depths in the Q 0302–003 sightline to those presented by Syphers & Shull (2014), finding very good agreement.

As detailed in Worseck et al. (2016), we suppressed geocoronal emission lines by considering only data taken during orbital night or at restricted Earth limb angles in the affected spectral

CHAPTER 2. SYSTEMATIC SEARCH FOR THE HE II TPE

ranges. Nevertheless, decontaminated regions had to be excluded from our analysis due to the vastly reduced sensitivity to strong He II absorption and sometimes extremely weak geocoronal residuals in the coadded data. Geocoronal Ly α emission was excluded. In addition we apply a liberal signal-to-noise (S/N) cut. Since most of our pathlength is within Gunn-Peterson troughs where the flux is consistent with zero, we cannot apply a real limit on the S/N but instead require the continuum level to correspond to at least five counts per spectral bin. This mostly affects the short wavelength end of the spectra where the efficiency of the instrument drops dramatically. The background quasar proximity zones were excluded by measuring the dropping He II transmission from the proximity zone to the strongly saturated He II absorption in the IGM (e.g. Zheng et al. 2015). By excluding the entire background quasar proximity zone we may have excluded the transverse proximity zones of foreground quasars at similar redshifts (Worseck & Wisotzki 2006; Syphers & Shull 2014), but as these cases are degenerate and therefore require detailed modeling we make sure that our sample is not affected by any background quasar proximity zone.

2.1.2 Deep Survey on 8 m class Telescopes

For our deep imaging survey we used the Large Binocular Cameras at the Large Binocular Telescope (LBT/LBC, Speziali et al. 2008; Giallongo et al. 2008) to obtain optical multiband photometry (U_{Spec}, g, r and i) over an area of $23' \times 25'$ approximately centered on the targeted He II sightline. Imaging for 10 He II sightlines was obtained over several runs in 2009, 2011 and 2013 (Table 2.2). We observed in binocular mode with U_{Spec} and g (r and i) filters on the blue (red) camera. Individual exposure times were short (around 120 seconds) to limit saturation of bright stars. Depending on the field and the observing conditions, total exposure times were 70 to 100 minutes in the U_{Spec} filter, 10 to 30 minutes in g , 18 to 35 minutes in r and 38 to 54 in the i filter. With this strategy we reached a homogeneous depth in U_{Spec} , which is due to the expected colors of $z \simeq 3$ quasars ($U_{\text{Spec}} - g \simeq 2$) the limiting factor for our target selection. Since we observed in binocular mode, the red filters naturally reached a sufficient depth.

Due to declination and scheduling constraints, the fields of HE 2347–4342 and SDSS J1237+0126 were not observed with LBT/LBC. For the field of HE 2347–4342 we obtained multiband imaging ($Ugr i$) with the $36' \times 36'$ Mosaic II camera at the 4 m Blanco Telescope at the Cerro Tololo Inter-American Observatory (Muller et al. 1998). The field of SDSS J1237+0126 was imaged in $gr i$ with Mosaic 1.1 at the 4 m Mayall Telescope at the Kitt Peak National Observatory, and in U with Magellan/Megacam (McLeod et al. 2015). Exposure times were increased to achieve an imaging depth similar to our LBC observations.

Data reduction, mosaicing of the individual dithered exposures, stacking, astrometry and photometry was done using our own custom pipeline based on IRAF routines and SCAMP, SWarf and SExtractor¹ (Bertin 2006; Bertin et al. 2002; Bertin & Arnouts 1996). An example for a reduced r band image is given in Figure 2.1. For fields covered by SDSS, the astrometric solution is tied to the SDSS reference frame using SDSS star positions, while the photometric calibration is tied to SDSS *ubercal* photometry (Padmanabhan et al. 2008) to define the zero point and to correct for non-photometric observations. For HE 2347–4342, which lies outside the SDSS footprint, we had to rely on the USNO-B1.0 catalog (Monet et al. 2003) and photometric standards. We used the reddest bands (r or i) for source detection and used forced photometry to extract fluxes at the identical positions in the other bands. Magnitudes were corrected for Galactic extinction assuming the reddening terms from SDSS (Stoughton et al. 2002) and $E(B - V)$ for the background quasar from Schlegel et al. (1998), i.e. not accounting for reddening variations across the field. Star-galaxy classification was also done

¹<http://www.astromatic.net/software>

2.1. DESCRIPTION OF THE SURVEY

in the reddest observed bands since they had the best image quality with a full width at half maximum (FWHM) of $\simeq 0.8''$. The 5σ point source imaging depth of our LBT/LBC images is typically $\simeq 26.5$ mag in U_{Spec} and g , and $\simeq 26.0$ mag in r and i , respectively.

Selection of quasar candidates was done by applying cuts in the $U_{\text{Spec}} - g$ vs. $g - r$ color space as shown in Figure 2.2. A theoretical color track and contours have been computed from SDSS mock photometry of quasars including the spread in color due variations in the spectral energy distribution (SED) and IGM absorption (Worseck & Prochaska 2011). The stochastic IGM Lyman continuum absorption leads to a large scatter around the median track, and in particular for $z \approx 3$ the range of expected quasar colors overlaps substantially with the stellar locus, highlighting again the difficulties of quasar color selection at these redshifts (Richards

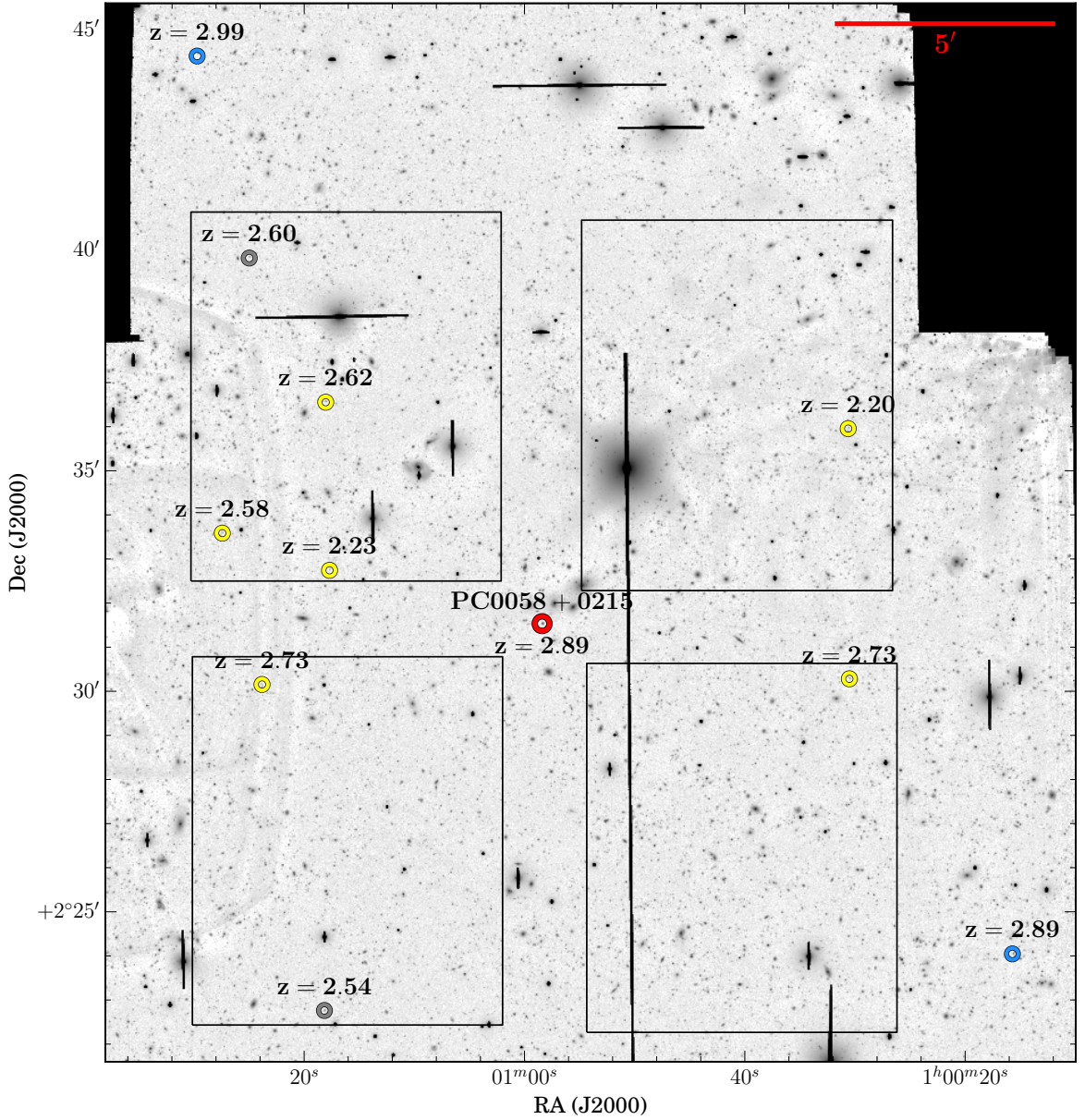


Figure 2.1: LBT/LBC r -band image of the field around PC 0058+0215 ($23' \times 25'$, $r < 26$ mag at 5σ). The He II-transparent background quasar is marked in the center (red). The approximate positions of the four quadrants of the VIMOS field of view are indicated. In this area our deep spectroscopic survey discovered six foreground quasars (yellow). Two additional quasars outside the VIMOS footprint were found by our wide survey with NTT/EFOSC2 (blue) and two quasars are from SDSS (gray).

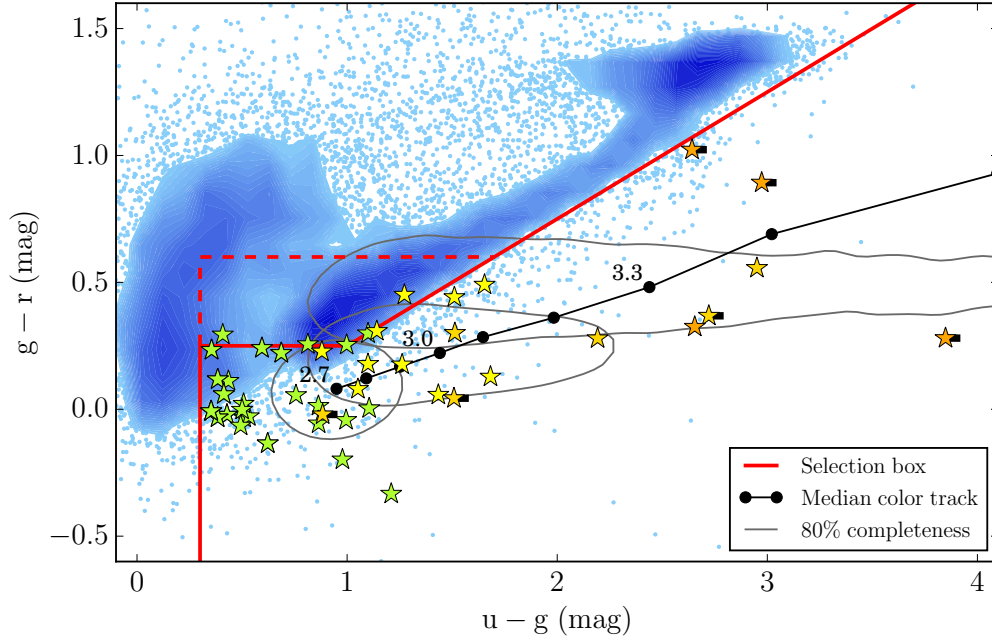


Figure 2.2: Candidate selection for our deep survey. Shown are all point-like objects with photometric detections in all bands ($S/N > 5$) as dots or contours (blue). A theoretical color track for $2.7 < z < 3.5$ quasars and corresponding completeness contours are shown in black (Worseck & Prochaska 2011). We selected high-priority quasar candidates from a box shown in solid red and lower-priority candidates from the dashed region. Confirmed quasars are overplotted as star symbols. Colors from green to orange indicate the redshift ($z < 2.5$, $2.5 < z < 3$, $3 < z < 3.5$, $z > 3.5$). Quasars having only a limit in U ($S/N < 5$) have a black tick to the right.

et al. 2002a; Worseck & Prochaska 2011). We used a selection box of the form

$$\begin{aligned} (U_{\text{Spec}} - g) > 0.3 \wedge \\ [(g - r) < 0.25 \vee (g - r) < 0.5 (U_{\text{Spec}} - g) - 0.25] \end{aligned} \quad (2.1)$$

which is visualized in Figure 2.2. It accounts for the expected range in color for $z \simeq 3$ quasars while limiting the stellar contamination. Lower-priority candidates were selected from an extended selection box $(g - r) < 0.6$ that overlapped with the stellar locus (Figure 2.2, dashed region).

Spectroscopic verification of the quasar candidates was done with the Visible MultiObject Spectrograph (VIMOS, Le Fèvre et al. 2003) at the Very Large Telescope (VLT), whose four $7' \times 8'$ quadrants cover most of the $23' \times 25'$ LBC field of view (Figure 2.1). Custom designed focal-plane slit masks were used to simultaneously take low-resolution spectra (LR Blue grism, $R \approx 180$, wavelength range $3700 - 6700 \text{ \AA}$) of ≈ 32 candidates per quadrant. Each of our 10 imaged fields was covered by a single VIMOS pointing with a typical exposure time of 2×30 minutes. The data were reduced with the standard EsoRex VIMOS pipeline² to which we added custom masking of zeroth-order contamination which is unavoidably present in the raw frames. An example spectrum of a quasar discovered by our VIMOS survey is shown in the middle panel of Figure 2.3.

For the field of Q 0302–003, additional quasar candidates outside our VIMOS pointing were observed with the DEep Imaging Multi-Object Spectrograph (DEIMOS, Faber et al. 2003) at Keck Observatory. We however did not find any additional quasar in this attempt.

²<http://www.eso.org/sci/software/cpl/esorex.html>

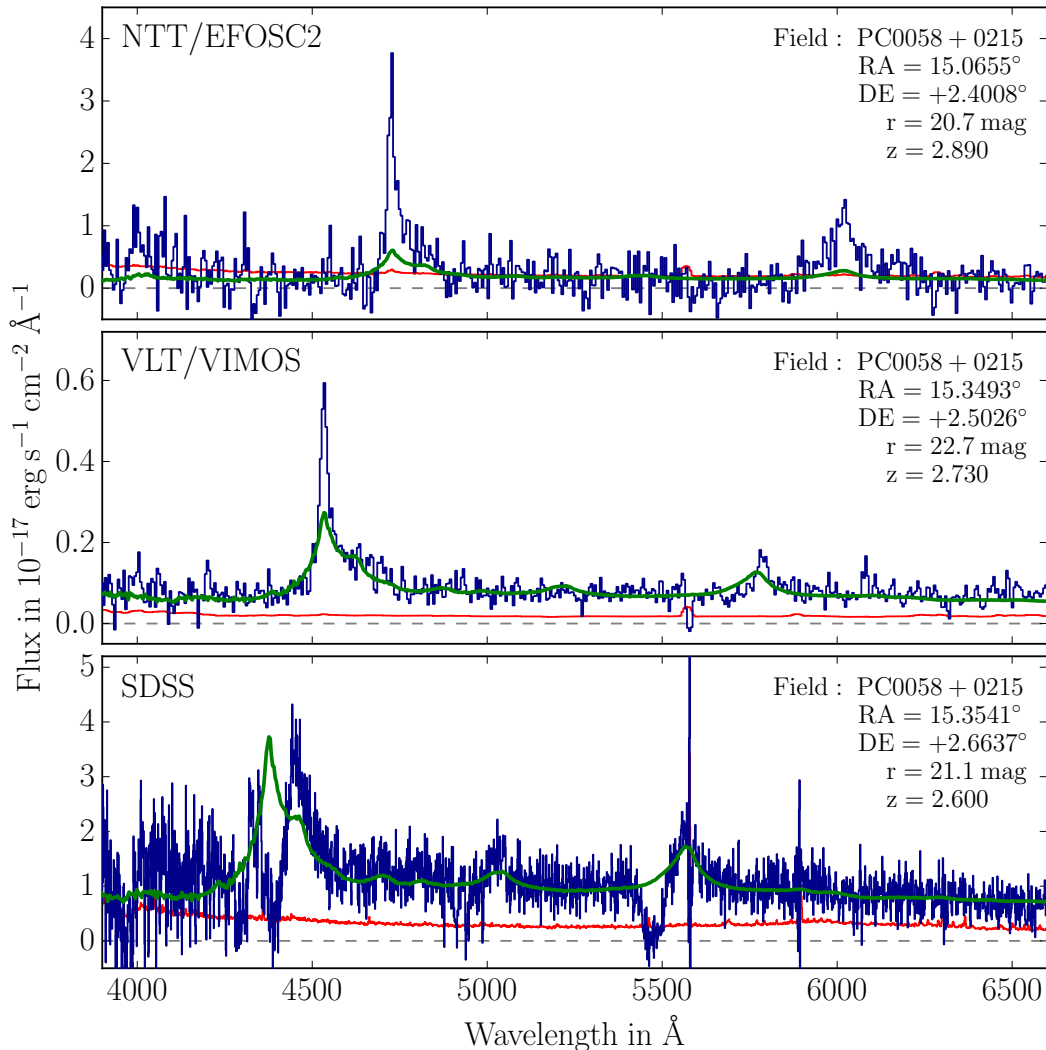


Figure 2.3: Spectra of three representative foreground quasars observed with different telescopes and instruments used for this study. All three quasars are located around the He II sightline toward PC 0058+0215 and marked in Figure 2.1. The observed spectral flux density is shown in blue and the 1σ error array in red. Overplotted is a quasar template (Vanden Berk et al. 2001) shifted to the redshift of the observed quasars but not adapted to match the different line strengths of the shown quasars.

2.1.3 Wide Survey on 4 m Class Telescopes

Our deep multi-object spectroscopy was complemented by individual longslit observations of brighter quasar candidates at larger angular separations ($10' \lesssim \Delta\theta \lesssim 90'$). Due to the large area on the sky and sparse target distribution, longslit spectroscopy of single targets is preferable to multi-object spectroscopy. It requires, however, a much higher selection efficiency than possible for $z \approx 3$ quasars from optical photometry alone. We selected candidates from the *XDQSOz* catalog (DiPompeo et al. 2015) based on the extreme deconvolution technique (Bovy et al. 2011, 2012) and the KDE catalog (Richards et al. 2015). Both catalogs are based on SDSS *ugriz* imaging but also incorporate infrared photometry from the *Wide-field Infrared Survey Explorer* (*WISE*, Wright et al. 2010). The *WISE* 3.6 μm and 4.5 μm bands are sensitive to the emission of hot dust surrounding AGN (Stern et al. 2012; Assef et al. 2013). This characteristic feature allows for very efficient separation of quasars from galaxies and stars. Both catalogs give a photometric redshift estimate or even a probability distribution. We used this information to maximize the probability for candidates to be confirmed with a redshift

CHAPTER 2. SYSTEMATIC SEARCH FOR THE HE II TPE

covered by the He II Ly α absorption spectra of the background quasars and prioritized targets accordingly. We also designed our wide survey to maximize the expected He II transverse proximity effect. Based on the position, brightness and photometric redshift, we estimated the photoionization rate $\Gamma_{\text{QSO}}^{\text{HeII}}$ that every of these putative quasars would cause at the background sightline (see § 2.1.6 for a definition of $\Gamma_{\text{QSO}}^{\text{HeII}}$). We then selected and prioritized according to cuts in $\Gamma_{\text{QSO}}^{\text{HeII}}$, primarily targeting objects with expected $\Gamma_{\text{QSO}}^{\text{HeII}} > 0.5 \times 10^{-15} \text{ s}^{-1}$.

For spectroscopic confirmation we used the ESO 3.5 m New Technology Telescope Faint Object Spectrograph and Camera (NTT/EFOSC2, Buzzoni et al. 1984) and the Calar Alto Observatory (CAHA) 3.5 m telescope TWIN spectrograph. We used the EFOSC2 grating g782 ($R = 180 - 450$, wavelength range 3700–9000 Å). For TWIN we used only the blue arm with grating T13 ($R = 620 - 1000$, wavelength range 3900–7000 Å). A slit width between 1.2'' and 1.5'' was used and the slit oriented at the parallactic angle. With these setups, the limiting magnitude for both instruments was $r \approx 21$ mag for the longest used integration times of one hour. The CAHA/TWIN spectra were taken in 32 nights between November 2014 and August 2015, while NTT/EFOSC2 observations were performed during 5 nights in December 2014.

Data were reduced using the XIDL Low-Redux package³. An example spectrum of a quasar confirmed with NTT/EFOSC2 is shown in Figure 2.3. Overall, 36 % of the observed targets were confirmed as quasars and 11 % had a redshift within the covered He II Ly α forest of the background quasar.

As part of the wide survey, we also verified a quasar with an uncertain redshift in the vicinity of HS 1700+6416 (Syphers & Shull 2013). We used the Keck Low Resolution Imaging Spectrometer (Keck/LRIS, Oke et al. 1995; McCarthy et al. 1998) to confirm its redshift. Data were as well reduced using the XIDL Low-Redux package.

2.1.4 Selection from SDSS and BOSS

For He II sightlines within the SDSS footprint we also use quasars from the SDSS DR12 catalog (Alam et al. 2015; P aris et al. 2017). This has the advantage that we can include large numbers of quasars out to very large separation from the background sightline. For our initial input catalog we selected all quasars within 240' of the background sightlines and with $z > 2.5$. For HS 1700+6416, whose COS spectrum covers lower redshifts, we adapted the latter criterion accordingly. This ensures that we include all objects that may contribute significantly to the ionizing background at the location of the background sightline. At later stages in our analysis, we will impose cuts on the expected photoionization rate at the background sightline. The vast majority of the selected quasars have $r < 21$ mag.

We note that Q 0302–003 and SDSS J2346–0016 lie within the SDSS Stripe 82 that was imaged multiple times, offering photometry approximately two magnitudes deeper than the standard SDSS imaging (Abazajian et al. 2009), and was also targeted by additional spectroscopy, using different selection algorithms (e.g. variability, see Butler & Bloom 2011; Palanque-Delabrouille et al. 2011). We actually find a higher density of foreground quasars near the SDSS J2346–0016 sightline but not for Q 0302–003.

2.1.5 Systemic Quasar Redshifts

Quasar redshifts determined from the rest-frame ultraviolet emission lines (redshifted into the optical at $z \simeq 3$) can differ by up to 1000 km s⁻¹ from the systemic frame, due to outflowing/inflowing material in the broad line regions of quasars (Gaskell 1982; Tytler & Fan 1992;

³<http://www.ucolick.org/~xavier/LowRedux/>

2.1. DESCRIPTION OF THE SURVEY

Vanden Berk et al. 2001; Richards et al. 2002b; Shen et al. 2007, 2016; Coatman et al. 2017). We estimate systemic redshifts by combining the line-centering procedure used in Hennawi et al. (2006) with the recipe in Shen et al. (2007) for combining measurements from different emission lines. The resulting typical redshift uncertainties using this technique are in the range $\sigma_z \simeq 270\text{--}770 \text{ km s}^{-1}$ depending on which emission lines are used. But given the low S/N ratio of ≈ 5 of many of our spectra, we conservatively assume our estimates of the systemic quasar redshift to be not better than 1000 km s^{-1} .

2.1.6 Estimate of the He II Photoionization Rate

To estimate the impact a foreground quasar has on the ionization state of the IGM we calculate the He II photoionization rate at the location of the background sightline. We use the Lusso et al. (2015) quasar template which is based on *HST* UV grism spectroscopy, corrected for IGM absorption and covers the restwavelength range down to 600 \AA . We redshift and scale this template to match our *r* band photometry which always falls redwards of Ly α and measures the quasar continuum flux. From the scaled template we infer the flux at 912 \AA and extrapolate to the He II Lyman limit at 228 \AA , assuming the specific luminosity to follow a power law of the form $L_\nu \propto \nu^\alpha$. The quasar spectral slope α beyond 912 \AA is not very well constrained since the frequencies between the extreme UV and soft X-rays are basically unobservable. We adopt a value of $\alpha = -1.7$ as determined by Lusso et al. (2015) (however with a large uncertainty of ± 0.6), which is consistent with the independent measurement of Stevans et al. (2014), as well as the slope between UV and X-ray regime (Lusso et al. 2015), but differs from the value of $\alpha = -0.73 \pm 0.26$ reported by Tilton et al. (2016). The uncertainty in α and the long range of extrapolation from 912 \AA beyond 228 \AA causes substantial uncertainty in the inferred photoionization rate, e.g. up to a factor of 2.5 for $\alpha = -1.7 \pm 0.6$. However, this mostly affects the absolute scaling of $\Gamma_{\text{QSO}}^{\text{HeII}}$. A relative comparison of different foreground quasars will not be severely affected.

We convert quasar luminosity to flux density F_ν at the background sightline according to

$$F_\nu = L_\nu \frac{1}{4\pi D^2} e^{-\frac{D}{\lambda_{\text{mfp}}}}. \quad (2.2)$$

This is a function of the transverse distance D between the foreground quasar and the background sightline measured at the redshift of the foreground quasar, and the mean free path to He II-ionizing photons in the IGM λ_{mfp} . However, quasars change the ionization state of the surrounding IGM by creating large proximity zones. Therefore, the mean free path relevant for us is not the one at random locations in the IGM but an effective mean free path within the proximity zone (e.g. McQuinn & Worseck 2014; Davies & Furlanetto 2014; Khrykin et al. 2016). The He II transverse proximity effect should in principle be able to constrain the mean free path, but at present it is not well constrained by observation or simulation. Current studies (e.g. Davies & Furlanetto 2014) suggest $\lambda_{\text{mfp}} \gtrsim 50 \text{ cMpc}$ at $z \approx 3$, longer than the scales probed by our study ($D \lesssim 40 \text{ cMpc}$). We therefore ignore IGM absorption for now and assume pure geometrical dilution of the radiation by setting $\lambda_{\text{mfp}} = \infty$.

Implicitly, we have assumed isotropic emission and infinite quasar lifetime with constant luminosity. Although current constraints suggest $t_{\text{Q}} \lesssim 10^8 \text{ yr}$, we assume for simplicity no time dependence in our fiducial model and constrain t_{Q} later. Also, the widely used unified AGN models (see, e.g. Antonucci 1993; Urry & Padovani 1995; Elvis 2000) assume a large-scale anisotropy of the UV and optical emission and relate the dichotomy between broad line quasars (Type I) and AGN displaying only narrow emission lines (Type II) to the presence of obscuring material that blocks the direct view on the accretion disc and broad line region if observed from certain directions. Studies focusing on the numbers of Type Is vs. Type IIs

CHAPTER 2. SYSTEMATIC SEARCH FOR THE HE II TPE

suggest (with large uncertainties) approximately equal numbers (e.g. [Brusa et al. 2010](#); [Lusso et al. 2013](#); [Marchesi et al. 2016](#)) which suggests opening angles of ≈ 120 degrees if one assumes a bi-conical emission. In consequence, the Type I quasars from our survey might be obscured towards parts of the background sightlines. However, we have no way to either infer the orientation or the exact opening angle of the foreground quasar and therefore no other choice than to assume isotropic emission for our fiducial model. A detailed modeling of obscuration effects will follow in [Chapter 3](#).

We therefore remain for now with the simplest isotropic model and convert UV flux density to He II photoionization rate by

$$\Gamma_{\text{QSO}}^{\text{HeII}} = \int_{\nu_0}^{\infty} \frac{F_{\nu} \sigma_{\nu, \text{HeII}}}{h_{\text{P}} \nu} d\nu \approx \frac{F_{\nu_0} \sigma_{\text{HeII}}}{h_{\text{P}} (3 - \alpha)} \quad (2.3)$$

in which h_{P} denotes Planck's constant and ν_0 the frequency of the He II ionization edge. For the second part we have assumed the quasar spectra to follow the power law description $F_{\nu} = F_{\nu_0} \times (\nu/\nu_0)^{\alpha}$ introduced above and for the He II cross-section the approximation $\sigma_{\nu, \text{HeII}} \approx \sigma_{\text{HeII},0} \times (\nu/\nu_0)^{-3}$ with $\sigma_{\text{HeII},0} = 1.58 \times 10^{-18} \text{ cm}^2$ ([Verner et al. 1996b](#)).

This calculation condenses the observed parameters (angular separation from background sightline, apparent magnitude, redshift) into one convenient number which can be used to estimate the possible influence of a foreground quasar on the background sightline. Although there is substantial uncertainty in the spectral slope and our calculation of the photoionization rate assumes simplifications like infinite lifetime, no IGM absorption and completely ignores obscuration effects, $\Gamma_{\text{QSO}}^{\text{HeII}}$ represents an important physical quantity and is (on average) a good proxy for the strength of the transverse proximity effect ([§ 2.3.3](#)). We will use $\Gamma_{\text{QSO}}^{\text{HeII}}$ extensively throughout the paper to select subsamples from our quasar catalog. Although we impose no universal threshold, we typically consider foreground quasars with $\Gamma_{\text{QSO}}^{\text{HeII}} > 2 \times 10^{-15} \text{ s}^{-1}$, i.e. similar to or exceeding current estimates of the UV background ($\Gamma_{\text{UVB}}^{\text{HeII}} \approx 10^{-15} \text{ s}^{-1}$ at $z \simeq 3$, [Haardt & Madau 2012](#); [Khrykin et al. 2016](#)). We caution that a direct comparison of our $\Gamma_{\text{QSO}}^{\text{HeII}}$ estimates to global UV background models is affected by substantial uncertainty due to different quasar SED parametrizations (see [Lusso et al. 2015](#) for a discussion). It gives, however, a rough indication of the value above which we expect a foreground quasar to substantially impact the IGM ionization structure. We also include objects with $0.5 \times 10^{-15} \text{ s}^{-1} < \Gamma_{\text{QSO}}^{\text{HeII}} < 2 \times 10^{-15} \text{ s}^{-1}$ to explore the effect of weaker quasars. See [§ 2.3.3](#) for a detailed analysis and [§ 2.4](#) for the impact of individual objects.

2.1.7 Final Quasar Sample

After restricting the combined quasar sample to have science-grade He II Ly α coverage along the background sightline ([§ 2.1.1](#)) and $\Gamma_{\text{QSO}}^{\text{HeII}} > 0.5 \times 10^{-15} \text{ s}^{-1}$, we end up with 66 foreground quasars, summarized in [Table 2.2](#). Here we have included quasars discovered in previous dedicated surveys in these fields ([Jakobsen et al. 2003](#); [Steidel et al. 2003](#); [Hennawi et al. 2006](#); [Worseck & Wisotzki 2006](#); [Worseck et al. 2007](#); [Syphers & Shull 2013](#)). Our survey yields in total 131 new quasars in the projected vicinity of the 22 He II-transparent quasars, 27 of which have $\Gamma_{\text{QSO}}^{\text{HeII}} > 0.5 \times 10^{-15} \text{ s}^{-1}$ and fall in regions with science-grade He II Ly α absorption.

Our final foreground quasar sample is illustrated in [Figure 2.4](#). With our deep survey (yellow symbols) we are able to detect quasars ≈ 2 mag fainter than SDSS, and preferentially discover quasars close to the background sightline ($D \lesssim 8 \text{ pMpc}$) with still high photoionization rates ($\Gamma_{\text{QSO}}^{\text{HeII}} > 2 \times 10^{-15} \text{ s}^{-1}$). [Figure 2.4](#) also shows that with our wide survey (blue and orange symbols) we find numerous quasars that have not been discovered by SDSS and BOSS. This substantially expands our sample in the region of interest, meaning foreground quasars with

2.2. THE TRANSVERSE PROXIMITY EFFECT IN INDIVIDUAL SIGHTLINES

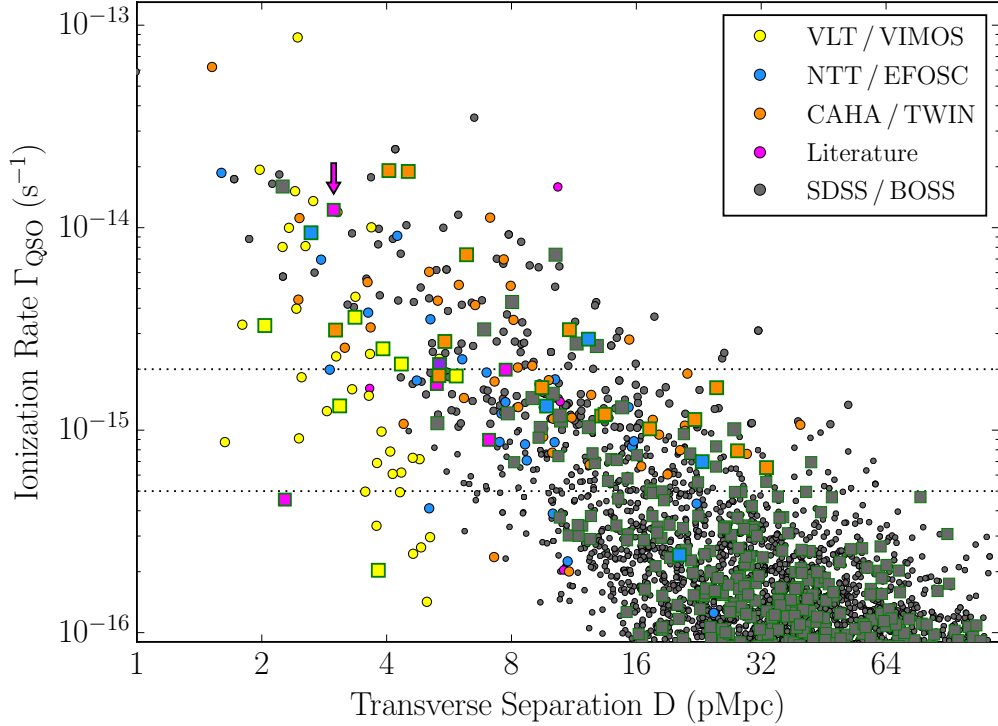


Figure 2.4: Properties of our foreground quasar sample. The panel shows the transverse separation of the foreground quasars from the background sightline and their estimated photoionization rate $\Gamma_{\text{QSO}}^{\text{HeII}}$ at the location of the background sightline. Colors indicate the origin of the objects. Horizontal dotted lines give the ranges for which we expect the objects to have a substantial impact on the background sightline ($\Gamma_{\text{QSO}}^{\text{HeII}} > 2 \times 10^{-15} \text{ s}^{-1}$) or at least include them for the extended selections ($\Gamma_{\text{QSO}}^{\text{HeII}} > 0.5 \times 10^{-15} \text{ s}^{-1}$). Only objects shown as green framed squares fall in usable parts of the HeII spectra (see Figure 2.5) and can be included in our statistical analysis. An arrow indicates the Jakobsen et al. (2003) quasar.

$\Gamma_{\text{QSO}}^{\text{HeII}} > 0.5 \times 10^{-15} \text{ s}^{-1}$. In fact, the two usable quasars with the highest photoionization rates in our sample ($\Gamma_{\text{QSO}}^{\text{HeII}} = 19.1$ and $19.0 \times 10^{-15} \text{ s}^{-1}$, see § 2.2.3 for details) are from our wide survey. Such bright ($r \simeq 19$) quasars outside the field of view of our deep survey are particularly important to constrain long quasar lifetimes.

Spectra of all He II sightlines are shown in Figure 2.5 together with their respective foreground quasars. Gaps in the spectra are due to masking of geocoronal residuals (§ 2.1.1). The regions that pass our quality criteria are indicated with a light green stripe at the bottom of the plots. Overplotted are the positions of foreground quasars.

2.2 Search for the Transverse Proximity Effect in Individual Sightlines

Although the main aim of this chapter is a statistical analysis of the He II transverse proximity effect, we will briefly discuss a few special objects to build intuition about the proximity effect signal.

2.2.1 HS 1700+6416

Near HS 1700+6416, four foreground quasars were discovered by Syphers & Shull (2013), one of which had an uncertain redshift assignment ($z = 2.625$) due to a single detected emission

CHAPTER 2. SYSTEMATIC SEARCH FOR THE HE II TPE

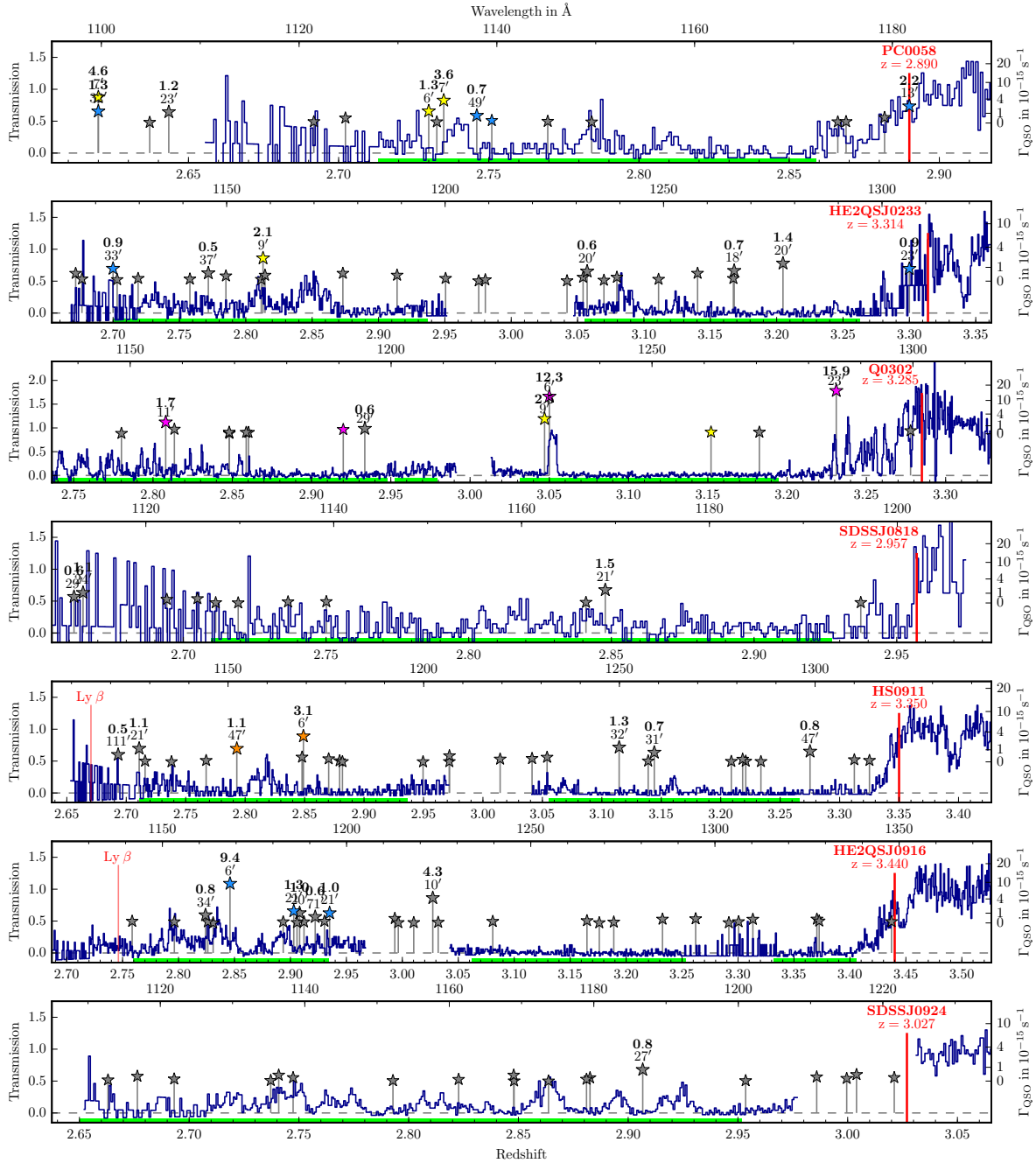


Figure 2.5: Gallery of the 22 HeII sightlines and the foreground quasar sample. The *HST*/COS G130M spectrum of Q 0302–003 has been binned to $\approx 0.15\text{\AA}$ per pixel for visualization purposes. Overplotted are positions of foreground quasars which are vertically displaced as indicated by the right axis to visualize their estimated He II photoionization rate at the background sightline. For foreground quasars with high impact, $\Gamma_{\text{QSO}}^{\text{HeII}}$ is also given as a label in units of 10^{-15}s^{-1} (bold top number) and the separation from the background sightline in arcminutes (bottom). Foreground quasars with $\Gamma_{\text{QSO}}^{\text{HeII}} < 0.1 \times 10^{-15}\text{s}^{-1}$ are omitted. Colors denote quasars discovered by us with different instruments (yellow: VLT/VIMOS; orange: CAHA/TWIN; blue: ESO NTT/EFOSC2; purple: Keck/LRIS), quasars from SDSS and BOSS (gray), and quasars from previous dedicated surveys (black). A green strip on the bottom edge of the plots indicates the regions of the He II spectra we use in the statistical analysis.

2.2. THE TRANSVERSE PROXIMITY EFFECT IN INDIVIDUAL SIGHTLINES

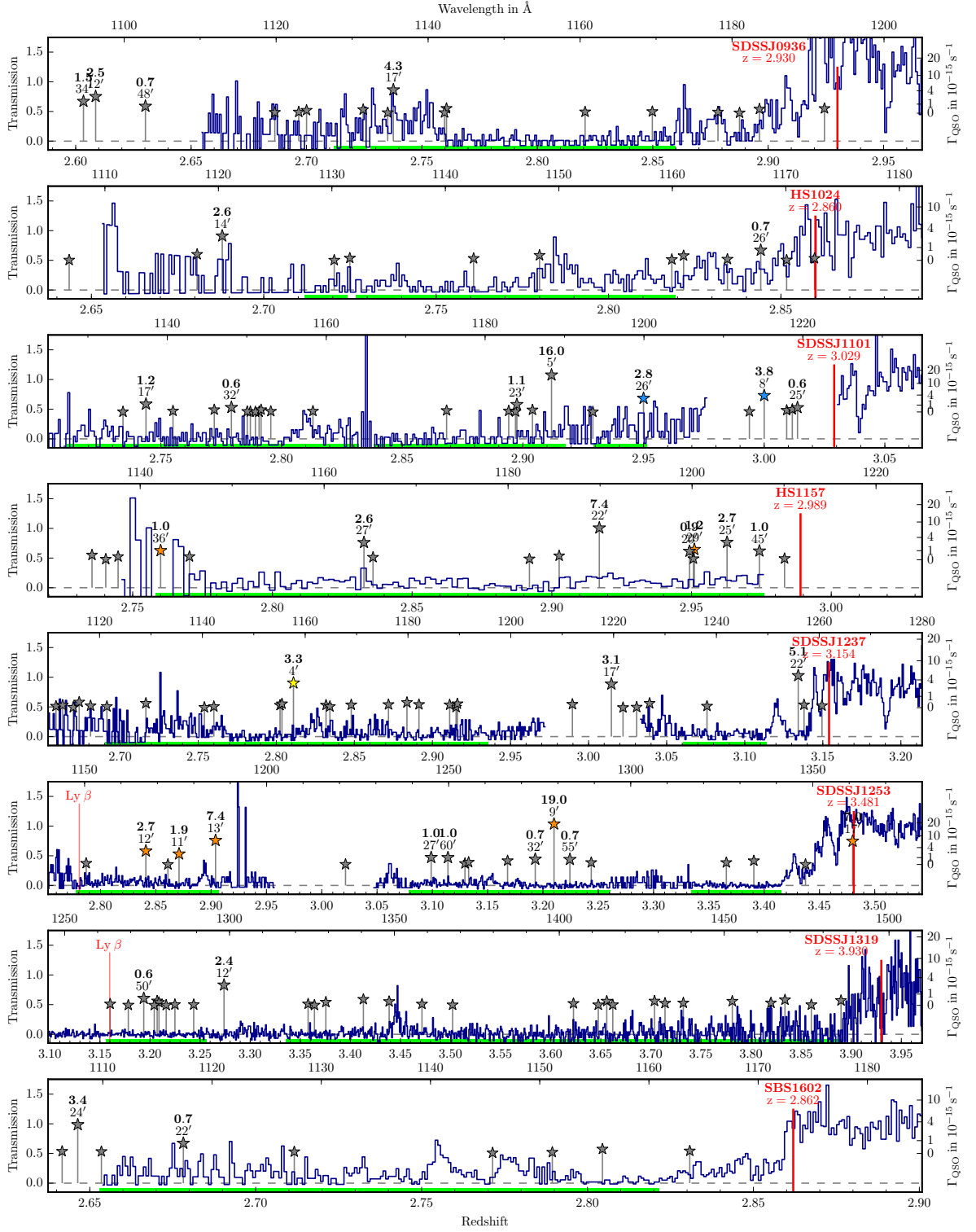


Figure 2.5: He II sightlines continued.

CHAPTER 2. SYSTEMATIC SEARCH FOR THE HE II TPE

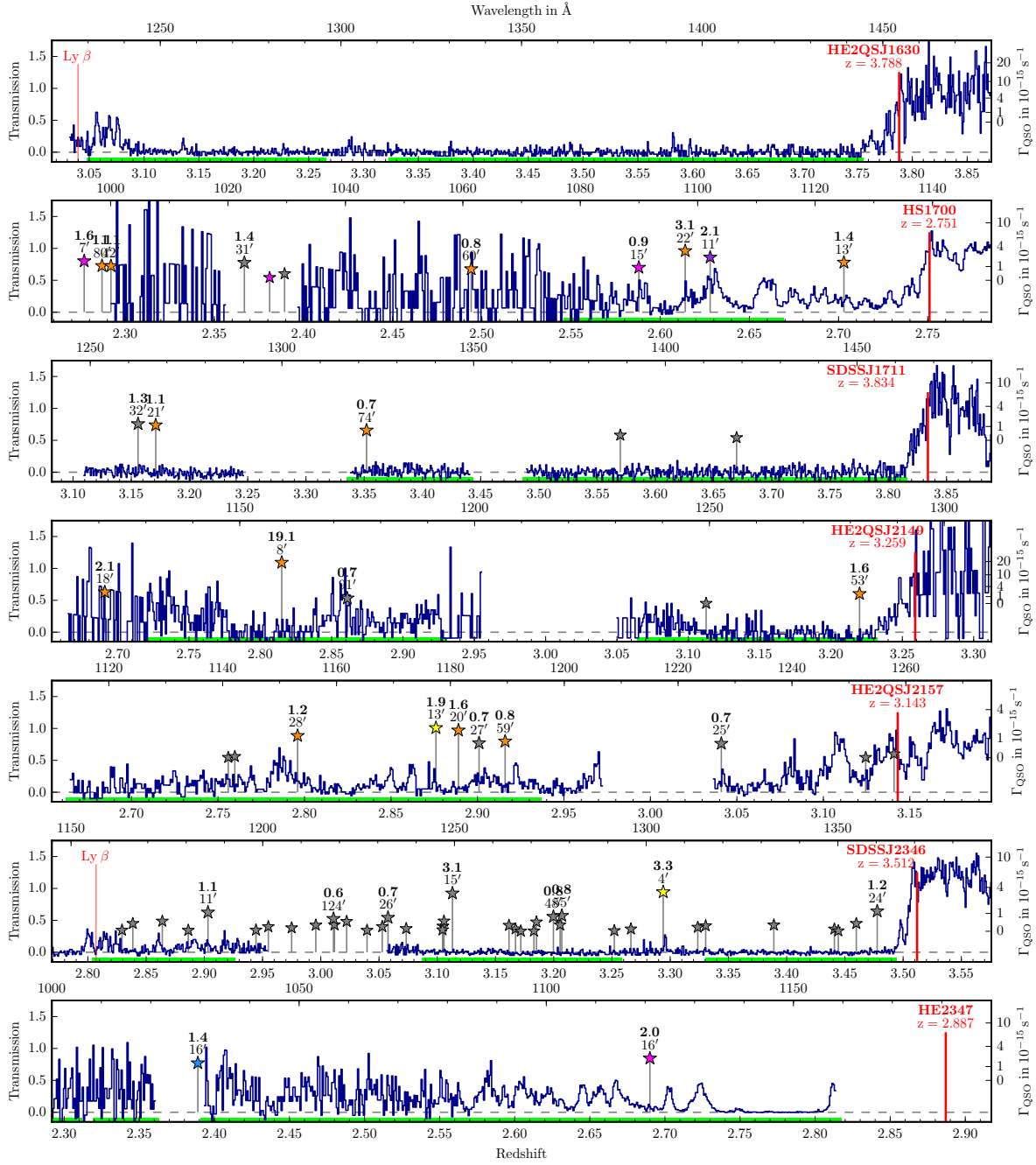


Figure 2.5: He II sightlines continued. The vicinity of HE2QS J1630+0435 was targeted as part of our wide survey but no relevant foreground quasar was found. Although this sightline does not add any transverse proximity effect data, we include it in the statistical analysis (in particular the Monte Carlo analysis § 2.3.2), and therefore show it in this figure.

2.2. THE TRANSVERSE PROXIMITY EFFECT IN INDIVIDUAL SIGHTLINES

Table 2.2. Overview of the He II sightlines and the number of foreground quasars with He II Ly α coverage in the background sightline.

Name	R.A. (J2000) hh : mm : ss	Dec. (J2000) hh : mm : ss	z_{BG}	LBT/LBC VIMOS	NTT/ EFOSC2	CAHA/ TWIN	SDSS ^a	Lit ^b
PC 0058+0215	01:00:58.40	+02:31:32.0	2.890	2	1	0	1	
HE2QS J0233–0149	02:33:06.01	–01:49:50.5	3.314	1	0	0	4	
Q 0302–003	03:04:49.85	–00:08:13.4	3.286	1	0		2	2
SDSS J0818+4908	08:18:50.02	+49:08:17.2	2.957	–	–	0	1	
HS 0911+4809	09:15:10.00	+47:56:59.0	3.350	–	–	2	2	
HE2QS J0916+2408	09:16:20.85	+24:08:04.6	3.440		2		3	
SDSS J0924+4852	09:24:47.36	+48:52:42.8	3.027	–	–		1	
SDSS J0936+2927	09:36:43.51	+29:27:13.6	2.930				1	
HS 1024+1849	10:27:34.13	+18:34:27.6	2.860	0	0	0	0	
SDSS J1101+1053	11:01:55.74	+10:53:02.3	3.029	0	1	0	4	
HS 1157+3143	12:00:06.25	+31:26:30.8	2.989			2	5	
SDSS J1237+0126	12:37:48.99	+01:26:07.0	3.154	1		0	0	
SDSS J1253+6817	12:53:53.70	+68:17:14.4	3.481	–	–	5	7	
SDSS J1319+5202	13:19:14.19	+52:02:00.3	3.930	–	–	0	1	
SBS 1602+576	16:03:55.93	+57:30:54.5	2.862	–	–	0	1	
HE2QS J1630+0435	16:30:56.34	+04:35:59.4	3.788			0	–	
HS 1700+6416	17:01:00.61	+64:12:09.0	2.751	–	–	1	0	1
SDSS J1711+6052	17:11:34.40	+60:52:40.5	3.834	–	–	1	0	
HE2QS J2149–0859	21:49:27.77	–08:59:03.6	3.259	1		2	1	
HE2QS J2157+2330	21:57:43.63	+23:30:37.3	3.143	1		3	1	
SDSS J2346–0016	23:46:25.66	–00:16:00.4	3.512	0	0	0	6	
HE 2347–4342	23:50:34.21	–43:25:59.6	2.887	0	0	0	–	1

Note. — For each telescope/instrument or catalog we only give the number of detected or used quasars that are included in our statistical analysis, therefore only counting quasars for which we have usable coverage in the He II Ly α spectrum (e.g. position not contaminated, not in the proximity zone or behind the He II quasar, see Figure 2.5) and which cause an estimated photoionization rate at the He II sightline of $\Gamma_{\text{QSO}}^{\text{HeII}} > 0.5 \times 10^{-15} \text{ s}^{-1}$ (see § 2.1.6). Blank fields denote that the sightline got not observed, dashes that it is not observable from the given site.

^aSDSS DR12, Alam et al. 2015; Pâris et al. 2017

^bLiterature objects from Jakobsen et al. 2003; Steidel et al. 2003; Hennawi et al. 2006; Worseck & Wisotzki 2006; Worseck et al. 2007; Syphers & Shull 2013.

line. With our Keck/LRIS spectrum we confirmed this quasar at a redshift $z = 2.628 \pm 0.003$, matching a broad He II transmission peak in the COS spectrum. Our CAHA survey discovered three additional foreground quasars at $z > 2.3$, one of which lines up with a narrow He II spike at $z = 2.614$.

However, at these low redshifts where He II reionization is likely to be already completed, it is unclear whether these features are caused by the additional ionizing radiation of foreground quasars or arise due to density fluctuations. Given the generally high He II transmission at $z < 2.7$, a random association of a foreground quasar with such a region is much more likely to occur than at higher redshifts. Chance alignments of the two foreground quasars with the HS 1700+6416 transmission spikes thus cannot be excluded.

2.2.2 Q 0302–003

The sightline towards Q 0302–003 presents the prototypical case for the He II transverse proximity effect. At $z < 3.19$, i.e. outside the large line-of-sight proximity zone of the background quasar ($\approx 80 \text{ cMpc}$), the He II spectrum shows almost no transmission down to redshifts 2.9.

CHAPTER 2. SYSTEMATIC SEARCH FOR THE HE II TPE

The exception is a striking transmission feature at $z = 3.05$ (Heap et al. 2000) with a width of $\approx 450 \text{ km s}^{-1}$ (5.7 cMpc) and a peak transmission of 80 %⁴. Jakobsen et al. (2003) found an $r = 20.6$ mag foreground quasar with a corresponding redshift $z = 3.050 \pm 0.003$ 6.5' away from the sightline and argued that this results from the He II transverse proximity effect.

Our survey uncovered a second quasar at a very similar redshift of $z = 3.047$, but further away from the background sightline (8.5') and 0.7 mag fainter than the Jakobsen et al. (2003) quasar (Figure 2.6). Based on its higher photoionization rate ($\Gamma_{\text{QSO}}^{\text{HeII}} = 12 \times 10^{-15} \text{ s}^{-1}$ vs. $\Gamma_{\text{QSO}}^{\text{HeII}} = 2.5 \times 10^{-15} \text{ s}^{-1}$) the Jakobsen et al. (2003) quasar seems to be the dominant source of He II-ionizing photons, but given the uncertain impact of obscuration, lifetime and quasar SED effects on the resulting photoionization rate from either quasar (§ 2.1.6), we cannot make any judgment about their relative contribution. The second quasar could still have a significant impact and it might be that the prominent He II transmission spike is the result of the combined ionizing power of both quasars. In any case, it demonstrates that a one-to-one assignment of transmission spikes to foreground quasars is an oversimplified approach that does not capture the full complexity of the He II transverse proximity effect.

2.2.3 Foreground Quasars with the Highest Observed Photoionization Rates

Our sample contains three new foreground quasars for which we infer a photoionization rate substantially higher than the Jakobsen et al. (2003) quasar. The respective regions in the He II spectra are shown in Figure 2.6. Near the sightline toward SDSS J1253+6817, we have discovered a $z = 3.20$ quasar with an estimated $\Gamma_{\text{QSO}}^{\text{HeII}} = 19.0 \times 10^{-15} \text{ s}^{-1}$, 60 % larger than for the Jakobsen et al. (2003) quasar. Despite this, there is no transmission spike observed even remotely comparable to the one in the Q 0302–003 sightline. The spectrum in this region is consistent with zero transmission ($\tau_{\text{eff}} > 4$). Despite the somewhat larger separation from the background sightline and the slightly higher redshift, this is a very surprising result. A

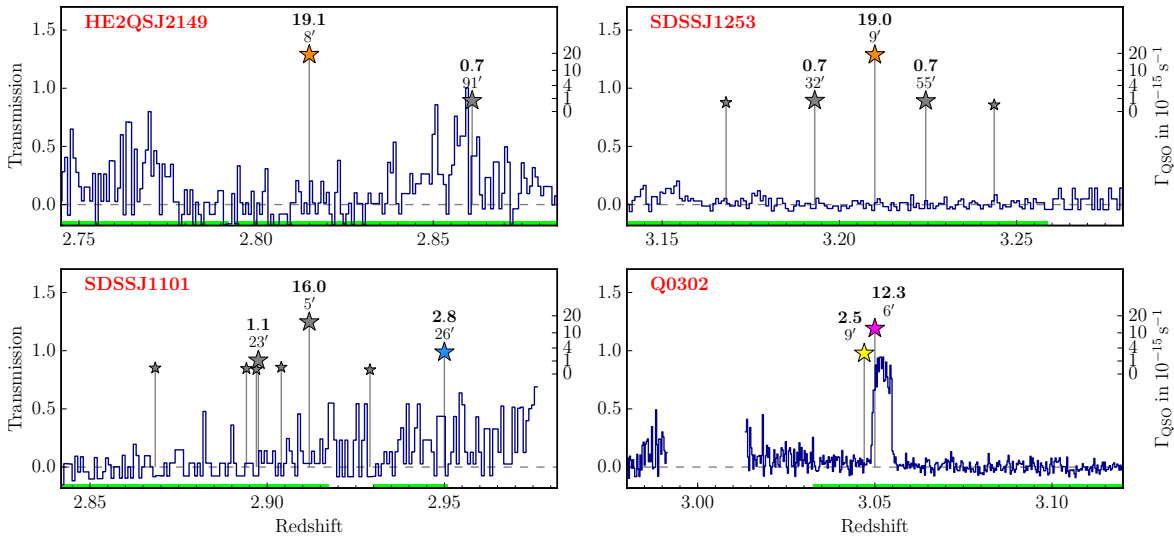


Figure 2.6: Enlarged versions of Figure 2.5 for the regions around the four foreground quasars with the highest $\Gamma_{\text{QSO}}^{\text{HeII}}$ (labeled in bold). Only for the Jakobsen et al. (2003) quasar near the Q 0302–003 sightline a He II transmission spike is observed. For the other three quasars, despite their higher He II photoionization rates, we observe strong absorption at the foreground quasar positions. All four panels have the same scale in the sense that they all show a pathlength of $\Delta z = 0.14$.

⁴Only for Q 0302–003 we use a high-resolution COS G130M spectrum. The spike would be marginally resolved at G140L resolution and show a lower peak transmission but would still be identified as an outstanding spectral feature.

similar situation is observed for HE2QS J2149–0859, where we find a foreground quasar at $z = 2.82$ with $\Gamma_{\text{QSO}}^{\text{HeII}} = 19.1 \times 10^{-15} \text{ s}^{-1}$ and no enhancement in transmission in the He II sightline. Another quasar with high $\Gamma_{\text{QSO}}^{\text{HeII}} = 16.0 \times 10^{-15} \text{ s}^{-1}$ but no visible impact on the He II transmission is located near the SDSS J1101+1053 sightline at $z = 2.91$.

We have discovered three additional quasars for which the inferred He II photoionization rate is in excess of the Jakobsen et al. (2003) system, and an order of magnitude above the estimated UV background. Whereas the precedent set by Jakobsen et al. (2003) might lead one to expect strong transmission spikes associated with all three of these new foreground quasars, this is clearly not the case. These new objects illustrate that there is no simple deterministic relationship between transmission spikes and our inferred He II photoionization rate. Instead they point to a large scatter in the transverse proximity effect which probably results from dependencies on other parameters (e.g. lifetime, obscuration, equilibration time, IGM absorption, IGM density fluctuations) which are not captured by our simple isotropic $\Gamma_{\text{QSO}}^{\text{HeII}}$ model (see § 2.1.6). This highlights that a statistical analysis on a large sample of foreground quasars is required to overcome the large sightline-to-sightline variation encountered in the analysis of individual associations, which is the main aim of this work.

2.3 Statistical Data Analysis of the He II Transverse Proximity Effect

2.3.1 Average He II Transmission near Foreground Quasars

Our strategy is to stack the He II Ly α spectra centered on the redshifts of the foreground quasars. This gives us an average He II transmission profile along the background sightlines which can then be tested for a local enhancement in the vicinity of the foreground quasars.

From the masked He II spectra (§ 2.1.1, Figure 2.5) we extract regions of $\pm 120 \text{ cMpc}$ (corresponding to $\Delta z = 0.125$ or 9400 km s^{-1} at $z = 3$) centered on the redshifts of the foreground quasars and rebin them to a common pixel scale of 5 cMpc (390 km s^{-1} or $\Delta z = 0.005$ at $z = 3$), much coarser than the typical resolution of our He II spectra ($R \approx 2000$). From this set of extracted and rebinned spectra, we select a subsample for which the individual foreground quasars exceed a threshold in the inferred He II photoionization rate (§ 2.1.6). We then compute for each spatial bin the mean transmission by averaging over all spectra in the subsample.

For each bin, we estimate uncertainties using the bootstrap resampling technique and compute the 15%–85% percentile interval. The bootstrap errors should give a combined estimate on the measurement error and the statistical fluctuations in the transverse proximity effect signal. However, bootstrapping is probably not converged for very small samples with $N \lesssim 5$ quasars. We therefore also propagate the formal photon-counting error of the initial spectra and take the maximum of propagated and bootstrap error. For bins with sufficient samples the bootstrap errors give the larger and more physical uncertainty. In cases where we have very few samples ($\lesssim 3$), the errors will be underestimated. However, these errors are only used for qualitative visualization purposes to provide an estimate of the error in our stack. Our analysis and estimate of the significance does not depend on these error estimates but is instead based on Monte Carlo simulations (see § 2.3.2).

A stack including all foreground quasars with $\Gamma_{\text{QSO}}^{\text{HeII}} > 2.0 \times 10^{-15} \text{ s}^{-1}$ is shown in Figure 2.7. The top panel shows the stacked He II spectra centered on the foreground quasars. The lower x-axis gives the distance in comoving Mpc from the points on the sightlines that are closest to the foreground quasars, denoted as R_{\parallel} . The upper x-axis converts this distance into an approximate velocity assuming Hubble flow and using the median redshift of the sample

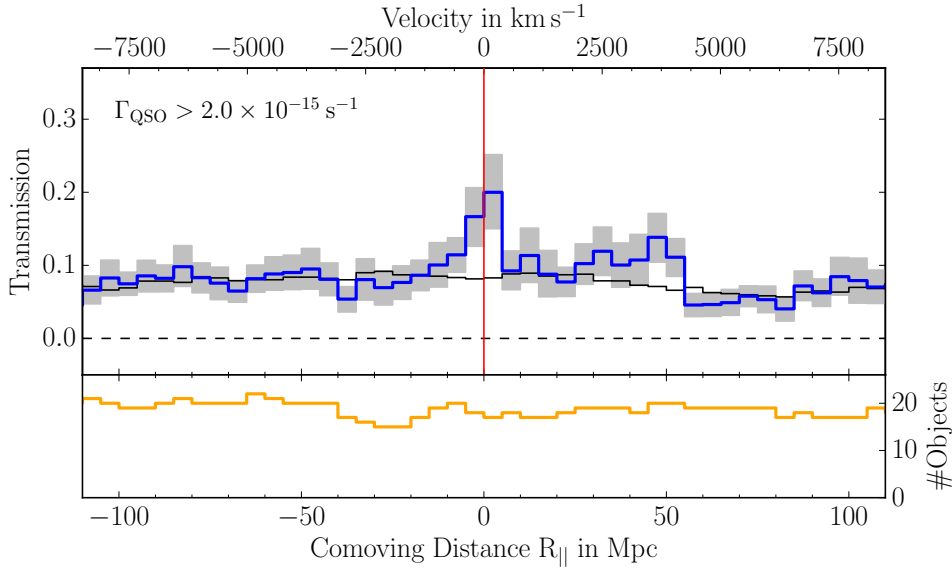


Figure 2.7: Average He II Ly α transmission profile close to foreground quasars with $\Gamma_{\text{QSO}}^{\text{HeII}} > 2.0 \times 10^{-15} \text{ s}^{-1}$, derived by stacking the 5 cMpc-binned He II spectra centered on the foreground quasar redshifts. The vertical red line marks the position of the foreground quasars. Conversion between comoving distance and velocity assumes the median redshift of the sample $z = 2.89$. Gray shaded areas give a bootstrap error estimate. The number of contributing spectra per bin is given in the bottom panel. The averaged He II transmission profile shows a clear enhancement within $|R_{\parallel}| < 15$ cMpc. As comparison, we show an estimate for an identical stack of the average IGM He II transmission (Figure 2.8) as a thin black line. We estimate the significance of the transmission enhancement to be 3.1σ , based on a Monte Carlo analysis.

$z = 2.89$ for the conversion. Bootstrap errors (15%–85% percentile range) are shown as the gray shaded area. Since we have to mask the He II spectra according to the conditions described in §2.1.1, the spectra do not necessarily have continuous coverage. This leads to some variation in the number of spectra contributing per bin which we therefore explicitly show in the bottom panel below the stack.

For the sake of illustration, we also show as a thin black line in Figure 2.7 the expected signal when stacking a mean IGM transmission model. To build such a model, we use all available He II spectra and bin them to a common grid with $\Delta z = 0.04$ sampling. For each redshift bin we compute the median transmission of all contributing spectra and fit a cubic spline through the resulting points. This smooth model we can then evaluate at arbitrary redshifts. The result is shown in Figure 2.8, clearly showing the high He II opacity of the IGM above $z > 3.2$ and the rapid increase in transmission below that redshift. For calculating the thin black line in Figure 2.7, we evaluate this spline fit at the redshifts corresponding to the pixels in the selected background sightlines and mask and stack these values in exactly the same way as the original data.

The stack in Figure 2.7 shows at line-of-sight distances $|R_{\parallel}| > 30$ cMpc a mean He II transmission of $\approx 8\%$. For $R_{\parallel} < -15$ cMpc the stacked signal is fairly flat and fully consistent with our mean transmission model. In the right half, the stack exhibits some structure, in particular slight excess transmission around $20 \text{ cMpc} < R_{\parallel} < 50 \text{ cMpc}$. However, fluctuations like these are not completely unexpected given the high stochasticity of our data and we will later estimate its statistical significance. Much more striking, the central part of the stack at $|R_{\parallel}| < 15$ cMpc shows a clear enhancement beyond 20% transmission that is centered on the position of the foreground quasars and falls off gradually to larger distances. As ≈ 20 sightlines contribute per 5 cMpc bin, this enhancement is a clear indication for the presence of a He II transverse proximity effect in the average IGM around quasars.

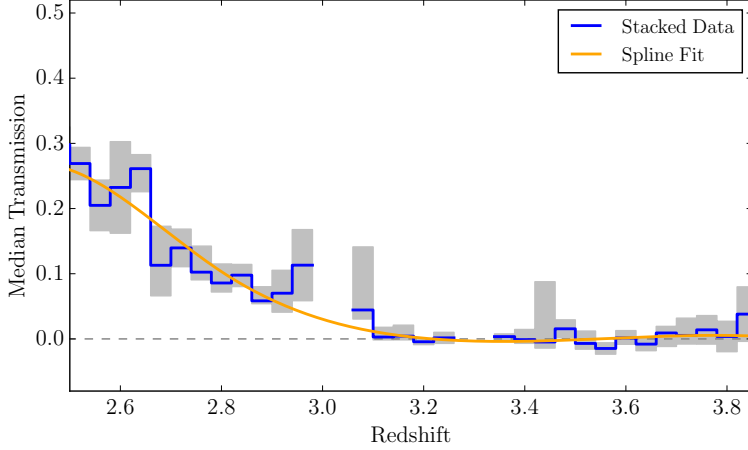


Figure 2.8: Redshift evolution of the median He II Ly α transmission, derived by binning the He II spectra to a common grid of width $\Delta z = 0.04$ and taking for each bin the median transmission values (blue line). Gray shaded regions represent bootstrap errors. Gaps in the data at $z = 3$ and $z = 3.3$ are due to geocoronal contamination. The orange curve shows a spline fit.

The shape of the observed transmission profile seems to be asymmetric, having the peak slightly behind the foreground quasar, falling off gradually to lower redshifts ($R_{\parallel} < 0$) and more steeply to higher redshifts ($R_{\parallel} > 0$). However, quasar redshift errors are large enough to significantly contribute to the observed shape of the transmission profile ($\sigma_z \approx 1000 \text{ km s}^{-1}$ corresponding to 13 cMpc at the median redshift $z = 2.89$). We therefore cannot make any statement about its intrinsic shape. In the following we will quantify the statistical significance of the central transmission feature as well as the transmission enhancement around +40 cMpc.

2.3.2 Monte Carlo Significance Estimate

To formally estimate the significance of the increased He II transmission in the vicinity of foreground quasars we perform a Monte Carlo analysis. The first step is to quantify the strength of the enhanced transmission. For this we require a measure for the amount of excess transmission. We define a kernel of ± 15 cMpc, i.e. slightly larger than the typical 13 cMpc position uncertainty of foreground quasars, and compute the average transmission of the stack inside this window. The average transmission within $|R_{\parallel}| < 15$ cMpc can then be compared to the average transmission in a control window ($15 \text{ cMpc} < |R_{\parallel}| < 120$ cMpc). The control window should yield a fair estimate of the average transmission since the bins sufficiently far away are unlikely to be correlated with the foreground quasar. They therefore represent the average IGM at approximately the same redshift and probed by the same sightlines which naturally incorporates the redshift distribution of the stacked subsample. The large size of our control window of 210 cMpc ensures that we do not add unnecessary noise to our statistic. We define the transmission enhancement as the difference of the He II transmission (T) within the central ± 15 cMpc and the transmission outside of this and denote it as

$$\xi = \langle T_{|R_{\parallel}| < 15 \text{ cMpc}} \rangle - \langle T_{15 \text{ cMpc} < |R_{\parallel}| < 120 \text{ cMpc}} \rangle. \quad (2.4)$$

To evaluate the probability distribution of the transmission enhancement at *random* locations in the IGM we create a large number of mock stacks. We take He II spectra centered on random redshifts drawn from a redshift distribution matching the redshift distribution of foreground quasars in the science stack, and keep adding such spectra to the random stacks until the average number of contributing spectra per spectral bin equals the one in the science stack. We stress that due to the limited number of He II sightlines and discontinuous coverage the number of contributing spectra can only be matched on average but not necessarily for each bin of the stack. Examples of mock stacks are shown in Figure 2.9. We then count for how many mock stacks the transmission enhancement ξ exceeds the measured value in the science stack. We create mock stacks until 500 of them fulfill this condition to ensure proper sampling of the tail of the distribution.

CHAPTER 2. SYSTEMATIC SEARCH FOR THE HE II TPE

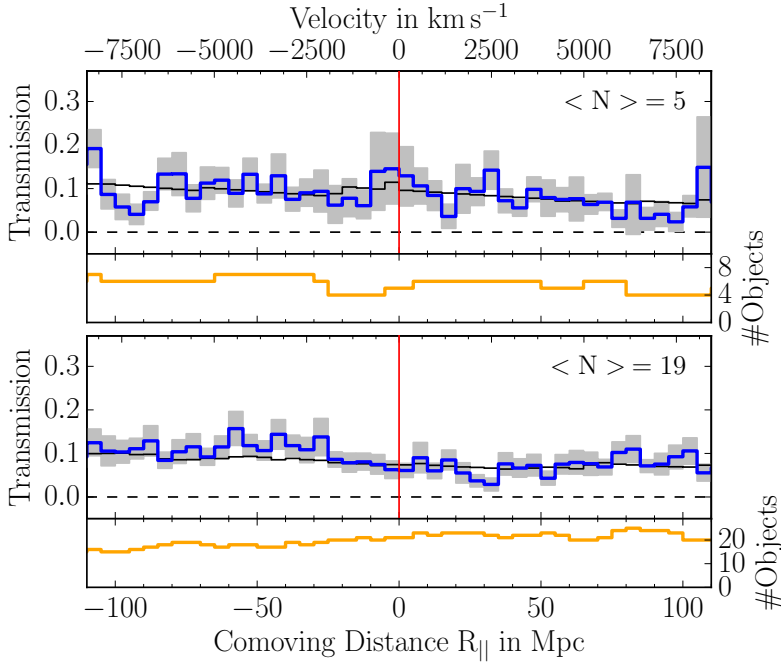


Figure 2.9: Examples of mock stacks used for the Monte Carlo analysis, created by stacking the He II spectra on random redshifts. The top (bottom) panel shows a stack with 5 (≈ 19) contributing spectra per bin.

The transmission enhancement in the science stack with $\Gamma_{\text{QSO}}^{\text{HeII}} > 2 \times 10^{-15} \text{ s}^{-1}$ (Figure 2.7) is $\xi = 0.058$. The blue histogram in Figure 2.10 shows the ξ distribution of random stacks matched to this science stack in terms of redshift distribution and number of contributing spectra per bin. We find that in 0.1% of the random stacks the transmission enhancement exceeds the measured $\xi = 0.058$. The ξ distribution is well approximated by a Gaussian (blue dotted curve in Figure 2.10), so we detect a transmission enhancement at a statistical significance of 3.1σ . In the following subsections we will create stacks with modified selection criteria. To illustrate how this influences the corresponding Monte Carlo analysis, we consider a science stack of all foreground quasars with a lower threshold value $\Gamma_{\text{QSO}}^{\text{HeII}} > 1 \times 10^{-15} \text{ s}^{-1}$ in which we measure $\xi = 0.019$. For $\Gamma_{\text{QSO}}^{\text{HeII}} > 1 \times 10^{-15} \text{ s}^{-1}$, the ξ distribution (green) is narrower than for $\Gamma_{\text{QSO}}^{\text{HeII}} > 2 \times 10^{-15} \text{ s}^{-1}$ (blue) due to the larger number of contributing spectra per bin (34 instead of 19). Still, 5.3% of the random stacks have $\xi > 0.019$, corresponding to a significance of 1.6σ (Figure 2.10).

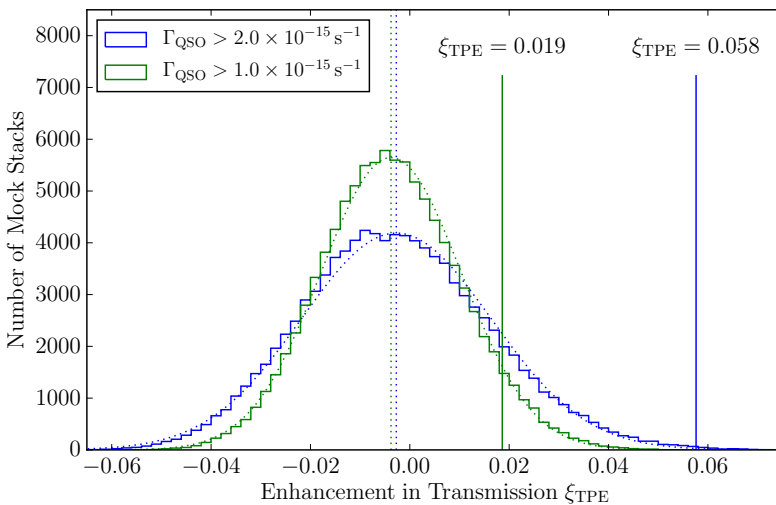


Figure 2.10: Distribution of the transmission enhancement in 10^5 mock stacks for two different cuts in $\Gamma_{\text{QSO}}^{\text{HeII}}$. The $\Gamma_{\text{QSO}}^{\text{HeII}} > 2 \times 10^{-15} \text{ s}^{-1}$ stacks contain 19 spectra per bin and therefore show a wider spread in ξ than the $\Gamma_{\text{QSO}}^{\text{HeII}} > 1 \times 10^{-15} \text{ s}^{-1}$ stacks which have 34 spectra per bin. The dotted lines give the mean and Gaussian approximation for the distributions. The ξ values measured in the science stacks are indicated with solid vertical lines. For $\Gamma_{\text{QSO}}^{\text{HeII}} > 1 \times 10^{-15} \text{ s}^{-1}$ ($\Gamma_{\text{QSO}}^{\text{HeII}} > 2 \times 10^{-15} \text{ s}^{-1}$) 5.3% (< 0.1%) of the mock stacks exceed the measured $\xi = 0.019$ ($\xi = 0.058$).

We confirm that the previously known transmission spike and foreground quasar in the Q 0302–003 sightline (Heap et al. 2000; Jakobsen et al. 2003) does not dominate our signal. Excluding the region of the transmission spike at $z = 3.05$ together with the two nearby foreground quasars and repeating our Monte Carlo analysis, we still end up with a chance probability of 1.5% for the measured enhanced transmission, corresponding to a 2.2σ detection. We show later in § 2.4 that while these two foreground quasars contribute significantly to our transverse proximity signal, they are however not the ones with the strongest transmission enhancements.

We further use our Monte Carlo scheme to evaluate the significance of the excess transmission seen in the stack (Figure 2.7) at $R_{\parallel} \approx +40$ cMpc. For this we define a window $+30 \text{ cMpc} < R_{\parallel} < +55 \text{ cMpc}$ and compute ξ for this range, while defining control windows at $R_{\parallel} < -15 \text{ cMpc}$ and $R_{\parallel} > +55 \text{ cMpc}$ to exclude the central transmission peak. We find a by-chance probability of 1.9% corresponding to a significance level of 2.1σ . Given that we specifically chose the limits of the window to maximize the impact of the secondary peak, it could still be consistent with a statistical fluctuation. It is, however, difficult to draw definitive conclusions without additional data.

2.3.3 Dependence on $\Gamma_{\text{QSO}}^{\text{HeII}}$

So far, we have focused on stacks with a photoionization rate threshold of $\Gamma_{\text{QSO}}^{\text{HeII}} > 2 \times 10^{-15} \text{ s}^{-1}$ that is similar to or higher than the estimated UV background photoionization rate (Haardt & Madau 2012; Khrykin et al. 2016) and gives the strongest signal. It is, however, informative to vary the range of $\Gamma_{\text{QSO}}^{\text{HeII}}$. Figure 2.11 shows spectral stacks centered on foreground quasars in four consecutive ranges of $\Gamma_{\text{QSO}}^{\text{HeII}}$. The upper panel includes foreground quasars with an estimated photoionization rate of $\Gamma_{\text{QSO}}^{\text{HeII}} > 4 \times 10^{-15} \text{ s}^{-1}$, which should result in the strongest impact on the background sightline. The next panel from the top includes quasars with intermediate impact ($2 \times 10^{-15} \text{ s}^{-1} < \Gamma_{\text{QSO}}^{\text{HeII}} < 4 \times 10^{-15} \text{ s}^{-1}$), and the lower two panels are for quasars with an estimated low impact.

The strength of the excess transmission clearly depends on the range in $\Gamma_{\text{QSO}}^{\text{HeII}}$. For foreground quasars with $\Gamma_{\text{QSO}}^{\text{HeII}} > 4 \times 10^{-15} \text{ s}^{-1}$, we detect a strong transmission enhancement of $\xi = 0.049$ despite the small number of $\simeq 7$ sightlines per 5 cMpc bin. The amplitude of the peak is even higher for the quasars with $2 \times 10^{-15} \text{ s}^{-1} < \Gamma_{\text{QSO}}^{\text{HeII}} < 4 \times 10^{-15} \text{ s}^{-1}$ ($\xi = 0.063$, second panel from top). For these two cases our Monte Carlo scheme yields a significance of 1.8σ and 2.1σ (probability $p = 0.035$ and $p = 0.017$), respectively. The foreground quasars included in these two stacks should dominate over the UV background of $\Gamma_{\text{UVB}}^{\text{HeII}} \approx 10^{-15} \text{ s}^{-1}$ (Haardt & Madau 2012; Khrykin et al. 2016), and we interpret the detected excess transmission as their transverse proximity effect.

For foreground quasars with lower estimated photoionization rates (lower two panels in Figure 2.11), any indication of the transverse proximity effect vanishes, in agreement with our expectation. We find $\xi = -0.019$ and $\xi = 0.0$, respectively. The increased absorption in the panel third from top has a significance of 0.85σ ($p = 0.2$) and is therefore consistent with the average transmission.

From the sequence of decreasing excess transmission with decreasing $\Gamma_{\text{QSO}}^{\text{HeII}}$ in Figure 2.11, we conclude that the transmission peaks are due to the transverse proximity effect of the foreground quasars. Additionally, this sequence confirms that $\Gamma_{\text{QSO}}^{\text{HeII}}$ is a useful estimator for the strength of the transverse proximity effect in an ensemble of foreground quasars, despite the assumptions in § 2.1.6. However, this is only true when averaging over a sample. As shown in § 2.2 and later in § 2.4, there is a large object-to-object variance.

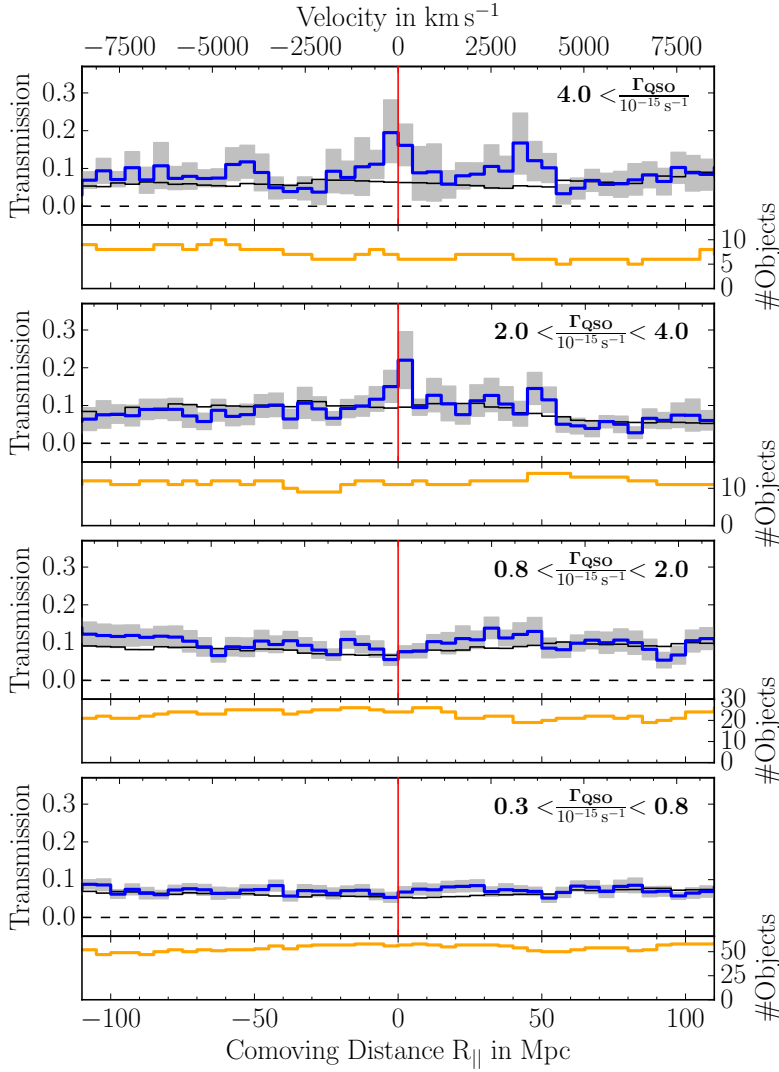


Figure 2.11: Average He II Ly α transmission profiles for foreground quasars with different ranges in $\Gamma_{\text{QSO}}^{\text{HeII}}$ (labeled). Small panels below the stacks show the number of contributing spectra per 5 cMpc bin. The dependence of the transmission enhancement on $\Gamma_{\text{QSO}}^{\text{HeII}}$ shows that the transmission enhancement is due to the transverse proximity effect.

2.3.4 Redshift Evolution

The foreground quasars with $\Gamma_{\text{QSO}}^{\text{HeII}} > 2.0 \times 10^{-15} \text{ s}^{-1}$ have a median redshift of $z = 2.89$ over a range $2.5 \lesssim z \lesssim 3.5$. We expect helium reionization to finish at these redshifts (Madau & Meiksin 1994; Reimers et al. 1997; Miralda-Escudé et al. 2000; McQuinn 2009; Haardt & Madau 2012; Compostella et al. 2013, 2014; Worsack et al. 2016) and it is thus expected that the average properties of the IGM are different around our high-redshift quasars compared to the ones at low redshift. The evolution in mean transmission was already illustrated in Figure 2.8 and it can also be seen in our stacks. In Figure 2.12 we show stacks of the He II transmission near foreground quasars with $\Gamma_{\text{QSO}}^{\text{HeII}} > 2.0 \times 10^{-15} \text{ s}^{-1}$ in three redshift ranges ($z < 2.7$, $2.7 < z < 3.1$, $z > 3.1$).

The $z > 3.1$ sample is consistent with zero transmission in most of the bins including the positions close to the foreground quasars. We see no indication for a transverse proximity effect ($\xi \approx 0$), but note that only ≈ 3 quasars contribute to this stack. For intermediate redshifts ($2.7 < z < 3.1$) we find a detectable non-zero average He II transmission in the IGM that is enhanced in the vicinity of foreground quasars ($\xi = 0.055$). The contrast between the transmission in the quasar vicinity and the average transmission in the IGM far from quasars is largest for this redshift interval, and we find a significance of 1.9σ ($p = 0.026$). At $z < 2.7$

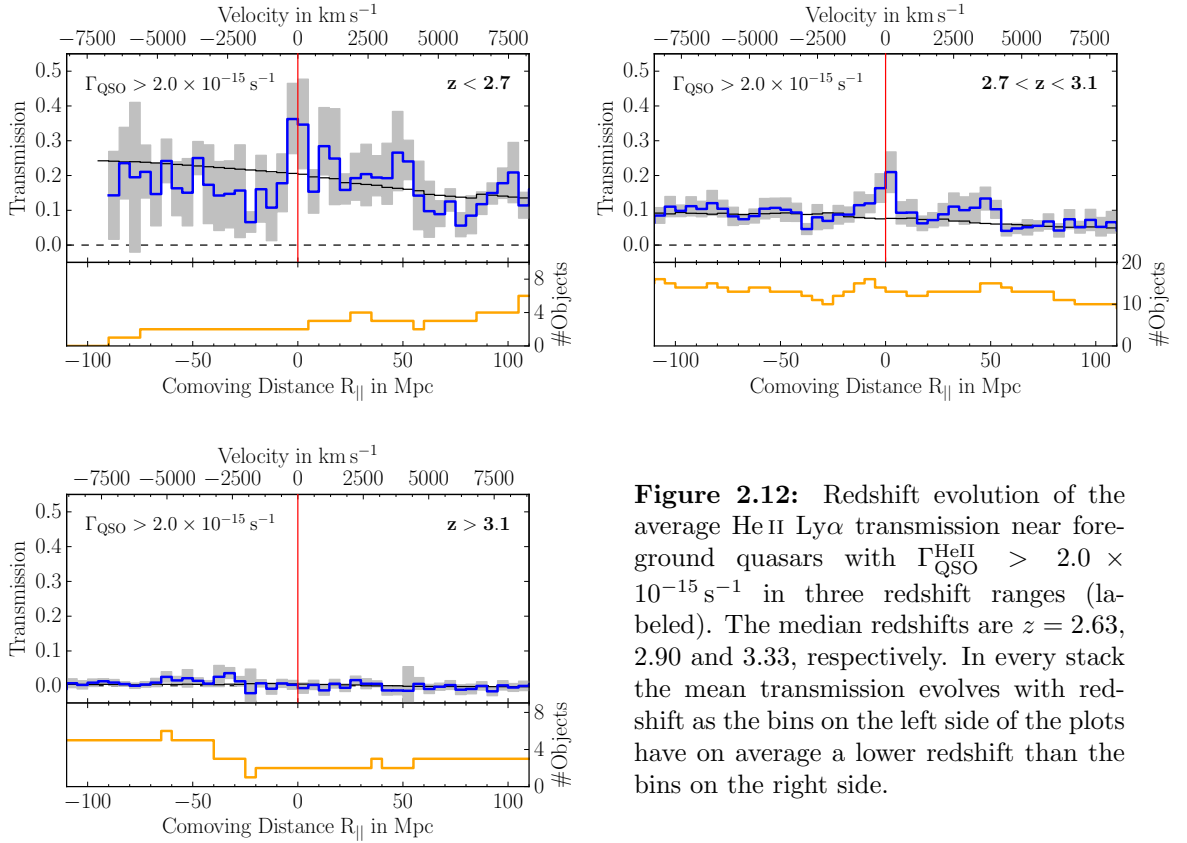


Figure 2.12: Redshift evolution of the average He II Ly α transmission near foreground quasars with $\Gamma_{\text{QSO}}^{\text{HeII}} > 2.0 \times 10^{-15} \text{ s}^{-1}$ in three redshift ranges (labeled). The median redshifts are $z = 2.63$, 2.90 and 3.33, respectively. In every stack the mean transmission evolves with redshift as the bins on the left side of the plots have on average a lower redshift than the bins on the right side.

the mean transmission rises quickly. We find a transmission enhancement of $\xi = 0.081$, but fluctuations in the Ly α forest and the relatively high mean transmission reduce its significance. Also, the COS sensitivity drops at $\lambda < 1110 \text{ \AA}$ ($z < 2.65$) and the few available spectra are very noisy. Therefore we find a significance of only 1.2σ ($p = 0.12$).

2.3.5 Constraining the Quasar Lifetime with the Transverse Proximity Effect

The detection of the He II transverse proximity effect presented in the previous subsections sets the stage for constraining quasar properties, in particular the quasar lifetime t_{Q} . Conceptually, this requires only a few further assumptions. If we attribute enhanced He II transmission to the transverse proximity effect of a nearby foreground quasar at the same redshift, we see the quasar and this IGM parcel at the same lookback time. However, to ionize the gas, the quasar had to emit He II-ionizing photons at least for the transverse light crossing time between the foreground quasar and the sightline (e.g. Jakobsen et al. 2003; Worseck & Wisotzki 2006; Furlanetto & Lidz 2011). If we assume a simple lightbulb model in which the quasar turns on, shines with constant luminosity for some time and turns off again, it had to shine for at least the light crossing time to allow simultaneous observation of the quasar and the additional ionization at the background sightline. We can therefore infer a geometric limit for how long the quasars already had to be active (t_{age}) which sets a lower limit on the lifetime of quasars (t_{Q}).

To do so, we create stacks for quasars above a minimum transverse separation from the background sightline. If the transverse proximity effect persists in the stack, the quasars on average have to shine for at least the light crossing time corresponding to that distance. This is presented in Figure 2.13. We select quasars with $\Gamma_{\text{QSO}}^{\text{HeII}} > 2 \times 10^{-15} \text{ s}^{-1}$ and apply cuts on the proper distance to the background sightline of $D_{\text{prop}} > 15 \text{ Mly}$ and $> 25 \text{ Mly}$.

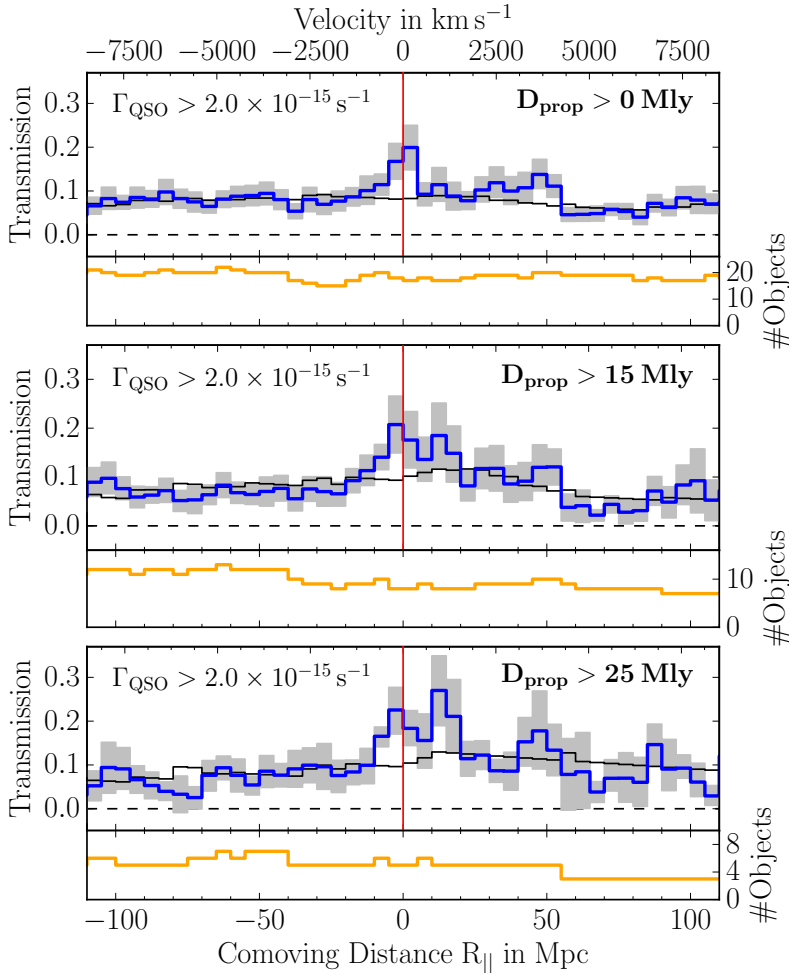


Figure 2.13: Constraint on the quasar lifetime from the He II transverse proximity effect. The top panel shows a stack including all foreground quasars (i.e. Figure 2.7) while the two others only include quasars above a minimum separation of $D_{\text{prop}} > 15$ Mly and > 25 Mly. The transverse proximity effect persists in these stacks with a significance of 3.2σ and 2.6σ , respectively. Since we simultaneously observe quasars and enhanced ionization at the background sightline, the quasars must shine for longer than the transverse light crossing time, implying a quasar lifetime of $t_Q > 25$ Myr.

For $D_{\text{prop}} > 15$ Mly we detect enhanced transmission ($\xi = 0.097$), and our Monte Carlo simulations with this cut in D_{prop} yield a significance level of 3.2σ or a by-chance probability $p = 0.0006$. The slightly higher significance compared to the stack including all foreground quasars (3.1σ) may be because at larger distances more luminous quasars are required to meet our threshold in $\Gamma_{\text{QSO}}^{\text{HeII}}$. These more luminous quasars probably have larger proximity zones (Khrykin et al. 2016) possibly explaining the slightly higher significance. However, this could also be due to stochasticity in the data. For the stack including only foreground quasars with $D_{\text{prop}} > 25$ Mly the enhanced transmission persists ($\xi = 0.116$) at 2.6σ significance ($p = 0.0053$). However, at $D_{\text{prop}} > 25$ Mly only ≈ 5 quasars are bright enough to yield a photoionization rate $\Gamma_{\text{QSO}}^{\text{HeII}} > 2 \times 10^{-15} \text{ s}^{-1}$. Note that our measurements at large separations do not include the prominent $z = 3.05$ He II transmission spike in the Q 0302–003 sightline, as both foreground quasars are at $D_{\text{prop}} < 13$ Mly (Figure 2.6).

We also test stacks with lower cuts on $\Gamma_{\text{QSO}}^{\text{HeII}}$ that yield consistent results, however at an overall lower confidence level. A detailed overview of the significance estimates for various QSO separations and cuts on $\Gamma_{\text{QSO}}^{\text{HeII}}$ is given in Figure 2.14. For all parameter combinations we first create the science stack and then run a Monte Carlo analysis matched to that sample. Figure 2.14 clearly illustrates the presence of a transverse proximity effect out to substantial distances. The corresponding lifetime constraints depend on the minimum requirements (sample size, $\Gamma_{\text{QSO}}^{\text{HeII}}$ cut, σ limit). We obtain a 2.6σ detection (which we call significant) for $\Gamma_{\text{QSO}}^{\text{HeII}} > 2 \times 10^{-15} \text{ s}^{-1}$ and $D_{\text{prop}} > 25$ Mly (i.e. 8 pMpc), resulting in a lower limit on the quasar lifetime of 25 Myr.

2.4. QUANTIFYING THE EFFECT FOR INDIVIDUAL QUASARS

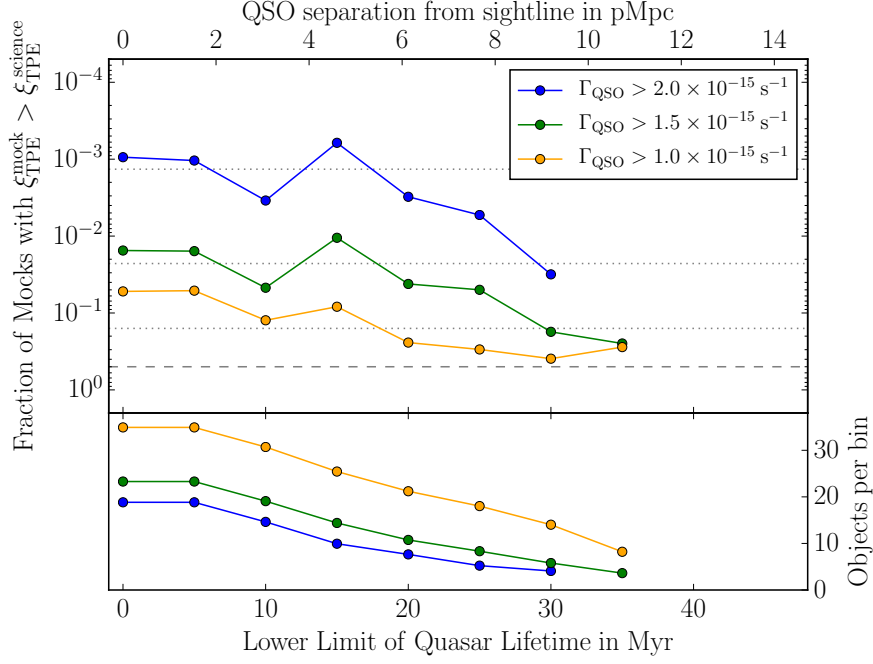


Figure 2.14: Significance estimate of the lower limit on the quasar lifetime from our Monte-Carlo analysis. The top panel gives the probability that the transmission enhancement ξ in our mock stacks exceeds the value that is measured in the science stack. This is given as function of the cuts on separation and $\Gamma_{\text{QSO}}^{\text{HeII}}$. In absence of the transverse proximity effect ($\xi = 0$) we expect 50% of the random stacks to exceed the measured transmission (dashed line). The probabilities corresponding to 1, 2 and 3σ detections are indicated by dotted lines. The bottom panel gives the average number of spectra contributing per bin in the stacks.

2.4 Quantifying the Transverse Proximity Effect for Individual Quasars

Given the apparently discrepant results that foreground quasars with high estimated He II photoionization rates often show no signs of a transverse proximity effect (§ 2.2) whereas the effect is clearly detected in stacked spectra (§ 2.3), we apply the ξ statistic (Equation 2.4) to individual sightlines and investigate the variance in ξ among our foreground quasar sample. This necessarily results in a noisy statistic since we do not average down fluctuations caused by e.g. the cosmic density structure or other sources of stochasticity in the transverse proximity effect, but it allows us to investigate the effect of individual foreground quasars.

Figure 2.15 shows a zoom-in of the He II spectra in the vicinity of each foreground quasar contributing to the stack shown in Figure 2.7. The regions are again chosen to extend for $\pm 120 \text{ cMpc}$ and binned to 5 cMpc , identical to the procedure adopted for stacking. The objects are sorted by transmission enhancement ξ in increasing order from top left to bottom right. As already mentioned in Section 2.2, there is a large diversity in the appearance of the He II spectra close to the foreground quasars. For some there is a substantial enhancement in transmission, e.g. for the quasars in the bottom row of Figure 2.15 including the $z = 3.05$ quasar near the Q 0302–003 sightline with $\xi = 0.14$. For others we see no significant transmission enhancement ($\xi \approx 0$). For the two highest redshift foreground quasars at $z > 3.1$, the He II spectra show no transmission at all ($\xi \approx 0$) and for one $z = 2.815$ quasar close to the HE2QS J2149–0859 sightline we even find substantially lower transmission at the quasar location than in the region around it ($\xi = -0.23$, upper left corner of Figure 2.15).

Although the transmission spike in the Q 0302–003 sightline is the most prominent feature in our sample, it does not have the highest ξ (Equation 2.4). The reason is that, although

CHAPTER 2. SYSTEMATIC SEARCH FOR THE HE II TPE

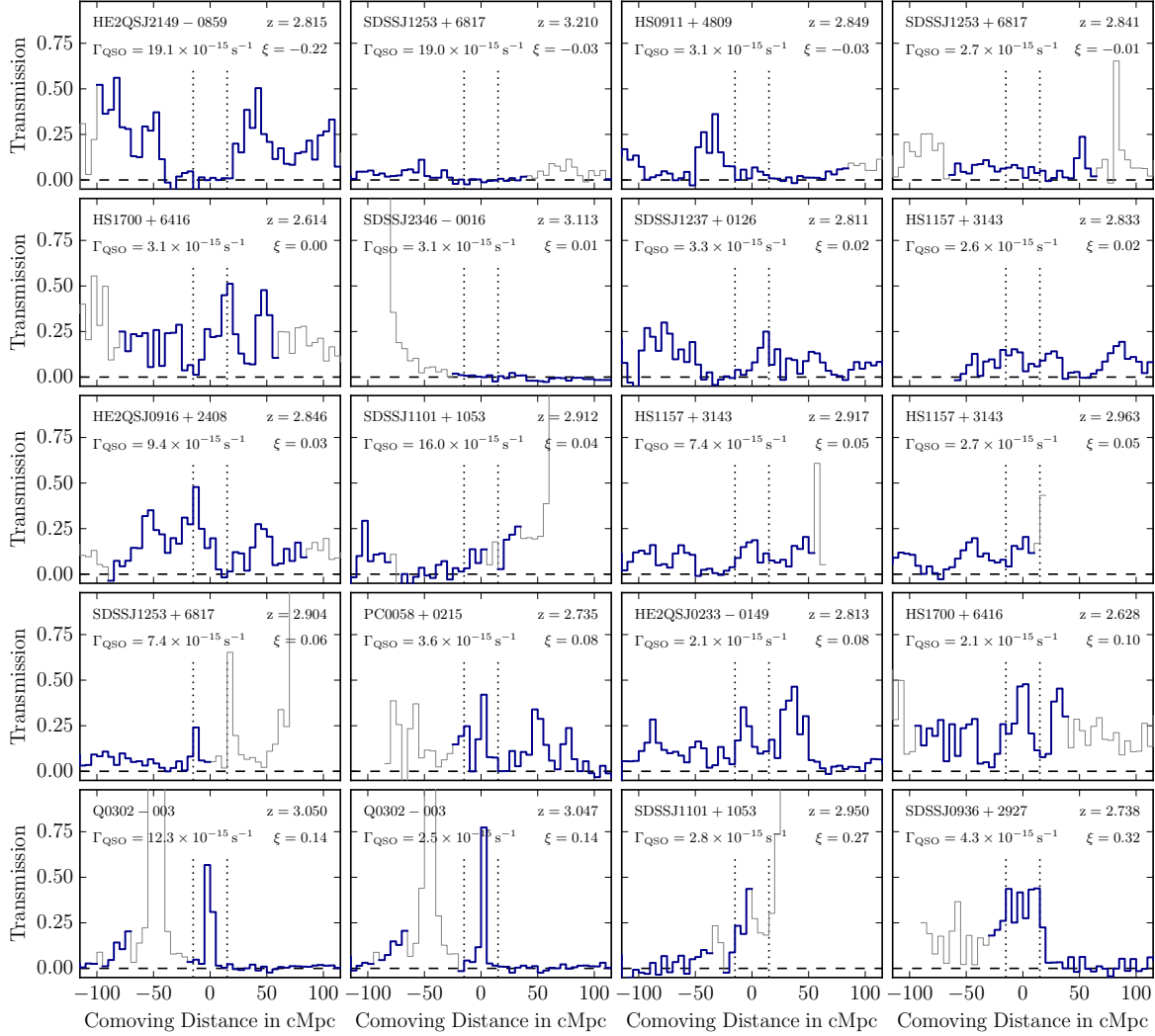


Figure 2.15: He II spectra in the vicinity of all foreground quasars with $\Gamma_{\text{QSO}}^{\text{HeII}} > 2 \times 10^{-15} \text{ s}^{-1}$. Masked and therefore ignored parts of the spectra are shown in gray. Foreground quasar redshifts, estimated $\Gamma_{\text{QSO}}^{\text{HeII}}$ values and He II sightlines are labeled. The transmission enhancement ξ is measured by taking the difference of the average transmission within the central $\pm 15 \text{ cMpc}$ (dotted lines) and outside of this. Panels are ordered by ξ from top left to bottom right. The transmission spike at $z = 3.05$ in the Q 0302–003 sightline appears twice since there are two associated foreground quasars. Due to their slightly different redshifts, the centered and rebinned He II spectra look differently, but their ξ values are identical.

the transmission spike is very strong, it is also rather narrow ($\approx 450 \text{ km s}^{-1}$ or 5.7 cMpc)⁵, far narrower than the $\pm 15 \text{ cMpc}$ window we average over, chosen to be slightly larger than the typical redshift uncertainty of 1000 km s^{-1} . The average transmission within this window is therefore not extreme and for two other quasars we find substantially higher enhancements. The sightline of SDSS J0936+2927 exhibits in the vicinity of the foreground quasar at $z = 2.738$ only 35 % He II transmission. However, this extends over the full width of the window, resulting in the highest measured transmission enhancement in our sample ($\xi = 0.33$, bottom right panel in Figure 2.15). However, note that at $z = 2.7$ it is unclear how much of this large transmission can be attributed to density fluctuations in the post-reionization IGM. Indeed, we adopt the stacking technique to average down these large fluctuations.

⁵The Q 0302–003 sightline is the only one for which we use the high-resolution COS G130M spectrum and therefore clearly resolve the transmission spike. However, since the average transmission within $\pm 15 \text{ cMpc}$ used by our ξ statistic is not affected by the resolution we do not smooth the spectrum to G140L resolution.

2.4. QUANTIFYING THE EFFECT FOR INDIVIDUAL QUASARS

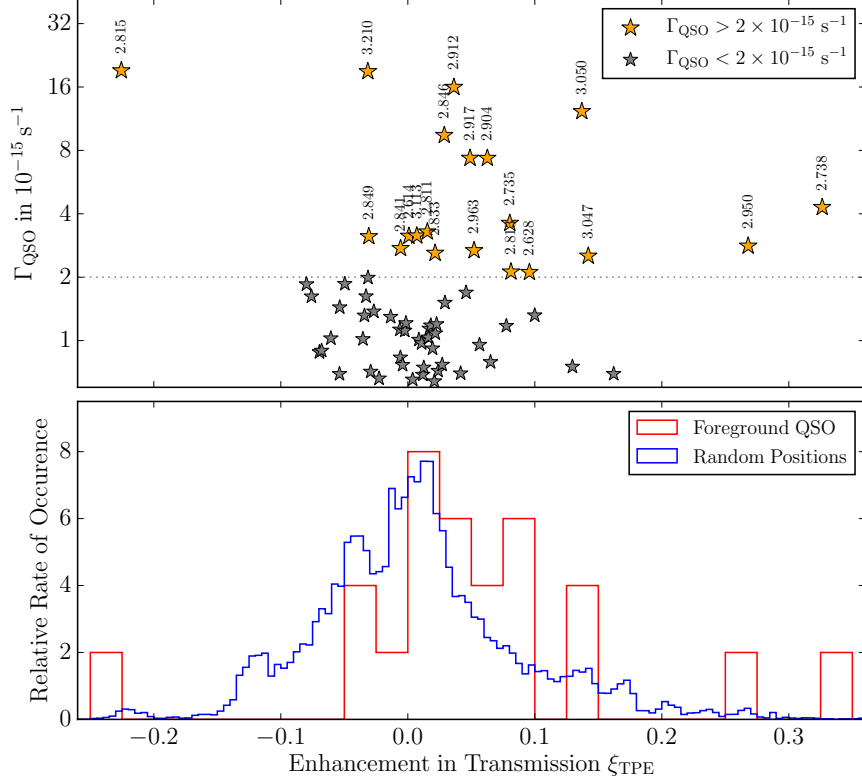


Figure 2.16: *Top panel:* Ionization rate $\Gamma_{\text{QSO}}^{\text{HeII}}$ compared to the transmission enhancement ξ for our sample of foreground quasars. Quasars with $\Gamma_{\text{QSO}}^{\text{HeII}} > 2 \times 10^{-15} \text{ s}^{-1}$ are shown in orange, quasars with $0.6 \times 10^{-15} \text{ s}^{-1} < \Gamma_{\text{QSO}}^{\text{HeII}} < 2 \times 10^{-15} \text{ s}^{-1}$ in gray. For identification, the quasars are labeled with their redshift. *Bottom panel:* Histogram of ξ for quasars with $\Gamma_{\text{QSO}}^{\text{HeII}} > 2 \times 10^{-15} \text{ s}^{-1}$ (red) and for 10^6 random positions in the He II spectra with a matched redshift distribution (blue). Both histograms are normalized to unity. The ξ distribution of foreground quasars with $\Gamma_{\text{QSO}}^{\text{HeII}} > 2 \times 10^{-15} \text{ s}^{-1}$ is inconsistent with being drawn from the random distribution ($p = 4.7\%$).

In Figure 2.16 we show the distribution of ξ and plot it against $\Gamma_{\text{QSO}}^{\text{HeII}}$. First, we find a large spread in ξ ($-0.23 \leq \xi \leq 0.33$) for quasars with $\Gamma_{\text{QSO}}^{\text{HeII}} > 2 \times 10^{-15} \text{ s}^{-1}$. Second, there is no obvious trend with $\Gamma_{\text{QSO}}^{\text{HeII}}$ or redshift (Figure 2.17). The $z = 2.815$ quasar near the HE2QS J2149–0859 sightline has the lowest value $\xi = -0.23$, but the highest photoionization rate in our sample ($\Gamma_{\text{QSO}}^{\text{HeII}} = 19.1 \times 10^{-15} \text{ s}^{-1}$, § 2.2.3). In contrast, the quasar at $z = 3.05$ near the Q 0302–003 sightline has a photoionization rate 30% lower ($\Gamma_{\text{QSO}}^{\text{HeII}} = 12.3 \times 10^{-15} \text{ s}^{-1}$) and

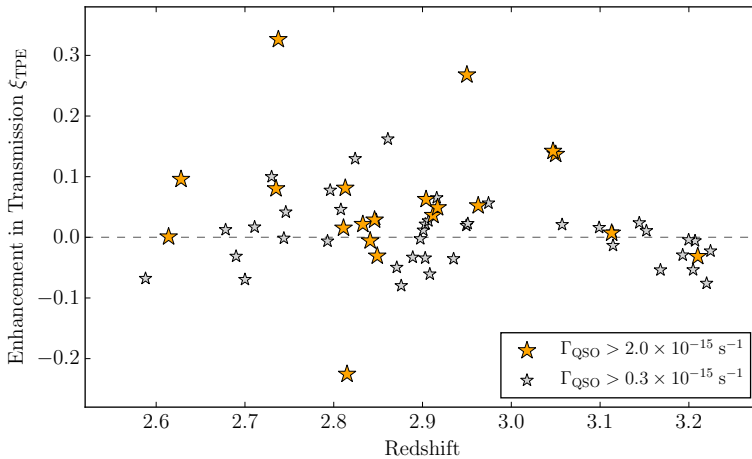


Figure 2.17: Distribution of the transmission enhancement with respect to redshift. No correlation with redshift is observed.

CHAPTER 2. SYSTEMATIC SEARCH FOR THE HE II TPE

shows a strong enhancement in transmission ($\xi = 0.14$). The ξ distribution has a mean value of $\bar{\xi} = 0.056$ which is consistent with $\xi_{\text{TPE}}^{\text{stack}} = 0.058$ in our stack (Figure 2.7). For comparison we also show foreground quasars with $0.6 \times 10^{-15} \text{ s}^{-1} < \Gamma_{\text{QSO}}^{\text{HeII}} < 2 \times 10^{-15} \text{ s}^{-1}$. These have $\bar{\xi} = 0.004$, indicating an insignificant transverse proximity effect, as expected given their low photoionization rates.

The bottom panel of Figure 2.16 shows a histogram of ξ for the sample of foreground quasars with $\Gamma_{\text{QSO}}^{\text{HeII}} > 2 \times 10^{-15} \text{ s}^{-1}$ (red). The blue histogram is based on our ξ statistic applied to 10^6 random positions along the He II sightlines with a redshift distribution matched to the one of the foreground quasars. We use a Kolmogorov-Smirnov test to investigate if the foreground quasar distribution is consistent with being drawn from the distribution of random positions. For the foreground quasars with $0.6 \times 10^{-15} < \Gamma_{\text{QSO}}^{\text{HeII}} < 2 \times 10^{-15} \text{ s}^{-1}$ this is the case ($p = 0.413$), however the sample with $\Gamma_{\text{QSO}}^{\text{HeII}} > 2 \times 10^{-15} \text{ s}^{-1}$ is inconsistent with the random distribution ($p = 0.047$). This is additional proof for the presence of the He II transverse proximity effect in our sample of foreground quasars, based on the full distribution of ξ rather than just its mean value as in the stack.

2.5 Discussion

2.5.1 Interpretation and Limitations of our Lifetime Constraint

In §2.3 we showed statistical evidence for a transverse proximity effect in our foreground quasar sample and derived a lower limit on the quasar lifetime. There are several reasons why the intrinsic quasar lifetime might in fact be larger than our limit. When creating stacks with a lower cut on the separation from the background sightline, we run out of bright foreground quasars with $\Gamma_{\text{QSO}}^{\text{HeII}} > 2 \times 10^{-15} \text{ s}^{-1}$ at $D_{\text{prop}} > 30 \text{ Mly}$. Lower photoionization rates are comparable to the UV background and apparently not sufficient to cause a detectable effect (Figures 2.11 and 2.14). With the given foreground quasar sample our geometrical method can therefore not probe lifetimes longer than this. In addition, it might be that IGM absorption limits the extent of the proximity zone and not the finite lifetime of the quasars (Khrykin et al. 2016). We estimate $\Gamma_{\text{QSO}}^{\text{HeII}}$ ignoring IGM absorption (assuming $\lambda_{\text{mfp}} = \infty$ in Equation 2.3). However, a mean free path of $\lambda_{\text{mfp}} \approx 50 \text{ cMpc}$ – consistent with Davies & Furlanetto (2014) – would cause a reduction of $\Gamma_{\text{QSO}}^{\text{HeII}}$ by 50% at 10 pMpc or 32 Mly separation. IGM absorption therefore limits the impact of distant quasars. Quasars at $D_{\text{prop}} = 10 \text{ pMpc}$ would have to be twice as luminous to still exceed our threshold of $\Gamma_{\text{QSO}}^{\text{HeII}} > 2 \times 10^{-15} \text{ s}^{-1}$ at the background sightline⁶. Such objects do not exist within our sample. On the other hand, our measurement of the transverse proximity effect constrains the mean free path to He II-ionizing photons. From our detection of the effect at $D_{\text{prop}} = 25 \text{ Mly}$ we conclude that the mean free path cannot be much shorter than this.

Our lifetime constraint on the quasar lifetime derived from the stacked He II transmission spectra (Figure 2.13) is sensitive to some average of the individual quasar ages. Under the assumption of a lightbulb model for the quasar lightcurve, the quasar age t_{age} is always shorter than the quasar lifetime t_Q . For a quasar population with fixed t_Q and flat distribution in t_{age} , the average age of a population is half its lifetime, i.e. $\overline{t_{\text{age}}} = t_Q/2$. From the observation of a proximity effect at a transverse distance of $D_{\text{prop}} = 25 \text{ Mly}$ we place a lower limit on $\overline{t_{\text{age}}} > 25 \text{ Myr}$, which could in principle indicate $t_Q > 50 \text{ Myr}$. However, due to our limited sample size ($N \approx 5$) we can not be sure that we have converged to this average or exclude that a few particularly old quasars dominate this measurement. We therefore conservatively only constrain $t_Q > 25 \text{ Myr}$.

⁶This threshold was derived in §2.3.3 from all available quasars and is dominated by small separations.

Furthermore, we have to consider the time the IGM requires to adjust to a new photoionization equilibrium. The equilibration timescale is the inverse of the ionization rate and is approximately 10^7 yr (Khrykin et al. 2016)⁷. This has to be added to the light crossing time to get a more precise estimate on the lifetime. However, the local equilibration time depends on the amplitude of the UV field which is heavily influenced by the quasar within its proximity zone and we consider the exact effects of this too uncertain to include it in our lifetime estimate. Additionally, equilibration effects render our method insensitive to quasar variability on scales shorter than the equilibration timescale. However, as shown in Section 2.3.3, $\Gamma_{\text{QSO}}^{\text{HeII}}$ is, at least when applied to a population, a reasonable proxy for the impact on the background sightline. The quasar luminosity is therefore not allowed to differ tremendously over the timescales probed by our analysis and the actual quasar lightcurve—even if it deviates from the lightbulb model—has to be consistent with sustained activity over 25 Myr.

2.5.2 Absence of Transmission Spikes for Large Photoionization Rate Enhancements

Our statistical sample shows that the presence of a foreground quasar close to the background sightline does not necessarily imply a prominent He II transmission spike, even when the expected photoionization rate should be greatly enhanced. Instead, out of the four foreground quasars with the highest $\Gamma_{\text{QSO}}^{\text{HeII}}$, only the one near the Q 0302–003 sightline is associated with an obvious transmission spike (Figure 2.6). So far we can only speculate why the other three sightlines do not show similar transmission spikes.

Possibly, these quasars might be active for too short a period ($t_{\text{age}} \lesssim 10$ Myr) to allow their radiation to reach the background sightline. However, these quasars are not substantially farther away from their background sightline or even closer than the quasar near Q 0302–003 (14.7, 13.5 and 7.3 Mly compared to 9.7 Mly) and all have a higher $\Gamma_{\text{QSO}}^{\text{HeII}}$. From our stacking analysis we find evidence for continued quasar activity over 25 Myr (Figure 2.14). If this is representative of the quasar population, it would be surprising if the three quasars with the highest $\Gamma_{\text{QSO}}^{\text{HeII}}$ are all very young.

Another possible explanation could be that due to variations in the quasar SED, in particular the poorly constrained part between 1 and 4 Ry, or because of substantial fluctuations in λ_{mfp} the ionizing rate at the background sightline is actually lower than our estimate. While this might be the case for individual quasars, our statistical detection of the transverse proximity effect for foreground quasars with $\Gamma_{\text{QSO}}^{\text{HeII}} > 2 \times 10^{-15} \text{ s}^{-1}$ (Figure 2.11) argues against a scenario where our estimates of $\Gamma_{\text{QSO}}^{\text{HeII}}$ are systematically off. Any fluctuation in the SED or λ_{mfp} would have to be very substantial to bring the $8\times$ higher estimated $\Gamma_{\text{QSO}}^{\text{HeII}}$ of our three strongest foreground quasars to a level for which we expect to see no effect.

Quasar obscuration could certainly be important, which we have so far ignored when calculating $\Gamma_{\text{QSO}}^{\text{HeII}}$ (see § 2.1.6). The effect of anisotropic emission on the appearance of a particular He II spectrum clearly needs further exploration. Since quasar orientation is random and only constrained to be unobscured towards Earth, one can in any case only expect a probabilistic answer (see e.g. Furlanetto & Lidz 2011). Determining how realistic it might be that three out of four foreground quasars do not illuminate the background sightline is an important question for future work. We perform a detailed modeling of these four foreground quasars including lifetime and obscuration effects in Chapter 3.

Despite the three discussed foreground quasars having no visible impact on the background sightlines, the quasar at $z = 3.05$ near Q 0302–003 might show a particularly strong signature.

⁷Recombination can be neglected since the recombination timescale for helium is comparable to the Hubble time

CHAPTER 2. SYSTEMATIC SEARCH FOR THE HE II TPE

Comparison of the H I and He II spectrum of the Q 0302–003 sightline indicates a substantial modulation of the He II transmission by the IGM density field, with the He II transmission spike being located in a region of high H I transmission (Worseck & Wisotzki 2006; Syphers & Shull 2014). One could speculate that a favorable association of one (or even two) foreground quasars with a low-density region in the IGM allows for an unusually strong He II transmission spike. Analyzing high-resolution H I spectra for the other He II sightlines might shed light on this point.

We conclude that a high photoionization rate ($\Gamma_{\text{QSO}}^{\text{HeII}} > 2 \times 10^{-15} \text{ s}^{-1}$, Figure 2.11) is a necessary condition to cause a significant transverse proximity effect, but is itself not sufficient. Apparently, there are other factors that govern the presence of excess transmission of which we have discussed a few. Additional data and better statistics will certainly help to constrain this, but we inevitably require further modeling with a realistic implementation of lifetime, obscuration and λ_{mfp} effects that accounts for the stochasticity in these quantities.

2.5.3 Toy Model for the Ionization Rate along the Sightline

Here, we present a toy model of the UV radiation field along a background sightline to illustrate effects that are relevant to the He II transverse proximity effect. A complete model requires 3D numerical radiative transfer calculations and is beyond the scope of this project. For now however, we want to build some intuition for the processes involved and highlight key aspects that would be part of a future modeling attempt.

The light crossing time between a foreground quasar and the background sightline is the governing effect we use to constrain the quasar lifetime. While the light from the foreground quasar travels to Earth on the direct path, the distance to any point on the background sightline and from there to the observer on Earth is longer. This difference in pathlength and therefore light travel time is the time difference $\Delta t(z)$. In the bottom panel of Figure 2.18 we show as an example the time difference for any point along the sightline of Q 0302–003 with respect to the foreground quasar at $z = 3.05$ at a separation of $6.5'$ (for formal derivations and similar models see e.g. Liske & Williger 2001; Smette et al. 2002; Adelberger & Steidel 2005). Evaluated at the redshift of the foreground quasar, the time difference equals the transverse light crossing time used so far in our analysis. Toward lower redshifts $\Delta t(z)$ decreases since the additional pathlength of the photons is shorter, whereas for gas behind the foreground quasar (at higher redshifts) the time difference rapidly increases. Taking a quasar that shines for a given time t_{age} , gas at lower redshift, when probed by the photons from the background quasar, has already been exposed to the quasar’s radiation for longer times than gas at higher

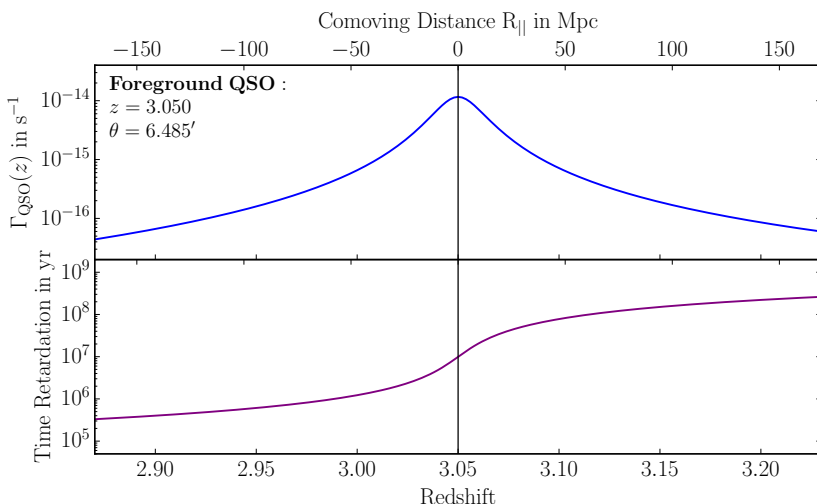


Figure 2.18: Photoionization rate $\Gamma_{\text{QSO}}^{\text{HeII}}(z)$ and time difference $\Delta t(z)$, denoted here as *time retardation*, along the Q 0302–003 sightline for the brighter of the two foreground quasars at $z = 3.05$. Note the monotonic increase of $\Delta t(z)$ toward higher redshifts.

redshifts. For locations with $\Delta t(z) > t_{\text{age}}$, the gas has not yet been exposed to the quasar radiation at all. The photoionization rate along the background sightline $\Gamma_{\text{QSO}}^{\text{HeII}}(z)$ (top panel in Figure 2.18) can be calculated as described in § 2.1.6, but using the luminosity distance to a given point on the background sightline instead of the transverse distance in Equation 2.2.

Given that we can model the time difference and photoionization rate caused by a single quasar as described above, we can synthesize the He II-ionizing radiation field along a sightline by summing the contributions of all foreground quasars as

$$\Gamma_{\text{SL}}^{\text{HeII}}(z) = \sum_i \Gamma_{\text{QSO}_i}^{\text{HeII}}(z). \quad (2.5)$$

Figure 2.19 shows an example of this model for the sightline toward Q 0302–003. The bottom panel displays again the He II transmission spectrum and the location of the foreground quasars, while the top panel shows several models of $\Gamma_{\text{SL}}^{\text{HeII}}(z)$. For the model shown in blue we assume isotropic emission and infinite quasar lifetime for all foreground quasars and no IGM absorption ($\lambda_{\text{mfp}} = \infty$). The right y-axis of Figure 2.19 indicates the He II photoionization timescale and therefore the equilibration timescale $t_{\text{eq}}^{\text{HeII}}$ (Khrykin et al. 2016). Note that the photoionization timescale is spatially varying, as it is the inverse of $\Gamma_{\text{SL}}^{\text{HeII}}(z)$. In general, $t_{\text{eq}}^{\text{HeII}}$ is of the order $\sim 10^7$ yr and therefore comparable to the transverse light crossing time. If quasars shine for a period comparable to our lifetime constrains inferred in § 2.3.5 ($t_{\text{Q}} \simeq 25$ Myr) and the photoionization rate at a given point along the sightline is dominated by a few close foreground quasars, He II at $z \simeq 3$ might not yet be in photoionization equilibrium. This would further complicate the interpretation of the He II Ly α forest transmission and its relation to the ionizing radiation provided by the observed quasar population since non-equilibrium effects would have to be taken into account.

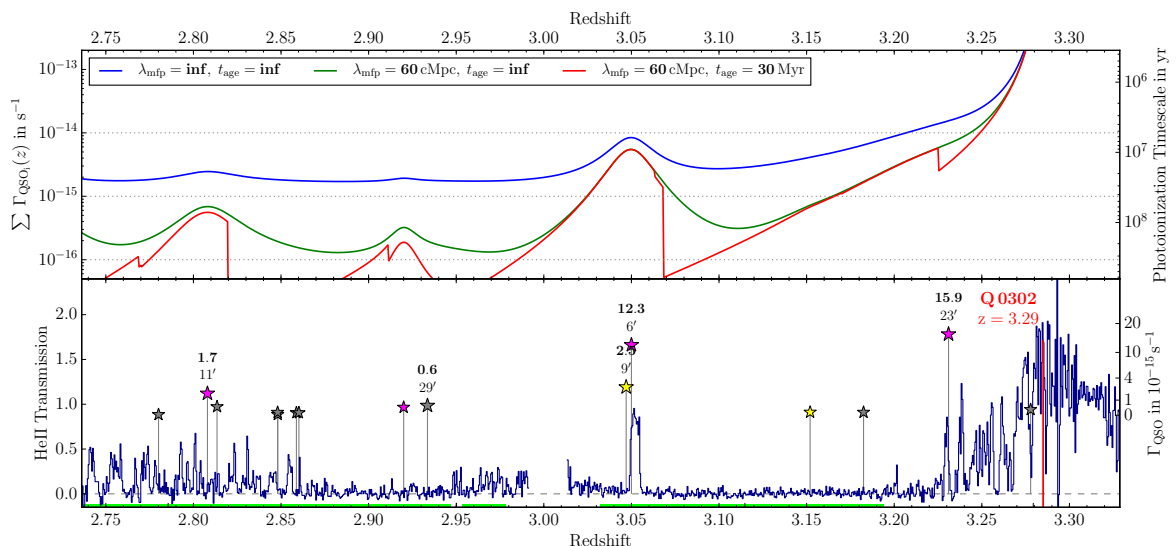


Figure 2.19: Models for the varying He II-ionizing radiation field along the He II sightline of Q 0302–003 (top) and its He II transmission spectrum indicating the locations of the quasars (bottom). We synthesize the photoionization rate $\Gamma_{\text{SL}}^{\text{HeII}}(z)$ based on the background quasar and the population of known foreground quasars by summing up their individual contributions. For computation of the $\Gamma_{\text{SL}}^{\text{HeII}}(z)$ model shown in blue we assume isotropic emission, infinite quasar lifetime and a transparent IGM. We show the effects of IGM absorption with a mean free path of $\lambda_{\text{mfp}} = 60 \text{ cMpc}$ (green curve) and in addition a finite quasar age of $t_{\text{age}} = 30 \text{ Myr}$ (red curve). Assuming a finite age causes a strong asymmetry in the radiation field around individual foreground quasars since these only illuminate regions in the background sightline for which the time difference is smaller than the quasar age ($\Delta t(z) < t_{\text{age}}$).

CHAPTER 2. SYSTEMATIC SEARCH FOR THE HE II TPE

Assuming an infinite mean free path and adding up quasar contributions out to arbitrary large separations from the background sightline leads to very high $\Gamma_{\text{SL}}^{\text{HeII}}(z)$. Relying only on the population of discovered foreground quasars we already end up with photoionization rates in excess of the average $\Gamma_{\text{UVB}}^{\text{HeII}}$ predicted by UV background models (e.g. Faucher-Giguère et al. 2009; Haardt & Madau 2012, $\Gamma_{\text{UVB}}^{\text{HeII}}(z = 3) \approx 10^{-15} \text{ s}^{-1}$) and inconsistent with highly saturated He II absorption (Khrykin et al. 2016).

We therefore show in Fig 2.19 (green curve) the effect of a reduced mean free path. We chose $\lambda_{\text{mfp}} = 60 \text{ cMpc}$ which is broadly consistent with the values from Davies & Furlanetto (2014). However, we stress that by creating proximity zones, the quasars heavily modify the mean free path in their vicinity (Khrykin et al. 2016). As expected (see e.g. McQuinn & Worseck 2014), a short mean free path not only reduces the average $\Gamma_{\text{SL}}^{\text{HeII}}(z)$ but also enhances the amplitude of the spatial fluctuations due to individual quasars.

In a third synthesis model of the UV radiation field we include the effect of a finite quasar lifetime. We assume all foreground quasars to have a fixed age $t_{\text{age}} = 30 \text{ Myr}$. This is clearly a simplification since even if all quasars would have exactly the same lifetime t_{Q} , they would turn on at a random point in time and t_{age} would be drawn from a flat distribution between zero and t_{Q} . Nevertheless, limiting the quasar age decreases the photoionization rate behind bright foreground quasars since the quasars do not shine long enough for the photons to reach these regions. The effect on the background sightline at redshifts lower than the foreground quasar redshift is much smaller since the time difference for these points is smaller (Figure 2.18). The ionization fronts of the individual foreground quasars at redshifts where $\Delta t(z) = t_{\text{age}}$ are also apparent in Figure 2.19. When increasing t_{age} , these ionization fronts shift to higher redshifts and an increasing fraction of the background sightline can be reached by the foreground quasar radiation. The shape and evolution of these ionization fronts is discussed in more detail in our subsequent work and presented in Chapter 3. In reality, radiation transfer effects should substantially smooth the rapid jump of $\Gamma_{\text{SL}}^{\text{HeII}}(z)$ at the location of the ionization front (e.g. Davies et al. 2017).

An additional important factor as described in § 2.1.6 and § 2.5.2 is quasar obscuration. Modeling the anisotropic emission of quasars detected as Type Is from Earth is straightforward – it would simply lead to some parts of the background sightline being not illuminated (e.g. Furlanetto & Lidz 2011). However, if quasar emission is significantly obscured in some directions, there should also be quasars illuminating the background sightline but appear as Type IIs from our vantage point on Earth. These obscured AGN are certainly not in our foreground quasar sample and would be extremely difficult to detect. Finally, there may be light-echoes in the He II spectra caused by quasars that have already turned off (e.g. Visbal & Croft 2008). Similar to obscured quasars, these objects evade detection and can not be included in the model individually but have to be treated in a statistical sense.

These simple models illustrate that the quasar lifetime, quasar obscuration, and λ_{mfp} strongly influence the He II ionizing radiation field. Exploring how this translates into an observable He II transverse proximity effect is a challenging task, in particular when including additional complications like variable quasar orientation and extinct quasars, non-equilibrium photoionization, and a realistic IGM density structure. Our toy models, however, show the wealth of information contained in the transverse proximity effect that is in principle accessible to observations.

2.6 Summary and Conclusions

The He II transverse proximity effect provides unique insights into the relationship between He II reionization and the quasars that power it. The effect also allows one to probe the geome-

try and timescales of quasar emission. We therefore conducted a dedicated ground-based optical imaging and spectroscopic survey for quasars in the foreground of 22 background quasars with science-grade *HST* FUV He II Ly α absorption spectra. Our two-tiered survey strategy, composed of a deep survey with 8 m class telescopes (LBT/LBC and VLT/VIMOS, $r \lesssim 24$ mag, $\Delta\theta \lesssim 10'$) and a wide survey with 4 m class telescopes (ESO NTT and CAHA 3.5 m, $r \lesssim 21$ mag, $\Delta\theta \lesssim 90'$) resulted in the discovery of 131 new quasars, 27 of which have redshifts probed by He II absorption along the background sightline (§ 2.1). Adding known quasars (mainly from SDSS and BOSS), we arrive at a total of 66 usable foreground quasars. We searched for the He II transverse proximity effect as enhanced He II transmission near individual foreground quasars (§ 2.2.3 and 2.4) and also statistically by stacking the data for our sample (§ 2.3).

Previous studies claimed a dramatic association of one foreground quasar with a strong He II transmission spike in the Q 0302–003 sightline (Heap et al. 2000; Jakobsen et al. 2003). Our substantially larger sample contains three new foreground quasars with even higher estimated photoionization rates at the background sightline that exceed the expected He II-ionizing background by an order of magnitude. However, none of these new sightlines exhibit a noticeable increase in He II transmission (Figure 2.6), suggesting that such associations are in fact rare.

Despite the large stochasticity, we find statistical evidence for the He II transverse proximity effect by stacking the He II spectra on the positions of the foreground quasars. The average transmission profile along the background sightlines shows increased He II transmission in the vicinity ($|R_{\parallel}| < 15$ cMpc) of the foreground quasar positions when compared to the average transmission observed further away (Figure 2.7). Using a Monte Carlo method, we estimate the probability for this excess transmission to occur by chance to 0.1%, corresponding to a significance of 3.1σ .

We show for the first time that the strength of this transverse proximity effect has the expected dependence on the photoionization rate of the foreground quasars (Figure 2.11). We see a local enhancement in the He II transmission when including foreground quasars with $\Gamma_{\text{QSO}}^{\text{HeII}} > 2 \times 10^{-15} \text{ s}^{-1}$. For lower $\Gamma_{\text{QSO}}^{\text{HeII}}$, comparable to UV background estimates, no enhancement is observed.

We use the transverse light crossing time to derive a purely geometric lower limit on the quasar lifetime by imposing cuts on the foreground quasar separation from the background sightline (Figure 2.13). When restricting to quasars with $D_{\text{prop}} \geq 7.7$ pMpc the transverse proximity effect persists in our stacked spectra with a 2.6σ significance, allowing us to derive a robust lower limit on the quasar lifetime of 25 Myr. Our analysis, based on a statistical sample and a model-independent method, puts stronger constraints on the quasar lifetime than previous studies of single objects or small samples (e.g. Jakobsen et al. 2003; Gonçalves et al. 2008; Furlanetto & Lidz 2011; Trainor & Steidel 2013; Borisova et al. 2016), and contrasts with studies finding short lifetimes (e.g. Kirkman & Tytler 2008; Schawinski et al. 2015). At the same time this constrains the mean free path to $\gtrsim 30$ cMpc at $z \approx 3$, consistent with current estimates (McQuinn & Worseck 2014; Davies & Furlanetto 2014).

The He II transverse proximity effect can reveal extensive information about the quasar opening angle, the quasar lifetime and the mean free path to He II-ionizing photons in the IGM (§ 2.5.3). However, due to the large sightline-to-sightline variance and the weak statistical signal, there is no simple interpretation of the data beyond the lifetime constraint. Deriving more stringent constraints clearly requires extensive modeling and additional data.

It is therefore crucial to observe additional He II sightlines to reduce the sample variance (§ 2.4). However, due to the rarity of He II-transparent quasars and the aging of *HST*/COS, a massive expansion ($> 2\times$) of the He II sample will probably only be possible with the next

CHAPTER 2. SYSTEMATIC SEARCH FOR THE HE II TPE

generation of FUV telescopes. Since these will only become available decades from now, it is important to exploit the current *HST*/COS capabilities to the limit and observe the available targets at $z \approx 3$.

Furthermore one should expand the deep foreground quasar survey to He II sightlines in the northern hemisphere (see Table 2.2), several of which show significant transmission spikes (see Figure 2.5). The redshifts of the foreground quasars were inferred from UV emission lines, subject to systematic uncertainties of up to 1000 km s^{-1} , corresponding to $\approx 13 \text{ cMpc}$. This is comparable to the width of the detected transverse proximity signal and nearly $3\times$ wider than the strong transmission spike in the Q 0302–003 sightline. Improved redshifts from Mg II or [O III] ($\sigma_z = 100 - 300 \text{ km s}^{-1}$) would increase our sensitivity and would allow us to better constrain the shape of the transverse proximity profile, which could bear additional information about lifetime and anisotropic emission.

In addition, it would be very informative, but probably infeasible, to also chart the population of Type II foreground AGN. An X-ray survey comparable in sensitivity and area to our optical surveys would require several 100 ks exposure time per He II sightline, so covering all sightlines would exceed the allocations for the largest X-ray surveys (e.g. *Chandra* COSMOS-legacy survey Civano et al. 2016). Alternatively, covering the large required area ($\gtrsim 20' \times 20'$) with optical spectroscopic IFU observations seems extremely expensive as well.

In the near future, substantial progress on the physics of the He II transverse proximity effect might stem from dedicated modeling of the effect. The toy model we used in §2.5.3 to highlight a few effects as a showcase example is a good starting point for more comprehensive modeling of the He II transverse proximity effect which would take into account the time difference along the sightline and finite quasar ages, non-equilibrium ionization effects, and quasar obscuration. A model tailored to our observations could for instance clarify if the absence of strong transmission spikes in the He II spectra close to bright foreground quasars is actually consistent with our current assumptions about lifetime and quasar obscuration or requires additional effects. This might also lead to tighter constraints on the quasar lifetime or the mean free path to He II ionizing photons. Evidently, the transverse proximity effect bears a wealth of information. Now that a statistical sample is available, it requires improved theoretical understanding to better interpret the signal we have observed.

Chapter 3

Detailed Modeling of the He II Transverse Proximity Effect

This Chapter is based on work published in [Schmidt et al. \(2018a\)](#). Outputs from NYX cosmological simulations were supplied by Z. Lukić. F. Davies contributed skewers from the fluctuation He II UV background model. Identical to Chapter 2, G. Worseck provided the He II spectra. All other parts are based on research conducted by author T. Schmidt, under supervision of J. Hennawi at MPIA and UCSB.

The He II transverse proximity effect, enhanced He II transmission in a background sightline caused by the ionizing radiation of a nearby foreground quasar, is a powerful tool to constrain quasar emission properties, in particular their lifetime and obscuration. Therefore, as described in Chapter 2, we conducted a comprehensive search for the He II transverse proximity effect, discovered many new foreground quasars and found in a stack of He II sightlines evidence for enhanced He II transmission close to the foreground quasar positions. However, the absence of transmission spikes for the foreground quasars with the highest He II ionization rates (Figure 2.6) remains puzzling and raises questions about the age of these objects or their obscuration properties. There is clear evidence that quasars do not emit isotropically. For example, one observes in the optical/UV regime a clear dichotomy of the spectral appearance of AGN which *unified models* of AGN ([Antonucci 1993](#); [Urry & Padovani 1995](#); [Netzer 2015](#)) explain as a pure orientation effect. While in Type I quasars one has a direct view on the nuclear accretion disk and the broad line region, a dusty torus on parsec scales in the equatorial plane of the AGN completely or partially blocks the view on these regions in Type II AGN, leaving only the narrow line region observable.

The He II transverse proximity effect offers a *second view* on the foreground quasar and provides a unique opportunity to constrain the emission geometries of individual quasars. While direct observations of the foreground quasar reveal its properties from Earth's vantage point, the observed He II Ly α transmission along the background sightline crucially depends on the emission of He II ionizing photons in roughly transverse direction. In addition, these photons require time to reach the background sightline. Therefore, the He II Ly α transmission is, depending on the position along the background sightline, sensitive to the emission of the foreground quasar approximately one transverse light crossing time ago. Hence, the transverse proximity effect is ideal to infer emission geometries and geometric constraints on quasar ages or lifetimes.

In Chapter 2 (see also [Schmidt et al. 2017a](#)) we presented the results of a dedicated foreground quasar survey targeting the vicinity of 22 He II sightlines and delivering statistical evidence

CHAPTER 3. MODELING OF THE HE II TPE

for the He II transverse proximity effect. This led to a heuristic constraint on quasar lifetime of $t_Q > 25$ Myr. However, among the four foreground quasars with the highest estimated He II photoionization rates at the background sightline, only the previously known prototype object along the Q 0302–003 sightline (Heap et al. 2000; Jakobsen et al. 2003) showed a strong He II transmission spike. Surprisingly, all three newly discovered foreground quasars – despite having higher estimated He II photoionization rates and exceeding the He II UV background by an order of magnitude – exhibit very low transmission or even saturated absorption along the background sightline. In Schmidt et al. (2017a) we therefore speculated that either short quasar emission episodes or a high level of obscuration is required to explain these three objects. However, there existed at that time no quantitative prediction for the appearance of the He II spectra in the vicinity of these quasars, in particular not encompassing IGM stochasticity, finite quasar ages and obscuration.

In this Chapter, we therefore follow up on our previous work with a detailed modeling of the expected He II transmission signal, focusing on the six foreground quasars with the highest He II photoionization rate. We use outputs from the NYX cosmological hydrodynamical simulations (Almgren et al. 2013; Lukić et al. 2015) and post-process these with a photoionization model composed of the radiation from a single, bright foreground quasar on top of a semi-numerical, fluctuating He II UV background model (Davies et al. 2017). For the foreground quasar, we vary the quasar age t_{age} and obscuration Ω_{obsc} and explore the combined effect for the He II transverse proximity effect. To embrace the stochastic nature of quasar orientation, He II UV background fluctuations and IGM density structure, we compute many Monte Carlo realizations, allowing us to quantify for the first time the expected amount of fluctuations in observations of the He II transverse proximity effect. Using a fully Bayesian statistical approach, we compare our specifically designed models to the observed He II spectra and infer joint probabilities for quasar ages t_{age} and obscured sky fractions Ω_{obsc} of the six individual quasars.

This Chapter is structured as follows. In § 3.1 we summarize the subset of foreground quasars and He II sightlines from our transverse proximity effect survey (Chapter 2 and Schmidt et al. 2017a) that are modeled here in detail. The computation of our models, starting from outputs of the cosmological hydrodynamical simulation, application of UV background and quasar emission models and the calculation of the final mock spectra are described in § 3.2. The statistical approach developed for the comparison of the models to the He II observations is described in § 3.3. We derive joint probability distributions of t_{age} and Ω_{obsc} in § 3.4, and discuss the implications of our measurements in § 3.5.

Throughout this Chapter we use a flat Λ CDM cosmology with $H_0 = 68.5 \text{ km s}^{-1} \text{ Mpc}^{-1}$, $\Omega_\Lambda = 0.7$, $\Omega_m = 0.3$ and $\Omega_b = 0.047$ which was used for the computation of the NYX hydro simulation and is broadly consistent with the Planck Collaboration et al. (2018) results. We use comoving distances and denote the corresponding units as cMpc. For most of the paper (except § 3.5.2) we consider a simple lightbulb model for the quasar lightcurve in which the quasar turns on, shines with constant luminosity for its full lifetime t_Q until it turns off. This timespan is however different from the quasar age t_{age} , which describes the time from turning on until emission of the photons that are observed on Earth today. Magnitudes are given in the AB system (Oke & Gunn 1983).

3.1 Data Sample

We use the sample of He II sightlines and foreground quasars from our He II transverse proximity effect survey (Chapter 2, Schmidt et al. 2017a). However, we restrict our analysis to the six foreground quasars with the highest He II photoionization rate at the background sightline (see

Table 3.1. Key properties of the foreground quasars used for this study.

He II Sightline	RA (2000) degree	Dec (2000) degree	z	r mag	M_{1450} mag	$\Delta\theta$ arcmin	D_{prop} pMpc	$\Gamma_{\text{QSO}}^{\text{HeII}},_{\text{max}}$ s^{-1}
HE2QS J2149–0859	327.23032	−9.02613	2.815	19.3	−26.0	8.4	4.0	1.91×10^{-14}
HE2QS J0916+2408	139.16456	+24.19545	2.846	21.0	−24.3	5.6	2.7	9.44×10^{-15}
SDSS J1101+1053	165.51796	+10.95631	2.912	20.8	−24.5	4.8	2.3	1.60×10^{-14}
HS 1157+3143	180.41579	+31.59376	2.917	18.4	−27.0	21.9	10.4	7.36×10^{-15}
Q 0302–003	46.14721	−0.04750	3.050	20.6	−24.9	6.5	3.0	1.23×10^{-14}
SDSS J1253+6817	193.87605	+68.33807	3.210	19.4	−26.1	9.4	4.4	1.90×10^{-14}

§ 3.2.5 for a formal definition), and therefore strongest expected transverse proximity effect signal. Under the assumption of isotropic emission and infinite quasar lifetime, these quasars should cause a peak ionization rate at the background sightline between 7.3 and $19 \times 10^{-15} \text{ s}^{-1}$, and therefore exceed the expected intergalactic He II UV background (Faucher-Giguère et al. 2009; Haardt & Madau 2012; Khrykin et al. 2016; Khaire & Srianand 2018) by approximately one order of magnitude. An overview of the objects studied is given in Table 3.1 and far UV spectra of all six He II sightlines are shown in § 3.4, Figure 3.6. Four of the six objects were also discussed in detail in the previous Chapter in § 2.2.3 and shown in Figure 2.6.

Despite their high peak photoionization rates at the background sightline, we observe no strong He II transverse proximity effect for most of these foreground quasars. Only the prototype object at redshift $z = 3.05$ close to the Q 0302–003 sightline is associated with a strong He II transmission peak (Heap et al. 2000; Jakobsen et al. 2003). The others show ordinary and sometimes saturated He II absorption, The absence of transmission spikes for three of the four strongest foreground quasars was already discussed in § 2.2.3.

For this study, we include two other objects with high He II ionization rates, one at $z = 2.846$ along the HE2QS J0916+2408 sightline and one close to HS 1157+3143 at $z = 2.917$. Owing to its lower redshift, the HE2QS J0916+2408 sightline shows in general higher He II transmission around 20 %, with a broad transmission structure that might be associated with the foreground quasar, or could just be a random UV background fluctuation. HS 1157+3143 shows low He II transmission around 8 % with a very subtle broad bump around the foreground quasar position. There exists another foreground quasar with comparably high ionization rate along the SDSS J1253+6817 sightline at $z = 2.904$. However, we have incomplete far UV coverage along the background sightline and therefore do not include this object.

In § 2.3.2 we quantified the strength of the observed transverse proximity effect by introducing the transmission enhancement statistic. We therefore measure the average He II transmission in a ± 15 cMpc wide window around the foreground quasar and compare this with the average transmission outside this window. We continue using this statistic which is formally defined as

$$\xi = \langle \mathbf{F}_{|R_{\parallel}| < 15 \text{ cMpc}} \rangle - \langle \mathbf{F}_{15 \text{ cMpc} < |R_{\parallel}| < 65 \text{ cMpc}} \rangle, \quad (3.1)$$

where F denotes the He II transmission and R_{\parallel} the coordinate along the background sightline. In contrast to Equation 2.4 in § 2.3.2, we reduce the extent over which the background transmission is measured from ± 120 cMpc to ± 65 cMpc since the NYX simulation box used for this study only offers a pathlength of 146 cMpc.

Using ξ instead of simply the average He II transmission $\langle \mathbf{F}_{|R_{\parallel}| < 15 \text{ cMpc}} \rangle$ has the advantage that, to first order, the dependence on the He II UV background is removed. It thus better isolates the effect of the foreground quasar from unassociated background fluctuations. This is for instance illustrated in Figure 3.2 in § 3.2.4 .

3.2 Models / Simulations

For our analysis, we use outputs from a cosmological hydrodynamical simulation and post-process these with a photoionization model. This photoionization model is composed of the radiation from a single, bright foreground quasar and a fluctuating He II UV background from [Davies et al. \(2017\)](#). In the following, we first line out the extraction of skewers from the simulation box, the general calculation of H I and He II ionization states and the computation of mock spectra. We then present in more detail the fluctuating He II UV background model and the calibration procedure to make this model match the He II observations. Finally, we describe our model for the quasar ionization radiation, including the effects of finite quasar age and quasar obscuration.

3.2.1 Nyx Cosmological Hydrodynamical Simulations

We use simulations computed with the Eulerian hydrodynamical simulation code NYX ([Almgren et al. 2013](#); [Lukić et al. 2015](#)). The simulation box has a large size of $100 h^{-1}$ cMpc which is required to capture the full extent of a bright quasars He II proximity zone. The hydrodynamics is computed on a fixed grid of 4096^3 resolution elements and the same number of dark matter particles are used for computation of the gravitational field. This results in a resolution of 36 cMpc per pixel, required and sufficient to resolve the H I ([Lukić et al. 2015](#)) and He II Ly α forest. The simulation runs make no use of adaptive mesh refinement since the H I Ly α forest signal originates from the majority of the volume ([Lukić et al. 2015](#)) and the He II signal actually stems from the underdense regions (e.g. [Croft et al. 1997](#)). Refining the resolution in the dense regions at the expense of underdense regions is therefore not beneficial for our case. Also, since the prime objective of the simulation is IGM science, no star or galaxy formation prescriptions was included. The simulation was run using a homogeneous, optically thin UV background with photoionization and heating rates from [Haardt & Madau \(2012\)](#). As described below, we rescale the H I and He II photoionization rates to closely match observations but keep the thermal structure unchanged.

We use the density, velocity and temperature fields of a single simulation output at $z = 3$ and extract skewers that will be post-processed to simulate the observed He II Ly α transmission along the background sightlines. We tailor these to match our data sample as closely as possible, in particular we create for each foreground quasar in our sample a set of skewers with matched transverse separation, redshift and quasar luminosity. We center the foreground quasars on $\approx 10^{12} M_{\odot}$ halos, the preferred mass of AGN halos (e.g. [White et al. 2012](#)). As described in more detail in [Sorini et al. \(2018\)](#), halos in the NYX simulations are identified by finding topologically connected components above $138\times$ mean density ([Lukić et al. in prep.](#)). This gives similar results than the particle-based friends-of-friends algorithm ([Davis et al. 1985](#)). From the NYX halo catalog we select for each model e.g. the 2500 halos with mass closest to $10^{12} M_{\odot}$ and from this set randomly reject 90% to avoid deterministic behavior.

Given the list of selected halos, skewers are extracted along one of the grid axes with a transverse offset from the halo center matched to the observed separation between the foreground quasar and background sightline. The position angle between halo and skewer is randomly chosen. Multiple, skewers (e.g. 20) are extracted around each halo. Along the line of sight, we center the skewer on the halo position in redshift space, taking the peculiar velocity of the halo into account. With the observed redshift of the foreground quasar as the origin, we assign individual redshifts to every pixel of the skewer. To better represent redshift evolution of the density field along the sightline, we rescale the density of each pixel according to

$$\rho(z) = \rho_{\text{sim}} \times \left(\frac{z+1}{z_{\text{sim}}+1} \right)^3. \quad (3.2)$$

However, since the relevant range in redshift only spans $2.75 < z < 3.25$ (see Table 3.1), this correction is small. We convert from simulated cosmic baryon density to hydrogen and helium number density n_{H} and n_{He} using the primordial abundances of these elements, 76 % and 24 % (Coc et al. 2015). The temperature and velocity field are taken directly from the simulation box without any change.

3.2.2 Ionization State for Hydrogen and Helium

After extracting temperature T , velocity and cosmic baryon density from the Nyx simulation box and converting these to n_{H} and n_{He} assuming primordial abundances, we solve for the ionization state of hydrogen and helium. This requires a description of the corresponding photoionization rates $\Gamma_{\text{tot}}^{\text{HI}}$ and $\Gamma_{\text{tot}}^{\text{HeII}}$. Related to the presence of a bright foreground quasar and due to the fluctuating He II UV background model, H I and He II photoionization rates are spatially variable along our skewers. A detailed description of the adopted photoionization model follows later in § 3.2.4 and § 3.2.5.

We assume ionization equilibrium and ignore time-evolution and non-equilibrium effects. The equilibration timescale for He II is rather large, depending on the He II photoionization rate of the order of a few million years. However, the timescales probed by the given sightline geometries are even longer. We discuss non-equilibrium effects and more complicated quasar lightcurves in § 3.5.2.

Within the regime we are operating, around $z \simeq 3$, hydrogen reionization as well as He I reionization is completed and all hydrogen in the IGM is highly ionized (e.g. Haardt & Madau 2012; Planck Collaboration et al. 2018). We thus can separate the calculation of hydrogen and helium ionization state and avoid solving a coupled problem. In a first step, we calculate the hydrogen ionization state, ignoring the He II \rightarrow He III transition, i.e. assuming $n_{\text{HeIII}} = 0$. We follow the general approach as it is described e.g. in Rahmati et al. (2013). Ionization equilibrium is expressed by

$$n_{\text{HI}} \Gamma_{\text{tot}}^{\text{HI}} = \alpha_{\text{A}}^{\text{HeIII}} n_{e^-} n_{\text{HeIII}} \quad (3.3)$$

with n_{HI} , n_{HeIII} and n_{e^-} denoting the number densities of neutral hydrogen, ionized hydrogen and free electrons, respectively. The ionization rate $\Gamma_{\text{tot}}^{\text{HI}}$ is the sum of photoionization $\Gamma_{\text{phot}}^{\text{HI}} = \Gamma_{\text{UVB}}^{\text{HI}} + \Gamma_{\text{QSO}}^{\text{HI}}$ and collisional ionization. For the photoionization we include the self-shielding prescription from Rahmati et al. (2013) in which the effective photoionization rate in high-density regions with $n_{\text{H}} \gtrsim 5 \times 10^{-3} \text{ cm}^3$ is substantially reduced. For collisional ionization we assume $\Gamma_{\text{col}}^{\text{HI}} = \Lambda^{\text{HI}} n_{e^-}$ with

$$\Lambda^{\text{HI}}(T) = 1.17^{-10} \frac{(T/\text{K})^{1/2} e^{-157809 \text{ K} / T}}{1 + \sqrt{T / 10^5 \text{ K}}} \text{ cm}^3 \text{ s}^{-1} \quad (3.4)$$

from Theuns et al. (1998). We tie the fraction of helium in the He I and He II states to the hydrogen ionization state by simply assuming $n_{\text{HeII}}/n_{\text{He}} = n_{\text{HeIII}}/n_{\text{H}}$. Given the similar ionization energies, this is justified and a common assumption. The electron density in Equation 3.3 therefore has to be $n_{e^-} = n_{\text{HeIII}} c_{e^-}^{\text{HeIII}}$ with $c_{e^-}^{\text{HeIII}} = 1.079$ being a correction factor that accounts for the electrons contributed by the singly ionization of helium at the level of the cosmic primordial mass fractions of hydrogen and helium. For $\alpha_{\text{A}}^{\text{HeIII}}(T)$ we use the Case A recombination coefficients from Storey & Hummer (1995). This is appropriate since H I and He II are highly ionized and the IGM optically thin on the relevant scales. With these inputs, Equation 3.3 becomes a simple quadratic equation that can be easily solved for the hydrogen ionized fraction.

In the second step, we compute the number densities of singly (He II) and doubly ionized helium (He III), which depend on the hydrogen ionization state. For this calculation we ignore

CHAPTER 3. MODELING OF THE HE II TPE

He I and assume that all helium is at least singly ionized ($n_{\text{HeII}} + n_{\text{HeIII}} = n_{\text{He}}$) which is an excellent approximation given that $n_{\text{HeI}}/n_{\text{HeII}} \simeq 10^{-5}$. In complete analogy to Equation 3.3 helium ionization equilibrium is expressed as

$$n_{\text{HeII}} \Gamma_{\text{phot}}^{\text{HeII}} = \alpha_{\text{A}}^{\text{HeIII}} n_{e^-} n_{\text{HeIII}}. \quad (3.5)$$

For He II we do not include collisional ionization or self-shielding corrections. We again use Case A recombination coefficients $\alpha_{\text{A}}^{\text{HeII}}(T)$ from Storey & Hummer (1995). The electron density is now dominated by the electrons supplied by ionized hydrogen:

$$n_{e^-} = n_{\text{HII}} c_{e^-}^{\text{HII}} + n_{\text{HeIII}}. \quad (3.6)$$

This is the reason n_{HII} had to be computed a priori. With all required information collected, Equation 3.5 can be solved for n_{HeIII} .

The additional electrons released by the He II \rightarrow He III transition in principle effect the hydrogen ionization state. The correct way would be to iterate over Equation 3.3 and 3.5 until convergence. However, the total effect on n_{e^-} is small ($< 8\%$) and has for highly ionized hydrogen a totally negligible impact on n_{HII} ($< 10^{-6}$) and therefore on n_{HeII} , completely insignificant compared to the uncertainties in the UV background and effective optical depth measurement. This justifies solving hydrogen and helium ionization state independent of each other.

3.2.3 Computing Synthetic Spectra

After determining n_{HI} and n_{HeII} along the skewers as stated above, the final step in our modeling procedure is to create synthetic spectra. For each pixel along the skewers we compute an individual Voigt absorption line profile with appropriate strength, line width and velocity shift corresponding to the physical conditions in that pixel. Oscillator strengths are taken from Verner et al. (1996a). We benefit here from the high resolution of the Nyx box (36 cMpc or 2.8 km s^{-1}) which is sufficient to resolve H I and He II Ly α forests ($\approx 7.6 \text{ km s}^{-1}$ and 3.8 km s^{-1}). Redshift space distortions (peculiar velocities) are included by displacing the absorption profile with the line of sight velocity from the NYX simulation. Thermal broadening is computed according to $\sigma_{\text{th}} = \sqrt{\frac{k_{\text{B}} T}{m_{\text{ION}}}}$ for the Doppler broadening¹ with T denoting the gas temperature in a pixel and m_{ION} the atomic masses of hydrogen or helium. The Lorentzian scale parameter is based on the transition probability from Verner et al. (1996a). The final transmission spectrum at a pixel in redshift space is the combination of all the absorption profiles along the skewer. We do not convolve the spectra with any instrumental line-spread function since the measurements are obtained in at least 16 cMpc wide bins, much broader than the typical $\approx 2 \text{ cMpc}$ resolution of the He II spectra.

Using the velocity structure from the hydrodynamical simulation is extremely important. In most cases, significant He II transmission stems predominantly from underdense regions. In these voids, the velocity field is usually divergent, making them appear larger in redshift space which leads to a He II mean transmission e.g. $3\times$ higher for $\Gamma_{\text{UVB}}^{\text{HeII}} = 10^{-15} \text{ s}^{-1}$ compared to the case without peculiar velocities.

3.2.4 H I and He II UV Background

To obtain realistic He II transmission spectra, in particular in the absence of a foreground quasar, we have to rely on models for the corresponding UV backgrounds. Oñorbe et al.

¹This describes the standard deviation of the Gaussian part of the Voigt profile. The often used *Doppler Parameter* is $b_{\text{th}} = \sqrt{2} \times \sigma_{\text{th}}$.

(2017) obtained an empirical fit for the cosmic mean transmitted H I flux $\langle F_{\text{HI}} \rangle$ to existing measurements (Fan et al. 2006; Becker et al. 2007; Kirkman et al. 2007; Faucher-Giguère et al. 2008b; Becker et al. 2013) of the form

$$\tau_{\text{HI}} = 0.00126 \times e^{3.294 \times \sqrt{z}} \quad (3.7)$$

where $\tau_{\text{HI}} = \ln \langle F_{\text{HI}} \rangle$ denotes the effective optical depth and z the redshift. For simulation snapshot available at $z = 2.0, 2.2, 3.0, 3.5, 4.0$ we measure the mean transmission in a large set of random skewers and iteratively adjust the homogeneous H I UV background until the mean transmission matches the fit from Oñorbe et al. (2017). We interpolate these $\Gamma_{\text{UVB}}^{\text{HI}}$ values determined for the fixed redshifts using a cubic spline to obtain a smooth function $\Gamma_{\text{UVB}}^{\text{HI}}(z)$. This allows us to assign the appropriate H I UV background matched to the redshift of each pixel.

Obtaining the correct He II UV background poses a bigger challenge. For redshifts $z > 2.7$ helium reionization is incomplete and no homogeneous UV background has formed yet. Instead, the metagalactic He II ionization field is patchy and fluctuating (e.g. McQuinn 2009; Worseck et al. 2016; Davies et al. 2017). Without using the correct ionizing background that includes these fluctuations we can not expect to obtain realistic models for the effect of individual quasars. We therefore use the fluctuating UV background model from Davies et al. (2017) and add on top of that the ionizing radiation of the foreground quasars (§ 3.2.5).

The adopted approach is clearly a simplification. However, solving the full He II reionization history using self-consistent radiative transfer hydrodynamical calculations in a cosmological volume at high resolution including a statistical population of quasars matched to a given quasar luminosity functions and at the same time including the sample of explicitly observed quasars along the He II sightlines with variation and inference of quasar emission properties (t_{age} , Ω_{obsc} , etc) is infeasible with current methods. We therefore have to investigate the effect of single isolated foreground quasars decoupled from the surrounding UV background. There might be by-chance proximity regions of observed or unobserved, Type I, Type II or even extinct quasars in the vicinity of the foreground quasar we focus on and it is impossible to model these explicitly. However, using the Davies et al. (2017) fluctuating He II UV background takes at least to some degree care of this since this UV background model is based on the combined and overlapping effect of proximity regions around a realistic quasar population. In addition, we only focus on the foreground quasars with the highest He II ionization rates at the background sightline which dominate over the He II UV background by approximately one order of magnitude. This makes our analysis less dependent on the exact details of the adopted He II UV background model.

Fluctuating He II UV Background Model

The Davies et al. (2017) He II UV background model is based on a large 500 cMpc box, sampled with 10 cMpc spatial resolution in which explicit sources of He II ionizing photons are randomly placed according to the Hopkins et al. (2007) quasar luminosity function. Each of these sources emits isotropically for a time span of 50 Myr and their radiation is propagated using a 3D radiative-transfer calculating with finite speed of light. The calculation includes an explicit treatment of a spatially varying He II mean free path computed self-consistently under the assumption of local photoionization equilibrium. Figure 3.1 shows a lightcone projection of the He II ionization rate $\Gamma_{\text{UVB}}^{\text{HeII}}$ along a random slice through the simulation volume. We calculate He II background photoionization rates along our skewers by randomly drawing $\Gamma_{\text{UVB}}^{\text{HeII}}$ lightcone skewers from the Davies et al. (2017) box (sampled on ≈ 6 cMpc pixels in the redshift direction) and interpolate these to the higher resolution of the NYX box using a cubic spline interpolation. This naturally includes the redshift evolution of the He II UV background along our sightlines. See lower panel of Figure 3.1 for an example.

CHAPTER 3. MODELING OF THE HE II TPE

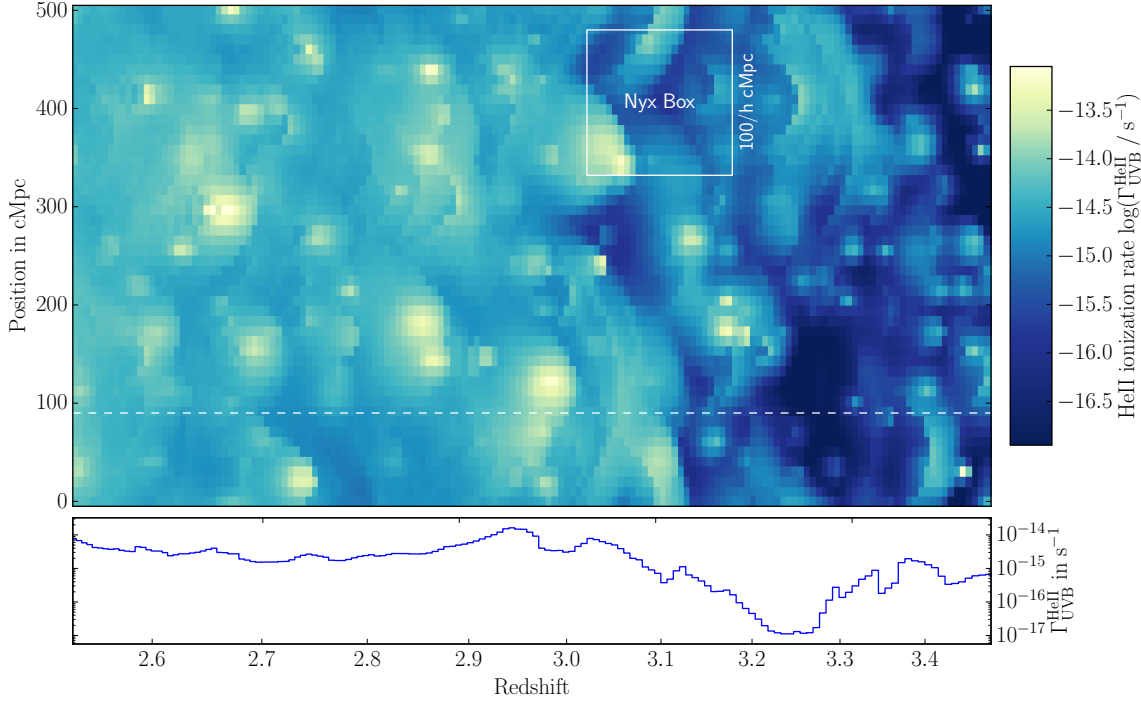


Figure 3.1: Visualization of the semi-analytic He II UV background model from [Davies et al. \(2017\)](#). The top panel shows the He II ionization rate along a slice through the box in lightcone projection, meaning the vertical axis represents spatial position and the horizontal axis indicates position in redshift space as it appears for an observer on Earth. Clearly visible are the parabolic ionization regions around individual quasars. The size of our high-resolution NYX box is indicated. The bottom panel shows $\Gamma_{\text{UVB}}^{\text{HeII}}(z)$ along the dashed skewer.

Calibration of the He II UV background model

As pointed out above, adopting the correct He II UV background including the right amount of fluctuations is absolutely crucial in the context of this study. We therefore thoroughly test different UV background schemes and calibrate the adopted model to make sure it reproduces existing He II observations.

For this quantitative comparison, we use the full He II dataset from [Worseck et al. \(2016\)](#) and [Schmidt et al. \(2017a\)](#), composed of the 22 He II sightlines shown in [Figure 2.5–2.5](#) in [§2.1.7](#). These sightlines represent a random sample and were selected independent of any possible foreground quasars. We measure the He II transmission as well as the transmission enhancement ξ (for a definition see [Equation 3.1](#)) in consecutive 30 cMpc wide bins along these sightlines. For each of the two statistics we obtain 212 measurements, considering only those bins that have full spectral coverage. To compare these measurements with He II UV background models, we compute for each of the 212 bins a large set of skewers centered on the same redshift and measure He II transmission and transmission enhancement in the simulated He II spectra. We measure the noise in the data and add this to our models as described in [§3.3.1](#).

The result is presented in [Figure 3.2](#). We show the cumulative histogram of the 212 measurements (blue) and 50 independent random realizations of the modeled He II dataset (black lines) for each of the three analyzed He II UV background models. As shown in the top row, using the [Haardt & Madau \(2012\)](#) He II UV background leads to a substantially higher He II transmission than seen in the observations ([left panel](#)). However, the transmission enhance-

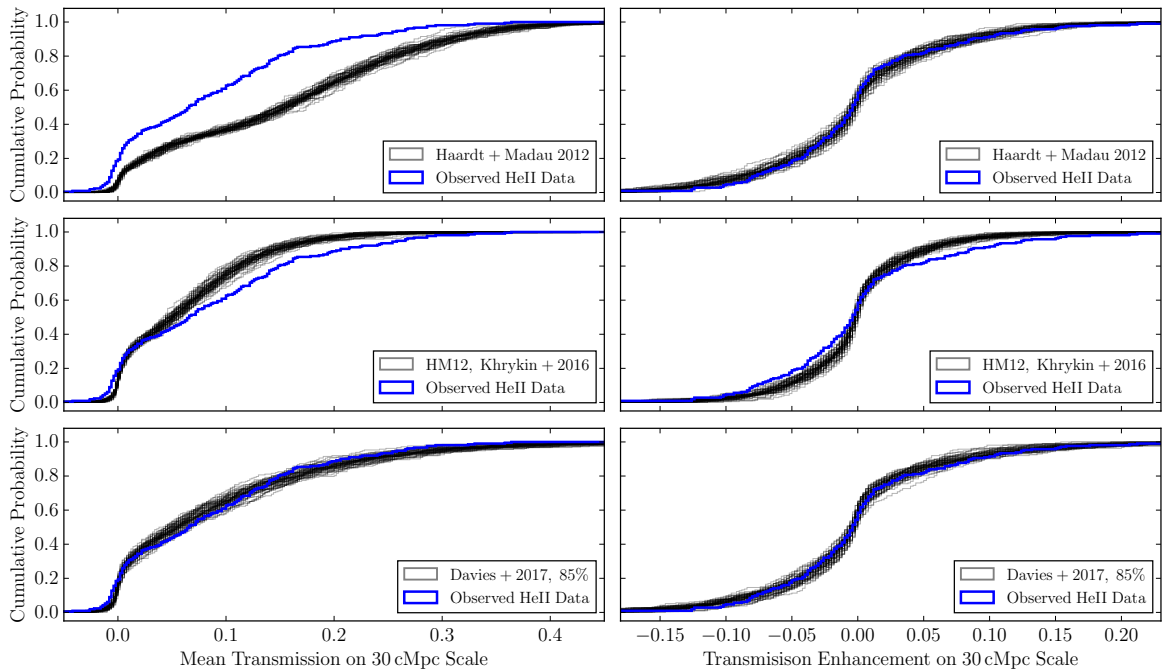


Figure 3.2: Cumulative histograms of the He II transmission (*left*) and transmission enhancement (*right*) measured in 30 cMpc wide bins along all 22 available He II sightlines. The blue curves show the actual data, black represent 50 random model realizations. The top row shows models using the homogeneous Haardt & Madau (2012) He II UV background model. This obviously produces too high transmission values. The central row therefore shows a case in which we rescale the UV background to $\Gamma_{\text{UVB}}^{\text{HeII}} = 10^{-14.9} \text{ s}^{-1}$ at $z = 3.1$ as found by Khrykin et al. (2016). Here, the models produce a too narrow distribution for the transmission enhancement statistic. Excellent match in both statistics is achieved using the Davies et al. (2017) fluctuating He II UV background model (*bottom row*).

ment ξ , being a differential measurement in nature, is far less susceptible to the absolute level of the He II mean transmission and yields a far better match to the data than the transmission statistic itself (right panel).

The middle row shows the same approach, but rescaling the Haardt & Madau (2012) UV background to $\Gamma_{\text{UVB}}^{\text{HeII}} = 10^{-14.9} \text{ s}^{-1}$ at $z = 3.1$ as found by Khrykin et al. (2016). Now, the model (black lines) shows too few high-transmission regions relative to the data (left panel, blue histogram). Also, the model does not produce enough fluctuation in the transmission enhancement (right panel), since the cumulative ξ probability distribution of the models is too steep to match the data (central right panel of Figure 3.2).

In contrast to these homogeneous UV background models, we achieve, as presented in the bottom row of Figure 3.2, excellent agreement between model and data for the flux statistic as well as for the transmission enhancement using the fluctuating He II UV background model from Davies et al. (2017). We found the best match when rescaling the Davies et al. (2017) UV background to 85% amplitude. This rescaling is well within the uncertainties of the model, which was not tuned to match any particular He II transmission level.

This test indeed compares the correct quantities. Our observed He II spectra do show signatures of quasar proximity zones but so do the $\Gamma_{\text{UVB}}^{\text{HeII}}$ skewers from the Davies et al. (2017) UV background model. In both cases we measure He II transmission at random positions which are uncorrelated to possible foreground quasars. The excellent agreement shows that our mildly rescaled Davies et al. (2017) fluctuating UV background model is actually capable of reproducing the observed He II transmission properties at random positions along the He II sightlines. This allows us to proceed by adding the ionizing radiation of individual quasars

CHAPTER 3. MODELING OF THE HE II TPE

on top of the UV background to calculate transmission profiles that will finally be compared to He II spectra in the vicinity of the bright foreground quasars that we consider in detail.

3.2.5 Modeling Foreground Quasar Emission and Ionization Rates

In a first step, we calculate the H I and He II ionizing fluxes for positions along the background sightlines, given that they are illuminated by of the foreground quasars. This is nearly identical to the approach outlined in § 2.1.6. The exact conditions under which points might not be illuminated due to obscuration or finite quasar age will be discussed in § 3.2.5 and § 3.2.5.

Based on the r -band magnitude and the Lusso et al. (2015) quasar template we compute M_{1450} and the quasar luminosity L_ν . Conversion to flux density F_ν at the background sightline is done according to

$$F_\nu = L_\nu \frac{1}{4\pi D_{\text{prop}}^2} e^{-\frac{D_{\text{prop}}}{\lambda_{\text{mfp}}}}. \quad (3.8)$$

Here, D_{prop} denotes the proper 3-D distance from the foreground quasar to a specific position at the background sightline and λ_{mfp} is the mean free path to He II ionizing photons. Since the separations we deal with in our analysis are moderate ($D_{\text{prop}} \lesssim 6.5$ pMpc, except for HS 1157+3143), we ignore IGM absorption by setting the mean free path to $\lambda_{\text{mfp}} = \infty$.

We calculate H I and He II ionization rates resulting from the quasar based on the Lusso et al. (2015) quasar template, assuming a power-law of slope $\alpha = -1.7$ beyond 912 Å. There is substantial uncertainty about quasar SEDs in the extreme UV part of the spectrum (e.g. Stevans et al. 2014; Lusso et al. 2015; Tilton et al. 2016). However, we make sure that this is not the dominant source of uncertainty for our analysis.

For simplicity, we assume that the spectral dependence of the ionization cross-sections of helium and hydrogen have a power-law of form $\sigma_\nu \propto (\nu/\nu_0)^{-3}$, and take the cross-sections at the ionizing-edges σ_0 from Verner et al. (1996b)². This leads to the H I and He II quasar ionizing rates of the form

$$\Gamma_{\text{QSO}}^{\text{ION}} = \int_{\nu_0^{\text{ION}}}^{\infty} \frac{F_\nu \sigma_\nu^{\text{ION}}}{h_{\text{P}} \nu} d\nu \approx \frac{F_{\nu_0^{\text{ION}}} \sigma_0^{\text{ION}}}{h_{\text{P}} (3 - \alpha)} \quad (3.9)$$

in which h_{P} denotes Planck's constant and ν_0^{ION} the frequency of the corresponding ionization edge. Due to the different cross sections and the chosen quasar spectral energy distribution, we find $\Gamma_{\text{QSO}}^{\text{HI}} \approx 42 \Gamma_{\text{QSO}}^{\text{HeII}}$. Evaluating $\Gamma_{\text{QSO}}^{\text{HeII}}(z)$ at the foreground quasar redshifts, therefore in exactly transverse direction, gives the $\Gamma_{\text{QSO, max}}^{\text{HeII}}$ values quoted in Table 3.1.

The additional ionization by the quasar might also have an effect on the thermal structure of the IGM (Bolton et al. 2009, 2010, 2012). However, proper treatment of this *thermal proximity effect* would require radiative transfer calculations (Meiksin et al. 2010; Khrykin et al. 2017) which is beyond the scope of this study. Also, the thermal proximity effect for He II should be sub-dominant compared to the enhanced He II ionization (Khrykin et al. 2016).

In the following, we calculate the regions of the background sightlines that are, depending on quasar age and obscuration, indeed illuminated by the foreground quasars.

Quasar Obscuration

For the geometry of the foreground quasars radiation we assume a simple biconical emission model with half-opening angle α of the cones. Such an emission pattern is suggested by the

²The exact spectral dependence of the He II ionization cross-section is of low importance due to substantial uncertainty in the quasar extreme UV continuum and the H I quasar ionizing rate is anyway lower than the UV background.

observations of local Seyfert galaxies (e.g. Pogge 1988; Tadhunter & Tsvetanov 1989; Wilson et al. 1993) and the quasar unification scheme (Antonucci 1993; Urry & Padovani 1995; Netzer 2015). The solid angle on the sky not illuminated by the quasar is then $\Omega_{\text{obsc}} = 4\pi \cos(\alpha)$. For simplicity, we usually state the obscured fraction of the sky (omitting the 4π). For $\alpha = 60^\circ$ half of the sky is illuminated ($\Omega_{\text{obsc}} = 50\%$) and $\alpha = 90^\circ$ corresponds to isotropic emission ($\Omega_{\text{obsc}} = 0\%$). The orientation of the foreground quasar's emission bicone with respect to the background sightline is described by two angles (θ, ϕ) . Here, θ denotes the angle between the quasars polar axis and the line of sight (*inclination*) where $\theta = 0^\circ$ describes the case in which the polar axis points directly towards Earth. The apparent direction on the sky, as seen from Earth, in which the quasars polar axis is tilted (*position angle*) is denoted with ϕ . A bicone pointing towards the background sightline corresponds to $\phi = 0^\circ$, $\phi = 90^\circ$ perpendicular to it and $\phi = 180^\circ$ away from it. For a given point on the background sightline the angle between the foreground quasars polar axis and a ray from the foreground quasar towards this point is

$$\beta = \arccos \left(\frac{R_{\perp} \sin(\theta) \cos(\phi) - R_{\parallel} \cos(\theta)}{\sqrt{R_{\parallel}^2 + R_{\perp}^2}} \right) \quad (3.10)$$

in which R_{\perp} denotes the comoving separation between the foreground quasar and background sightline and R_{\parallel} the comoving distance along the background sightline, measured from the point of closest approach towards the background quasar. All locations for which $\beta < \alpha$ or $\beta > 2\pi - \alpha$ are illuminated. All other positions do not receive any quasar radiation. Instead, the foreground quasar appears as an obscured Type II from these vantage points.

Within our model, the quasar half-opening angle α or equivalently the fraction of the sky which is obscured, Ω_{obsc} , is chosen explicitly while the quasar orientation (θ, ϕ) is randomly drawn. The foreground quasars in our sample appear as unobscured Type I from Earth. This constrains the orientation to $\theta < \alpha$. We achieve this by drawing ϕ from a flat distribution between $0 < \phi < 2\pi$ and $\cos(\theta)$ from a flat distribution between $1 > \cos(\theta) > \cos(\alpha)$.

Finite Quasar Age

A key element for our sensitivity to quasar age is the fact that the background sightline probes the foreground quasars emission at earlier times than the light we directly receive from the quasar (see e.g. Adelberger 2004; Kirkman & Tytler 2008; Furlanetto & Lidz 2011; Schmidt et al. 2017a). This arises because of the geometric path length differences between the longer path from the foreground quasar to a location along the background sightline, and from there to the observer (as probed by the background sightline), compared to the direct path from the foreground quasar to Earth. The relevant quantities to compute this path length difference are the distance (from Earth) to a location along the background sightline at redshift z , and the distance from this point to the foreground quasar³. When measuring both distances in comoving units, their sum can be converted to a redshift z_{em} and corresponding lookback time t_{em} at which the ionizing radiation from the foreground quasar had to be emitted.

The lookback time at emission can be compared to the lookback time corresponding to the redshift of the foreground quasar z_{QSO} . The difference is the additional time $\Delta t(z)$ it takes to first reach a certain point on the background sightline. This time difference depends on the redshift of the point in question and of course quasar redshift and sightline separation. For points at redshifts lower than the foreground quasars ($z < z_{\text{QSO}}$) the time difference $\Delta t(z)$ is relatively small. For $z = z_{\text{QSO}}$ it is exactly the transverse light crossing time $\Delta t = R_{\perp} c^{-1}$

³The comoving distance between a location on the background sightline and the foreground quasar for an angular sightline separation of $\Delta\theta$ can be computed via $\sqrt{R_{\parallel}^2 + R_{\perp}^2} \equiv r(z, z_{\text{QSO}}, \Delta\theta) = \sqrt{r(z)^2 + r(z_{\text{QSO}})^2 - 2r(z)r(z_{\text{QSO}})\cos(\Delta\theta)}$ (e.g. Liske & Williger 2001)

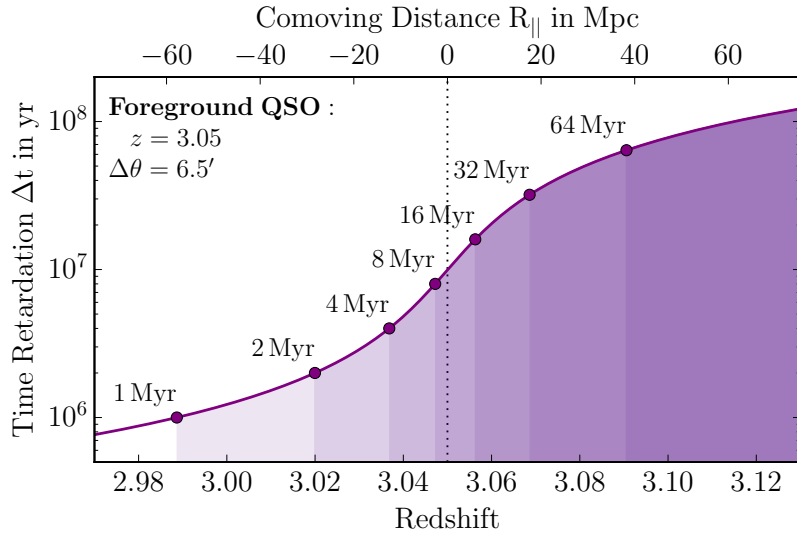


Figure 3.3: Visualization of the time difference Δt along the Q 0302–003 sightline with respect to the $z = 3.05$ foreground quasar at angular separation of $\Delta\theta = 6.5'$. For a given age of the foreground quasar t_{age} , only the part of the background sightline for which $\Delta t < t_{\text{age}}$ appears illuminated.

with the transverse separation R_{\perp} now measured in proper length and c denoting the speed of light. For positions at higher redshift than the foreground quasars, therefore behind it, $\Delta t(z)$ quickly increases. See Figure 3.3 for a visualization.

Whether or not a given location along the background sightline is illuminated now depends on the age of the foreground quasar, since there had to be enough time for its ionizing radiation to arrive at a given location (Figure 3.3). For the quasar lightcurve we assume a simple lightbulb model in which the quasar turns on and shines with constant luminosity for its entire lifetime t_Q . In this case, the age of a quasar t_{age} is well defined and represents the time between turning on and emission of the photons that arrive at Earth today. For a discussion about more complicated quasar lightcurves see § 3.5.2. Points on the background sightline for which $\Delta t(z) < t_{\text{age}}$ appear for an observer on Earth illuminated by the quasar. Since $\Delta t(z)$ monotonically increases with z (see Figure 3.3), all points at redshifts higher than the dividing line where $\Delta t(z) = t_{\text{age}}$ appear not yet illuminated since there was not enough time for the photons to reach these locations.

3.2.6 Example of the Simulated Data

In Figure 3.4 we visualize one of our photoionization models. Sightline geometry and quasar luminosity are matched to the foreground quasar at $z = 3.05$ along the Q 0302–003 sightline (Jakobsen et al. 2003). The top panel shows the computed He II Ly α transmission in a slice through the simulation box as it would appear for an observer on Earth⁴. The quasar is placed in a $10^{12} M_{\odot}$ halo and emits in a biconical pattern with $\alpha = 60^{\circ}$ and therefore illuminates half of the sky. It is tilted by $\theta = 20^{\circ}$ against the line of sight towards the observer (yellow). The assumed finite quasar age of $t_{\text{age}} = 35$ Myr limits the extend of the ionized area towards the right. The positions for which the quasar emission had sufficient time to reach them lie in a parabolic shaped region with the quasar at the focal point. This parabola expands with increasing quasar age.

The middle panel of Figure 3.4 shows the He II ionization rate along the background sightline (green) separated from the quasar by $R_{\perp} \approx 12$ cMpc. Clearly visible is the effect of quasar obscuration ($-17 \text{ cMpc} < R_{\parallel} < 2 \text{ cMpc}$) and finite quasar age ($R_{\parallel} > 20 \text{ cMpc}$).

The bottom panel shows synthetic H I and He II transmission spectra along the sightline. No transverse proximity effect is visible for hydrogen but a clear enhancement in He II transmission

⁴Not including peculiar velocities / redshift space distortions

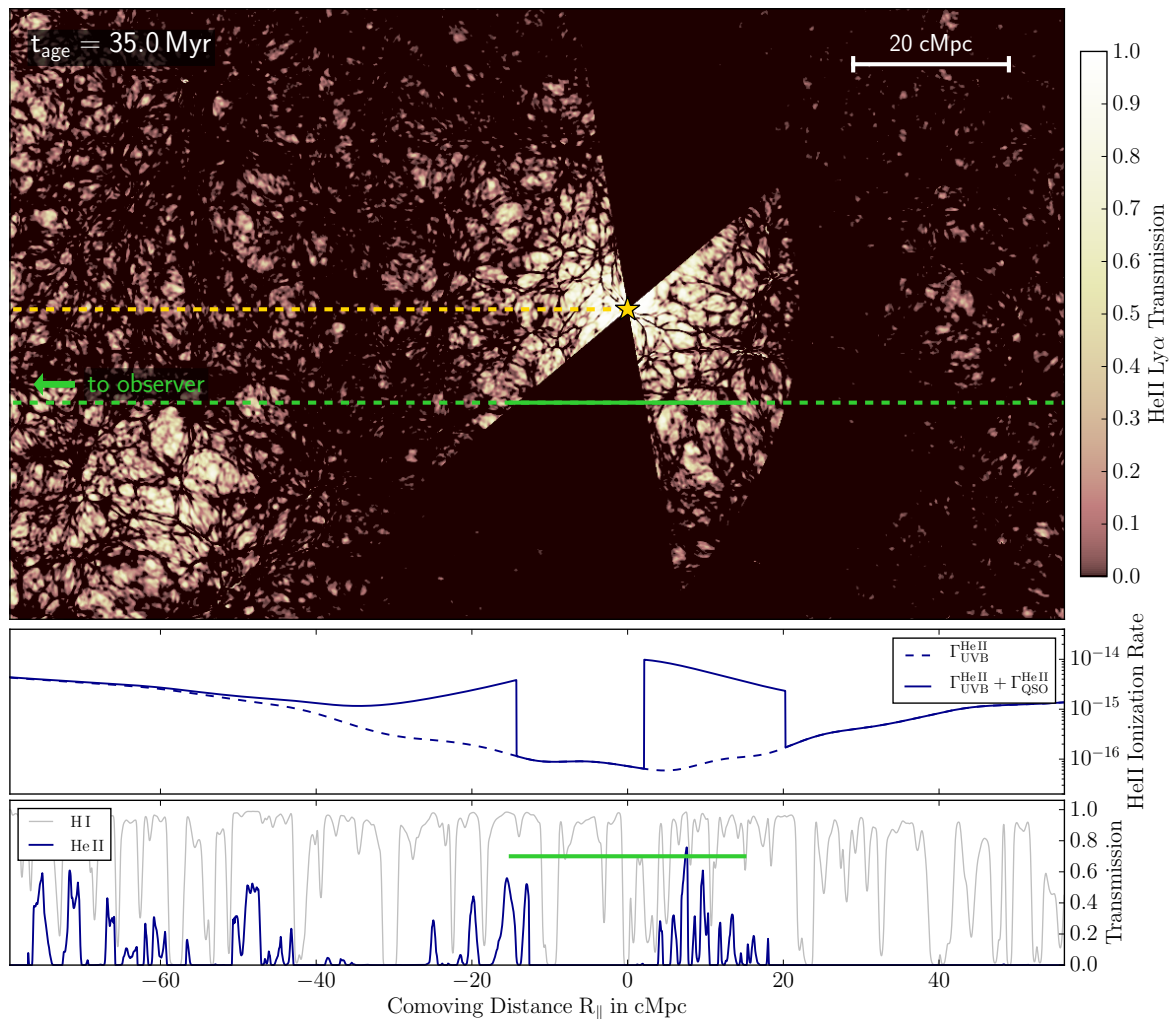


Figure 3.4: Illustration of our model, showing quasar obscuration, finite quasar age and He II UV background fluctuations. The top panel displays for a slice through the simulation the He II transmission in realspace, clearly showing the bi-conical emission of the quasar and the parabolic shaped region that can be reached for the given quasar age. The middle panel indicates the resulting He II ionization rate along the green marked background sightline. The bottom panel shows the computed hydrogen and helium transmission spectra, as observed in redshift space. A strong He II transmission enhancements is visible in regions that are illuminated by the quasar. The solid green bar marks the the ± 15 cMpc we defined as *proximity region* in Schmidt et al. (2017a).

is visible in regions that are illuminated by the foreground quasar, e.g. around $R_{\parallel} \approx -20$ cMpc and $R_{\parallel} \approx 10$ cMpc. One can see that this He II transmission is highly modulated by the cosmic density structure, as traced by the H I Ly α absorption. Whenever there is a substantial H I absorber, we observe saturated He II absorption. On the other hand, substantial He II transmission is not necessarily associated with the presence of our bright foreground quasar. It can also be caused by the fluctuating He II UV background as can be seen in the top panel of Figure 3.4 in particular in the lower left corners of the transmission slice. For $R_{\parallel} < -40$ cMpc along the sightline through the box (lower panel of Figure 3.4) these fluctuations result in He II transmission nearly comparable to the values in the transverse proximity zone, despite having no explicit foreground quasar there. Such situations are indeed consistent with observations. In Chapter 2 we showed several strong transmission spikes in the He II spectra without a clear association to foreground quasars and our test in § 3.2.4 showed that large fluctuations in the He II UV background are actually required to match the observed data.

CHAPTER 3. MODELING OF THE HE II TPE

The region we defined previously as the *proximity region* and used to quantify the He II transmission enhancement (§ 2.3.2, Equation 2.4), ± 15 cMpc around the foreground quasar position, is indicated in Figure 3.4 as a solid green bar. For the quasar orientation shown in Figure 3.4, a substantial part of this region is not illuminated by the quasar and shows no transmission enhancement while at the same time some extra transmission falls outside the chosen window. However, the signature of the transverse proximity effect is highly stochastic and depends not only on sightline geometry, quasar age, and obscured sky area but in particular on the random orientation of the quasar, cosmic density structure and UV background fluctuations. It is therefore important to investigate the statistical properties of the expected transverse proximity signal which we address in the next section.

3.2.7 Average Transmission Profiles

We illustrate the average He II transmission profile and the associated scatter for models with different quasar properties in Figure 3.5. For each of these models we compute a large number of skewers that sample the stochastic He II UV background model and IGM density fluctuations. Obscuration Ω_{obsc} (i.e. α) and quasar age t_{age} are fixed, but the quasar orientation (θ, ϕ) is randomly drawn. The quasar luminosity and sightline geometry are again chosen to match the Q 0302–003 $z = 3.05$ foreground quasar. The dark blue lines in Figure 3.5 represent the averages (mean and median) of 2000 skewers, each binned to 2 cMpc bins, ap-

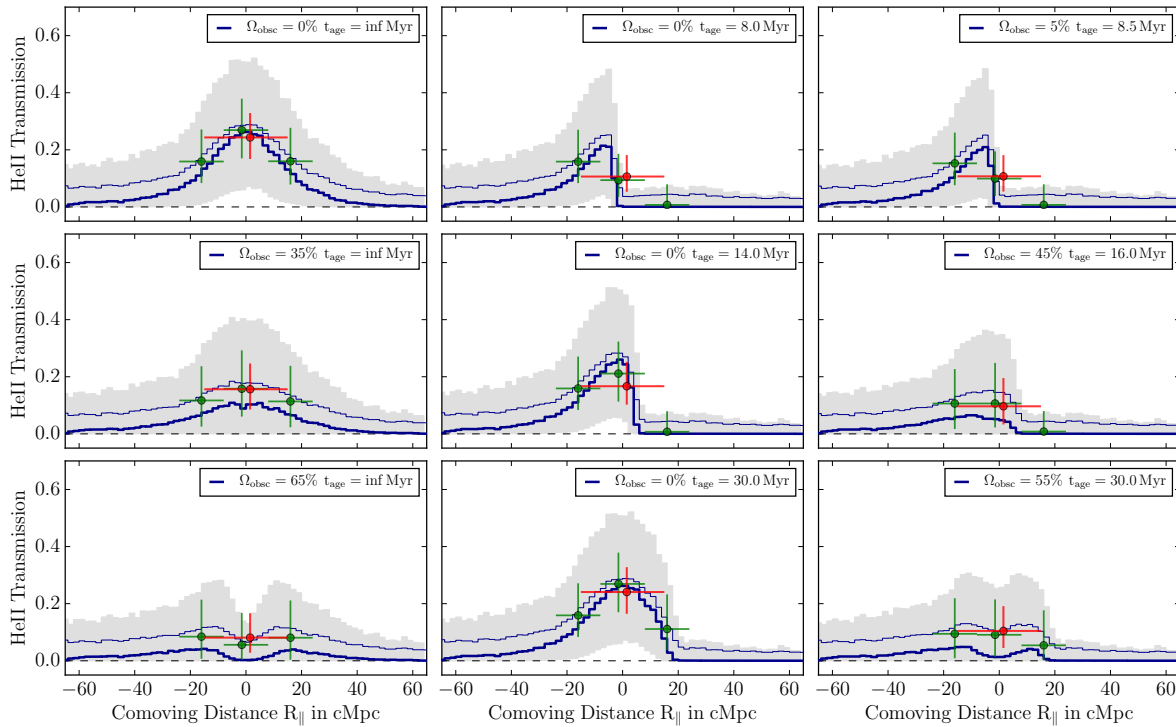


Figure 3.5: Visualization of our models for different quasar properties. Sightline geometry and quasar luminosity are matched to the Q 0302–003 $z = 3.05$ object. The thick blue line shows the median He II transmission in 2 cMpc bins, the gray shaded area the 16th–84th percentile scatter. We also show the mean transmission as thin blue line. Due to the large non-Gaussianities in the distributions the mean can be vastly different from the median. The colored points show the median and expected scatter of the He II transmission averaged over 16 cMpc (green) and 30 cMpc (red) wide windows. Symbols are slightly displaced for clarity. Models in the first column show the effect of obscuration, models in the second column lifetime effects. Models in the last column are selected to give the same average transmission over the ± 15 cMpc window but have different signal shapes that in principle could be distinguished using transmission measurement in three bins.

proximately the typical pixel size of He II spectra. The gray shaded region represents the scatter (16th to 84th percentile region) within the set of 2000 skewers. Observational effects like photon counting noise are not included here. Instead, only the variance within the model is shown. This illustrates the extreme stochasticity of the He II transverse proximity effect and the concomitant challenge of interpreting single absorption spectra.

However, note that the transmission values in the small 2 cMpc bins are highly correlated and the transmission distribution highly non-Gaussian. To better illustrate the expected variance, we show a synthetic measurement of the transmission averaged over our chosen window of ± 15 cMpc. The red point shows the median value for this measurement. The horizontal bar indicates the size of the region while the vertical bar indicates the expected scatter in this measurement derived from the 16th and 84th percentile of the distribution. In addition, we show measurements in three consecutive 16 cMpc wide bins (green points) that allow one to better capture the shape of the signal.

The upper left panel of Figure 3.5 shows a model for which the quasar emission is isotropic and the quasar age infinite. The scatter therefore arises from density and He II UV background fluctuations alone. The other panels in the left column show models which also have infinite age, but with the quasar emission restricted to 65 % and 35 % of the sky. This clearly reduces the amplitude of the transverse proximity effect signal, and for the 35 % model even results in a dip in the average transmission at $R_{\parallel} = 0$ cMpc. Here, the quasar emission is so highly beamed that it may hit the background sightline in front and behind the foreground quasar and causes additional He II transmission there ($R_{\parallel} \approx \pm 15$ cMpc), but since it is constrained to shine towards it Earth basically cannot illuminate the background sightline at $R_{\parallel} = 0$ cMpc.

The second column shows models with isotropic emission but varying quasar age between 8 and 30 Myr. As described above, only points on the background sightline for which the time difference is shorter than the quasar age ($\Delta t(z) < t_{\text{age}}$) can be reached by the quasar radiation and therefore show enhanced transmission. These points all lie to the left (lower redshifts, lower R_{\parallel}) of where $t_{\text{age}} = \Delta t$. To the right of this, one only observes transmission caused by the He II UV background. With increasing quasar age, this cut-off moves to the right (higher redshift, higher R_{\parallel}). The position of the cut-off is of course also influenced by the separation between foreground quasar and background sightline.

The right column in Figure 3.5 shows models with different combinations of quasar age and obscuration. The three sets of model parameters (Ω_{obsc} and t_{age}) are selected to give approximately the same transmission enhancement in the ± 15 cMpc window (red measurements). Since the quasar lifetime has a very asymmetric effect on the background sightline, it is, at least in principle, possible to break this degeneracy by measuring the transmission enhancement in multiple bins (green points). However, the large estimated scatter in the measurement (again, this includes only model stochasticity, no measurement uncertainties) sets limits on the confidence with which these models can be distinguished.

In general, one can deduce from Figure 3.5 that distinguishing different models at very high significance will probably not be possible. The expected variance in the He II transverse proximity effect is simply too high in single spectra. However, it should be possible to rule out some extreme cases and broadly distinguish between scenarios. This however requires a sophisticated statistical analysis and calls for a fully Bayesian approach that can naturally deal with non-Gaussian distributions, strong degeneracies, and weakly constrained parameters, which is our task in the next section.

3.3 Comparison to Data and Inference of Parameters

Our aim is to infer individual quasar ages and obscuration properties for the six foreground quasars with the highest estimated He II photoionization rate at the background sightline. In several cases, there might not be a single definitive answer to this. We however intend to calculate, in a fully Bayesian way, the joint probabilities for a wide range of $\Omega_{\text{obsc}} - t_{\text{age}}$ combinations which then hints towards certain regions in the parameter space or rules out others.

To this end, for each foreground quasar we compute a grid of models that covers the parameter space from $\Omega_{\text{obsc}} = 5\%$ to $\Omega_{\text{obsc}} = 95\%$ and quasar ages from 5 Myr to 46 Myr. For simplicity, we decided to sample the parameter space with a rectangular model grid of size 10×12 for $(\Omega_{\text{obsc}}, t_{\text{age}})$ and avoid any interpolating between models but instead just evaluate the likelihood at the points of the model grid. Since our constraints will be broad anyway, this is not a substantial disadvantage. To properly capture the stochasticity in the He II transverse proximity effect and to adequately map the distribution of the expected He II transmissions, we calculate 5000 skewers per model with randomly drawn quasar orientation, and sampling of the UV background and cosmic density field along the different skewers. This then allows us to infer the probability of each model given the observed data.

3.3.1 Likelihood Computation

To simplify the explanation of the likelihood calculation and make it easier to understand for the reader, we adopt for this part the mean He II transmission statistic \mathbf{F} . However, for the actual analysis we use the transmission enhancement statistic ξ (see Equation 3.1). The necessary modifications to the likelihood computation are straight forward and described later in §3.3.1.

Our measurement in the spectra are the photon counts C_i in pixels $i = 1 \dots N$. Additional information computed during the data reduction are the sensitivity function \mathcal{S}_i , the exposure time \mathcal{T}_i ⁵, the total number of expected background counts \mathcal{B}_i and a fit for the quasar continuum \mathcal{C}_i . For details see [Worseck et al. \(2016\)](#). These information are sufficient to translate the measured counts into transmission values. However, the Poisson nature of the count distribution requires a forward modeling to calculate proper uncertainties. Often, the detector received only a handful of counts per pixel, but in regions of saturated absorption this can be as low as one or zero source counts. Clearly, assuming Gaussian errors, described by mean and standard deviation, is not appropriate for our case. Instead, we have to propagate full Poisson errors.

Our model parameters are quasar age t_{age} and obscured sky fraction Ω_{obsc} . We therefore have to compute the following likelihood:

$$\mathcal{L} = p(C_{i=1\dots N} | \mathcal{S}_i, \mathcal{T}_i, \mathcal{C}_i, \mathcal{B}_i, t_{\text{age}}, \Omega_{\text{obsc}}). \quad (3.11)$$

However, we do not apply the complete forward model directly to our skewers but instead separate the measurement process from the IGM physics. The first part only deals with the noisy detection process and therefore measurement uncertainties, the second part represents the physics of the He II transverse proximity effect and captures the associated stochasticity.

To make this separation, we introduce the intrinsic, noise-free average transmission \mathbf{F} , measured over a given bin, as an intermediate quantity (*observable*). In practice, we extract from

⁵The exposure time varies from pixel-to-pixel, in particular due to grid wires in front of the COS FUV detector

3.3. COMPARISON TO DATA AND INFERENCE OF PARAMETERS

the models the He II transmission averaged over the region ± 15 cMpc around the foreground quasar position

$$\mathbf{F} = \langle \mathbf{F} |_{R_{\parallel} < 15 \text{ cMpc}} \rangle \quad (3.12)$$

and then assume this average value for the forward modeling of the photon-counting noise⁶. The separation of IGM physics and measurement process not only saves a large amount of computation time but is also intuitive. It can be formally written as

$$p(C_i | t_{\text{age}}, \Omega_{\text{obsc}}) = \int p(C_i | \mathbf{F}) p(\mathbf{F} | t_{\text{age}}, \Omega_{\text{obsc}}) d\mathbf{F}. \quad (3.13)$$

The first term in the integral is the Poisson probability of measuring the counts C_i given an intrinsic transmission \mathbf{F} within the bin:

$$P_{X_i}(C_i) = \frac{X_i^{C_i}}{C_i!} e^{-X_i} \quad (3.14)$$

with the definition of the most-likely photon count

$$X_i = \mathbf{F}_i \cdot \mathcal{C}_i \cdot \mathcal{S}_i \cdot \mathcal{T}_i + \mathcal{B}_i \quad (3.15)$$

which combines continuum estimate, sensitivity, exposure time and total background counts for each individual pixel. These values are derived within the data reduction process described in [Worseck et al. \(2016\)](#).

At this point it is convenient to combine all pixels within the selected bin, denoted with $C = \{C_i\}$, to the joint probability

$$p(C | \mathbf{F}) = \prod_i p(C_i | \mathbf{F}). \quad (3.16)$$

This operation is permitted since the photon-counting noise in the individual pixels is uncorrelated and \mathbf{F} represents the transmission averaged over the bin and is therefore a constant. The probability computed in Equation 3.16 reflects the combined measurements of many pixels and the resulting probability distribution is therefore more Gaussian than the Poisson distributions of the individual pixels. We made use of this for the noise estimate in §3.2.4. and avoid propagating single pixel Poisson noise for that case.

The second term in Equation 3.13, $p(\mathbf{F} | t_{\text{age}}, \Omega_{\text{obsc}})$, represents the expected He II transmission along a sightline given our model parameter t_{age} and Ω_{obsc} . Since quasar orientation, He II UV background and cosmic density structure are stochastic, this term is not a single value but as shown in Figure 3.5 a broad distribution which we sample with 5000 skewers per model. To overcome the discrete sampling of $p(\mathbf{F} | \Omega_{\text{obsc}}, t_{\text{age}})$ caused by the finite number of skewers, we apply a kernel density estimate (KDE) with Scott's rule for the kernel width to approximate the distribution. The KDE makes $p(\mathbf{F}_i | t_{\text{age}}, \Omega_{\text{obsc}})$ a smooth and continuous function and at the same time ensures that the probability is nowhere exactly zero, which would lead to numerical problems.

After estimating the distribution of our observable in this way, we can finally compute the integral in Equation 3.13. This is done via a discrete Monte Carlo approach by randomly sampling the KDE with 10^5 points and evaluating the Poisson distribution (Equation 3.14 and 3.16) for each sample. Averaging these samples yields the desired likelihood in Equation 3.11.

⁶This simplification has only minimal impact on the precision of our noise estimate. Also, the intrinsic variance in the transverse proximity effect anyway dominates over the photon-counting noise.

CHAPTER 3. MODELING OF THE HE II TPE

Transmission Enhancement Statistic ξ

While the above description illustrates our approach using the intrinsic transmission F as the main observable, we prefer to use the flux enhancement statistic ξ , since it is to first order independent of the He II mean transmission and better isolates the effect of the foreground quasar (see Figure 3.2). As already mentioned in §3.1, ξ is similar to the statistic used in §2.3.2, and is defined as the difference between the transmission in the proximity region and in a wider background region:

$$\xi = \langle F_{|R_{\parallel}| < 15 \text{ cMpc}} \rangle - \langle F_{15 \text{ cMpc} < |R_{\parallel}| < 65 \text{ cMpc}} \rangle. \quad (3.17)$$

Calculating the likelihood using ξ is essentially identical to the approach outlined above, by simply replacing F by ξ . Slight adaptations are only required to include the measurement uncertainty in the background transmission (outside the ± 15 cMpc proximity region, second term in Equation 3.17). The background transmission is calculated over $3\times$ the pathlength of the ± 15 cMpc proximity region and the photon counting noise is therefore far less important. Still, we propagate the associated uncertainty in a fully Bayesian way into our analysis. The remaining part of the likelihood calculation is completely analogous and just requires a computation of ξ in the simulated skewers instead of F .

Three-Bin Statistic

As illustrated in Figure 3.5 and discussed in §3.2.7, degeneracies may arise between the parameters t_{age} and $\Omega_{\text{obs c}}$, in particular if we extract only one transmission measurement from the spectra. However, this degeneracy can to some degree be broken by measuring the He II transmission in several consecutive bins along the background sightline. The last column of Figure 3.5 shows three models with different combinations of t_{age} and $\Omega_{\text{obs c}}$ that result in a nearly identical He II transmission measured over ± 15 cMpc, but due to the asymmetric effect of quasar age show different transmission levels in the three 16 cMpc wide bins. We therefore try to use this additional information about the signal shape to better disentangle t_{age} and $\Omega_{\text{obs c}}$ effects. However, this significantly complicates our statistical method. Instead of one transmission in the ± 15 cMpc region we have to deal with multiple (e.g. three) transmission measurements and our observable F becomes a multi-dimensional quantity F_k . Calculating a full Bayesian likelihood for such a multi-bin measurements including all correlations is extremely challenging in the context of our study.

Based on our analysis, we conclude that the transmission values in multiple bins are highly correlated. It is therefore not possible to separate the likelihood computation into three one-dimensional problems. Due to the non-Gaussian nature of He II transmission (illustrated in Figure 3.5) it is also not possible to assume that a multivariate Gaussian distribution describes this multivariate process. Indeed, the non-Gaussianities were already the reason we could not condense our models to mean and standard deviation in the one-dimensional case. The only possible approach in our view is (again) a full description of the multivariate probability distribution.

Mathematically, this is simple. Nothing in the procedure outlined above for computing the likelihood (§3.3.1) assumes the transmission F to be a one-dimensional quantity. In principle, the approach can be extended to arbitrary dimensionality. However, the computational effort for this brute-force method increases dramatically with increasing dimensionality.

The required increase in the number of Monte Carlo evaluations from 10^5 to 10^7 for computing the integral in Equation 3.13 is merely an inconvenience. The ultimate limitation however poses the immense number of mock skewers required to properly sample the multivariate probability distribution in high dimension. For a measurement in three bins we found 5000

simulated skewers per model to be sufficient to adequately map the probability density. For more dimensions, the required number of skewers quickly increases dramatically. The number of three bins therefore poses the practical maximum. Also, when using more but smaller bins, the stochasticity of the measurements increases and it becomes increasingly important to have a correct model for the small-scale fluctuations in the He II UV background.

In practice, we implement the three-bin statistic in complete analogy with the single bin measurement, and similarly use ξ rather than the raw He II transmission F . For the three bins, the transmission is measured in three consecutive 16 cMpc wide windows between $-24 \text{ cMpc} < R_{\parallel} < 24 \text{ cMpc}$ and the background for all three bins in the region $24 \text{ cMpc} < |R_{\parallel}| < 65 \text{ cMpc}$.

3.3.2 Priors

We impose uninformative flat priors on Ω_{obsc} and t_{age} . A strong prior by itself however is the extent of the parameter grid. For Ω_{obsc} we explore the full possible range from nearly isotropic emission ($\Omega_{\text{obsc}} = 5\%$) to almost complete obscuration ($\Omega_{\text{obsc}} = 95\%$) in steps of 10%. For t_{age} we limit our analysis to possible quasar ages between 5 Myr and 46 Myr since the sightline geometries for the six foreground quasars allow only very limited sensitivity to timescales outside this range.

3.3.3 Posterior Probabilities

Having computed likelihood and priors as described above, now allows us to *invert* the problem using Bayes' Theorem and calculate posterior probabilities for our model parameter t_{age} and Ω_{obsc} , given the observed photon counts $C_{i=1\dots N}$, i.e.

$$p(t_{\text{age}}, \Omega_{\text{obsc}} | C_{i=1\dots N}) = \frac{p(C_{i=1\dots N} | t_{\text{age}}, \Omega_{\text{obsc}}) p(t_{\text{age}}, \Omega_{\text{obsc}})}{p(C_{i=1\dots N})}. \quad (3.18)$$

Here, the term $p(C_{i=1\dots N})$, sometimes called the *evidence*, is merely a normalization factor and can easily be determined by integrating the numerator over the full model parameter space.

3.4 Results

For the six foreground quasars with the highest He II ionization rate from our He II transverse proximity effect survey (Chapter 2, Schmidt et al. 2017a) we have modeled the He II transmission along the background sightline and derived joint constraints on quasar age t_{age} and obscured sky fraction Ω_{obsc} . The results are shown in Figure 3.6. The left column shows 130 cMpc long sections of the observed He II transmission spectra around the position of the six analyzed foreground quasars. The red horizontal bars indicate the average transmission in the $\pm 15 \text{ cMpc}$ window $\langle F_{|R_{\parallel}| < 15 \text{ cMpc}} \rangle$ and the dotted lines the background transmission $\langle F_{15 \text{ cMpc} < |R_{\parallel}| < 65 \text{ cMpc}} \rangle$. The transmission enhancement ξ is the difference of these averages as given in Equation 3.17. Green horizontal bars indicate in full analogy the transmission measured in the three 16 cMpc wide bins. Measurement error are usually $< 3\%$ and therefore not visible in the plot.

Middle and right column of Figure 3.6 show the joint posterior probabilities for quasar age and obscured sky fraction. The results in the central column are derived from the transmission enhancement measured in the single 30 cMpc wide bin, the ones in the right columns from the transmission enhancement statistic in three consecutive 16 cMpc wide bins. Contours

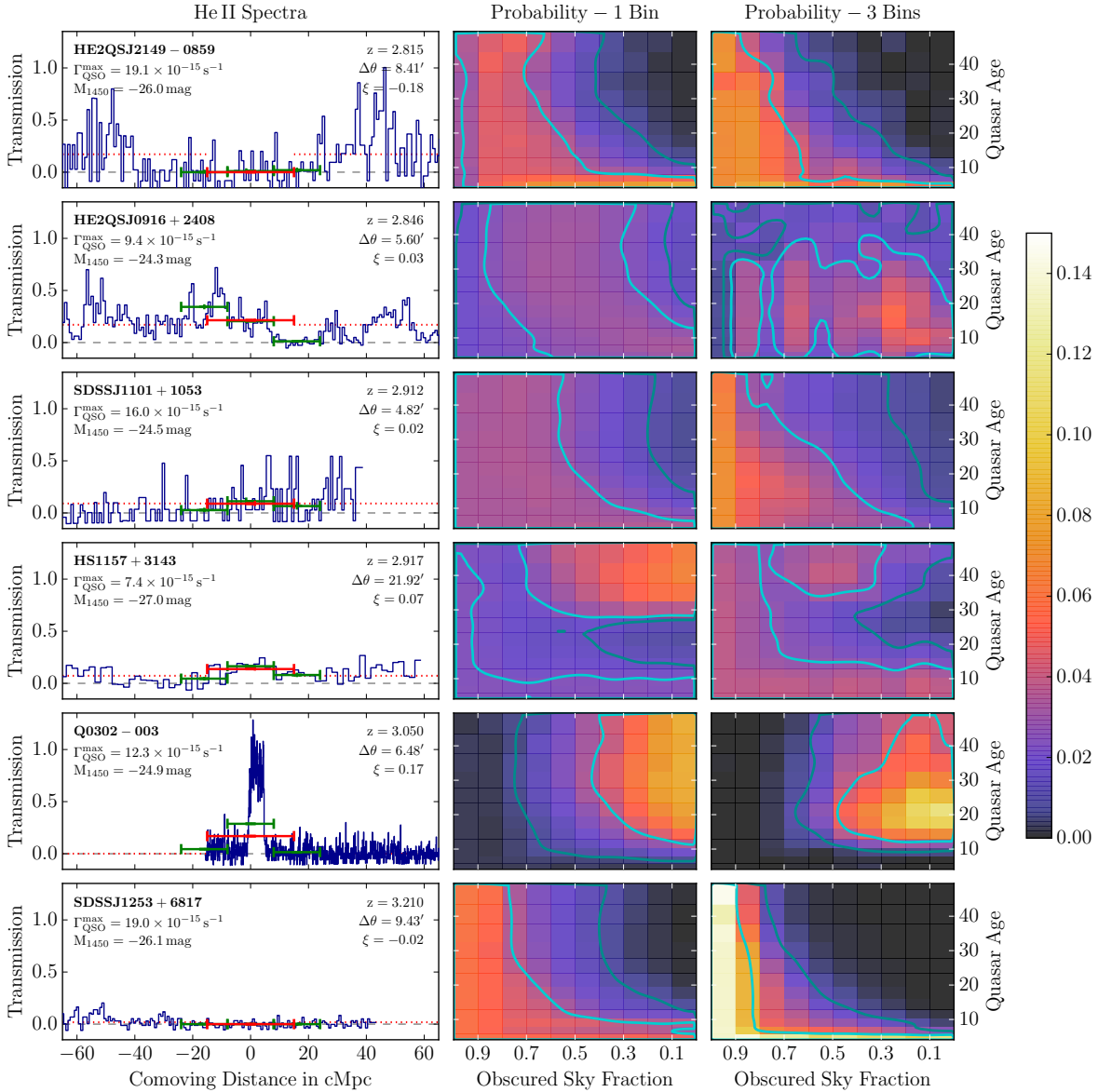


Figure 3.6: Joint posterior probabilities for age and obscured sky fraction of the six quasars analyzed in this study. The left column shows the FUV spectra of the He II background sightline. The red bars marks the measured He II transmissions in the 30 cMpc wide bins, the dotted red lines indicate the background transmissions. The green bars show the measured transmission in the three 16 cMpc wide bins. Some key information about the foreground quasars are given as well. The middle and right columns give the inferred posterior probabilities for quasar age and obscured sky fraction. Bright and dark cyan contours indicate regions enclosing 68% and 95% of the probability. The probabilities in the central column are derived using the transmission enhancement in a single ± 15 cMpc wide window. The ones in the right column are based on the transmission enhancement in three 16 cMpc wide bins. Both statistics give consistent results but the three-bin statistic has improved sensitivity to quasar age. For the three foreground quasars with the highest ionization rate, our analysis prefers scenarios in which the quasars are very young (< 10 Myr) or highly obscured ($\Omega_{\text{obsc}} > 70\%$), which in both cases would prevent ionizing radiation from reaching the background sightline. For the foreground quasar associated with the large transmission spike in the Q 0302–003 sightline, we find low obscuration ($\Omega_{\text{obsc}} < 40\%$) and an age above 15 Myr with a peak probability in the three-bin statistic around 22 Myr. For the other two quasars we derive only very weak constraints or even bimodal distributions.

enclosing 68 % and 95 % total probability are shown as bright and dark cyan lines, determined by smoothing the pixelated likelihood surface.

In general, the results from the single-bin statistic and the three-bin statistic are in agreement which is highly encouraging given the substantial differences between the statistics and the 60 % longer pathlength used in the three-bin statistic. Consistent with expectation, the three-bin contours are typically slightly better constrained than the contours derived using the single bin statistic. Note that in basically all cases, the contours are not closed. We therefore obtain just limits on the parameters, in particular the quasar age⁷. This was expected given the high level of fluctuations in our transverse proximity models illustrated in Figure 3.5. Since the likelihood distributions are not localized, the adopted priors do have a substantial effect on the posterior probabilities.

Based on our analysis of the six quasars shown in Figure 3.6, a very heterogeneous picture emerges. For the objects along the HE2QS J2149–0859 (top) and SDSS J1253+6817 (bottom) sightlines, our analysis rules out combinations of long lifetime (> 15 Myr) and substantial illumination (> 50 %) and indicates that these objects are either very young ($t_{\text{age}} < 8$ Myr) or highly obscured ($\Omega_{\text{obsc}} > 70$ %). Both cases have in common that no ionizing radiation from the foreground quasar reaches the background sightline and no excess He II transmission is observed. Given that we do not see evidence for a transverse proximity effect at the background sightline, it is not possible to discriminate between these degenerate cases. For the SDSS J1101+1053 sightline (third row) the picture is similar but less constrained. Our 68 % contour encloses the full lower-left corner (low t_{age} , high Ω_{obsc}) of our parameter space and our analysis only securely rules out the extreme case of $\Omega_{\text{obsc}} < 20$ % and $t_{\text{age}} > 20$ Myr.

We find a totally different result for the $z = 3.05$ quasar (Jakobsen et al. 2003) along the Q 0302–003 sightline. This is the only foreground quasar associated with a strong He II transmission spike and therefore our analysis prefers scenarios in which a large amount of ionizing radiation reaches the background sightline, therefore low obscuration ($\Omega_{\text{obsc}} < 40$ %) and quasar ages longer than 15 Myr (fifth row in Figure 3.6). The Q 0302–003 sightline also shows the strongest difference between single and three-bin statistic. The posterior probability for the single-bin statistic is constant for quasar ages above 30 Myr, because for lifetimes this long, the quasar radiation would modify the transmission at $R_{\parallel} > 15$ cMpc (see Figure 3.3), outside the window used for the single-bin statistic. The rightmost of the three small bins however extends to higher comoving distance and is therefore sensitive to longer quasar ages. For the three-bin statistic, we thus find that the posterior probability decreases towards high quasar ages and the 68 % contour is almost closed with a peak around 22 Myr. The analysis therefore associates the right cutoff of the transmission peak ($R_{\parallel} \gtrsim 6$ cMpc) with some probability to a finite age of the quasar. Quasar ages substantially longer than 30 Myr become less likely, but are however not ruled out at high significance.

For the quasar close to the HE2QS J0916+2408 sightline, the posterior probability derived from the single bin statistic is rather flat (second row in Figure 3.6). The shape of the 68 % contour does look different for the three-bin statistic, but the actual probabilities are not that different. In both cases, a large fraction of the probed parameter space is allowed. The three-bin statistic slightly disfavors quasar ages longer than 35 Myr, probably related to the very low He II transmission around $R_{\parallel} \approx 16$ cMpc.

For the HS 1157+3143 sightline (forth row) we measure a generally low He II transmission with a slight increase in the $|R_{\parallel}| < 15$ cMpc region. Our analysis does not clearly indicate whether this small enhancement is caused by the foreground quasar or by a UV background fluctuation. This is clear from our posterior probability distributions, which are clearly bi-

⁷The obscured sky fraction is naturally constrained between 0 % and 100 %. Contours not closed in Ω_{obsc} therefore have slightly different quality than contours open in t_{age} direction.

CHAPTER 3. MODELING OF THE HE II TPE

modal. If the extra transmission is due to fluctuations in the UV background, the quasar should not illuminate the background sightline, indicated by the 68% contour encompassing high obscured sky area ($> 80\%$) and young quasar age (< 15 Myr). If the transmission enhancement is actually caused by the quasar, it corresponds to the other 68% contour at large quasar ages ($t_{\text{age}} > 30$ Myr) and moderate obscured sky fractions. The single bin statistic indicates $\Omega_{\text{obsc}} < 60\%$ while the 3-bin statistic prefers $\Omega_{\text{obsc}} \approx 50\%$. We consider both statistics to be consistent here, given that slightly different parts of the spectra are used for the measurements and the overall high stochasticity of the He II transverse proximity effect.

To summarize, our analysis delivers very different results for the six quasars. The three quasars with the highest estimated He II photoionization rate at the background sightline (HE2QS J2149–0859, SDSS J1101+1053, HS 1157+3143) are not associated with He II transmission spikes and either young ($\lesssim 10$ Myr) or highly obscured ($\Omega_{\text{obsc}} \gtrsim 70\%$). The constraints for the foreground quasar along the Q 0302–003 sightline are almost exactly the opposite, with an age most likely > 15 Myr and obscuration $< 35\%$. For the two other quasars we infer only very weak constraints. One shows moderate age and moderate obscuration, the other bimodal posteriors. These two objects cause the lowest expected He II ionization rate at the background sightline in our sample, only $7.4 \times 10^{-15} \text{ s}^{-1}$ and $9 \times 10^{-15} \text{ s}^{-1}$. This probably represents the limit for deriving constraints on individual foreground quasars.

3.5 Discussion

Given the surprisingly dissimilar appearance of the He II spectra for the six quasars with the highest He II photoionization rate at the background sightline (presented in Chapter 2), one might have expected substantial differences in the emission of ionizing radiation for these quasars. In this Chapter we quantified this by comparing the transmission spectra of each quasar’s background sightline to detailed models of the transverse proximity effect, parametrized by quasar age (t_{age}) and degree of obscuration (Ω_{obsc}). Nevertheless, it remains challenging to interpret our results in the context of a single model of quasar emission.

In the simplest picture, all quasars are drawn from the same underlying population with a unique set of properties, in our case Ω_{obsc} and t_{Q} . From previous studies one might have expected a fiducial quasar model with e.g. $\sim 50\%$ obscuration (Simpson 2005; Brusa et al. 2010; Assef et al. 2013; Lusso et al. 2013; Buchner et al. 2015; Marchesi et al. 2016) and a lifetime of ~ 25 Myr (Schmidt et al. 2017a). This fiducial model lies in the center of the posterior distributions in Figure 3.6. Although our confidence contours are relatively broad, such that this parameter combinations is never formally ruled out at high confidence, it is rather intriguing that none of our posterior distributions actually have a peak at this location in parameter space. Of course, a substantial amount of variation around a fiducial model has to be expected and in particular the quasar age is, even for a fixed quasar lifetime t_{Q} , a random variable drawn from $0 < t_{\text{age}} < t_{\text{Q}}$. The weak and degenerate nature of our constraints and the small number of objects makes it challenging to formally compare the probability of different models. However, visual inspection of the posterior distributions in Figure 3.6 suggests that quasars tend to live in two different regions of this parameter space with dissimilar emission properties, suggesting one group being very young or highly obscured and the other old and unobscured.

A thorough test of this hypothesis is not straight-forward and requires a detailed and careful analysis which is beyond the scope of this work. However we conduct a very simple test to check if a monomodal model is a good representation for our ensemble of six quasars. For this, we just multiply the six likelihood distributions shown in Figure 3.6 which gives us the

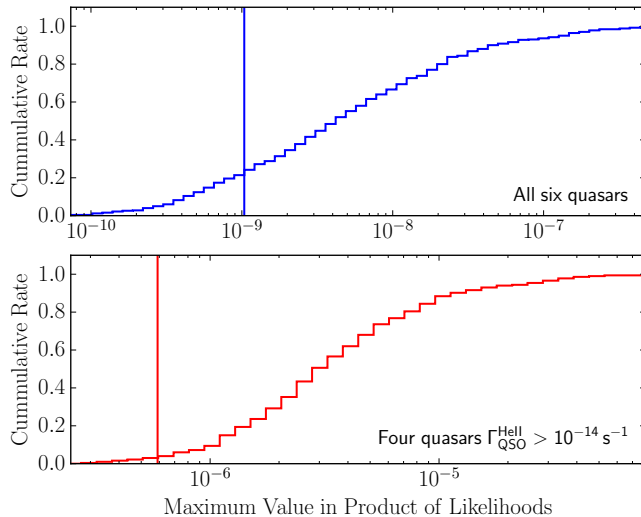


Figure 3.7: Maximum of the joint likelihood product of all six (top) or just the four $\Gamma_{\text{QSO}}^{\text{HeII}} > 10 \times 10^{-15} \text{ s}^{-1}$ quasars (bottom). The vertical line indicates the value measured in the data while the cumulative histogram shows the distribution measured from 500 mock datasets drawn from a monomodal distribution of t_{age} and Ω_{obsc} . We find that 77% and 96% of the mock measurements lie above the observed values.

joint likelihood under the assumption that all quasars are drawn from the same underlying distribution. Fitting this distribution in $(t_{\text{age}}, \Omega_{\text{obsc}})$ with a Gaussian yields a mean of $\mu = (14.6 \text{ Myr}, 61\%)$ and a dispersion $\sigma = (5.2 \text{ Myr}, 14\%)$. This is our best estimate of the underlying distribution of quasar parameters. We then draw 500 sets of six quasars from this distribution and create mock He II observations adopting the same sightline separations, luminosities, sensitivities, etc. as in the real data. These we then fit with our full analysis machinery, resulting in 500 posterior probability distributions similar to the real ones shown in Figure 3.6, and calculate for each group the product of the six individual likelihood distributions. We can now find for each mock realization of our dataset the maximum value of the 2D $(t_{\text{age}}, \Omega_{\text{obsc}})$ joint likelihood distribution, which is a coarse indicator for how well the model fits the (mock) data. Figure 3.7 shows the distribution of this estimator for our 500 mocks and compares it to the value we get for the real data.

Considering all six quasars, we find that 77% of the mock realizations have a higher maximum likelihood value than our real data set. This means, our mock data are on average more likely to be drawn from the monomodal distribution than the six real observations. If we exclude the two quasars with $\Gamma_{\text{QSO}}^{\text{HeII}} < 10 \times 10^{-15} \text{ s}^{-1}$ (HE2QS J0916+2408 and HS 1157+3143) for which our analysis gives rather uninformative results and focus on the four strong quasars with meaningful constraints, the picture gets clearer. In this case, 96% of the mock realizations achieve a higher maximum likelihood, which would make the data a 2σ outlier from this distribution. We interpret this result as indication that the quasar emission properties we measure might result from a distribution more complex than the simple monomodal distribution we assumed here, e.g. the bimodal behavior we mentioned above. However, given the simplicity of this test, the small number of analyzed objects and the in general low significance of our results, this matter required additional exploration, based on a more thorough statistical analysis and most importantly more objects.

In the mean time, one can speculate that the position at which a quasar lives in this possibly bimodal emission parameter space might somehow correlate with other quasar properties. For instance, in receding torus models (Lawrence 1991; Simpson 1998; Hönig & Beckert 2007) the obscured sky fraction depends strongly on luminosity. Figure 3.6 lists numerous quantities for the six foreground quasars. However, there are no obvious trends with quasar properties such as absolute magnitude or redshift, or other parameters like He II ionization rate or separation from the background sightline. It would be interesting to investigate the dependence on black hole masses or Eddington ratios. However, there are so far no observations enabling measurements of these quantities for the analyzed foreground quasars. We therefore at present do not have a convincing explanation for the origin of this suggestive bimodality.

CHAPTER 3. MODELING OF THE HE II TPE

3.5.1 Generalization to Quasar Population Properties and Constraints of Additional Parameter

On the other hand, assuming that all quasars do represent a common population, it is intriguing to use our analysis of individual quasars to derive properties of the general quasar population. However, this is, given our non-localized posterior probabilities and the strong degeneracies a rather difficult task. We point out that a proper Bayesian answer to this requires more than just multiplying our individual likelihoods and marginalizing them over one of the two parameter. Instead, such an attempt requires a very careful analysis to avoid introducing any subtle biases, in particular due to the inevitable strong influence of explicit and implicit priors. In particular for a lifetime estimate, we would have to distinguish between general lifetime t_Q and individual quasar ages t_{age} , in contrast to our highly simplified approach we show above. A more appropriate analysis would require drawing the quasar ages from a distribution between $0 < t_{\text{age}} < t_Q$, which turns t_{age} from a deterministic parameter to a random variable, requiring a large number of additional skewers to properly sample the parameter space.

One might also wish to include additional parameters in the analysis like the IGM mean free path for He II ionizing photons or the ionizing output of quasars. This is in principle possible, it would however substantially complicate the analysis and require the sampling of a much larger parameter grid. In addition, as illustrated in Figure 3.5, the constraining power of the observations is limited due to the high expected variance. The possible constraints from single sightlines would therefore likely be unsatisfactory.

3.5.2 Non-Lightbulb Quasar Lightcurves and Non-Equilibrium Effects

As stated before, we use a lightbulb model for the quasar lightcurve and assume instantaneous photoionization equilibrium. Both aspects are clearly a simplification.

As described e.g. in Khrykin et al. (2016), the characteristic timescale helium requires to react to a change in the photoionization rate and adopt a new ionization equilibrium, the equilibration timescale, is rather long. It depends on the recombination and photoionization timescale as $t_{\text{eq}} = (t_{\text{phot}}^{-1} + t_{\text{recom}}^{-1})^{-1}$. The recombination timescale $t_{\text{recom}}^{\text{HeII}} = (\alpha_{\text{A}}^{\text{HeII}} n_{e^-})^{-1}$ in the IGM of our simulations lies between 1.1 Gyr and 3.5 Gyr. The He II equilibration timescale is therefore always dominated by the photoionization timescale $t_{\text{phot}}^{\text{HeII}} = \Gamma_{\text{HeII}}^{-1}$, which itself depends on the intensity of the quasars radiation and the UV background. If our quasars illuminate the background sightline, the photoionization timescale is rather short, about 2.5 Myr. If the background sightline is not illuminated, the UV background determines the photoionization timescale and common values are between $4.8 \times 10^{-15} \text{ s}^{-1}$ and $5.7 \times 10^{-16} \text{ s}^{-1}$, corresponding to 6.6 Myr and 55 Myr, respectively (see Figure 3.1). The latter case might be important if a quasar turns off. It determines how fast a possible transverse proximity effect vanishes.

Neglecting these non-equilibrium effects can have different effects on our measurement. For three of the four strongest foreground quasars we find no evidence for an influence on the background sightline and explain this with either high obscuration or young quasars ($t_{\text{age}} < 10 \text{ Myr}$). In the latter case, heuristically one should add the photoionization timescale of $\approx 2.5 \text{ Myr}$ to this constraint. In the case of the Q 0302–003 $z = 3.05$ object, our most-likely quasar age of 22 Myr should be longer by a similar amount.

In cases like Q 0302–003, where we find a clear transverse proximity effect, the exact constraint is only that the quasar is observed today to be active (as seen on the direct view, $\Delta t = 0$) and had to be active approximately one transverse light crossing time earlier ($5 \text{ Myr} \lesssim \Delta t \lesssim$

20 Myr, see Figure 3.3) as probed by the background sightline. Technically, the quasar could have been inactive in between these times. If one allows such a quasar lightcurve composed of (at least) two (shorter) bursts, our measurement constrains their separation in time instead of the duration of one long, continuous burst. In addition, the first burst, responsible for the enhanced He II transmission at the background sightline, must have been longer than the He II equilibration timescale to actually have an impact on the ionization state, thus > 2.5 Myr. Clearly, allowing rather flexible quasar lightcurves and considering non-equilibrium effects, makes an already rich problem even more complicated.

Another scenario one might consider is *quasar flickering* (e.g. Novak et al. 2011; Segers et al. 2017). In such a case, the quasar switches rapidly, e.g. with periods of 10^5 yr, between on and off states. For the He II ionization state only the ionizing flux averaged over the equilibration timescale is relevant. Flickering on timescales 10^5 yr, much shorter than t_{eq} , would therefore be indistinguishable from continuous emission with the quasar luminosity reduced by the appropriate amount. However, flickering with the cosmic average duty cycle of $\approx 1\%$ (Conroy & White 2013; Eftekharzadeh et al. 2015) would probably not provide sufficient ionizing photons to cause an observable effect. In Chapter 2 we found statistical evidence for a transverse proximity effect for estimated photoionization rates $\Gamma_{\text{QSO}}^{\text{HeII}} > 2 \times 10^{-15} \text{ s}^{-1}$ (see Figure 2.11), roughly comparable with the UV background. If the actual, time-averaged He II ionizing flux output from quasars were lower by more than a factor of a few, the quasars would not cause any significant enhancement over the UV background and no proximity effect would be visible. This sets limits to the minimum duty cycle of a possible quasar flickering. The cosmic average of 1% would certainly be too low. The quasars therefore would have to be, despite their flickering, in an extended phase of high activity and our measurement constrains the duration of this phase.

For arbitrary or very complicated lightcurves (e.g. Novak et al. 2011) it becomes challenging to arrive at firm constraints. With a proper parametrization of the quasar lightcurve, radiative transfer calculations could in principle deliver the required models, but given the large amount of expected scatter in He II transverse proximity effect measurements (Figure 3.5), it appears unlikely to derive meaningful results. Instead of developing more sophisticated models, it seems more appropriate to focus future efforts towards reducing the variance in the measurement.

3.6 Summary

In Chapter 2 (Schmidt et al. 2017a) we presented the results of our dedicated He II foreground quasar survey and provided statistical evidence for the presence of the He II transverse proximity effect, which resulted in a heuristic constraint on the quasar lifetime $t_{\text{Q}} > 25$ Myr. However, among the six foreground quasars with the highest He II photoionization rates, only one is associated with a strong He II transmission spike. For the other ones, no comparable signature on the background sightline is observed, which might point towards very young or highly obscured quasars.

In this Chapter we investigate the implications of these high photoionization rate sightlines via detailed modeling of the He II transverse proximity effect, encompassing finite quasar ages t_{age} , light travel time effects, opening angle/obscuration Ω_{obsc} , and stochasticity of both the IGM and quasar orientation. We use outputs from the NYX cosmological hydrodynamical simulations (Almgren et al. 2013; Lukić et al. 2015) and post-process these with the fluctuating He II UV background model from Davies et al. (2017) (see Figure 3.1) plus the added effect of one isolated foreground quasar. The UV background model is calibrated to match existing He II observations (Figure 3.2). For the foreground quasar, we vary quasar age t_{age}

CHAPTER 3. MODELING OF THE HE II TPE

and obscuration Ω_{obsc} to explore their combined effect on the He II transverse proximity effect signal, as well as obtain the first estimates of its variance resulting from IGM density fluctuations, UV background fluctuations, and the unknown orientation of the foreground quasars (Figure 3.5). We adopt a fully Bayesian statistical approach to deal with the large non-Gaussian fluctuations in the expected He II transmission, Poisson photon-counting noise, and strong parameter degeneracies (§ 3.3).

We derive joint constraints on t_{age} and Ω_{obsc} (Figure 3.6), for the six foreground quasars with the highest He II photoionization rates from our He II transverse proximity effect survey (Chapter 2, Schmidt et al. 2017a). A highly inhomogeneous picture of quasar emission properties emerges from this analysis. For the prototype quasar associated with the He II transmission spike in the Q 0302–003 sightline, our analysis prefers $t_{\text{age}} \approx 22$ Myr and low obscuration ($\Omega_{\text{obsc}} < 35\%$). For three other foreground quasars however, we rule out long lifetimes (> 10 Myr) and low obscuration $\Omega_{\text{obsc}} < 60\%$. Although a fiducial quasar model with $t_{\text{age}} = 25$ Myr and 50% obscuration is marginally consistent ($\approx 5\%$) with most of our derived probability contours, our analysis shows indications for a bimodal distribution of quasar properties with one group being old and nearly unobscured while the other one is very young or highly obscured. An analysis of trends with other quasar parameters, e.g. luminosity, redshift, He II ionization rate, does not lead to a convincing explanation for the origin of this apparent dichotomy.

Further progress in deriving constraints on quasar or IGM properties is hindered by the large intrinsic variance of the He II transverse proximity effect as shown in Figure 3.5. This poses a fundamental limitation for similar studies of the He II transverse proximity effect. A possible solution to this issue could be the statistical combination of individual measurements as discussed in § 3.5.1 or stacking as in § 2.3. However, the available foreground quasar sample is limited and including fainter quasars increases sensitivity to the exact details of the fluctuating He II UV background model. Alternatively, the discovery of individual foreground quasars with substantially higher He II photoionization rate than the quasars analyzed in this study might offer a viable opportunity to derive firmer constraints. Here, the transverse proximity effect would be stronger, reducing the relative uncertainty. However, despite our survey efforts (see § 2.1), such objects could so far not be discovered. Maybe the best option to overcome the intrinsic IGM variance associated with the He II transverse proximity effect could be the use of coeval hydrogen Ly α forest spectra. In principle, high-resolution H I absorption spectra could deliver information about the local IGM density structure and possibly allow a more precise measurement of the He II ionization state (e.g. Worseck & Wisotzki 2006). Developing models and a statistical framework to exploit this additional information constitutes an interesting task for the future.

Chapter 4

Mapping Quasar Light Echoes in 3D with H I Ly α Forest Tomography

This Chapter is based on work submitted for publication in [Schmidt et al. \(2018b\)](#). Outputs from NYX cosmological simulations were supplied by Z. Lukić. All other parts are based on research conducted by author T. Schmidt, under supervision of J. Hennawi at UCSB.

In the previous chapters we have presented a detailed analysis of the He II transverse proximity effect and inferred joint constraints on lifetime and obscuration for six individual foreground quasars (Figure 3.6). However, our detailed models revealed that a large amount of scatter in the amplitude of the He II transverse proximity effect has to be expected (Figure 3.5). This is in parts caused by the unknown orientation of the foreground quasar but also stems from the stochastic IGM absorption itself. This scatter adds substantial uncertainty to the measured quasar properties and in consequence our inference delivered only broad constraints. Our impression is, that the available He II dataset only holds little extra constraining power and improving the quality of our measurements or determining additional quasar or IGM properties appears quite challenging. Also, the capabilities of *HST*/COS are nearly exhausted and a substantial expansion of the He II dataset in the next decades seems unlikely.

In this chapter, we therefore develop a novel method to measure quasar emission properties that relies on observations of the H I Ly α forest. This can be observed with powerful ground-based optical telescopes with large collecting areas and offers the possibility to acquire far more spectra. These advantages should overcome many of the limitations encountered in our studies of the He II transverse proximity effect and allow a detailed three-dimensional mapping of quasar light echoes.

For this, we refer to a special variant of the transverse proximity effect that does not rely on quasars as background source but uses faint (e.g. $r > 24$ mag) star forming galaxies. These are sufficiently abundant that the proximity zone of the foreground quasar can be probed by the H I Ly α forest absorption along many background sightlines. This technique, first proposed by [Adelberger \(2004\)](#) and [Visbal & Croft \(2008\)](#), allows one to map quasar light echoes in three dimensions and in much more detail than possible with single background sightlines. The concept is illustrated in Figure 4.1 which clearly shows how the parabolic-shaped appearance of the quasar proximity zone, which is caused by the finite age of the quasar (see §4.2.3), can be seen in the Ly α forest absorption along the background sightlines. Despite the great potential, this tomographic mapping of quasar light echoes has so far never been attempted in practice, probably because the observational requirements were judged to be too challenging.

CHAPTER 4. MAPPING QUASAR LIGHT ECHOES IN 3D

Tomographic reconstructions of the large-scale structure of the Universe using the Ly α forest absorption in the spectra of faint background galaxies were recently pioneered by Lee et al. (2014a,b). They showed that at $z \simeq 2.4$ the use of faint $r > 24$ mag star forming galaxies as background sources delivers sightline densities around 700 deg^{-2} , which is sufficient to interpolate between sightlines and to reconstruct a tomographic map of the IGM absorption on Mpc scales. By clearly assessing the observational requirement, Lee et al. (2014a) determined that Ly α tomography is indeed possible with current-generation facilities, in particular 8–10 m class telescopes and existing multi-object spectrographs. Since then, the COSMOS Lyman-Alpha Mapping And Tomography Observations (CLAMATO) survey has proven the feasibility in practice and delivered the first tomographic map of the IGM (Lee et al. 2014b, 2018). Prime objective of the CLAMATO survey is to map the large-scale structure of the Universe to find e.g. protoclusters (Stark et al. 2015a; Lee et al. 2016) and to study the cosmic web (Stark et al. 2015b; Krolewski et al. 2018). Similar techniques, based however on SDSS/BOSS spectra, were employed by Cai et al. (2016, 2017) to map large-scale overdensities.

In light of these developments, we revisits the question of mapping quasar light echoes with Ly α forest tomography. Our aim is to demonstrate feasibility, assess sensitivity, and determine the optimal observing strategy by conducting an end-to-end analysis of the experiment, starting from the observational requirements, computation of realistic models, and finally a

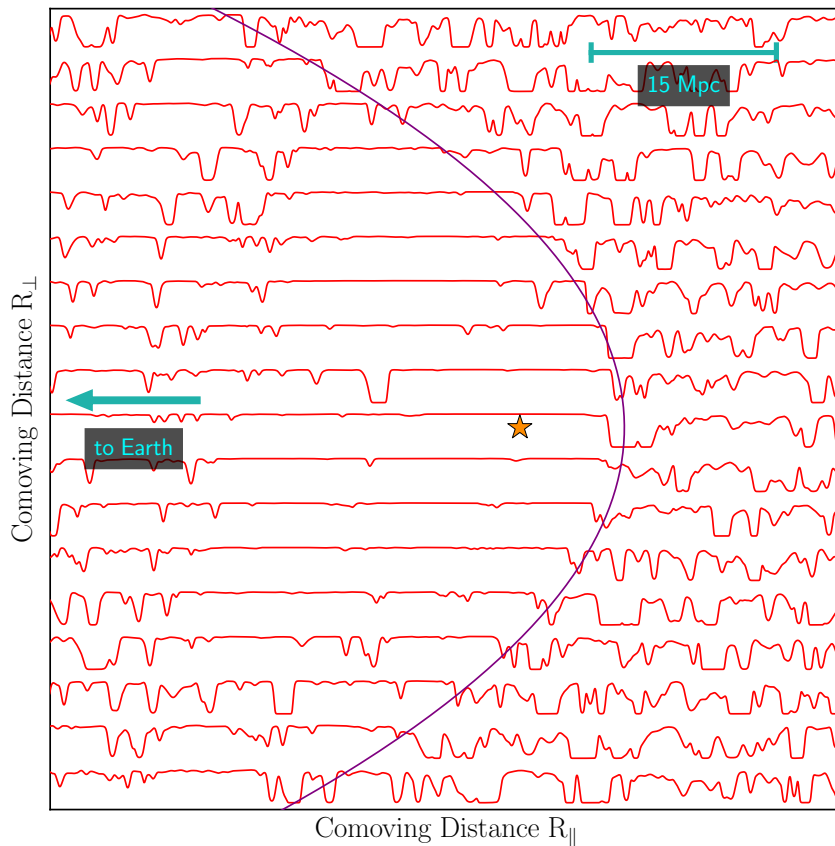


Figure 4.1: Illustration of the observational concept for mapping quasar light echoes with H I Ly α forest tomography. The UV radiation of a bright quasar (center) enhances the ionization state of the IGM in its surrounding. This proximity zone is then probed by many background sightlines (red). The Ly α forest absorption along this ensemble of spectra clearly reveals the shape and structure of the proximity zone. In this case, the region influenced by the quasars radiation has a parabolic shape due to the finite age of the quasar (purple). See also Visbal & Croft (2008). This Figure is based on our models described in § 4.2, but simplified and idealized to act as a sketch. A more realistic simulation of the proximity effect is shown in Figure 4.9.

fully Bayesian inference of parameter constraints. To keep the complexity of this pilot study at an acceptable level and to limit the computational expense, we adopt a simple isotropic *lightbulb* model for the quasar emission and focus only on measurements of the quasar age. In the future, we will relax these assumptions and consider more realistic anisotropic emission from quasars as well as more complex lightcurves.

The structure of this chapter is as follows. We summarize all relevant observational parameters like quasar luminosity, instrument properties (sensitivity, spectral resolution, field-of-view), and achievable background sightline density in § 4.1. We will then describe our models of the 3D proximity effect, which are based on state-of-the-art cosmological hydrodynamical simulations postprocessed with a quasar emission model (§ 4.2, § 4.3). To compare observational data to our models and infer posterior probability distributions for the quasar age, we develop a sophisticated Bayesian method based on likelihood-free inference (§ 4.4). Finally, we apply this analysis pipeline to mock observations and determine the achievable precision on quasar age and assess dependencies on various observational parameters (§ 4.5), allowing us to choose the optimal observing strategy.

Throughout this Chapter we use a flat Λ CDM cosmology with $H_0 = 68.5 \text{ km s}^{-1} \text{ Mpc}^{-1}$, $\Omega_\Lambda = 0.7$, $\Omega_m = 0.3$ and $\Omega_b = 0.047$ which has been used for the computation of the NYX hydro simulation and is broadly consistent with the Planck Collaboration et al. (2018) results. We use comoving distances and denote the corresponding units as cMpc. In this study, we consider a simple lightbulb model for the quasar lightcurve in which the quasar turns on, shines with constant luminosity for its full lifetime t_Q until it turns off. This timespan is however different from the quasar age t_{age} , which describes the time from turning on until emission of the photons that are observed on Earth today (see Figure 4.8). Magnitudes are given in the AB system (Oke & Gunn 1983).

4.1 Observational Setup

To set the stage for our undertaking and to define the observational framework of our study, we discuss all relevant observational parameters in this section. This includes the luminosity of potential quasar targets, achievable background sightline densities, required spectral resolution, exposure times, field-of-view (FoV), and other elements. For most of these parameters we will motivate some initial estimates and build up a fiducial observing strategy. We will later in § 4.5 explore in detail how the quality of the parameter inference depends on these choices and show how the strategy can be optimized.

A key question for mapping quasar light echoes with Ly α forest tomography is the optimal quasar redshift to operate at. At low redshift, the average IGM transmission is quite high, e.g. 85 % at $z = 2.2$, and in consequence even the brightest foreground quasar can only cause a very limited enhancement in the Ly α forest transmission. In such conditions, the stochastic nature of the Ly α forest absorption and unavoidable uncertainties in estimating the continuum of the background sources might conceal the transmission enhancement. With increasing redshift and thus lower mean IGM transmission (e.g. 45 % at $z = 3.8$), foreground quasars can cause a stronger transmission enhancement that is easier to detect in a tomographic map. This clearly motivates working at higher redshifts. On the other hand, the number density and brightness of available background galaxies drops dramatically with increasing redshift. One therefore has to accept a much sparser sampling of the proximity region by background sightlines, work with lower S/N spectra or substantially increase the exposure times. Finding the best compromise between strong transmission enhancement at high redshift and fine sampling of the tomographic map at low redshift is one of the primary intentions of this work and requires a detailed assessment of the relevant observational parameters.

CHAPTER 4. MAPPING QUASAR LIGHT ECHOES IN 3D

4.1.1 Quasar Luminosities

One would ideally target the brightest quasars at a given redshift since these cause the strongest enhancement in transmission and have the largest proximity zone. We have therefore compiled a collection of the most luminous quasars at each redshift based on the SDSS DR14Q spectroscopic quasar catalog (Pâris et al. 2018). For each redshift bin of size $\Delta z = 0.05$, we selected the ten brightest objects and show the resulting sample in Figure 4.2. Conversion from observed SDSS i -band magnitude to monochromatic luminosity at 1450 \AA (M_{1450}) is based on the Lusso et al. (2015) quasar template and Galactic extinctions from Schlafly & Finkbeiner (2011)¹.

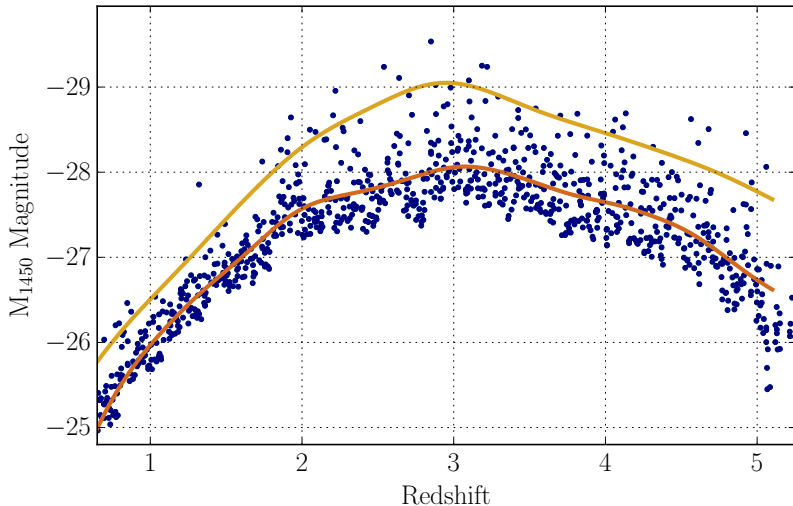


Figure 4.2: Most luminous quasars from the SDSS/BOSS DR14Q quasar catalog (Pâris et al. 2018). For each $\Delta z = 0.05$ bin we have selected the ten brightest quasars. Solid lines show running averages of the full selected sample (dark line) and just the most luminous quasars in each redshift bin (light line).

Clearly, the most luminous quasars exist around $z \approx 3$ and reach absolute UV magnitudes around $M_{1450} = -29$ mag. For higher redshifts, the peak luminosity slowly decreases to $M_{1450} = -28$ mag at $z = 5$ while it steeply drops for redshifts below $z < 2.5$. By computing a running average (Gaussian filter of $\Delta z = 0.2$ width) of the brightest quasar per $\Delta z = 0.05$ redshift bin, we obtain a suitable representation of the evolution of the most luminous quasars in the universe. These are indeed the ideal targets for our experiment and for the rest of this paper we will use this smooth function (shown in Figure 4.2 in light brown color) as the fiducial quasar luminosity.

We stress that other quasar catalogs (e.g Schmidt & Green 1983; Véron-Cetty & Véron 2010; Flesch 2015; Schindler et al. 2018) list additional ultraluminous quasars. However, including these affects predominantly redshifts $z_{\text{QSO}} < 2$ and does not change the overall picture at the redshifts $2 < z_{\text{QSO}} < 5$ for which the Ly α forest is accessible from the ground.

4.1.2 Field-of-View

The region of interest around the foreground quasar is clearly set by the size of its proximity region, i.e. the region where the photoionization rate of the quasar $\Gamma_{\text{QSO}}^{\text{HI}}$ substantially exceeds the UV background photoionization rate $\Gamma_{\text{UVB}}^{\text{HI}}$. The optical depth in the Ly α forest scales approximately inversely proportional to the ionization rate, see e.g. Equation 1.6. Therefore, naively a $\simeq 100\%$ increase in $\Gamma_{\text{total}}^{\text{HI}}$ due to the quasars ionizing flux should result in a detectable effect.

In Figure 4.3, we show the expected quasar photoionization rate as a function of transverse distance R_{\perp} , assuming a fiducial quasar luminosity of $M_{1450} = -29$ mag, consistent with the most luminous quasars in the universe (see Figure 4.2), the Lusso et al. (2015) quasar

¹<https://irsa.ipac.caltech.edu/applications/DUST/>

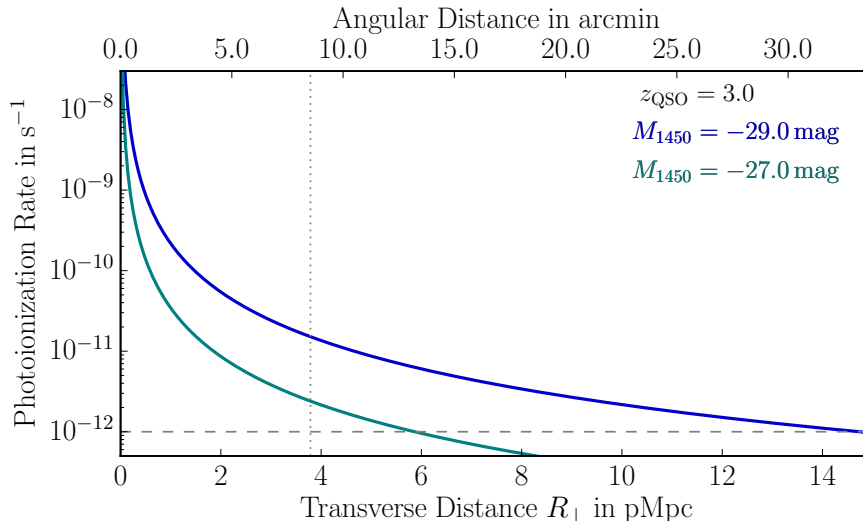


Figure 4.3: Expected quasar photoionization rate (see §4.2.3 for the derivation) for two $z = 3.0$ quasars of different luminosity as function of transverse distance R_{\perp} , compared to the metagalactic UV background of $\Gamma_{\text{UVB}}^{\text{HI}} \approx 10^{-12} \text{ s}^{-1}$ (Becker & Bolton 2013). We show angular and proper distance (instead of comoving) since in these coordinates the size of the proximity zone has only a weak dependence on redshift. The vertical dotted line indicates the radius of the adopted FoV adopted.

template and no Lyman limit absorption by the IGM (see Equation 4.5 and 4.6 in §4.2.3 for more details). The UV background photoionization rate is of order 10^{-12} s^{-1} (Becker & Bolton 2013). Therefore, hyperluminous quasars dominate the photoionization rate out to $\approx 14 \text{ pMpc}$ distance, corresponding to $30'$ or 56 cMpc at $z_{\text{QSO}} = 3$ (Figure 4.3). However, as listed in Table 4.1, the field-of-view (FoV) of classical multi-object spectrographs is usually $\ll 10'$. This implies that, for typical spectrographs, covering the full extent of a proximity zone would require multiple pointings. But to remain efficient, one might rather focus on the central region where the quasar radiation will cause the strongest impact on the Ly α IGM transmission. The exception is the Subaru Prime Focus Spectrograph (first light in 2021) which will have a circular field-of-view with 1.3 degree diameter that could cover the full proximity region with a single pointing. However, our reference concept focuses on the capabilities of currently existing instruments and therefore assumes a circular FoV with $16'$ diameter. This could be covered by a 2×2 VLT / FORS II or Keck / LRIS mosaic, or a 3×1 mosaic with DEIMOS. Within this region the photoionization rate of an $M_{1450} = -29 \text{ mag}$ quasar exceeds the UV background by more than an order of magnitude and will strongly alter the Ly α IGM transmission. The usefulness of larger fields will be explored later in §4.5.8.

Table 4.1. Key Properties of Spectrographs Usable for this Project.

Instrument	FoV	R^a	Multiplex	r_{lim}^b
VLT / FORS II	$6.8' \times 6.8'$	945	≈ 30	24.7 mag
Keck / LRIS	$7.8' \times 6.0'$	1435	≈ 30	24.4 mag
Keck / DEIMOS	$16.7' \times 5.0'$	1852	≈ 50	24.5 mag
Subaru / PFS	78' diameter	2300	2400	t.b.d

^aResolving Power at 5600 \AA and with $1.0''$ slit

^bLimiting r band magnitude to reach $S/N_{1000} = 5.0$ at 5600 \AA in $t_{\text{exp}} = 10 \text{ ks}$

CHAPTER 4. MAPPING QUASAR LIGHT ECHOES IN 3D

For the calculation Figure 4.3 is based upon, we have assumed $z_{\text{QSO}} = 3$, but we stress that the amplitude of the UV background as well as the conversion from proper transverse distance to angular size depends only weakly on redshift. Therefore, Figure 4.3 is representative for the full redshift range $2 < z_{\text{QSO}} < 5$ we consider in this paper.

4.1.3 Spectral Resolution

As already pointed out by Adelberger (2004), peculiar velocities in the IGM pose a substantial limitation to tomographic quasar light echo measurements, since they introduce non-trivial distortions of the order of a few 100 km s^{-1} into the reconstructed map. Without a priori knowledge of the density field, which sources these motions, it is of little benefit to take spectra with substantially better resolution than the amplitude of these velocities. Motions of 300 km s^{-1} correspond to a resolving power of $R = \frac{\lambda}{\Delta\lambda} = 1000$ or 3.9 cMpc at $z = 3$. For now, we take this as the reference resolution and later explore in detail, how the fidelity of our reconstructed tomographic map depends on the spectral resolution of the initial spectra (§ 4.5.6).

4.1.4 Required S/N and Exposure Times

The stochastic nature of the Ly α forest absorption causes substantial fluctuations when measuring the mean IGM transmission. For example, in a 4 cMpc long chunk of a spectrum, the scatter about the mean transmission is $\approx 20\%$ (see Figure 4.11). There is therefore limited gain in obtaining high S/N spectra and for $S/N \gtrsim 5$, intrinsic fluctuations in the IGM absorption dominate the measurement uncertainty. The exact numbers depend of course on the IGM mean transmission and therefore redshift, however, the in general quite modest requirements on data quality is one of the key factors that makes Ly α forest tomography feasible with current generation telescopes (Lee et al. 2014a).

To allow for easier comparison between different instruments and spectral resolutions, we define S/N_{1000} as the achieved S/N per $R = 1000$ or 300 km s^{-1} resolution element, independent of the actual resolution or pixel scale of the observations.² Specifying S/N_{1000} ensures that for higher resolving power the light is more dispersed and finer sampled but the overall number of detected photons and therefore the required exposure time to reach a certain S/N_{1000} is conserved. The choice of $R = 1000$ as reference resolution is arbitrary, however it is close to the minimum resolving power we require for this project. In addition, to be independent of the actual IGM absorption, we define S/N_{1000} as the continuum-to-noise in the region of the Ly α forest .

In Table 4.1 we have listed the approximate limiting r -band magnitude to reach a $S/N_{1000} = 5$ within a 10 ks exposure for different spectrographs. This calculation assumes the background galaxies have a power-law spectrum of the form $f_{\lambda} \propto \lambda^{-1.4}$ (Bouwens et al. 2009). The limiting magnitude r_{lim} quoted is that which yields a continuum $S/N_{1000} = 5.0$ in the Ly α forest at 5600 \AA , corresponding to a quasar redshifts of $z_{\text{QSO}} \approx 3.6$. We have chosen to parametrize the apparent magnitude of the background galaxies in the r -band filter since it is conveniently observable and for $z_{\text{bg}} < 3.8$ samples the UV continuum of the galaxies redwards of Ly α . For higher redshifts, one technically has to specify i -band magnitudes to avoid contamination by the Ly α forest. However, for the purpose of this work this is of no concern since we anyway specify unabsorbed continuum magnitudes.

²Spectrographs might have a higher spectral resolution (see Table 4.1) and certainly a finer pixel scale to sample the line-spread function with up to 8 pixels. Therefore, a 300 km s^{-1} wide chunk of a spectrum will be sampled by several (N) pixels and the actual S/N per pixel will be lower by \sqrt{N} .

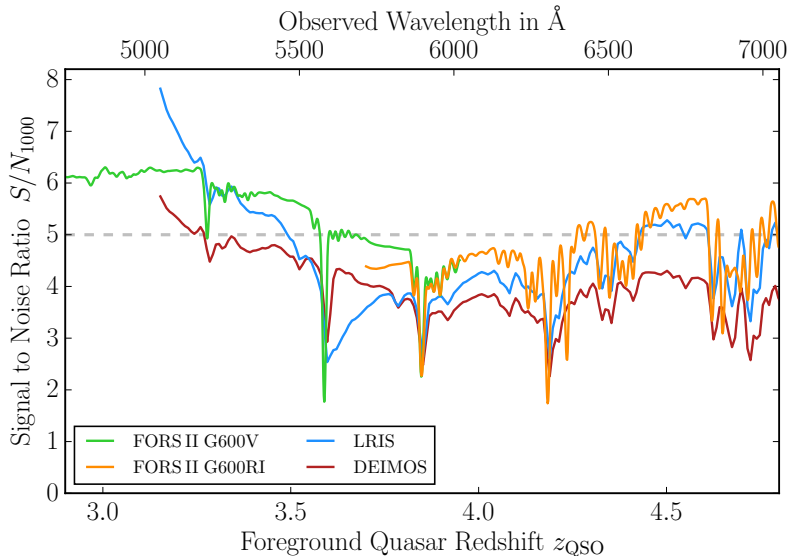


Figure 4.4: Sensitivity of different spectrographs as function of wavelength. Shown is the expected S/N_{1000} at various foreground quasar redshifts achieved for an $r = 24.7$ mag background galaxy in a $t_{\text{exp}} = 10$ ks exposure. For FORS II, we show the S/N_{1000} calculation for a blue setup (grating G600V, E2V CCD) and a red setup (grating G600RI, MIT CCD). For LRIS we show the 400/4000 + 600/7500 and for DEIMOS the 900ZD setup. All calculations assume no Moon contribution.

The sensitivity of spectrographs is in general wavelength dependent and the S/N at the quasar position achieved in a fixed exposure time (or vice versa the limiting magnitude) depends – even for the identical background galaxy – on the redshift of the foreground quasar. We show this dependence for FORS II, LRIS and DEIMOS in Figure 4.4. The exposure time estimates are based on the Keck³ and ESO⁴ exposure time calculators and assume good but realistic conditions⁵. However, the dependence of achieved S/N_{1000} on wavelength is relatively weak (see Figure 4.4) and can to some degree mitigated by using either red or blue optimized instrument setups. To not complicate matters any further, we ignore this wavelength dependence for the rest of our study and simply assume that for a limiting magnitude of $r_{\text{lim}} = 24.7$ a $S/N_{1000} = 5.0$ can be achieved in $t_{\text{exp}} \approx 10$ ks, independent of the instrument or quasar redshift. In practice, when planning actual observations, the true sensitivity of the instruments has to be taken into account and the exposure times, limiting magnitudes or S/N ratios adjusted accordingly. If adjustments to the observational parameters are necessary, these scale approximately like $t_{\text{exp}} \propto (S/N_{1000})^2$ and $S/N_{1000} \propto 10^{-\frac{2}{5} m_r}$ as long as the objects are substantially fainter than the sky brightness.

4.1.5 Background Sightline Density

The most crucial factor for our experiment is probably the achievable density of background sightlines n_{los} . We estimate this closely following the approach outlined in Lee et al. (2014a). Based on a luminosity function $\Phi(z_{\text{bg}}, m)$, which specifies the number of galaxies per luminosity and comoving volume, the sightline density is given by

$$n_{\text{los}} = \int_{z_1}^{z_2} \int_{-\infty}^{m_{\text{lim}}} \Phi(z_{\text{bg}}, m) dm \frac{dl_c}{dz_{\text{bg}}} dz_{\text{bg}}, \quad (4.1)$$

where m_{lim} is the limiting apparent magnitude of our survey and dl_c the comoving line element along the line-of-sight. Background galaxies can contribute to the tomographic map at the quasar redshift z_{QSO} if their redshift z_{bg} falls in the redshift interval $z_1 < z_{\text{bg}} < z_2$ defined by

$$(1 + z_{\text{QSO}}) \lambda_{\text{Ly}\alpha} = (1 + z_i) \lambda_i \quad (4.2)$$

³http://etc.ucolick.org/web_s2n/lris, http://etc.ucolick.org/web_s2n/deimos

⁴<https://www.eso.org/observing/etc/bin/gen/form?INS.NAME=FORNS.MODE=spectro>, Version P102.5

⁵FORNS II: E2V blue detector and G600V grating or MIT red detector and G600RI grating, Airmass = 1.2, Fractional Lunar Illumination (FLI) = 0.0, Seeing = 0.7" (47% chance), Slit = 1", $f_\lambda \propto \lambda^{-1.4}$

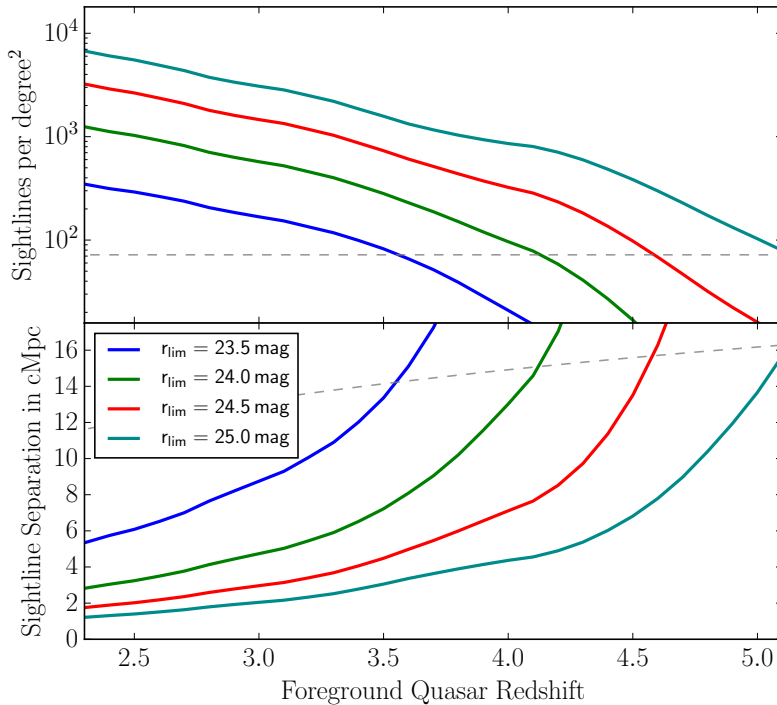


Figure 4.5: Achievable sightline density for different limiting SDSS r band magnitudes. Based on the Cucciati et al. (2012) and Bouwens et al. (2015) luminosity functions and assuming a power-law spectra of $f_\lambda \propto \lambda^{-1.4}$ (Bouwens et al. 2009) for the background galaxies. The shown limiting magnitudes correspond to exposure times of approximately 1000, 2700, 7000 and 17000 s. The dashed lines indicate the limit of one sightline per 50 arcmin², approximately the LRIS or FORS II FoV.

in which λ_1 and λ_2 denote—in rest wavelengths—the usable part of the background spectra, i.e. $\lambda_1 \approx \lambda_{\text{Ly}\alpha} = 1216 \text{ \AA}$ and $\lambda_2 \approx \lambda_{\text{Ly}\beta} = 1025 \text{ \AA}$.

We use the luminosity functions of Cucciati et al. (2012) for $z \leq 4$ and combine it with the Bouwens et al. (2015) measurements at higher redshifts. In both cases, we use the analytic Schechter representation of the luminosity function and interpolate the function parameters between redshifts. To convert from the absolute UV magnitude specified around 1600 \AA in the luminosity functions to the apparent magnitude in our observed bandpass (SDSS r band), we use the standard conversion (Hogg 1999) and assume a galaxy SED of the form $f_\lambda \propto \lambda^{-1.4}$ (Bouwens et al. 2009).

We show the result in Figure 4.5, expressed once in terms of sightlines per square degree and once as average comoving separation between sightlines. Clearly, fainter limiting magnitudes allow a higher sightline density and a finer sampling of the tomographic map. However, the achievable density of background sources drops rapidly with increasing quasar redshift. At $z_{\text{QSO}} = 2.5$, an average sightline separation of about 3 cMpc can be reached when only considering $r < 24$ mag background galaxies. At $z_{\text{QSO}} = 3.5$, one has to go half a magnitude deeper and still only reaches an average sightline separation of 4.5 cMpc. For $z_{\text{QSO}} = 4.5$, even with background galaxies as faint as $r < 25$ mag, average separations will be larger than 6 cMpc.

4.1.6 Summary of Observational Parameters

In the sections above we have collected all dependencies of the observational parameters relevant for our Ly α forest tomography project. This now allows us to explore the parameter space by varying single quantities like the desired S/N₁₀₀₀, the field-of-view observed, or the spectral resolution. This also allows us to explore certain paths through the parameter space, e.g. vary the foreground quasar redshift z_{QSO} while simultaneously adjusting to the correct quasar brightness, limiting magnitude and therefore background sightline density, to keep the required exposure time constant. We will use this later in §4.5 to find the optimal observing strategy for the project.

4.2 Models / Simulations

Given the observational framework outlined above, we create realistic models of the Ly α forest in the vicinity of bright quasars. Our models are based on outputs of cosmological hydrodynamical simulations which we postprocess with a photoionization model that explicitly incorporates finite quasar ages. From these we create mock Ly α forest spectra that resemble a given (e.g. the actually observed) pattern of background sightlines in the vicinity of a foreground quasar. In a final step, we forward model observational effects, in particular finite spectral resolution, finite S/N, and continuum fitting errors. The overall scheme is nearly identical to the one we developed in §3.2 to create He II Ly α forest spectra.

4.2.1 Nyx Cosmological Hydrodynamical Simulations

As in Chapter 3, we use simulations computed with the Eulerian hydrodynamical simulation code NYX (Almgren et al. 2013; Lukić et al. 2015). The simulation box has a large size of $100 h^{-1} \text{cMpc}$, required to capture the full extent of the proximity zone of hyperluminous quasars. The hydrodynamics is computed on a fixed grid of 4096^3 resolution elements and the same number of dark matter particles is used to compute the gravitational forces. This results in a resolution of 36 ckpc per pixel, sufficient to resolve the H I Ly α forest at $2.0 < z < 5.0$ (Lukić et al. 2015). The simulation runs make no use of adaptive mesh refinement since the H I Ly α forest signal originates from the majority of the volume (Lukić et al. 2015). Refining the resolution in the dense regions at the expense of underdense regions is therefore not beneficial for our case. Also, since the prime objective of the simulation is IGM science, no star or galaxy formation prescriptions were included. The simulations were run using a homogeneous, optically thin UV background with photoionization and heating rates from Haardt & Madau (2012). As described below, we rescale the H I photoionization rates to closely match the observed mean transmission but keep the thermal structure unchanged. We have simulation outputs available at redshifts $z = 2.0, 2.5, 3.0, 3.5, 4.0, 4.5$ and 5.0. Depending on the desired foreground quasar redshift, we take the snapshot closest in redshift and extract density, velocity and temperature along skewers. These will later be post-processed to simulate the observed H I Ly α transmission along background sightlines. For the dark matter host halos of the foreground quasars, we randomly choose halos with masses $\gtrsim 10^{12} M_{\odot}$ ($> 7 \times 10^{11} M_{\odot}$ for $z_{\text{QSO}} \geq 4.8$) from the NYX halo catalog. This corresponds to the minimum host halo mass suggested by quasar clustering studies (e.g Richardson et al. 2012; White et al. 2012).

Sightline Pattern and Skewer Extraction

Given the selected halos, skewers are extracted along one of the grid axes using the sightline pattern illustrated in Figure 4.6. The whole pattern is rescaled, i.e. stretched or compressed in radial direction, to match the desired average sightline density (see Figure 4.5) and sightlines with a transverse separation larger than the adopted field-of-view (usually $16'$ diameter) are discarded. Along the line-of-sight (i.e. velocity space), we center the skewers on the halo position in redshift space, taking the peculiar velocity of the halo into account. With the redshift of the foreground quasar as the origin, we assign individual redshifts to every pixel along the skewers.

To better represent redshift evolution of the density field, we rescale the density of each pixel according to

$$\rho(z) = \rho_{\text{sim}} \times \left(\frac{z+1}{z_{\text{sim}}+1} \right)^3. \quad (4.3)$$

We convert from simulated cosmic baryon density to hydrogen number density n_{H} using the

CHAPTER 4. MAPPING QUASAR LIGHT ECHOES IN 3D

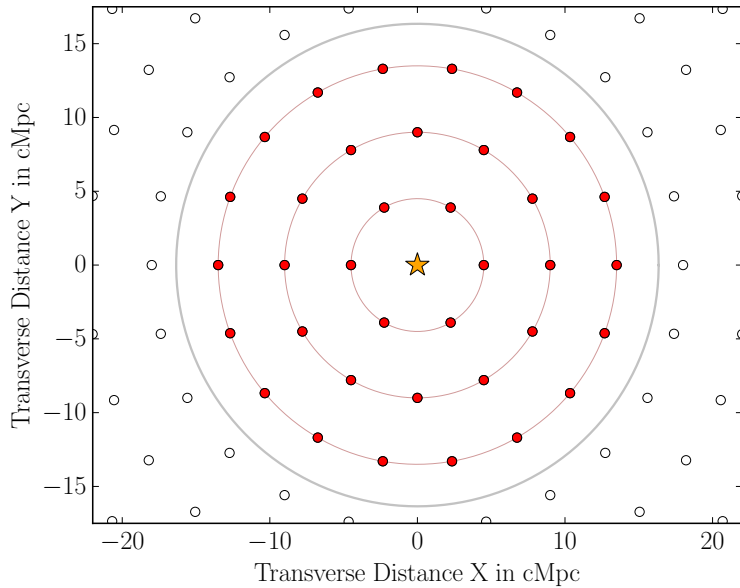


Figure 4.6: The sightline pattern adopted within this study, seen along the line-of-sight with the foreground quasar located in the center (orange star). The background sightlines (red points) are arranged on concentric circles with multiples of six sightlines per circle. An average sightline separation of $D_{\text{SL}} = 4.5 \text{ cMpc}$ is shown but the whole pattern might be rescaled to the desired sightline density. Sightlines outside the $16'$ diameter FoV (gray circle) are discarded (open points).

primordial abundances of 76 % (Coc et al. 2015). The temperature and velocity field are taken directly from the simulation box without any change.

4.2.2 Background Photoionization Rates

Apart from the ionizing radiation of the foreground quasar, we adopt a spatially uniform UV background. Oñorbe et al. (2017) presented an empirical relation for the cosmic mean transmitted H I flux $\langle F_{\text{HI}} \rangle$ fitted to existing measurements (Fan et al. 2006; Becker et al. 2007; Kirkman et al. 2007; Faucher-Giguère et al. 2008b; Becker et al. 2013) of the form

$$\tau_{\text{HI}} = 0.00126 \times e^{3.294 \times \sqrt{z}} \quad (4.4)$$

where $\tau_{\text{HI}} = \ln \langle F_{\text{HI}} \rangle$ denotes the effective optical depth and z the redshift. For simulation snapshot available at $z = 2.2, 2.5, 3.0, 3.5, 4.0, 4.5, 5.0$, we determine the mean transmission in a large set of random skewers and iteratively adjust the homogeneous H I UV background until the mean transmission matches the relation from Oñorbe et al. (2017). We interpolate these $\Gamma_{\text{UVB}}^{\text{HI}}$ values determined for the fixed redshifts using a cubic spline to obtain a smooth function $\Gamma_{\text{UVB}}^{\text{HI}}(z)$. This allows us to assign to each pixel the appropriate H I UV background matched to its redshift.

4.2.3 Foreground Quasar Photoionization Rates

Based on the the assumed M_{1450} magnitude of the foreground quasars and assuming the Lusso et al. (2015) template for the spectral energy distribution of the quasars, we compute the quasar luminosity L_ν , and from this the flux density F_ν at the background sightline according to

$$F_\nu = L_\nu \frac{1}{4\pi D_{\text{prop}}^2} e^{-\frac{D_{\text{prop}}}{\lambda_{\text{mfp}}}}. \quad (4.5)$$

Here, D_{prop} denotes the proper 3-D distance from the foreground quasar to a specific position at the background sightline and λ_{mfp} is the mean free path to H I ionizing photons. We ignore IGM absorption by setting $\lambda_{\text{mfp}} = \infty$, which is appropriate for the redshifts and scales we probe.⁶

⁶For $z_{\text{QSO}} \gtrsim 5$, λ_{mfp} becomes comparable to the size of the proximity region (Worseck et al. 2014) and IGM absorption can no longer be neglected.

We assume the quasar spectra to be of power-law shape $f_\nu \propto \nu^\alpha$ with slope $\alpha = -1.7$ beyond 912 Å (Lusso et al. 2015) and for simplicity also treat the spectral dependence of the hydrogen ionization cross-section as a power-law of form $\sigma_\nu \propto (\nu/\nu_0)^{-3}$. Using the cross-sections at the ionizing-edges σ_0 from Verner et al. (1996b) leads to the H I photoionization rate

$$\Gamma_{\text{QSO}}^{\text{HI}} = \int_{\nu_0^{\text{HI}}}^{\infty} \frac{F_\nu \sigma_\nu^{\text{HI}}}{h_{\text{P}} \nu} d\nu \approx \frac{F_{\nu_0^{\text{HI}}} \sigma_0^{\text{HI}}}{h_{\text{P}} (3 - \alpha)}, \quad (4.6)$$

where h_{P} denotes Planck's constant and ν_0^{HI} is the frequency of the H I ionization edge, i.e. 912 Å.

The photoionization of He II by the quasar might also have an effect on the thermal structure of the IGM (Bolton et al. 2009, 2010, 2012). However, proper treatment of this *thermal proximity effect* would require radiative transfer calculations (Meiksin et al. 2010; Khrykin et al. 2017) which is beyond the scope of this study.

Finite Quasar Age

The above calculation implicitly assumes isotropic emission and a quasar luminosity L_ν that is constant for all times. In this section, we relax the latter assumption and compute which part of the background sightlines are illuminated by a foreground quasar of a given finite age.

A background sightline at transverse distance R_\perp probes the foreground quasars emission at earlier times than the light we directly receive from the quasar (see e.g. Adelberger 2004; Kirkman & Tytler 2008; Furlanetto & Lidz 2011; Schmidt et al. 2017a, 2018a). This arises from the fact that the geometric path length from the foreground quasar to a location along the background sightline, and from there to the observer (as probed in absorption by the background sightline) is longer compared to the direct path from the foreground quasar to Earth. The total comoving path length is composed of the comoving distance from Earth to a point on the background sightline at redshift z and from there to the foreground quasar. The sum of both can be converted to a redshift z_{initial} and corresponding lookback time t_{initial} at which the ionizing radiation from the foreground quasar had to be emitted. This lookback time at emission can be compared to the lookback time corresponding to the redshift of the foreground quasar z_{QSO} . The difference is the additional time $\Delta t(z)$ it takes to first reach a certain point on the background sightline. If one neglects cosmic expansion (which we *do not do* in practice but do here for the sake of illustration), this simplifies to

$$\Delta t \approx \frac{a(z_{\text{QSO}})}{c} \left(\sqrt{R_\perp^2 + R_\parallel^2} + R_\parallel \right), \quad (4.7)$$

with R_\perp and R_\parallel denoting transverse and line-of-sight comoving separation from the quasar, c the speed of light, and $a(z_{\text{QSO}})$ the cosmic scale factor at the quasar redshift. Curves of constant time difference Δt are thus parabolas. In Figure 4.7 we give a detailed illustration of this behavior showing $\Delta t(R_\parallel)$ along four background sightlines that pass by a foreground quasar with transverse separations R_\perp between 1 cMpc and 16 cMpc.

Since any point on a background sightline probes the quasar luminosity at a (different) earlier time than we observe the quasar today, we have to specify a quasar lightcurve $L_\nu(t)$. For this we assume a simple lightbulb model of the form

$$L_\nu(t) = L_\nu^0 \times H(t + t_{\text{age}}) \times H(t_{\text{Q}} - t_{\text{age}} - t), \quad (4.8)$$

in which $L_\nu^0 = L_\nu(t = 0)$ is the currently observed quasar luminosity and the two $H(t)$ terms are Heaviside step functions to turn the quasar *on* and *off*. That is, we define the time at which the photons we observe today on Earth were emitted as $t = 0$. In this model, the

CHAPTER 4. MAPPING QUASAR LIGHT ECHOES IN 3D

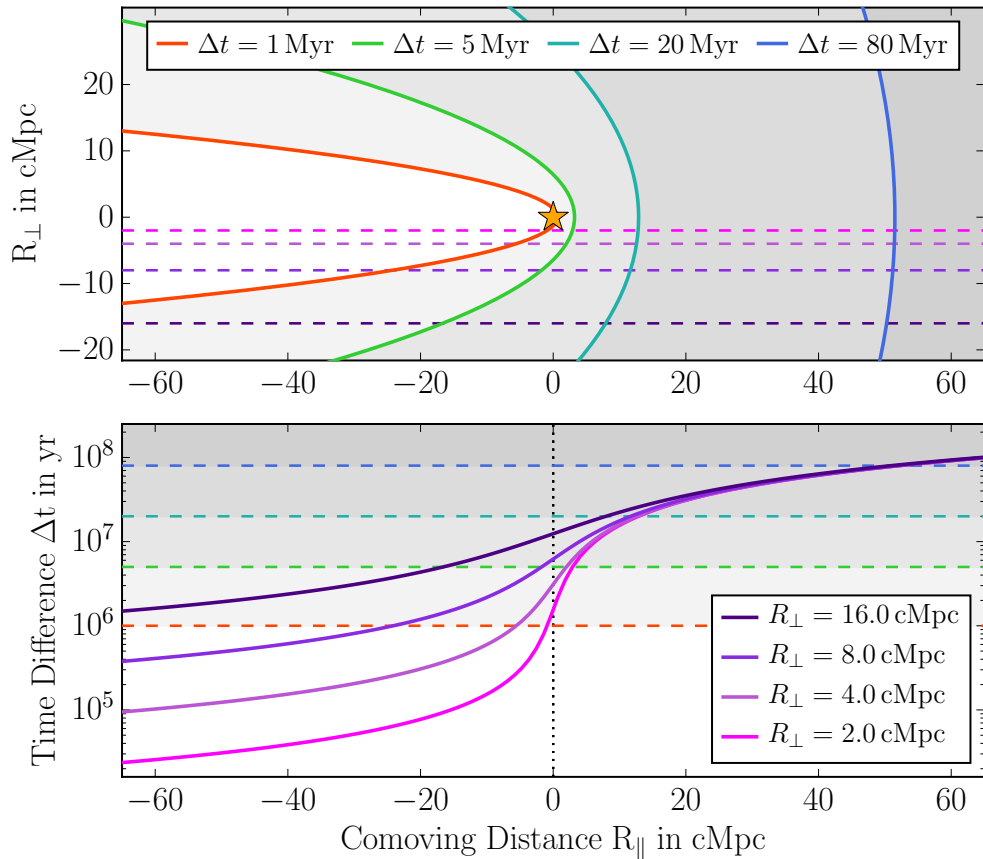


Figure 4.7: Visualization of the time difference Δt in a slice around a $z_{\text{QSO}} = 3.2$ quasar (top panel). Curves of constant time difference appear as parabolas with the quasar located in the focal point. For $t_{\text{age}} = \Delta t$, only the region left of the corresponding Δt curve appears to be illuminated. The bottom panel shows Δt along four sightlines that pass by the quasar at different transverse separations R_{\perp} . For $R_{\parallel} = 0$, the time difference equals the transverse light crossing time. In front of the quasar ($R_{\parallel} < 0$, $z < z_{\text{QSO}}$), all sightlines probe smaller time differences, but the exact value has a strong dependence on the transverse separation. Behind the quasar ($R_{\parallel} > 0$, $z > z_{\text{QSO}}$), Δt increases quickly with little dependence on R_{\perp} and approaches $\Delta t = 2 R_{\parallel} c^{-1}$.

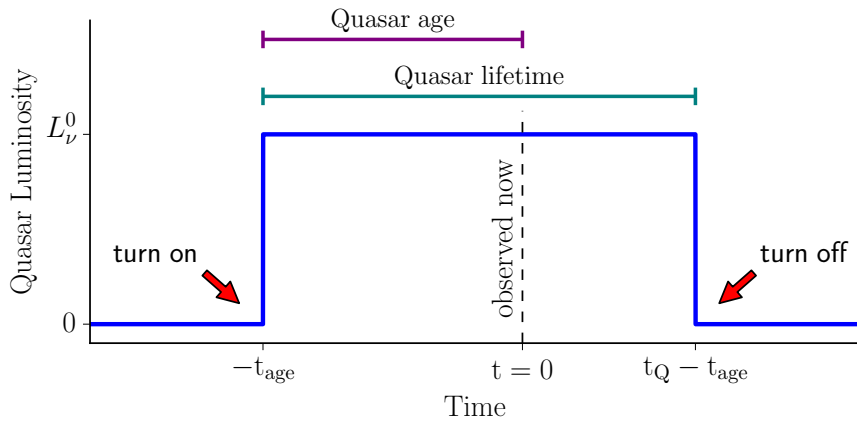


Figure 4.8: Visualization of the assumed quasar lightcurve.

quasar *turned on* at $t = -t_{\text{age}}$ and therefore we currently observe it at the age t_{age} . Its total lifetime is t_{Q} and it will *turn off* at time $t = t_{\text{Q}} - t_{\text{age}}$. Since we observe the quasar *on* today, $t_{\text{Q}} > t_{\text{age}}$ and *turn-off* will happen at some point $t > 0$, i.e. *in the future*. This diagram in Figure 4.8 illustrates these various times and aids visualization.

A certain point on a background sightline with time difference $\Delta t = \Delta t(R_{\perp}, R_{\parallel})$ probes $L_{\nu}(-\Delta t)$. Therefore, points on a background sightline for which $\Delta t < t_{\text{age}}$ appear for an observer on Earth to be illuminated by the foreground quasar. Since Δt increases monotonically along the line of sight, i.e. with R_{\parallel} or z (see Figure 4.7), all points at R_{\parallel} higher than the dividing line where $\Delta t = t_{\text{age}}$ appear not yet illuminated, simply because there was not enough time for the photons to reach these locations.

There is of course the possibility to assume different and probably more realistic quasar lightcurves. Ly α forest tomography should in principle be able to map the full emission history and able to constrain quasar variability over Myr timescales. For the moment however, we adopt the most basic lightbulb model and will explore the potential to constrain more complex quasar lightcurves in a future paper.

Quasar Obscuration

Contrary to the established AGN unification paradigm (e.g Antonucci 1993; Urry & Padovani 1995; Elvis 2000; Netzer 2015; Assef et al. 2013; Lusso et al. 2013; Padovani et al. 2017) which suggests that all quasars are obscured from some vantage points, for the purposes of this paper we assume that quasars emit isotropically. The method we present here is capable of determining the quasar emission history as well as the quasar emission geometry. However, modeling the quasar radiation e.g. like in Chapter 3 as a bi-conical emission pattern caused by an obscuring torus, adds a substantial amount of complexity to the analysis. Such a non-isotropic quasar emission model requires three more parameters, two angles θ and ϕ describing the orientation of the quasar emission cone or bi-cone, and an opening angle α setting the amount of obscuration or the opening angle of the emission cone(s). We will demonstrate in a future paper how these parameters can also be inferred from tomographic Ly α observations, but for the sake of simplicity focus here solely on quasar age and assume isotropic quasar emission.

4.2.4 Ionization State of Hydrogen

Based on the temperature T , velocity, and cosmic baryon density extracted from the Nyx simulation boxes, and adopting quasar and UV background photoionization rates as described above, we solve for the hydrogen ionization state. At the redshifts we have in mind for this experiment ($z < 5$), hydrogen in the IGM is highly ionized by the metagalactic UV background (e.g. Haardt & Madau 2012; Planck Collaboration et al. 2018). We therefore assume ionization equilibrium, and that the IGM instantaneously adjusts to a change in the photoionization rate. This is well justified since the equilibration timescale for H I at these redshifts is short, e.g. $\approx 10^4$ yr, compared to the timescales of interest.

For calculating the H I density n_{HI} we follow like in § 3.2.2 the approach described in Rahmati et al. (2013). We take the total ionization rate $\Gamma_{\text{tot}}^{\text{HI}}$ as the sum of photoionization $\Gamma_{\text{phot}}^{\text{HI}} = \Gamma_{\text{UVB}}^{\text{HI}} + \Gamma_{\text{QSO}}^{\text{HI}}$ and collisional ionization. For the photoionization we include the self-shielding prescription from Rahmati et al. (2013) in which the effective photoionization rate in high-density regions with $n_{\text{H}} \gtrsim 5 \times 10^{-3} \text{ cm}^{-3}$ is substantially reduced. For the collisional ionization we adopt the prescription by Theuns et al. (1998). We tie the fraction of helium in the He I and He II states to the hydrogen ionization state by simply assuming $n_{\text{HeII}}/n_{\text{He}} = n_{\text{HII}}/n_{\text{H}}$. Given the similar ionization energies, this is justified and a common assumption. We ignore the

CHAPTER 4. MAPPING QUASAR LIGHT ECHOES IN 3D

double ionization of helium for this study, i.e. assuming $n_{\text{HeIII}} = 0$, since it adds unnecessary complications and has no substantial effect on the results. We adopt the Case A recombination coefficients from [Storey & Hummer \(1995\)](#). This is appropriate since H I is highly ionized and the IGM optically thin on the relevant scales. With these inputs, the hydrogen ionized fraction can be easily computed.

4.2.5 Computing Synthetic Spectra

After determining n_{HI} along the skewers as stated above, the next step in our modeling procedure is to create synthetic spectra. For each pixel along the skewers we compute an individual Voigt absorption line profile with appropriate strength, line width and velocity shift corresponding to the physical conditions in that pixel. Oscillator strengths are taken from [Verner et al. \(1996a\)](#). We benefit here from the high resolution of the NYX box (36 cMpc or 2.8 km s^{-1}) which is sufficient to resolve the Ly α forest ($\approx 7.6 \text{ km s}^{-1}$). Redshift space distortions (peculiar velocities) are included by displacing the absorption profile with the line-of-sight velocity from the NYX simulation. Thermal broadening is computed according to $\sigma_{\text{th}} = \sqrt{\frac{k_{\text{B}} T}{m_{\text{H}}}}$ for the Doppler broadening with T denoting the gas temperature in a pixel and m_{H} the atomic mass of hydrogen. The Lorentzian scale parameter is based on the transition probability from [Verner et al. \(1996a\)](#). The final transmission spectrum at a pixel in redshift space is the combination of all absorption profiles along a skewer.

4.2.6 Error Forward Model

Finally, we degrade these idealized spectra to account for observational effects by forward modeling finite spectral resolution, continuum errors, and photon-counting and instrumental noise.

Resolution

We convolve the spectra with a Gaussian line spread function of appropriate width to simulate finite resolution of the spectrograph utilized, parametrized by its resolving power R . We also rebin the spectra in chunks of 1 cMpc, which results in Nyquist sampling for resolving powers $R < 2000$.

Adding Noise to the Spectra

We add random Gaussian noise to the rebinned spectra to mimic the desired S/N ratio. As already stated in § 4.1.4, we specify the signal to noise per $R = 1000$ or 300 km s^{-1} resolution element to keep the S/N measure independent of spectral resolution. The actual S/N per pixel will be lower by \sqrt{N} , with N denoting the number of bins or pixels that sample a 300 km s^{-1} chunk of a spectrum.⁷ This procedure makes the exposure time required to reach a certain S/N₁₀₀₀ (approximately) independent of the adopted spectral resolution.

Continuum Error

In addition to a random uncertainty per pixel due to photon-counting and instrumental noise, there is a more systematic effect related to uncertainties in the continuum fitting. This effect could have a potentially severe impact on the measured Ly α forest transmission and therefore

⁷For extremely low spectral resolution, N might be < 1 and the S/N per pixel in fact higher.

4.3. SIMULATED OBSERVATIONS OF QUASAR LIGHT ECHOES

on the reconstruction of the quasar light echo. Thus, we forward model continuum fitting uncertainties following the description given in [Krolewski et al. \(2018\)](#). Our final forward modeled Ly α transmission is therefore of the form

$$F_{\text{obs}} = \frac{F_{\text{true}} + \delta_1}{1 + \delta_2} \quad (4.9)$$

where F_{true} is the simulated transmission while δ_1 and δ_2 are random Gaussian deviates with zero mean and standard deviations σ_1 and σ_2 . The first term δ_1 is related to the photon-counting and instrumental noise already mentioned above and drawn for each 1 cMpc bin individually. The standard deviation σ_1 is related to the desired S/N₁₀₀₀ and for 1 cMpc wide bins at $z_{\text{QSO}} = 3$ approximately

$$\sigma_1 \approx \frac{1.98}{\text{S/N}_{1000}}. \quad (4.10)$$

The second term δ_2 corresponds to the continuum uncertainty and is identical for all bins along the same background sightline. Following [Lee \(2012\)](#), [Krolewski et al. \(2018\)](#) presented an empirical relation for the continuum uncertainty as function of the S/N of the data. Converting the given relation to the sampling used in this study we obtain

$$\sigma_2 = \frac{0.409}{\text{S/N}_{1000}} + 0.015 \quad (4.11)$$

which we will use throughout this study to model continuum uncertainties.

4.3 Simulated Observations of Quasar Light Echoes

In what follows, we briefly discuss the results of our simulations and try to build some intuition about the appearance of the H I quasar proximity effect in 3D. In [Figure 4.9](#) we show a two-dimensional slice through our simulation box. The quasar has a redshift $z_{\text{QSO}} = 3.2$ and an apparent magnitude of $r = 17$ mag, corresponding to $M_{1450} = -28.5$ mag. Without the foreground quasar, the IGM has a mean transmission of $\approx 70\%$, however with substantial scatter ($\approx 15\%$ on 4 cMpc scales) around this value due to cosmic density fluctuations. The ionizing radiation of the quasar increases the ionization state of hydrogen and pushes the H I transmission to nearly 100% in its immediate vicinity. Even out to larger scales of several tens of megaparsec, a clear enhancement in the H I Ly α forest transmission is visible. The region of enhanced Ly α transmission has a clear boundary towards higher redshift (positive R_{\perp} , right in [Figure 4.9](#)), caused by the finite speed of light and the finite age of the quasar. The parabolic shaped surface corresponding to a path length difference of $\Delta t = t_{\text{age}} = 10$ Myr marks the boundary between the illuminated and non-illuminated region. For all points to the right (higher redshift, larger R_{\perp}), the quasar does not shine long enough to make these region appear illuminated for an observer on Earth.

However, while the sharp boundary of the quasar light echo exists in real space, this will not be the case in redshift space. A comparison of the top two panels in [Figure 4.9](#) illustrates the impact of redshift space distortions on the light echo structure. The large-scale velocity field displaces the apparent position of absorption features in a non-trivial way and causes the quasar light echo to be in some regions less and in some regions more extended in redshift space than in real space. This spatial distortion is related to the large-scale density field, since these density fluctuations source the bulk velocity flows. This can most easily be seen close to a large overdensity behind the quasar (at $R_{\perp} \approx 12$ cMpc, upper half of the plot) that appears to drag the quasar light echo to the right towards the overdensity.

In principle, Ly α forest tomography delivers a map of the large-scale density structure, which might allow one to derive a model of the peculiar velocities and remove at least some part

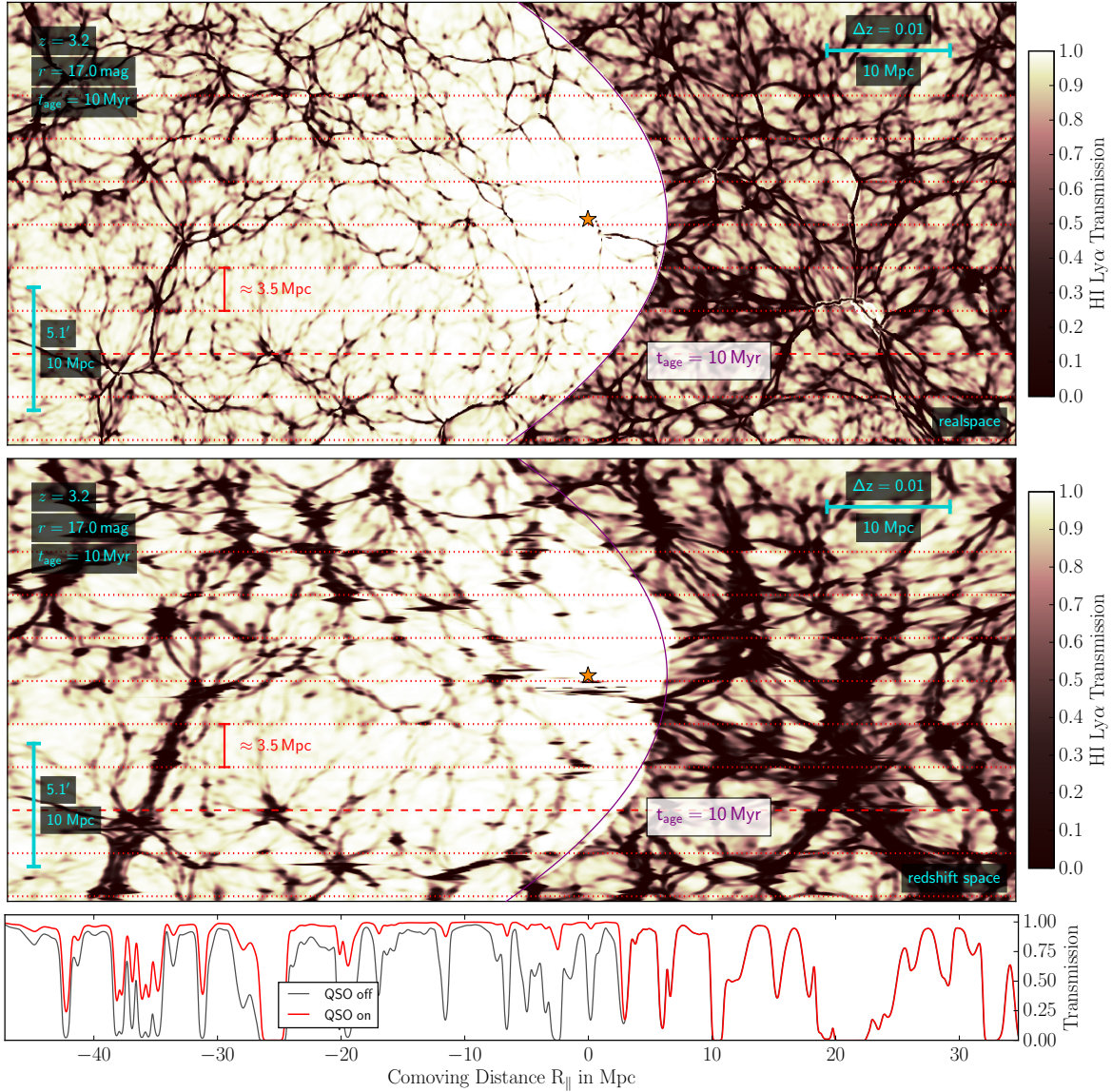


Figure 4.9: Visualization of the quasar proximity effect. The plot shows the H I Ly α transmission in a slice through the simulation box. The snapshot of the hydrodynamical simulation was postprocessed with a photoionization model of a $z_{\text{QSO}} = 3.2$ foreground quasar with an r -band magnitude of $r = 17$ mag, corresponding to $M_{1450} = -28.5$ mag that does shine for 10 Myr. The top panel shows the situation in realspace, i.e. ignoring redshift space distortions and displaying directly the H I transmission in each pixel without convolving with a line profile. Therefore, the region with enhanced transmission has exactly parabolic shape. The panel below displays the same but in redshift space. Here, peculiar velocities and the thermal broadening of the absorption lines was properly taken into account, which distorts the region of enhanced transmission and *blurs* the overall picture. The bottom panel shows a computed mock spectrum along the red dashed sightline, once including the photoionization of the foreground quasar and once based solely on the photoionization of the metagalactic UV background. No binning was applied to the data and no noise or continuum errors added. A tomographic observation would probe the quasar proximity region with numerous background sightlines, on average spaced by e.g. ≈ 3.5 cMpc (red dotted lines).

4.3. SIMULATED OBSERVATIONS OF QUASAR LIGHT ECHOES

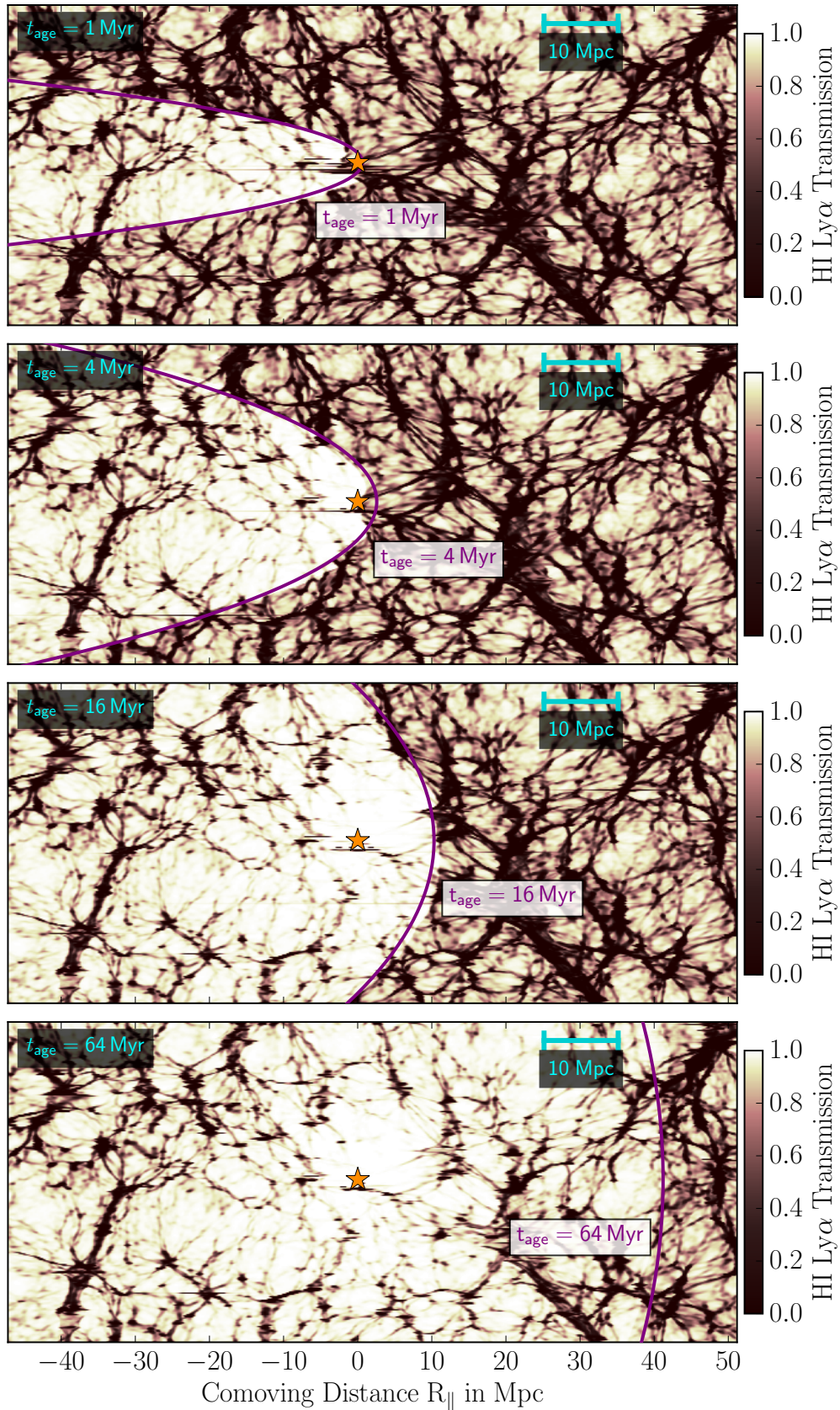


Figure 4.10: Appearance of the HI proximity effect for four different quasar ages. The panels are similar to Figure 4.9 and display redshift space. The sequence of plots clearly visualizes how the illuminated region expands with increasing quasar age into the IGM. For $t_{\text{age}} = 64 \text{ Myr}$, the quasar light echo blends with the surrounding IGM, making it difficult to determine the extend of the proximity zone.

CHAPTER 4. MAPPING QUASAR LIGHT ECHOES IN 3D

of these distortion from the tomographic map. However, due to the complex nature of the redshift space distortion, we do not undertake such a reconstructions here. Peculiar velocities will therefore result in a form of correlated noise for the characterization of quasar light echoes.

We quantify the amount of redshift space distortions in the map shown in Figure 4.9 and find that the distribution of line-of-sight velocities is approximately Gaussian with a standard deviation of 125 km s^{-1} . This corresponds to a FWHM of 295 km s^{-1} or 3.75 cMpc at $z_{\text{QSO}} = 3.2$. Although redshift space distortions are correlated and not directly comparable to the effects of finite spectral resolution, one can already see that the line-of-sight velocities correspond approximately to a resolving power $R = \frac{\lambda}{\Delta\lambda} \approx 1000$. Taking observations with substantially higher spectral resolution should therefore be of little benefit. We explore this dependence more thoroughly in §4.5.6.

In Figure 4.10 we illustrate the time evolution of the proximity zone. Here, we again show the same slice through the simulation box as in Figure 4.9 but compute the ionization state and Ly α forest transmission for different quasar ages between $t_{\text{age}} = 1 \text{ Myr}$ and 64 Myr . This demonstrates how the quasar light echo expands into the IGM and how an increasingly large region around the quasar appears to be illuminated from Earth.

4.3.1 IGM Transmission Statistics

In Figures 4.11 we illustrate the flux probability distribution of the pixels within our tomographic map. For three background sightlines at transverse separations of $R_{\perp} = 2.5, 7.5$ and 15 cMpc we show the expected median transmission in 4 cMpc wide bins as well as the

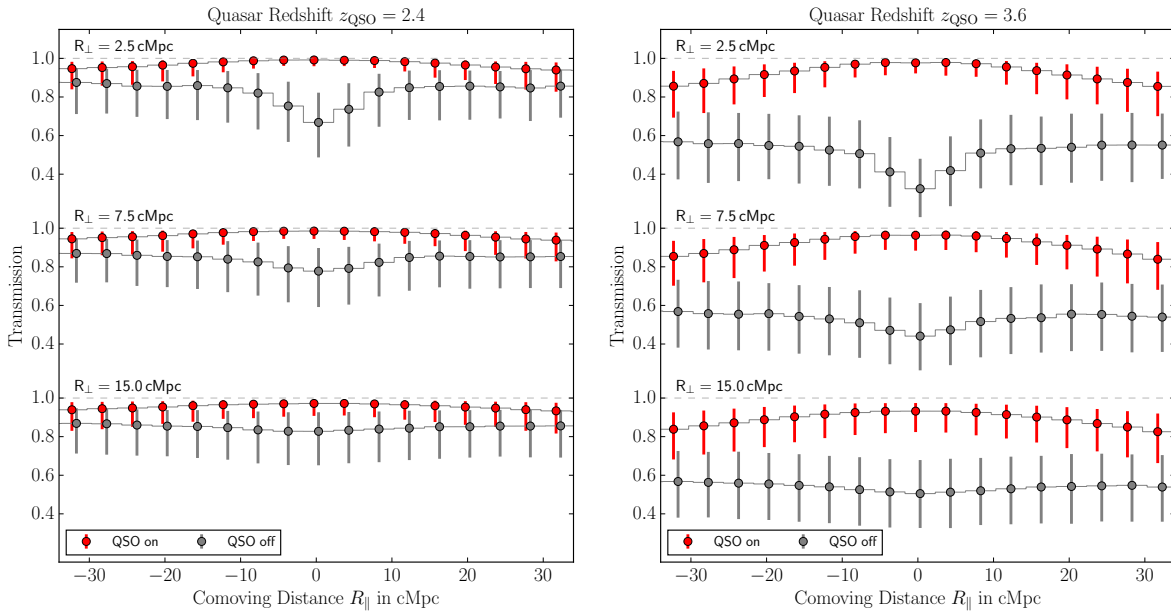


Figure 4.11: Average IGM transmission measured in 4 cMpc wide bins along background sightlines with transverse separations of $R_{\perp} = 2.5, 7.5$ and 15 cMpc from an $M_{1450} = -28.7 \text{ mag}$ foreground quasar. The left panel shows the situation at $z_{\text{QSO}} = 2.4$, while the right displays $z_{\text{QSO}} = 3.6$. For each bin we show the case in which the sightlines are fully illuminated by the foreground quasar and the unilluminated case in which photoionization stems solely from the metagalactic UV background. Close to the foreground quasar, excess absorption is visible due to the cosmic overdensity in which the quasar resides. Errorbars indicate the 16th–84th percentile interval of the expected IGM absorption in each bin, not including any observational noise. Since the transmission is bounded at 100%, the distributions in particular the for illuminated sightlines are highly skewed with the bulk of the distribution located at very high transmission values.

4.4. INFERRING PARAMETERS FROM QUASAR LIGHT ECHOES

16th–84th percentile region. At low redshift ($z_{\text{QSO}} = 2.4$; Figure 4.11 left) it is difficult to determine if a specific part of a background sightline is illuminated by the quasar. Although the ionizing radiation from the foreground quasar dominates over the UV background, the expected median transmission for the illuminated case overlaps with the 84th percentile of the distribution for the unilluminated case in nearly all R_{\parallel} bins. A significant difference between illuminated and unilluminated case exists only very close to the quasar ($|R_{\parallel}| < 10$ cMpc and $R_{\perp} = 2.5$ cMpc or 7.5 cMpc) where the cosmic overdensity of the host halo causes in absence of the quasars ionizing radiation excess absorption whereas the transmission is ≈ 1 if the quasar illuminates this region. Therefore, it will be very challenging to detect and characterize quasar light echoes at such low redshifts.

The situation substantially improves at higher redshift. At $z_{\text{QSO}} = 3.6$ (Figure 4.11 right), the mean IGM transmission drops below 60 % while the expected transmission in the illuminated case remains basically the same and still reaches > 85 % for $|R_{\parallel}| < 30$ cMpc. Given that the IGM scatter only slightly increases, the 16th–84th percentile regions of the two distributions have basically no overlap and one can in principle for any individual bin along a background sightline infer with high confidence if that bin is illuminated by the foreground quasar. This higher contrast between illuminated and unilluminated parts of the IGM at high redshift makes a detection of the proximity effect far easier than at low redshift, however at the expense of reduced background sightline density (see Figure 4.5).

4.4 Inferring Parameters from Quasar Light Echoes

Inferring quasar properties from tomographic observations requires a statistical comparison of the observed data to a set of models. The analysis scheme we develop for this task has to be able to cope with several challenges.

First, it has to combine and jointly fit the information from all transmission measurements along all background sightlines. This can, depending on the quasar redshift and limiting magnitude of the observations, result in up to twenty thousand individual measurements per tomographic map.

Second, the statistical analysis has to keep track of the correlations between individual measurements and cope with the intrinsically non-Gaussian transmission distributions in individual bins. This is of particular concern in the illuminated parts of the background sightlines which have transmissions close to 100 % (see Figure 4.11). Also, the measured IGM transmission has a very non-linear behavior with respect to the model parameters. Roughly speaking, it switches for a given spatial position between two binary states, depending on whether this part of the sightline is illuminated by the foreground quasar or not.

Third, we require the analysis to be fully Bayesian. This will allow us to deduce posterior probabilities for the inferred parameters and to determine meaningful confidence intervals. Additionally, it is desirable to have an analysis method that can handle degeneracies between model parameters. This is technically not necessary in the current situation since we focus on inferring a single parameter, the quasar age, but our goal for the future is to generalize the modeling and inference to enable joint fits for quasar age, quasar orientation, and quasar obscuration. Particularly for short quasar age and high obscuration, one expects significant degeneracies between parameters.

Our approach to solve the issues outlined above using a set of dedicated models of the proximity effect and a Bayesian approach employing so called *likelihood free inference*.

CHAPTER 4. MAPPING QUASAR LIGHT ECHOES IN 3D

4.4.1 Transmission Probability Distribution Functions

For a given foreground quasar (z_{QSO}, M_{1450}), proximity effect models are created as described in § 4.2, based on outputs of a cosmological hydrodynamical simulation and postprocessed with a quasar photoionization model. We compute a model grid in t_{age} that spans from 0.7 Myr to 128 Myr with 16 logarithmically spaced values of t_{age} . For each of these models, we create 100 different model realizations which have the same quasar properties (i.e. $t_{\text{age}}, M_{1450}, z_{\text{QSO}}$) and employ the same sightline pattern (illustrated in Figure 4.6) but are centered on different host halos and therefore have different IGM density, velocity and temperature structure. These 100 independent model realizations are necessary to properly characterize the stochasticity of the IGM absorption. We forward model observational effects like finite spectral resolution, signal to noise ratio and continuum fitting errors to make the model outputs directly comparable to observed spectra. Each spectrum extends for ± 65 cMpc around the foreground quasars position and we bin the spectra in chunks of 1 cMpc length.

For each chunk we obtain a kernel density estimate (KDE) of the probability distribution (PDF) of the transmission values in the chunk based on the 100 independent realizations of that model. This results in smooth functions, $p(F_{n,m} | \Theta)$, that describe the probability for measuring an IGM transmission $F_{n,m}$ in bin n, m , given the model parameter Θ . Here, the index n identifies the different background sightlines within the sightline pattern while m denotes a certain chunk along the sightline. As long as we only focus on the quasar age, the parameter vector Θ has only one component $\Theta = \{t_{\text{age}}\}$. However, we still denote it as a vector since this approach allows for easy and straight-forward generalization of the inference to additional parameters like quasar obscuration or orientation. Following this, each model of the HI proximity effect is fully described by a set of transmission probability functions $\mathcal{M}^\Theta = \{p(F_{n,m} | \Theta)\}$.

4.4.2 Likelihood Computation

Due to the high dimensionality of the observable, $\mathbf{F} = \{F_{n,m}\}$, i.e. several thousand individual transmission measurements, determining the likelihood $\mathcal{L} = p(\mathbf{F} | \Theta)$ poses a very challenging task. The usual approach of approximating the likelihood as a multi-variate Gaussian is inadequate for our problem since the individual transmission PDFs are not well described by Gaussians. In addition, determining the significant correlations between all the elements of $\{F_{n,m}\}$ would likely require an excessive number of model realizations. Therefore, we follow a likelihood free approach for which we never have to actually write down an analytic form for the likelihood function.

In Chapter 3 we solved a similar problem. There however, the dimensionality of the problem was low (at most three transmission measurements and two model parameters) which made it feasible to simply map the full likelihood space by brute-force sampling. An approach like this would be completely impossible for our current case. A fully Bayesian treatment is only achievable if the dimensionality of the problem can be drastically reduced. We do this by first computing a so called *pseudo-likelihood* which acts in many ways like a proper likelihood except that it ignores correlations between the $\{F_{n,m}\}$. In a second step, we then map this *pseudo-likelihood* to a proper posterior probability distribution. Our approach is in many ways inspired by Alsing et al. (2018) and Davies et al. (2018), but is customized to the problem at hand and is in many ways different from either of these strategies.

For a given set of observed IGM transmissions \mathbf{F} , we define the *pseudo-likelihood* \mathcal{L}' as

$$\mathcal{L}'(\mathbf{F} | \Theta) = \prod_{n,m} p(F_{n,m} | \Theta). \quad (4.12)$$

4.4. INFERRING PARAMETERS FROM QUASAR LIGHT ECHOES

Therefore, we evaluate the transmission probability function of each chunk at the observed transmission level $F_{n,m}$, and compute the product of these probabilities. If the individual bins were uncorrelated, this pseudo-likelihood would indeed represent the true likelihood function. However, since this is in general not true, the pseudo-likelihood will not result in the correct parameter uncertainties and may also produce biased results.

We therefore only use it to find a parameter vector $\hat{\Theta}$ that maximizes this *pseudo-likelihood* \mathcal{L}' . This acts as a data compression and reduces the dimensionality of the data (up to several thousand) to the dimensionality of the model parameter space (a few or in our current case only one, i.e. t_{age}). During this process, some information might be lost, however, $\hat{\Theta}$ does retain the essence of information contained in the data and an approach like this has been proven to be a rather efficient and successful data compression algorithm (Davies et al. 2018).

Since we only have models available for a set of discrete Θ values, the maximization process described above requires interpolation between models. We do this by interpolating the logarithm of the transmission probabilities, $\log(p(F_{n,m}|\Theta))$, evaluated at the specific observed value of $F_{n,m}^{\text{obs}}$, using a simple quadratic interpolation scheme.

Compressing the dimensionality of the observable to the dimensionality of the model as described above now allows a fully Bayesian treatment of the problem. This requires that we determine the mapping between our summary statistic $\hat{\Theta}$ and the true parameter vector Θ , which means we require the conditional probability distribution $p(\Theta|\hat{\Theta})$. The technical feasibility of this approach was presented by Alsing et al. (2018), however based on a different data compression scheme. Using Bayes' theorem, the conditional probability distribution $p(\Theta|\hat{\Theta})$ can be written as

$$p(\Theta|\hat{\Theta}) = \frac{p(\hat{\Theta}|\Theta)p(\Theta)}{p(\hat{\Theta})}. \quad (4.13)$$

Here $p(\Theta)$ is our prior on the model parameters, which we here assume to be flat in $\log(t_{\text{age}})$, and $p(\hat{\Theta})$ is the evidence, which is basically just a normalization. Since we have a generative model that can create mock data realizations for a given parameter set Θ , we can relatively easily determine $p(\hat{\Theta}|\Theta)$. The low dimensionality of the problem, only 1 + 1, makes it computationally feasible to approximate this distribution by simply computing samples. In practice, we draw 1600 parameters values Θ from the prior $p(\Theta)$, compute model realizations for these values that yield the mock measurements $\{F_{n,m}\}$, and straightforwardly determine $\hat{\Theta}$ for each realization. The latter is done by evaluating the transmission probabilities $\mathcal{M}^{\Theta} = \{p(F_{n,m}|\Theta)\}$ for each of the 1600 mock realization $\{F_{n,m}\}$, computing the *pseudo-likelihood* in Equation 4.12, and finding the value $\hat{\Theta}$ that maximizes it.

The resulting distribution of the 1600 samples in $(\hat{t}_{\text{age}}|t_{\text{age}})$ space is shown in Figure 4.12. As one can see, most samples are located relatively close to the 1:1 relation. Clearly, the $\{\hat{t}_{\text{age}}\} = \hat{\Theta}$ that maximizes the *pseudo-likelihood* \mathcal{L}' is a good proxy for the maximum of the true likelihood \mathcal{L} . The width of the distribution around the 1:1 relation is a measure for the width of the posterior and therefore the uncertainty in the parameter estimate.

We note however, that in addition to this general scatter around the 1:1 relation, there are some outliers and artifacts in the distribution. For $z_{\text{QSO}} < 3$, where our method is less sensitive (see Figure 4.11), the *pseudo-likelihood* maximizer has the tendency to run towards the upper boundary of the grid at $\hat{t}_{\text{age}} = 128$ Myr. This effect happens mostly at low redshift (high mean IGM transmission) and long quasar ages. However, this issue quickly disappears for $z_{\text{QSO}} \geq 3$ and has in general very little impact on our analysis. Also, the \mathcal{L}' maximizer has a slight tendency to pick \hat{t}_{age} values that lie exactly on the model grid. This behavior is related to the relatively simple interpolation scheme we use for interpolation between the discrete models. Using a more sophisticated interpolator (e.g. Gaussian process interpolation, Habib et al. 2007; Walther et al. 2018a,b.) would likely eliminate this issue. For now however, we

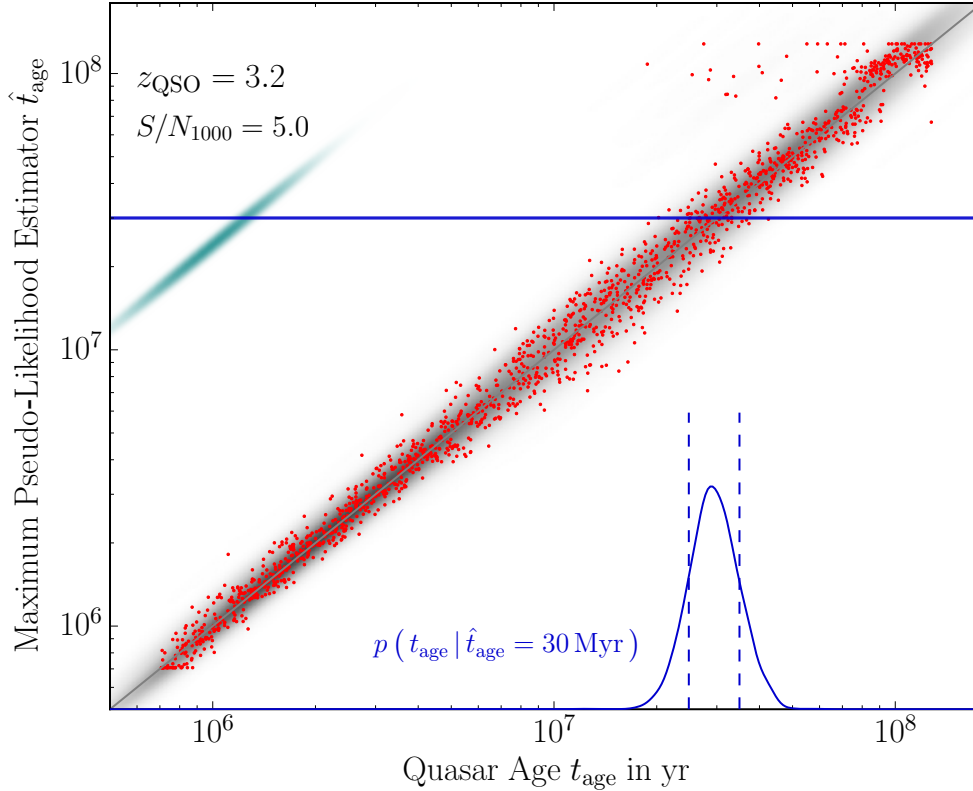


Figure 4.12: Mapping from maximum *pseudo-likelihood* parameter \hat{t}_{age} to true posterior probabilities, based on 1600 model realizations (red points). These samples are converted to a smooth distribution (gray) by means of a KDE. The utilized kernel is shown in green in the top-left corner. In blue, we illustrate the procedure to obtain posterior probabilities. The $p(\hat{t}_{\text{age}} | t_{\text{age}}) p(t_{\text{age}})$ distribution is sliced at $\hat{t}_{\text{age}} = \hat{t}_{\text{age}}^{\text{obs}}$ (here 30 Myr) and re-normalized. The resulting posterior probability $p(t_{\text{age}} | \hat{t}_{\text{age}} = \hat{t}_{\text{age}}^{\text{obs}})$ is shown in the bottom right. Confidence intervals (16th and 84th percentile) are indicated with dashed lines.

monitor this behavior and ensure that, even if this artifact appears in our mapping procedure, it does not negatively impact our mapping.

To derive proper posterior probabilities, we require a smooth and continuous version of the $p(\hat{t}_{\text{age}} | t_{\text{age}}) p(t_{\text{age}})$ distribution. We therefore apply a kernel density estimate to the 1600 computed samples which yields slightly better results than a Gaussian mixture model employed by Alsing et al. (2018). We show the resulting interpolated distribution as gray shading in Figure 4.12. Note that the conditional probability $p(\hat{t}_{\text{age}} | t_{\text{age}}) p(t_{\text{age}})$ is nothing else than the joint probability $p(\hat{t}_{\text{age}}, t_{\text{age}})$. Slicing this now smooth distribution at a specific value of $\hat{t}_{\text{age}} = \hat{t}_{\text{age}}^{\text{obs}}$ and re-normalizing the result to unity, finally yields the proper posterior probability $p(t_{\text{age}} | \hat{t}_{\text{age}} = \hat{t}_{\text{age}}^{\text{obs}})$.

Having set up our transmission probabilities $\mathcal{M}^{\Theta} = \{p(F_{n,m} | \Theta)\}$ for a set of discrete values of Θ and then determining the posterior $p(\Theta | \hat{\Theta})$ via the procedure described above, we can for any simulated mock or observed IGM transmission $\mathbf{F} = \{F_{n,m}\}$ first determine the parameter vector $\hat{\Theta}$ that maximizes the *pseudo-likelihood* \mathcal{L}' and then convert this into a proper posterior probability $p(\Theta | \mathbf{F})$. In this way, we have a powerful and computationally feasible method to derive posterior probabilities in a fully Bayesian way that includes all effects related to correlations and non-Gaussianities without the requirement to write-down a likelihood function. It is simply based on the fact that we have a generative model capable of completely forward modeling mock observations.

4.5 Results

In the following, we will present which constrains Ly α forest tomography can impose on the quasar age. To validate that our complex statistical analysis works as expected, we will create mock observations, analyze these with the fitting scheme described above and derive realistic posterior probabilities. Furthermore, we will conduct an extensive parameter study to explore how the precision of the inferred t_{age} depends on the properties of the foreground quasar, namely its redshift z_{QSO} and UV luminosity M_{1450} , as well as the observational setup. The latter is defined by the spectral resolution R , the covered field-of-view and the limiting magnitude r_{lim} for achieving the desired S/N₁₀₀₀ in a given exposure time. In consequence, these parameters also define the average sightline density D_{SL} and the number of sightlines N_{SL} that will probe the proximity region of the foreground quasar. Determining the dependencies between these various parameters will be essential for choosing the optimal survey strategy for this project.

4.5.1 Simulation Grid

We create models of the 3D proximity effect for foreground quasar with redshifts ranging from $z_{\text{QSO}} = 2.4$ to $z_{\text{QSO}} = 5.0$ in steps of $\Delta z_{\text{QSO}} = 0.2$. The fiducial setup assumes a limiting magnitude of $r_{\text{lim}} = 24.7$ mag. For background sources of this brightness, existing multi-object spectrographs on 8–10 m class telescopes (e.g. VLT / FORS II or Keck / DEIMOS) should in good conditions achieve a S/N₁₀₀₀ = 5 in 10 ks (see Figure 4.4 in § 4.1.4). As shown in Figure 4.5, the same limiting magnitude corresponds, depending on the foreground quasar redshifts, to different average sightline separations D_{SL} . In Table 4.2, we list the adopted values together with the number of background sightlines N_{SL} that fall into our 16' diameter FoV. We adopt the sightline pattern shown in Figure 4.6. Table 4.2 also lists the adopted luminosity M_{1450} of the brightest available quasars at these redshifts (see Figure 4.2).

For each of the models in Table 4.2, we randomly select $N_{\text{Halo}} = 100$ halos from the simulation box which define 100 independent sets of temperature, density and line-of-sight velocity along the background skewers. Each sightline pattern created in the above way is then processed with our photoionization model as described in § 4.2, assuming 16 different quasar ages $t_{\text{age}} = \{0.7, 1.0, 1.4, \dots, 128\}$ Myr, corresponding to $2^{\{-0.5, 0.0, 0.5, \dots, 7.0\}}$ Myr. The background sightline spectra extend from $-65 \text{ cMpc} < R_{\parallel} < 65 \text{ cMpc}$ and are binned in chunks of 1 cMpc length, resulting in 131 independent transmission measurements per sightline. This defines for each model listed in Table 4.2 and each t_{age} a set of transmission probabilities $\mathcal{M}^{t_{\text{age}}} = \{p(F_{n,m} | t_{\text{age}})\}$.

To realize the mapping from \hat{t}_{age} to $p(t_{\text{age}} | \hat{t}_{\text{age}})$ as shown in Figure 4.12, we compute a second set of models adopting the same parameters as listed in Table 4.2. However, instead of simulating 16 discrete t_{age} values for 100 IGM realizations, we compute 1600 realizations for which we draw t_{age} randomly from our prior and pair it with a randomly selected halo above the minimum halo mass. As stated in § 4.4.2, we adopt a prior that is flat in $\log(t_{\text{age}})$.

For validation of our method, we create a set of models that act as mock observations. For these we adopt quasar ages $t_{\text{age}} = \{1.0, 2.0, 4.5, 9.0, 20.0, 45.0, 80.0\}$ Myr and choose random halos above the minimum halo mass. All other parameters are identical to the ones listed in Table 4.2. For each quasar age, we compute 25 different IGM realizations. All models described above are post-processed to mimic a desired spectral resolution (usually $R = 1000$), signal to noise ratio (e.g. S/N₁₀₀₀ = 5) and continuum uncertainties (see § 4.2.6).

After computing the various kinds of models, we have everything together for an end-to-end test of our method. For this, we apply the statistical analysis to the the mock observations and infer posterior probabilities for t_{age} , following the procedures described in § 4.4.

CHAPTER 4. MAPPING QUASAR LIGHT ECHOES IN 3D

Table 4.2. Parameter of the Main Simulation Grid.

z_{QSO}	M_{1450} mag	r_{lim} mag	D_{SL} cMpc	FoV '	N_{SL}	R	S/N ₁₀₀₀
2.4	-28.7	24.7	1.62	16	216	1000	5.0
2.6	-28.9	24.7	1.87	16	168	1000	5.0
2.8	-29.0	24.7	2.22	16	126	1000	5.0
3.0	-29.0	24.7	2.54	16	90	1000	5.0
3.2	-29.0	24.7	2.91	16	90	1000	5.0
3.4	-28.8	24.7	3.47	16	60	1000	5.0
3.6	-28.7	24.7	4.24	16	36	1000	5.0
3.8	-28.6	24.7	5.02	16	36	1000	5.0
4.0	-28.5	24.7	5.82	16	18	1000	5.0
4.2	-28.3	24.7	6.79	16	18	1000	5.0
4.4	-28.2	24.7	8.76	16	18	1000	5.0
4.6	-28.1	24.7	12.03	16	6	1000	5.0
4.8	-27.9	24.7	14.31	16	6	1000	5.0
5.0	-27.8	24.7	16.81	16	6	1000	5.0

Note. — Parameters are chosen to keep the total observing time approximately constant, e.g. 3×10000 ks with VLT / FORS II or Keck / DEIMOS.

In this fitting process, we assume perfect knowledge of the foreground quasar redshift and do not include any uncertainties on this quantity. Given the overall expense of the tomographic observations and the extreme luminosity of the foreground quasar, it would in reality only add insignificant additional effort to obtain highly-precise redshift estimates e.g. from the [O III] line ($\Delta z \leq 100 \text{ km s}^{-1}$) using infrared spectroscopy or alternatively CO or [C II] 158 μm fine-structure lines ($\Delta z \leq 50 \text{ km s}^{-1}$) in the sub-mm regime.

We also assume perfect knowledge about the UV background and the quasars ionizing emissivity. This means in practice that the models we use for fitting have exactly the same mean transmission and quasar ionizing emissivity as the mock observations. The mean IGM transmission is relatively well known (to better than 2%, Becker et al. 2013) and the uncertainties probably dominated by the statistical fluctuations within the map. The quasar luminosity in the non-ionizing UV (m_{1450}) is directly observable and should be known to very high precision. The extrapolation from there to the ionizing regime adds some uncertainty due to the a prior unknown quasar SED. However, variations in the quasar spectral slope relate to only moderate uncertainties in the ionizing flux, e.g. about 13% based on Lusso et al. (2015). In addition, we would preferentially select target quasars that have confirmed flux beyond the Lyman limit ($\lambda_{\text{rest}} = 912 \text{ \AA}$), which could give additional constraints on the quasar SED. In the future, we anyway intend to include the (possibly time dependent) quasar luminosity in the analysis procedure and fit for the quasar ionizing flux.

4.5.2 Example Posteriors

A set of posterior probabilities derived in the described way for a model with $z_{\text{QSO}} = 3.6$ are shown in Figure 4.13. The figure clearly shows that our method works well and yields satisfying estimates for the quasar age. The posterior probabilities are localized and in the right place. In most of the cases, the true t_{age} value is well within the extent of the confidence interval (16th – 84th percentile) and there are very few cases in which the derived t_{age} estimate deviates

substantially from the true value. Averaging the 25 individual posterior probabilities of each model gives an estimate of the achieved accuracy. This also shows that our method yields unbiased results. A slight exception from this might be the 80 Myr case, which approaches the highest quasar ages that can be constrained with Ly α forest tomography. At such long t_{age} , as can be seen in Figure 4.10, the edge of the proximity region starts to blend smoothly with the IGM and the proximity region extends far beyond the adopted 16' FoV. The exact behavior depends however on the luminosity of the quasar and the mean transmission of the IGM and therefore redshift. Also note that the cut-off of the posterior probabilities towards high t_{age} might to some degree be artificial since our model grid only extends up to 128 Myr. At some point the results should be treated as lower limits. In general, this test proves that Ly α forest tomography is indeed able to constrain quasar ages in a precise and reliable fashion.

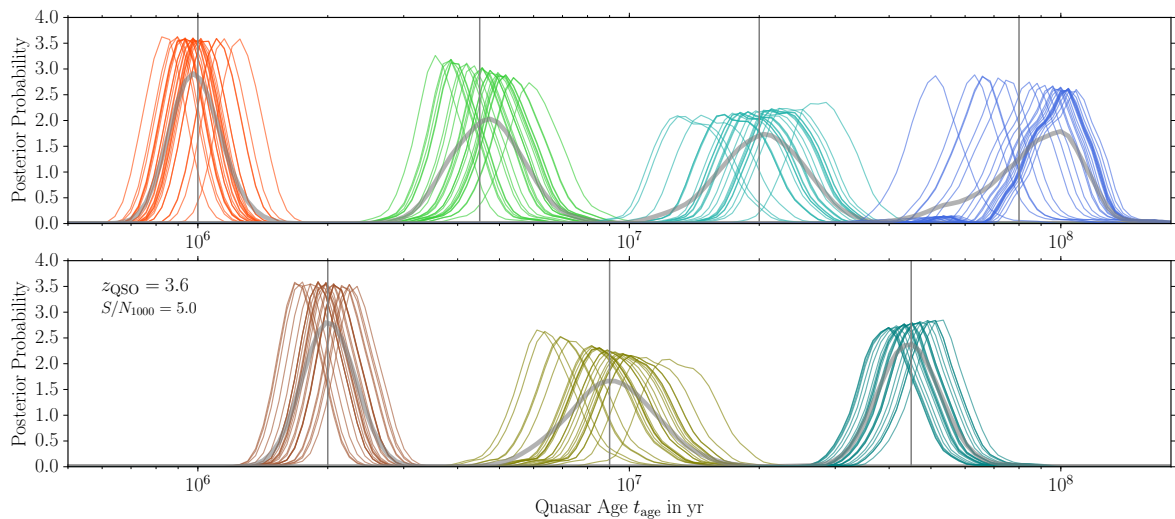


Figure 4.13: Posterior probability distributions for seven sets of mock observations with quasar ages (vertical lines) between 1.0 and 80 Myr. For each of the seven t_{age} , 25 independent realizations are shown (colored curves) and as a thick gray curve the average of the individual posterior probabilities. The adopted foreground quasar redshift is $z_{\text{QSO}} = 3.6$, spectral resolution is $R = 1000$ and $S/N_{1000} = 5.0$. Further properties of the models are listed in Table 4.2.

Figure 4.13 also reveals that, at least to first order, all seven models show a similar width of the posterior probabilities, more or less independent of the true age of the quasar. Since the axis in Figure 4.13 is scaled logarithmically, this translates to an approximately constant relative uncertainty $\frac{\Delta t_{\text{age}}}{t_{\text{age}}} \approx 20\%$. This general behavior can also be seen in the mapping from \hat{t}_{age} to $p(t_{\text{age}} | \hat{t}_{\text{age}})$ which defines the width of the derived posterior probabilities. The distribution shown in Figure 4.12 has approximately constant width around the 1:1 relation. However, there is some dependence on the quasar age which we discuss in more detail below.

4.5.3 Dependence on t_{age}

To quantify the precision of the derived t_{age} estimate, we define the relative uncertainty as the 16th–84th percentile interval of the posterior probability parametrized as function of $\log(t_{\text{age}})$ which yields $\frac{\Delta t_{\text{age}}}{t_{\text{age}}}$.

Figure 4.14 shows this relative precision derived from individual posteriors averaged over the 25 realizations per model as function of quasar age. As one can see, the highest relative precision around 10% is achieved for young quasars ($t_{\text{age}} \approx 1$ Myr). For very long quasar ages, similarly small uncertainties around 15% can be reached. At intermediate ages around $t_{\text{age}} \approx 10$ Myr, the precision is only around 20%. However, this depends on the quasar redshift.

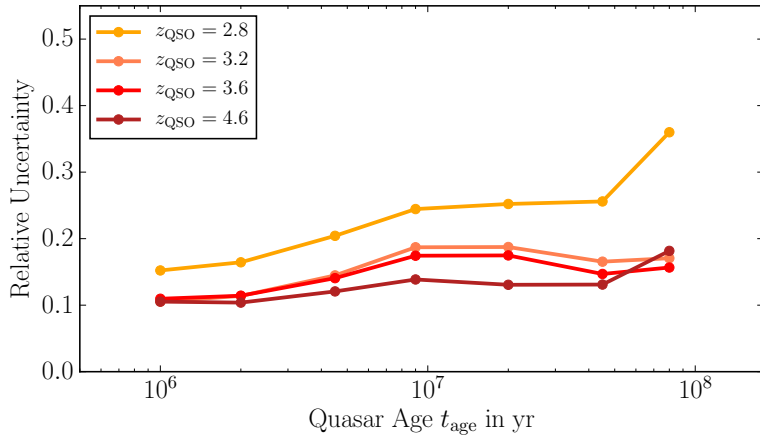


Figure 4.14: Dependence of the achieved precision on the adopted quasar age t_{age} . For each quasar age and three different quasar redshifts, the average precision of 25 mock datasets is shown. Further model parameters are listed in Table 4.2.

Quantitatively understanding the origin of the dependence of the precision on quasar age is not a trivial task, but we believe it is related to a combination of the smearing effect of redshift space distortions and the geometry of the region illuminated by the quasar.

As shown, the quality of the derived constraints depends slightly on the adopted foreground quasar redshift. For low quasar redshifts, e.g the $z_{\text{QSO}} = 2.8$ case, the achieved precision is in general not as good as for $z_{\text{QSO}} > 3.0$ and deteriorates in particular for long quasar ages.

4.5.4 Dependence on z_{QSO}

In Figure 4.15, we explore the redshift dependence of our method in more detail. In what follows we keep the limiting magnitude for achieving $S/N_{1000} = 5$ fixed at $r_{\text{lim}} = 24.7$, which results in an approximately constant exposure time around 10 ks (see Figures 4.4 and 4.5). We also assume the same fixed FoV of $16'$. As already outlined in § 4.1, one has to find a compromise between sampling the quasar light echo by many background sightlines at low z_{QSO} and the overall stronger proximity at higher redshift, owing to the lower average IGM transmission and thus increased contrast in the proximity zone (see Figure 4.11).

Figure 4.15 indicates that the latter effect clearly dominates. For $z_{\text{QSO}} > 3.3$, we achieve a precision on t_{age} better than 20%, nearly independent of redshift. Below this however, the t_{age} precision degrades substantially, despite sampling the quasar proximity zone with up to 216 background sightlines at $z_{\text{QSO}} = 2.4$. The deterioration is particularly dramatic

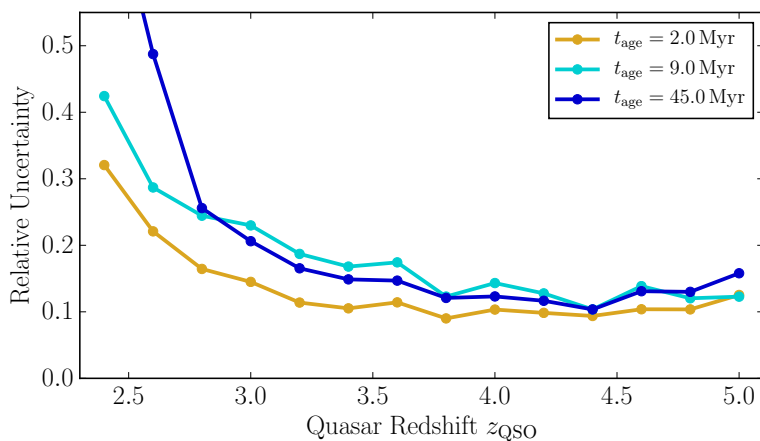


Figure 4.15: Dependence of the achieved precision on the adopted quasar redshift z_{QSO} . For each quasar redshift and three different quasar ages, the average precision of 25 mock datasets is shown. The chosen sightline separation and number of background sightlines within the $16'$ FoV corresponds to a constant limiting magnitude of $r_{\text{lim}} = 24.7$ mag at all redshifts. For $S/N_{1000} = 5$, this limiting magnitude should be achievable in ≈ 10 ks exposures. Further model parameters are listed in Table 4.2.

for long quasar ages, where the transmission enhancement caused by the quasars ionizing radiation would have to be detected at large distances from the quasar, at which point the corresponding small transmission enhancement becomes indistinguishable from the average (high) IGM transmission, considering the relatively large stochastic fluctuations. As already discussed in §4.3.1 and shown clearly in Figure 4.11, redshifts $z_{\text{QSO}} \leq 2.8$ are not well suited to map quasar light echoes and one should in general aim for higher redshift where the mean IGM transmission is lower.

At very high quasar redshift, ($z_{\text{QSO}} \gtrsim 4.5$) the average separation between sightlines becomes comparable to the size of our adopted field-of-view and the number of contributing background sightlines rather low (see Table 4.2). The rigid sightline pattern we adopt in our analysis (see Figure 4.6) is not optimized for this regime. The discretization in background sightline density causes undesired jumps and wiggles in the curves shown in Figure 4.15, e.g at $z_{\text{QSO}} = 4.4$.⁸ For the low sightline density regime, a random placement of background sightlines in the FoV would clearly be more appropriate.

A better assessment of the performance of our method at $z_{\text{QSO}} \approx 5$ and beyond might therefore require a slightly different approach and a dedicated study. This might reveal that the method can be pushed to even higher redshifts. However, one has to note that in this study we model the proximity effect with a rather simple model that has only one free parameter. Therefore, a single background sightline theoretically delivers sufficient information to fully constrain the model. However, our previous studies of the He II transverse proximity effect (Chapter 2 and 3, Schmidt et al. 2017a, 2018a) showed that measurements along single background sightlines, even in the case of low mean IGM transmission and high contrast, are often not sufficient to deliver strong and unique constraints on quasar properties when quasar age, obscuration and orientation effects are taken into account. We expect that in general a higher number of background sightlines is necessary to constrain models more complex than we consider here. We will address these questions in more detail in a future paper.

4.5.5 Dependence on S/N

In §4.1.4, we argued that a relatively low S/N is sufficient for our analysis since the stochastic IGM absorption caused by itself a substantial amount of noise in the transmission measurement. In this section, we now quantify this effect and determine the actual dependence of our parameter inference on the data quality. We therefore take the models listed in Table 4.2 and re-compute them with different S/N_{1000} . The associated continuum error is adjusted as well, following the procedure described in §4.2.6.

The dependence on the achieved S/N_{1000} shows some diversity for different quasar redshifts and quasar ages. We therefore show a broad selection of curves in Figure 4.16. The top panel varies S/N at fixed $t_{\text{age}} = 20$ Myr illustrating different redshifts; the bottom panel fixes the redshift to $z_{\text{QSO}} = 3.6$, and varies the the quasar age. In general one sees that for $S/N_{1000} < 2$, the achieved precision quickly deteriorates, whereas, above $S/N_{1000} \gtrsim 2.5$ the curves flatten, indicating that the uncertainty on the inferred quasar age depends only very weakly on the data quality. Increasing the S/N of the data slightly improves the precision, but this gain is so small that it is in practice probably not worth acquiring data with $S/N_{1000} > 3.5$.

Our generally adopted value of $S/N_{1000} = 5$ is for all t_{age} and z_{QSO} very much on the flat region of the curves in Figure 4.16, where the precision of the parameter inference is not limited by the S/N of the data. It is therefore worthwhile to consider substantially relaxing the requirement on data quality e.g. to $S/N_{1000} = 2.5$, which might yield only slightly inferior

⁸At $z_{\text{QSO}} = 4.4$, $D_{\text{SL}} = 8.8$ cMpc and two rings of our pattern fit into the FoV, resulting in $N_{\text{SL}} = 18$. At $z_{\text{QSO}} = 4.6$, the average sightline separation is $D_{\text{SL}} = 12$ cMpc and the quasar proximity region is only sampled by 6 background sightlines.

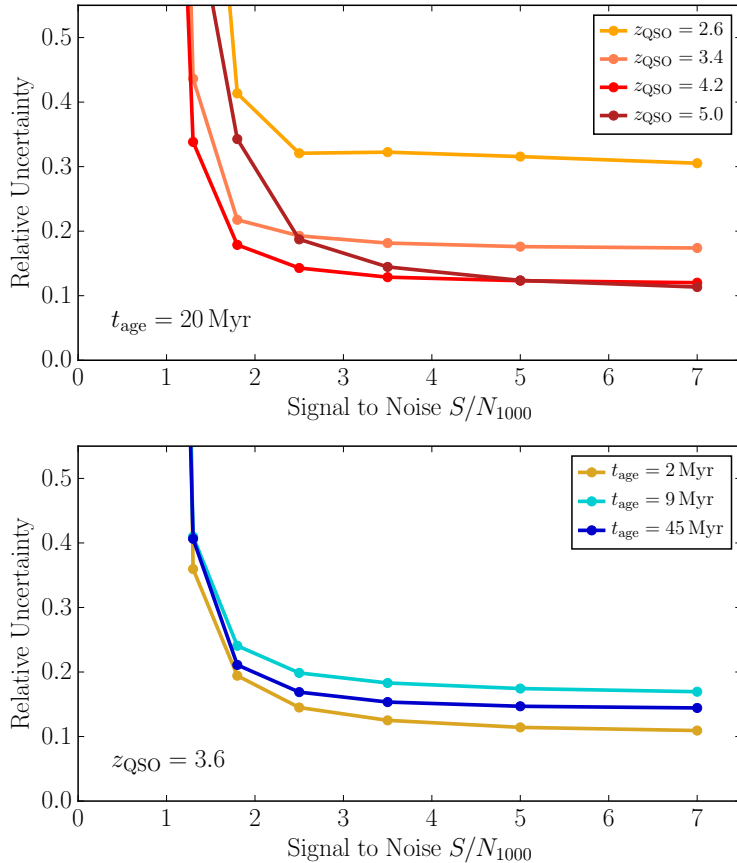


Figure 4.16: Dependence of the achieved precision on the achieved S/N_{1000} of the data. For each data quality, quasar age and quasar redshift we show the achieved precision averaged over 25 mock datasets. The top panel displays the behavior for four different redshifts at fixed $t_{\text{age}} = 20$ Myr. The bottom panel shows three different quasar ages for $z_{\text{QSO}} = 3.6$. Further model parameters are listed in Table 4.2.

results at approximately one fourth of the exposure time. However, data quality still has to be good enough to properly identify the objects as high-redshift background galaxies and determine their redshifts which in practice often requires $S/N \simeq 5$ for sources which do not have strong emission lines.

4.5.6 Dependence on Spectral Resolution

Another aspect of the observing strategy is the required spectral resolution. As argued in § 4.1.3, $\text{Ly}\alpha$ tomography will at some point be limited by the peculiar velocities in the IGM and in § 4.3 we determined that these redshift space distortions have an amplitude of $\approx 300 \text{ km s}^{-1}$, indicating that spectral resolving powers of the order of $R \approx 1000$ should be sufficient. In Figure 4.17 we show that the actual requirement is even lower. Provided $R \geq 750$, we observe an extremely weak dependence of the resulting t_{age} precision on the resolution. Even below this, the achieved precision is only moderately impacted.

Therefore, spectral resolution is essentially of no concern for characterizing quasar light echoes. Nearly every multi-object spectrograph should deliver sufficient resolution, even in low resolution modes. Resolving powers of $R \lesssim 200$ already come close to the regime of slitless grism or prism spectroscopy. It might be possible to benefit from these observing strategies for $\text{Ly}\alpha$ forest tomography without resulting in a significant penalty on the achieved precision⁹. However, the adopted spectral resolution has to be good enough to identify the objects as high-redshift background galaxies. In any case, our adopted fiducial resolving power of $R = 1000$ is more than sufficient.

⁹We stress however, that slitless spectroscopy suffers from substantially higher sky noise compared to slit spectroscopy. If at all, slitless spectroscopy is therefore only an option for space based observations.

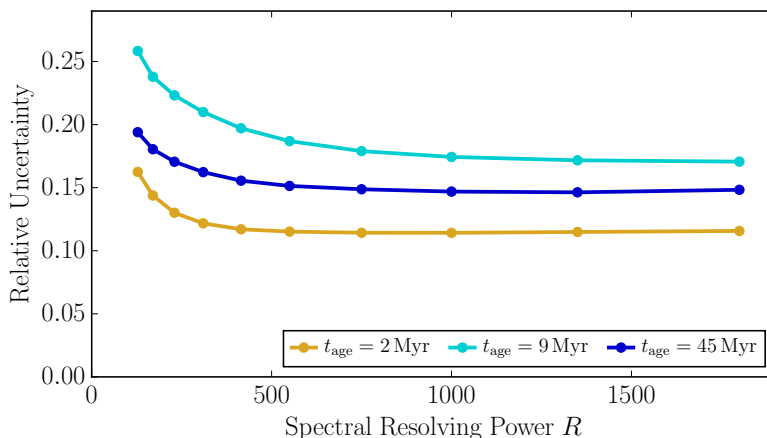


Figure 4.17: Dependence of the achieved precision on the spectral resolution of the data. The models are based on the $z_{\text{QSO}} = 3.6$ model listed in Table 4.2 and recomputed with varying spectral resolutions. For each resolving power R and three different quasar ages, the average precision of 25 mock datasets is shown. The S/N per 300 km s^{-1} resolution element is kept fixed at $S/N_{1000} = 5$, corresponding to the same number of detected photons and therefore same exposure time for all shown models.

4.5.7 Dependence on Sightline Density

A further key parameter for the tomographic mapping of quasar light echoes is the density of background sightlines. Clearly, this depends on the limiting magnitude of the observations and the redshift of the foreground quasar. The exact relations between these parameters is illustrated in Figure 4.5.

To explore how our precision depends on the sightline density, we compute another set of models for which we vary the limiting magnitude of the observations. This alters the average separation of sightlines and, since we keep the FoV constant, the number of sightlines. For simplicity, we only conduct this exercise for a quasar redshift of $z_{\text{QSO}} = 3.6$. The exact details of the models used for this are given in Table 4.3.

The results of this analysis are shown in Figure 4.18. As one can see, there is no strong dependence of the precision on the sightline density (or the limiting magnitude). Apparently, sampling the proximity zone with six background sightlines ($r_{\text{lim}} = 23.8 \text{ mag}$) already gives a reasonable estimate of the quasar age. Increasing the sightline density to yield 18 background sightlines ($r_{\text{lim}} = 24.2 \text{ mag}$) reduces the uncertainty by $\approx 20\%$. Any further increase yields only a marginal improvement. The strongest effect is seen for short quasar ages. Here, the region illuminated by the quasar is the smallest (see Figure 4.9) and a finer sampling by background sightlines leads to the biggest improvement. In general, Figure 4.18 indicates that a survey somewhat shallower than our fiducial $r_{\text{lim}} = 24.7 \text{ mag}$ might be sufficient to constrain quasar ages.

Table 4.3. Parameter of Simulations used in §4.5.7

z_{QSO}	M_{1450} mag	r_{lim} mag	D_{SL} cMpc	FoV '	N_{SL}	R	S/N_{1000}
3.6	-28.7	25.0	3.36	16	60	1000	5.0
3.6	-28.7	24.6	4.57	16	36	1000	5.0
3.6	-28.7	24.2	6.57	16	18	1000	5.0
3.6	-28.7	23.8	10.18	16	6	1000	5.0

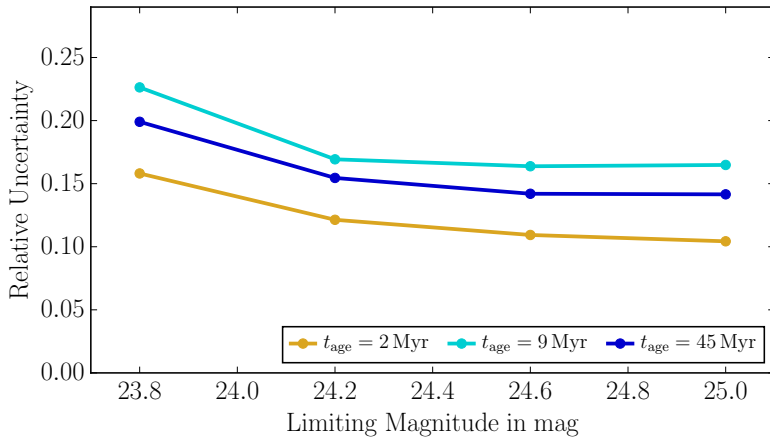


Figure 4.18: Dependence of the achieved precision on the limiting magnitude of the observations and therefore on the background sightline density. The curves are based on the $z_{\text{QSO}} = 3.6$ model listed in Table 4.2 and recomputed for different limiting magnitudes $23.8 \text{ mag} \leq r_{\text{lim}} \leq 25.0 \text{ mag}$. This results in average sightline separations D_{SL} between 10 cMpc and 3.4 cMpc. Since the FoV is fixed at $16'$, the number of background sightlines N_{SL} varies between 6 and 60. See Table 4.3 for details of the models.

However, we must stress that we so far consider only a highly simplified quasar emission model with t_{age} as the only free parameter. In reality, quasar UV emission is expected to be anisotropic (Antonucci 1993; Urry & Padovani 1995; Netzer 2015). A proper treatment of this would require a model that includes obscuration and orientation effects. Constraining all four parameter that specify such a model would probably require a larger number of background sightlines and smaller sightline separations. For our current isotropic emission model, even with relatively coarse background sightlines sampling, the size of the illuminated region and therefore t_{age} can still easily be inferred from locations in front of the quasar ($R_{\perp} \ll 0$, $z < z_{\text{QSO}}$, left in Figure 4.9) where these sightlines intersect the parabolic shaped illuminated region. This can also be seen in Figure 4.7, where even sightlines with $R_{\perp} = 16 \text{ cMpc}$ probe time differences shorter than $\Delta t < 2 \text{ Myr}$. The situation will be different if the emission geometry of the quasar must be determined as well. In that case, an average sightline separation comparable or smaller than the age of the quasar, i.e. $D_{\text{SL}} < c t_{\text{age}}$, are likely to be required. We will characterize the exact requirements for this more complex case in a future paper.

We also stress that throughout our analysis in this section we used the brightest quasar at any given redshift (see Figure 4.2). When using fainter quasars, the proximity zone is less extended and we expect that in return one requires a denser packed background sightline pattern to achieve the same precision.

4.5.8 Dependence on Field-of-View

Similar to the limiting magnitude of the observations, the achievable precision is influenced by the field-of-view covered by the observations. Both aspects together define the number of sightlines that sample the proximity zone. We compute a set of models at $z_{\text{QSO}} = 3.6$ with fixed $r_{\text{lim}} = 24.2 \text{ mag}$ and therefore fixed $D_{\text{SL}} = 6.6 \text{ cMpc}$, but vary the diameter of the field between $7'$ and $35'$. Details of the models are listed in Table 4.4 and the results are shown in Figure 4.19.

Again, given the relatively high z_{QSO} and simple single parameter quasar emission model, a small number of background sightlines is sufficient to constrain the model parameter t_{age} . However, increasing the FoV and therefore the number of background sightlines does improve the precision substantially from $\approx 20\%$ at $7'$ FoV to better than 10% at $42'$. The dependence is different for different quasar ages. While for $t_{\text{age}} = 2 \text{ Myr}$ we find no significant improvement,

Table 4.4. Parameter of Simulations used in § 4.5.8

z_{QSO}	M_{1450} mag	r_{lim} mag	D_{SL} cMpc	FoV '	N_{SL}	R	S/N ₁₀₀₀
3.6	-28.7	24.2	6.57	7	6	1000	5.0
3.6	-28.7	24.2	6.57	14	18	1000	5.0
3.6	-28.7	24.2	6.57	21	36	1000	5.0
3.6	-28.7	24.2	6.57	28	60	1000	5.0
3.6	-28.7	24.2	6.57	35	90	1000	5.0
3.6	-28.7	24.2	6.57	42	126	1000	5.0

longer quasar ages and in particular intermediate ages around $\sim 10^7$ yr, which usually have the largest uncertainties, gain the most from a larger FoV.

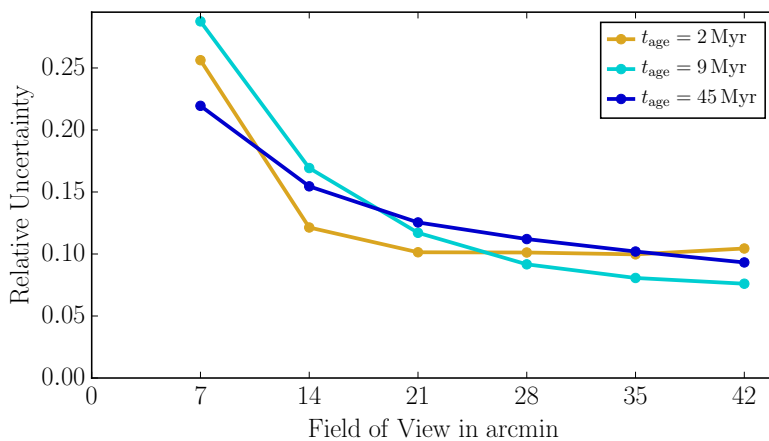


Figure 4.19: Dependence of the achieved precision on the field-of-view covered by the observations. The curves are based on the $r_{\text{lim}} = 24.2$ mag model listed in Table 4.3 and recomputed for different fields between $7'$ and $35'$ diameter and therefore different number of background sightlines. The average sightline separations is kept fixed at $D_{\text{SL}} = 6.6$ cMpc. See also Table 4.4 for details of the models.

Our understanding is that the precision of the analysis is limited primarily by redshift space distortions. Probing a larger field helps to average these down. Since redshift space distortions are coherent over large length scales, this can only be done by actually probing a larger volume but not by increased sightline density in a confined volume. A larger field-of-view is therefore clearly beneficial, provided the quasar ages are sufficiently long that their proximity zones extend beyond the adopted FoV. However, most currently existing multi-object spectrographs have a rather limited FoV $< 10'$, requiring multiple pointings to cover a large field. The gain in precision is therefore probably not big enough to justify the substantial increase in observing time required to map the full extent of the proximity region. The exception is the Subaru Prime Focus Spectrograph which will have a field-of-view $78'$ in diameter. This new instrument will be able to cover the full proximity zone and deliver spectra of a large number of background sightlines in a single pointing, highly beneficial for our application.

4.5.9 Dependence on Quasar Luminosity

The luminosity of the foreground quasar is clearly another crucial factor for our analysis. Brighter quasars have larger proximity zones that can be probed by more background sightlines. Even in cases where the proximity zone extends beyond the FoV and the number of background sightlines is limited by the instrument rather than the quasar, the proximity zone of brighter quasars has a larger extent along the line-of-sight. Also, for a given separation from the foreground quasar, a more luminous quasar will cause a stronger IGM transmission

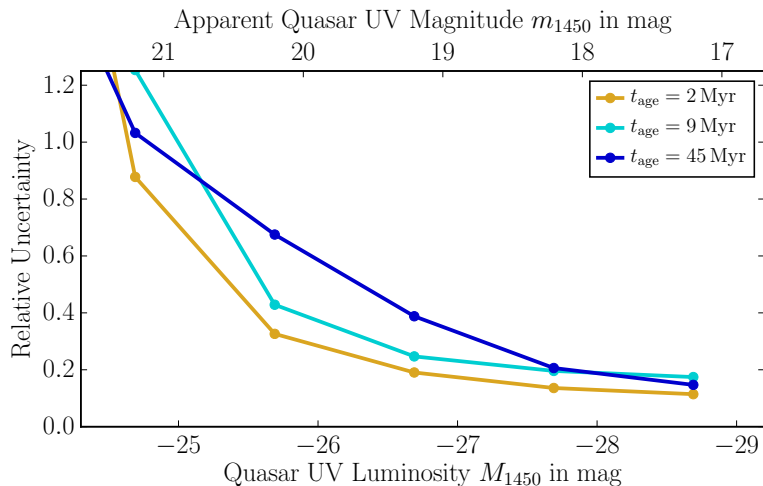


Figure 4.20: Dependence of the achieved precision on the luminosity of the foreground quasar. The curves are based on the $z_{\text{QSO}} = 3.6$ model listed in Table 4.2 and recomputed for different values of M_{1450} . For each quasar luminosity and three quasar ages, the average precision of the 25 mock datasets is shown.

enhancement, even though the transmission is anyway close to unity in a substantial fraction of the illuminated volume (see Figure 4.11). It is therefore always beneficial to target the brightest quasars.

In Figure 4.20, we show the dependence of the t_{age} precision on quasar luminosity. Clearly, the highest precision is achieved for the brightest quasars and the precision steadily decreases for fainter quasars. When comparing to Figure 4.3, one can see that a quasar with $M_{1450} = -29$ mag exceeds the UV background up to an angular distance of $30'$ and therefore far beyond our fiducial FoV which has a $8'$ radius. The proximity zone size scales as the square root of the quasar luminosity. One can therefore estimate at which luminosity the quasar and UV background contribute equally to the H I photoionization rate at the edge of the FoV. This happens for $M_{1450} \approx -26.2$. Moving from the brightest quasars down to this luminosity, one observes that the precision for t_{age} deteriorates relatively slowly. For fainter quasars however, the outermost background sightlines do not probe the proximity zone anymore, leading to a rapid loss of precision.

In general, mapping quasar light echoes with Ly α forest tomography works best for the absolutely brightest quasars. However, also quasars up to break magnitude of the quasar luminosity function $M_{1450}^* \approx -27.3$ mag (Kulkarni et al. 2018a), are reasonable targets for which quasar ages could be deduced with only slightly reduced precision. Therefore, as can be seen in Figure 4.2, many quasars ($\gg 100$) are available as potential targets which offers, at least in principle, the opportunity to apply Ly α forest tomography to a substantial number of quasars and to study the distribution of lifetimes.

4.5.10 Impact of Continuum Uncertainties

Continuum uncertainties could in principle have a substantial impact on our analysis. All plots shown above do include our standard scheme for modeling continuum uncertainties as described in §4.2.6. However, it is also worthwhile to understand how much continuum uncertainties are degrading our precision relative to the ideal case of no continuum errors. We therefore re-run the full analysis procedure with model parameters identical to the ones listed in Table 4.2, but assuming perfect knowledge of the continuum. The result is shown in Figure 4.21.

Clearly, continuum uncertainties at level indicated by Equations 4.9 and 4.11 (10% for $S/N_{1000} = 5$) have a negligible impact on our results. This slightly changes when considering poorer data quality. For example, for $S/N_{1000} = 2.5$ (18% continuum error), we find a noticeable deviation between the fit including the continuum uncertainty and a perfect con-

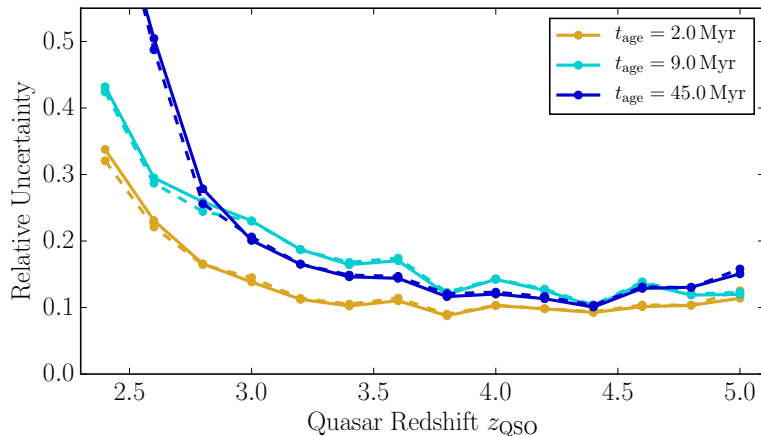


Figure 4.21: Dependence of the achieved precision on the adopted continuum uncertainty. The plot is similar to Figure 4.15 and shows for each quasar redshift and three different quasar ages the average precision of 25 mock datasets. However, we show as dashed lines the achieved precision when using the usual scheme for continuum uncertainties (see § 4.2.6) and as solid lines the case with perfect continuum fits.

tinuum. However, the effect is rather small and the uncertainty in the t_{age} estimate increases only from e.g. 20 % to 23 %, emphasizing that continuum errors are no major concern in the context of our study.

4.6 Conclusion

In this Chapter we have presented a novel method to map quasar light echoes and infer quasar ages, employing $\text{Ly}\alpha$ forest tomography. The method utilizes the $\text{Ly}\alpha$ forest absorption in the spectra of faint background galaxies ($m_r \approx 24.7$ mag) to probe the ionization state of the intergalactic medium in the vicinity of bright foreground quasars. The UV radiation of quasars has a strong impact on the IGM and can substantially enhance the ionization state of the gas, resulting in enhanced IGM transmission which is known as *proximity effect*. Relying on faint galaxies as background sources results in a high sightline density (1000 per degree) and allows one to probe the proximity zone of individual foreground quasars with many (10 to 100) background sightlines. These detailed observations allow one to construct a three-dimensional map of the quasar light echo and ultimately to constrain the quasars emission history and emission geometry.

In this study, we developed a full end-to-end simulation pipeline to model this experiment and we demonstrated that it is feasible on current 8m class telescopes. In this context, we described a collection of observational parameters (quasar luminosities, sightline densities, etc) which set the framework for future tomographic observations of light echoes (§ 4.1). We then constructed a suite of models of the $\text{Ly}\alpha$ transmission in the quasar proximity region, based on NYX cosmological hydrodynamical simulations which were postprocessed with a photoionization model (§ 4.2, 4.3). We introduced a novel *likelihood-free* Bayesian analysis formalism (§ 4.4) which enables a statistical comparison of tomographic IGM observations to these models and delivers robust posterior probability distributions for the model parameter (t_{age}), fully accounting for the strong correlations in the tomographic map and the non-Gaussian nature of the IGM transmission. We thoroughly tested this new machinery on mock observations (§ 4.5) which leads to the following conclusions:

- IGM tomography observations of quasar light echoes are capable of yielding precise unbiased constraints on the quasar emission history. The achievable relative precision on the quasar age assuming realistic observing times (10 ks) with existing instruments on 8-10 m class telescopes is $\approx 20\%$.
- The highest relative precision (10%) is achieved for very short (1 Myr) or very long

CHAPTER 4. MAPPING QUASAR LIGHT ECHOES IN 3D

(100 Myr) quasar ages, while for intermediate $t_{\text{age}} \simeq 10$ Myr we can measure t_{age} to about 20% precision.

- Our new method delivers satisfactory ($< 25\%$) constraints for all quasar redshifts $3 < z_{\text{QSO}} < 5$ with weak dependence of the precision on redshift.
- A spectral resolution as low as $R = 750$ is completely sufficient. Using even lower resolution down to $R \approx 200$ might be possible without a significant loss in precision.
- The minimal required signal to noise ratio per 300 km s^{-1} bin is $S/N_{1000} \approx 2.5$. Higher S/N data does improve the precision but only slightly.
- The brightest quasars are the best targets. However, quasars as faint as $M_{1450} < -27.3$ mag can be used with little loss of precision. This implies that $\gg 100$ targets are available at $3 < z_{\text{QSO}} < 5$, opening up the possibility for mapping out the distribution of quasar ages in statistical samples.

This demonstrates that Ly α forest tomography has the potential to measure the emission properties of individual bright quasars and in particular constrain the age of quasars in the range from 1 Myr up to 100 Myr with $\approx 20\%$ precision. While we focused in this study on the general feasibility of the method, the observational requirements, and the ability to constrain the quasar age, we will in upcoming papers investigate more complex models for the quasar emission, like a more realistic lightcurve and non isotropic emission, which involves a straightforward generalization of the modeling and statistical framework presented here. In particular, we intend to infer for individual quasars their orientation and obscuration geometry which is so far even in a statistical sense only poorly constrained (Brusa et al. 2010; Assef et al. 2013; Lusso et al. 2013; Marchesi et al. 2016). Such measurements will then allow to test quasar unification models (Antonucci 1993; Urry & Padovani 1995; Netzer 2015) and compare them to other explanations for quasar obscuration (e.g. Elvis 2000; Elitzur & Shlosman 2006; Hönig & Kishimoto 2017). There might also be synergies with other quasar lifetime measurements, in particular the ones derived from the He II line-of-sight proximity effect. Some of the quasars for which Khrykin et al. (2018) have recently presented constraints are viable targets for our Ly α forest tomography. This offers the opportunity for a cross-check between two rather different methods.

We showed that the current generation of instruments on 8–10 m class telescopes are capable of deriving meaningful constraints on quasar emission properties via Ly α forest tomography. However, the introduction of new highly-multiplexed multi-object spectroscopic facilities on 8–10 m telescopes in the near future, in particular the Subaru Prime Focus Spectrograph, will give a tremendous boost to tomographic observations like the one described in this work. This will make Ly α forest tomography one of the key techniques to study the emission histories and emission geometries of quasars and deliver unprecedented insight into quasar activity cycles, quasar physics, and the buildup of supermassive black holes.

Chapter 5

Concluding Remarks and Outlook

As described in §1.3, the transverse proximity effect bears detailed information about the emission properties of quasars. In particular, two so far fairly unconstrained properties can be determined, the quasar age (or lifetime) and the amount of obscuration or alternatively the opening angle of the ionizing UV emission.

Here, the He II Ly α forest offers in principle a much higher contrast between the average IGM transmission, which at the commonly used redshifts $z_{\text{QSO}} \simeq 3$ still shows Gunn-Peterson troughs, and the high transmission regions in the proximity zone of a quasar, compared to the classical H I Ly α forest. Therefore, the first convincing discovery of a transverse proximity effect was in the He II sightline towards Q 302–003 (Heap et al. 2000; Jakobsen et al. 2003). The installation of the Cosmic Origins Spectrograph on board the *Hubble Space Telescope* during Service Mission 4 in 2009 offered the opportunity to substantially expand the sample of He II sightlines from just a few ones to the current sample of 25 sightlines.

The initial goal for this thesis was therefore to conduct a systematic, optical spectroscopic foreground survey around the newly observed He II sightlines and find additional associations of foreground quasars with features in the He II Ly α forest along the background sightlines, in particular transmission spikes indicative of a transverse proximity effect (Chapter 2).

With our efficient survey strategy, composed of a deep survey on 8 m class telescopes using multi-object spectroscopy and complemented by a shallow but wide survey on 4 m class telescopes, we discovered 131 new foreground quasars. Many of these did fall in front or behind the usable part of the He II sightlines, however, by also mining existing quasar catalogs like SDSS/BOSS DR12 (Alam et al. 2015; Pâris et al. 2017), we were able to assemble a sample of 20 useful foreground quasars with an expected He II ionizing rate at the background sightline of $\Gamma_{\text{QSO}}^{\text{HeII}} > 2 \times 10^{-15} \text{ s}^{-1}$, which is larger or at least comparable to the He II UV background (Haardt & Madau 2012; Khrykin et al. 2016; Khaire & Srianand 2018) and should cause an observable He II transverse proximity effect.

However, none of the few foreground quasars was associated with a prominent transmission spike like the one discovered previously by Jakobsen et al. (2003). In general, the transmission along the He II sightlines did not seem to correlate strongly with the foreground quasar population (Figure 2.5). We could still find statistical evidence for the He II transverse proximity effect by stacking the He II sightlines on the position of the foreground quasars. This revealed excess transmission close to the foreground quasars (Figure 2.7). However, the measurement was hampered by a large amount of fluctuations in the He II Ly α forest spectra which even in the stack limited the significance of the observed transmission enhancement to only 3.1σ . Restricting the stack to objects with a transverse separation $> 25 \text{ Mly}$ and still finding enhanced transmission (at 2.6σ significance) constrained the quasar lifetime to $t_{\text{Q}} > 25 \text{ Myr}$ (Figure 2.13).

CHAPTER 5. CONCLUDING REMARKS AND OUTLOOK

Most puzzling were the observations of the quasars with the highest He II ionization rates which did in contrast to the prototype quasar (Jakobsen et al. 2003) not show any evidence for a transverse proximity effect (Figure 2.6). However, their high ionization rates, more than an order of magnitude higher than the He II UV background, allowed a detailed investigation of these objects, based on purpose-developed numerical simulations (Chapter 3). These simulations represent the first realistic predictions for the appearance of the He II transverse proximity effect, are based on cosmological hydrodynamical simulations (NYX, Almgren et al. 2013; Lukić et al. 2015) and include the effects of anisotropic quasar emission and finite lifetime. Our simulations showed that the transverse proximity effect should in principle be observable but also revealed that a huge amount of scatter in the strength of the associated He II transmission enhancement has to be expected (Figure 3.5). This scatter is to some degree related to the unknown orientation of the foreground quasar in combination with the anisotropic emission. However, even for isotropic emission, the scatter is quite large. This immediately showed that detecting the He II transverse proximity effect in individual sightlines and deriving constraints on quasar properties, even for quasars that clearly dominate over the UV background, is far more challenging than initially anticipated.

Nevertheless, we were able to derive joint constraints on the age and the amount of obscuration for the six quasars with the highest $\Gamma_{\text{QSO}}^{\text{HeII}}$ (Figure 3.6). However, these constraints are rather broad, represent in many cases just limits and often show strong degeneracies. Still, it is obvious that the properties of the prototype quasar along the Q 0302–003 sightline have to be quite different from the three newly discovered quasars with even higher $\Gamma_{\text{QSO}}^{\text{HeII}}$. We see this as an indication for a possible bimodality of the quasar population in which some objects are old and emit nearly isotropically while other objects are either very young or highly obscured (§ 3.5).

Although we were able to derive some constraints on the average quasar lifetime and joint constraints on the emission geometry and emission history of a few selected objects, the most significant insights gained from the work presented in Chapter 2 and 3 is probably to acknowledge how diverse and complicated the appearance of the He II transverse proximity effect can be and how difficult it actually is to derive solid constraints on quasar properties. The impression in the end was, that how sophisticated a statistical analysis of the existing He II data might ever be, the inferred constraints would probably remain quite uncertain, fuzzy and of relatively low significance. It seemed, the constraining power of the available He II data had been mostly exhausted and might simply not hold sufficient information to break the existing degeneracies or constrain further properties.

These challenges became a real concern since a substantial expansion of the He II data sample is most-likely not possible within the next decades. The capabilities of current UV space telescopes, in particular *GALEX* and *HST/COS*, have been mostly exhausted and many of the He II sightlines that could be discovered, have been discovered. There is still the opportunity for a survey on the southern hemisphere, but it would probably less than double the number of available He II sightlines. In addition, *HST/COS* is aging and by now has only a fraction of its initial sensitivity in 2009, when it was installed.

A successor for *HST*, which is currently the only workhorse for UV spectroscopy, is not even on the horizon. A Russian-Spanish collaboration currently develops the *World Space Observatory Ultraviolet* (WSO-UV, Shustov et al. 2018), but it will only be equipped with a 1.8 m mirror and probably far less capable in the FUV than *HST*. In addition, the project is behind schedule and launch not expected before 2023. *LUVOIR* (The LUVOIR Team 2018) and *HabEx* (Gaudi et al. 2018) are concepts for new UV space telescopes, proposed for the NASA 2020 decadal survey. However, even if one of these would be selected in 2020, it is, given the massive delays and cost overruns of the *James Webb Space Telescope* and the *Wide Field Infrared Survey Telescope*, completely unrealistic to expect first-light before the end of the 2030s.

In light of this, it seemed unreasonable to spend additional efforts on the He II transverse proximity effect. However, the potential of the transverse proximity effect to constrain quasar properties was still there and I had developed a powerful machinery to simulate the proximity effect based on cosmological hydrodynamical simulations and a fully Bayesian framework to compare these simulations to actual observations and infer quasar properties. The analytical tools for further discoveries were therefore available and the only thing needed was a way to obtain new observations that would be more informative than the existing He II sample.

These came in the form of H I Ly α forest tomography, a method recently pioneered by former group member K.G. Lee. The use of faint galaxies as background sources offers the opportunity to obtain a dense grid of Ly α forest sightlines ($\gtrsim 1000$ per square degree for $m_r \approx 24.5$ mag, corresponding to sightline separations < 4 cMpc) and to interpolate between sightlines to reconstruct a 3D map of the IGM absorption. This initial concept (Lee et al. 2014a) turned out to be successful and delivered the first map of the large scale structure of the Universe (Lee et al. 2014b), allowed the characterization of cosmic voids (Krolewski et al. 2018) and led to the discovery of protoclusters (Lee et al. 2016). Since Ly α forest absorption depends on the comoving density structure and the ionization state of the gas (see Equation 3.3), this method should as well be capable of detecting the quasar transverse proximity effect in 3D and thereby map quasar light echoes. The only thing one would have to do, would be to obtain a tomographic map of the IGM in the surrounding of a luminous quasar.

This formed the starting point for the project described in Chapter 4. This time, we started with a detailed modeling of the experiment, based on the simulation techniques developed for the second project (Chapter 3). This theoretical analysis confirmed the feasibility of the undertaking and allowed an end-to-end test of the full analysis pipeline. We could show that with reasonable exposure times (e.g. $t_{\text{exp}} \approx 10$ ks and a $16'$ FoV) precise constraints (10%–20% uncertainty) on the quasar age of individual ultraluminous quasars could be achieved (e.g. Figure 4.13).

Our models also allowed us to explore a large parameter space and to optimize the observing strategy (Figures 4.14–4.21). It was clear from the beginning that observations of the H I transverse proximity effect suffer from the high IGM transmission at intermediate redshifts ($z \simeq 3$) and the low resulting contrast of the proximity zone. This had so far prevented an unambiguous detection of the proximity effect in hydrogen (e.g. Liske & Williger 2001; Schirber et al. 2004; Croft 2004; Hennawi et al. 2006; Hennawi & Prochaska 2007; Kirkman & Tytler 2008). However, we were confident that the high number of measurements along the many background sightlines contributing to the tomographic map and the possibility to target the most luminous quasars in the Universe would outweigh this disadvantage. This was indeed confirmed by our analysis. Also, our study revealed that (in contrast to our initial intuition) the advantage of lower IGM transmission at high redshift outweighs the disadvantage of coarser sampling by background sightlines. Therefore foreground quasars at $z_{\text{QSO}} < 3$ are not well suited for our experiment and higher redshifts are clearly preferred (Figure 4.15).

The analysis presented here in Chapter 4 is only the first step. To limit the complexity of this pilot study, we focused on an isotropic quasar emission geometry and the simplest possible lightbulb model for the quasar lightcurve. However, as mentioned already, we clearly intend to relax these restrictions and constrain more complex quasar emission models. Preliminary results are highly encouraging and show that the tomographic mapping of quasar light echoes bear great potential.

In Figure 5.1 we show a joint constraint on the quasar obscured fraction and its age. This is similar to our attempts presented in Chapter 3, Figure 3.6, however, the constraints from the H I tomography are much tighter than from the He II spectra. The tomographic observations allow to determine t_{age} to $\simeq 20\%$ and the obscuration $\Omega_{\text{obs}} to $\approx 10\%$, much better than the$

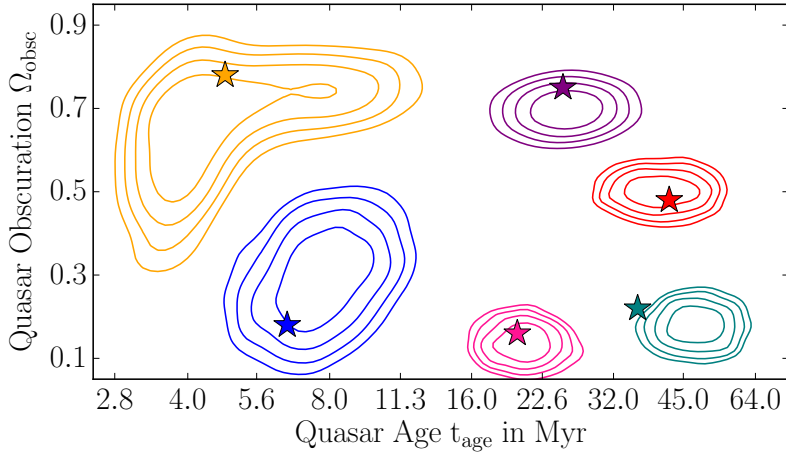


Figure 5.1: Joint constraints on quasar age t_{age} and obscuration Ω_{obsc} derived from mock data. Observational parameters are similar to the one used in §4.5. Stars show the true parameter of six different models, contours the recovered posterior probabilities. The results are preliminary but will be published in an upcoming publications.

very broad constraints derived from the He II transverse proximity effect. It has to be noted that for the results shown in Figure 5.1 the quasar orientation was fixed and only obscuration and lifetime determined by the analysis. The full fit constraining all four model parameters (θ , ϕ , Ω_{obsc} and t_{age}) still requires some work, in particular due to substantial computational effort required to map the four dimensional parameter space of the model. However, it already shows that our Bayesian analysis scheme described in §4.4 can be expanded to higher dimensions.

Another possible application of Ly α forest tomography is to determine full quasar lightcurves in a non-parametric way. An example of this is shown in Figure 5.2 where we constrain the luminosity of a quasar in 7 logarithmically spaced bins over a total timespan of nearly 100 Myr. For this, we make use of the fact that each point within the tomographic map is sensitive to the quasar luminosity at a different lookback time Δt , which is shown e.g in Figure 4.7. The possibility to constrain a full quasar lightcurve seems extremely tempting. Such a measurement on these timescales would be completely unprecedented. So far, all studies, including our own ones presented in this thesis, have modeled the quasar lightcurve as lightbulb or some other simple parametric model. These models are neither physical nor well motivated and simply reflect the sheer incapability to constrain more complex and more realistic models. Although only possible for the brightest quasars, it seems that Ly α forest tomography could deliver a detailed, model-independent measurement of quasar emission histories. Measuring the quasar luminosity at certain lookback times instead of a quasar age also offers the opportunity to describe the variability in a statistical sense, e.g. by structure functions, a very successful technique that is currently used to characterize quasar variability

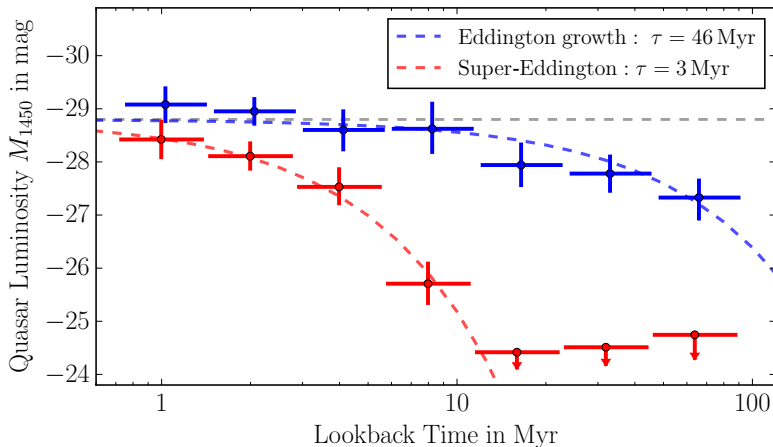


Figure 5.2: Possible constraint of a full quasar lightcurve over the past 100 Myr. Shown is a model in which the quasar luminosity grows Eddington-limited with a Salpeter e -folding time of 46 Myr (blue dashed) and a model with much faster increases in luminosity (red dashed), corresponding to either super-Eddington growth or a young quasar. For both cases, our Ly α forest tomography can accurately recover the quasar emission histories (points with errorbars).

on timescales up to $\simeq 100$ yr (e.g. Sesar et al. 2007; MacLeod et al. 2010, 2012). Such an approach also allows to combine our measurements with observations sensitive to different (i.e. shorter) timescales for which Ly α forest tomography is insensitive.

In contrast to the primarily theoretical suggestions by Adelberger (2004) and Visbal & Croft (2008), our aim was right from the beginning to implement our method in practice. Therefore, we collected detailed information about the observational framework (§ 4.1), used realistic assumptions for our models and conducted a detailed parameter study to determine the best observing strategy (§ 4.5). We have applied for observing time with Subaru / Hyper Suprime-Cam and Keck / Deimos. If everything goes as scheduled, the first data for our pilot survey will arrive by Summer 2019 and the first constraints on quasar properties might be available soon afterward.

As lined out above, a tomographic mapping of quasar light echoes is feasible with existing facilities. However, new instruments are under development that will be much more capable. At the moment, several massively parallel spectroscopic surveys are under development, e.g. DESI, WEAVE, 4MOST and SDSS V. The corresponding instruments will be installed on 4 m class telescopes and probably have limiting magnitudes of $\simeq 22$ mag. This is not deep enough to facilitate tomographic observations like our quasar light echo mapping. However, these projects are only the precursors for the next generation of surveys that will utilize 8–10 m class telescopes. The first of these new instruments is the Subaru / Prime Focus Spectrograph (Tamura et al. 2016) which is already under construction and scheduled to commence full operation in 2021. This instrument will have a FoV of 1.3 degree diameter and nearly 2400 deployable fibers, making it ideally suited for our project and allowing to gather the required observations in a fraction of the time compared to e.g. Keck / DEIMOS or VLT / FORS II. Other groups consider as well the development of similar or even more powerful instruments like Keck / FOBOS, TMT / WFOS (Pazder et al. 2006), the Maunakea Spectroscopic Explorer (Hill et al. 2018) and others (see e.g. Ellis et al. 2017).

Therefore, Ly α forest tomography might become in the near future a powerful tool to gain detailed and unprecedented insights into quasar emission properties and will certainly benefit from the currently ongoing development of new powerful multi-object spectrographs.

List of Author's Publications

- **Schmidt, T. M.**, Hennawi, J. F., Lee, K.-G., et al. 2018b, submitted to ApJ, ArXiv e-prints, [arXiv:1810.05156](https://arxiv.org/abs/1810.05156), [ADS](#)
- **Schmidt, T. M.**, Hennawi, J. F., Worseck, G., et al. 2018a, The Astrophysical Journal, 861, 122, [doi: 10.3847/1538-4357/aac8e4](https://doi.org/10.3847/1538-4357/aac8e4), [ADS](#)
- **Schmidt, T. M.**, Worseck, G., Hennawi, J. F., et al. 2017b, Frontiers in Astronomy and Space Sciences, 4, 23, peer-reviewed conference proceeding, [doi: 10.3389/fspas.2017.00023](https://doi.org/10.3389/fspas.2017.00023), [ADS](#)
- **Schmidt, T. M.**, Worseck, G., Hennawi, J. F., Prochaska, J. X., & Crighton, N. H. M. 2017a, The Astrophysical Journal, 847, 81, [doi: 10.3847/1538-4357/aa83ac](https://doi.org/10.3847/1538-4357/aa83ac), [ADS](#)

Bibliography

- Abazajian, K. N., Adelman-McCarthy, J. K., Agüeros, M. A., et al. 2009, *ApJS*, 182, 543, [doi](#), [ADS](#)
- Adelberger, K. L. 2004, *ApJ*, 612, 706, [doi](#), [ADS](#)
- Adelberger, K. L., & Steidel, C. C. 2005, *ApJ*, 630, 50, [doi](#), [ADS](#)
- Alam, S., Albareti, F. D., Allende Prieto, C., et al. 2015, *ApJS*, 219, 12, [doi](#), [ADS](#)
- Almgren, A. S., Bell, J. B., Lijewski, M. J., Lukić, Z., & Van Andel, E. 2013, *ApJ*, 765, 39, [doi](#), [ADS](#)
- Alpher, R. A., & Herman, R. 1948, *Nature*, 162, 774, [doi](#), [ADS](#)
- Alsing, J., Wandelt, B., & Feeney, S. 2018, *MNRAS*, 477, 2874, [doi](#), [ADS](#)
- Anderson, S. F., Hogan, C. J., Williams, B. F., & Carswell, R. F. 1999, *AJ*, 117, 56, [doi](#), [ADS](#)
- Antonucci, R. 1993, *ARA&A*, 31, 473, [doi](#), [ADS](#)
- Antonucci, R. R. J. 1984, *ApJ*, 278, 499, [doi](#), [ADS](#)
- Antonucci, R. R. J., & Miller, J. S. 1985, *ApJ*, 297, 621, [doi](#), [ADS](#)
- Assef, R. J., Stern, D., Kochanek, C. S., et al. 2013, *ApJ*, 772, 26, [doi](#), [ADS](#)
- Baade, W., & Minkowski, R. 1954, *ApJ*, 119, 206, [doi](#), [ADS](#)
- Bajtlík, S., Duncan, R. C., & Ostriker, J. P. 1988, *ApJ*, 327, 570, [doi](#), [ADS](#)
- Baldwin, J. A., Burbidge, E. M., Burbidge, G. R., et al. 1974, *ApJ*, 193, 513, [doi](#), [ADS](#)
- Becker, G. D., Rauch, M., & Sargent, W. L. W. 2007, *ApJ*, 662, 72, [doi](#), [ADS](#)
- Becker, G. D., Bolton, J. S., Haehnelt, M. G., & Sargent, W. L. W. 2011, *MNRAS*, 410, 1096, [doi](#), [ADS](#)
- Becker, G. D., Hewett, P. C., Worseck, G., & Prochaska, J. X. 2013, *MNRAS*, 430, 2067, [doi](#), [ADS](#)
- Becker, G. D., & Bolton, J. S. 2013, *MNRAS*, 436, 1023, [doi](#), [ADS](#)
- Becker, G. D., Bolton, J. S., Madau, P., et al. 2015, *MNRAS*, 447, 3402, [doi](#), [ADS](#)
- Bertin, E., & Arnouts, S. 1996, *A&AS*, 117, 393, [doi](#), [ADS](#)
- Bertin, E., Mellier, Y., Radovich, M., et al. 2002, in *Astronomical Society of the Pacific Conference Series*, Vol. 281, *Astronomical Data Analysis Software and Systems XI*, ed. D. A. Bohlender, D. Durand, & T. H. Handley, 228, [ADS](#)
- Bertin, E. 2006, in *Astronomical Society of the Pacific Conference Series*, Vol. 351, *Astronomical Data Analysis Software and Systems XV*, ed. C. Gabriel, C. Arviset, D. Ponz, & S. Enrique, 112, [ADS](#)
- Blumenthal, G. R., Faber, S. M., Primack, J. R., & Rees, M. J. 1984, *Nature*, 311, 517, [doi](#), [ADS](#)
- Boera, E., Murphy, M. T., Becker, G. D., & Bolton, J. S. 2014, *MNRAS*, 441, 1916, [doi](#), [ADS](#)

BIBLIOGRAPHY

- Boera, E., Becker, G. D., Bolton, J. S., & Nasir, F. 2018, [ArXiv e-prints](#), [ADS](#)
- Bolton, J. S., Haehnelt, M. G., Viel, M., & Carswell, R. F. 2006, *MNRAS*, 366, 1378, [doi](#), [ADS](#)
- Bolton, J. S., & Haehnelt, M. G. 2007, *MNRAS*, 382, 325, [doi](#), [ADS](#)
- Bolton, J. S., Viel, M., Kim, T.-S., Haehnelt, M. G., & Carswell, R. F. 2008, *MNRAS*, 386, 1131, [doi](#), [ADS](#)
- Bolton, J. S., Oh, S. P., & Furlanetto, S. R. 2009, *MNRAS*, 395, 736, [doi](#), [ADS](#)
- Bolton, J. S., Becker, G. D., Wyithe, J. S. B., Haehnelt, M. G., & Sargent, W. L. W. 2010, *MNRAS*, 406, 612, [doi](#), [ADS](#)
- Bolton, J. S., Becker, G. D., Raskutti, S., et al. 2012, *MNRAS*, 419, 2880, [doi](#), [ADS](#)
- Bolton, J. S., Puchwein, E., Sijacki, D., et al. 2017, *MNRAS*, 464, 897, [doi](#), [ADS](#)
- Bond, J. R., Kofman, L., & Pogosyan, D. 1996, *Nature*, 380, 603, [doi](#), [ADS](#)
- Borisova, E., Lilly, S. J., Cantalupo, S., et al. 2016, *ApJ*, 830, 120, [doi](#), [ADS](#)
- Bouwens, R. J., Illingworth, G. D., Franx, M., et al. 2009, *ApJ*, 705, 936, [doi](#), [ADS](#)
- Bouwens, R. J., Illingworth, G. D., Oesch, P. A., et al. 2015, *ApJ*, 803, 34, [doi](#), [ADS](#)
- Bovy, J., Hennawi, J. F., Hogg, D. W., et al. 2011, *ApJ*, 729, 141, [doi](#), [ADS](#)
- Bovy, J., Myers, A. D., Hennawi, J. F., et al. 2012, *ApJ*, 749, 41, [doi](#), [ADS](#)
- Brusa, M., Civano, F., Comastri, A., et al. 2010, *ApJ*, 716, 348, [doi](#), [ADS](#)
- Buchner, J., Georgakakis, A., Nandra, K., et al. 2015, *ApJ*, 802, 89, [doi](#), [ADS](#)
- Buchner, J., & Bauer, F. E. 2017, *MNRAS*, 465, 4348, [doi](#), [ADS](#)
- Busca, N. G., Delubac, T., Rich, J., et al. 2013, *A&A*, 552, A96, [doi](#), [ADS](#)
- Butler, N. R., & Bloom, J. S. 2011, *AJ*, 141, 93, [doi](#), [ADS](#)
- Buzzoni, B., Delabre, B., Dekker, H., et al. 1984, *The Messenger*, 38, 9, [ADS](#)
- Cai, Z., Fan, X., Peirani, S., et al. 2016, *ApJ*, 833, 135, [doi](#), [ADS](#)
- Cai, Z., Fan, X., Bian, F., et al. 2017, *ApJ*, 839, 131, [doi](#), [ADS](#)
- Calverley, A. P., Becker, G. D., Haehnelt, M. G., & Bolton, J. S. 2011, *MNRAS*, 412, 2543, [doi](#), [ADS](#)
- Cantalupo, S., Lilly, S. J., & Haehnelt, M. G. 2012, *MNRAS*, 425, 1992, [doi](#), [ADS](#)
- Cantalupo, S., Arrigoni-Battaia, F., Prochaska, J. X., Hennawi, J. F., & Madau, P. 2014, *Nature*, 506, 63, [doi](#), [ADS](#)
- Carswell, R. F., Whelan, J. A. J., Smith, M. G., Boksenberg, A., & Tytler, D. 1982, *MNRAS*, 198, 91, [doi](#), [ADS](#)
- Cisternas, M., Jahnke, K., Inskip, K. J., et al. 2011, *ApJ*, 726, 57, [doi](#), [ADS](#)
- Civano, F., Marchesi, S., Comastri, A., et al. 2016, *ApJ*, 819, 62, [doi](#), [ADS](#)
- Coatman, L., Hewett, P. C., Banerji, M., et al. 2017, *MNRAS*, 465, 2120, [doi](#), [ADS](#)
- Coc, A., Petitjean, P., Uzan, J.-P., et al. 2015, *Phys. Rev. D*, 92, 123526, [doi](#), [ADS](#)
- Compostella, M., Cantalupo, S., & Porciani, C. 2013, *MNRAS*, 435, 3169, [doi](#), [ADS](#)
- . 2014, *MNRAS*, 445, 4186, [doi](#), [ADS](#)
- Conroy, C., & White, M. 2013, *ApJ*, 762, 70, [doi](#), [ADS](#)
- Croft, R. A. C., Weinberg, D. H., Katz, N., & Hernquist, L. 1997, *ApJ*, 488, 532, [doi](#), [ADS](#)
- Croft, R. A. C. 2004, *ApJ*, 610, 642, [doi](#), [ADS](#)

- Croom, S. M., Boyle, B. J., Shanks, T., et al. 2005, *MNRAS*, 356, 415, [doi](#), [ADS](#)
- Cucciati, O., Tresse, L., Ilbert, O., et al. 2012, *A&A*, 539, A31, [doi](#), [ADS](#)
- Dall’Aglio, A., Wisotzki, L., & Worseck, G. 2008, *A&A*, 491, 465, [doi](#), [ADS](#)
- Davies, F. B., & Furlanetto, S. R. 2014, *MNRAS*, 437, 1141, [doi](#), [ADS](#)
- Davies, F. B., Furlanetto, S. R., & Dixon, K. L. 2017, *MNRAS*, 465, 2886, [doi](#), [ADS](#)
- Davies, F. B., Hennawi, J. F., Bañados, E., et al. 2018, *ApJ*, 864, 142, [doi](#), [ADS](#)
- Davis, M., Efstathiou, G., Frenk, C. S., & White, S. D. M. 1985, *ApJ*, 292, 371, [doi](#), [ADS](#)
- Dawson, K. S., Schlegel, D. J., Ahn, C. P., et al. 2013, *AJ*, 145, 10, [doi](#), [ADS](#)
- Dekker, H., D’Odorico, S., Kaufer, A., Delabre, B., & Kotzlowski, H. 2000, in *Proc. SPIE*, Vol. 4008, *Optical and IR Telescope Instrumentation and Detectors*, ed. M. Iye & A. F. Moorwood, 534–545, [doi](#), [ADS](#)
- Di Matteo, T., Springel, V., & Hernquist, L. 2005, *Nature*, 433, 604, [doi](#), [ADS](#)
- DiPompeo, M. A., Bovy, J., Myers, A. D., & Lang, D. 2015, *MNRAS*, 452, 3124, [doi](#), [ADS](#)
- DiPompeo, M. A., Hickox, R. C., Eftekharzadeh, S., & Myers, A. D. 2017, *MNRAS*, 469, 4630, [doi](#), [ADS](#)
- Dobrzycki, A., & Bechtold, J. 1991, *ApJ*, 377, L69, [doi](#), [ADS](#)
- Dullemond, C. P., & van Bemmell, I. M. 2005, *A&A*, 436, 47, [doi](#), [ADS](#)
- Edge, D. O., Shakeshaft, J. R., McAdam, W. B., Baldwin, J. E., & Archer, S. 1959, *Mem. R. Astron. Soc.*, 68, 37, [ADS](#)
- Eftekharzadeh, S., Myers, A. D., White, M., et al. 2015, *MNRAS*, 453, 2779, [doi](#), [ADS](#)
- Eilers, A.-C., Davies, F. B., Hennawi, J. F., et al. 2017, *ApJ*, 840, 24, [doi](#), [ADS](#)
- Eisenstein, D. J., Weinberg, D. H., Agol, E., et al. 2011, *AJ*, 142, 72, [doi](#), [ADS](#)
- Elitzur, M., & Shlosman, I. 2006, *ApJ*, 648, L101, [doi](#), [ADS](#)
- Ellis, R. S., Bland-Hawthorn, J., Bremer, M., et al. 2017, [ArXiv e-prints](#), [ADS](#)
- Elvis, M. 2000, *ApJ*, 545, 63, [doi](#), [ADS](#)
- Faber, S. M., Phillips, A. C., Kibrick, R. I., et al. 2003, in *Proc. SPIE*, Vol. 4841, *Instrument Design and Performance for Optical/Infrared Ground-based Telescopes*, ed. M. Iye & A. F. M. Moorwood, 1657–1669, [doi](#), [ADS](#)
- Fan, X. 1999, *AJ*, 117, 2528, [doi](#), [ADS](#)
- Fan, X., Strauss, M. A., Becker, R. H., et al. 2006, *AJ*, 132, 117, [doi](#), [ADS](#)
- Fanaroff, B. L., & Riley, J. M. 1974, *MNRAS*, 167, 31P, [doi](#), [ADS](#)
- Faucher-Giguère, C.-A., Prochaska, J. X., Lidz, A., Hernquist, L., & Zaldarriaga, M. 2008a, *ApJ*, 681, 831, [doi](#), [ADS](#)
- Faucher-Giguère, C.-A., Lidz, A., Hernquist, L., & Zaldarriaga, M. 2008b, *ApJ*, 688, 85, [doi](#), [ADS](#)
- Faucher-Giguère, C.-A., Lidz, A., Zaldarriaga, M., & Hernquist, L. 2009, *ApJ*, 703, 1416, [doi](#), [ADS](#)
- Flesch, E. W. 2015, *PASA*, 32, e010, [doi](#), [ADS](#)
- Furlanetto, S. R., & Oh, S. P. 2008, *ApJ*, 681, 1, [doi](#), [ADS](#)
- Furlanetto, S. R., & Dixon, K. L. 2010, *ApJ*, 714, 355, [doi](#), [ADS](#)
- Furlanetto, S. R., & Lidz, A. 2011, *ApJ*, 735, 117, [doi](#), [ADS](#)
- Gaskell, C. M. 1982, *ApJ*, 263, 79, [doi](#), [ADS](#)

BIBLIOGRAPHY

- Gaudi, B. S., Seager, S., Mennesson, B., et al. 2018, [ArXiv e-prints](#), [ADS](#)
- Giallongo, E., Ragazzoni, R., Grazian, A., et al. 2008, *A&A*, 482, 349, [doi](#), [ADS](#)
- Gilfanov, M., & Merloni, A. 2014, *Space Science Reviews*, 183, 121, [doi](#), [ADS](#)
- Giommi, P., Padovani, P., & Polenta, G. 2013, *MNRAS*, 431, 1914, [doi](#), [ADS](#)
- Gonçalves, T. S., Steidel, C. C., & Pettini, M. 2008, *ApJ*, 676, 816, [doi](#), [ADS](#)
- GRAVITY Collaboration, Sturm, E., Dexter, J., et al. 2018, [ArXiv e-prints](#), [ADS](#)
- Green, J. C., Froning, C. S., Osterman, S., et al. 2012, *ApJ*, 744, 60, [doi](#), [ADS](#)
- Greenstein, J. L. 1963, *Nature*, 197, 1041, [doi](#), [ADS](#)
- Greenstein, J. L., & Schmidt, M. 1964, *ApJ*, 140, 1, [doi](#), [ADS](#)
- Gunn, J. E., & Peterson, B. A. 1965, *ApJ*, 142, 1633, [doi](#), [ADS](#)
- Haardt, F., & Maraschi, L. 1993, *ApJ*, 413, 507, [doi](#), [ADS](#)
- Haardt, F., & Madau, P. 2012, *ApJ*, 746, 125, [doi](#), [ADS](#)
- Habib, S., Heitmann, K., Higdon, D., Nakhleh, C., & Williams, B. 2007, *Phys. Rev. D*, 76, 083503, [doi](#), [ADS](#)
- Hazard, C., Mackey, M. B., & Shimmins, A. J. 1963, *Nature*, 197, 1037, [doi](#), [ADS](#)
- Heap, S. R., Williger, G. M., Smette, A., et al. 2000, *ApJ*, 534, 69, [doi](#), [ADS](#)
- Hennawi, J. F., Prochaska, J. X., Burles, S., et al. 2006, *ApJ*, 651, 61, [doi](#), [ADS](#)
- Hennawi, J. F., & Prochaska, J. X. 2007, *ApJ*, 655, 735, [doi](#), [ADS](#)
- Hennawi, J. F., Prochaska, J. X., Cantalupo, S., & Arrigoni-Battaia, F. 2015, *Science*, 348, 779, [doi](#), [ADS](#)
- Hill, A., Flagey, N., McConnachie, A., et al. 2018, [ArXiv e-prints](#), [ADS](#)
- Hiss, H., Walther, M., Hennawi, J. F., et al. 2018, *ApJ*, 865, 42, [doi](#), [ADS](#)
- Hogan, C. J., Anderson, S. F., & Rugers, M. H. 1997, *AJ*, 113, 1495, [doi](#), [ADS](#)
- Hogg, D. W. 1999, *ArXiv Astrophysics e-prints*, [ADS](#)
- Hönig, S. F., & Beckert, T. 2007, *MNRAS*, 380, 1172, [doi](#), [ADS](#)
- Hönig, S. F., & Kishimoto, M. 2017, *ApJ*, 838, L20, [doi](#), [ADS](#)
- Hopkins, P. F., Richards, G. T., & Hernquist, L. 2007, *ApJ*, 654, 731, [doi](#), [ADS](#)
- Hopkins, P. F., Hernquist, L., Cox, T. J., & Kereš, D. 2008a, *ApJS*, 175, 356, [doi](#), [ADS](#)
- Hopkins, P. F., Cox, T. J., Kereš, D., & Hernquist, L. 2008b, *ApJS*, 175, 390, [doi](#), [ADS](#)
- Hui, L., & Gnedin, N. Y. 1997, *MNRAS*, 292, 27, [doi](#), [ADS](#)
- Jakobsen, P., Jansen, R. A., Wagner, S., & Reimers, D. 2003, *A&A*, 397, 891, [doi](#), [ADS](#)
- Jiang, L., Fan, X., Brandt, W. N., et al. 2010, *Nature*, 464, 380, [doi](#), [ADS](#)
- Johnson, H. L. 1964, *ApJ*, 139, 1022, [doi](#), [ADS](#)
- Keating, L. C., Puchwein, E., & Haehnelt, M. G. 2018, *MNRAS*, 477, 5501, [doi](#), [ADS](#)
- Keating, S. K., Everett, J. E., Gallagher, S. C., & Deo, R. P. 2012, *ApJ*, 749, 32, [doi](#), [ADS](#)
- Kellermann, K. I., Sramek, R., Schmidt, M., Shaffer, D. B., & Green, R. 1989, *AJ*, 98, 1195, [doi](#), [ADS](#)
- Kelly, B. C., Vestergaard, M., Fan, X., et al. 2010, *ApJ*, 719, 1315, [doi](#), [ADS](#)
- Khachikian, E. Y., & Weedman, D. W. 1974, *ApJ*, 192, 581, [doi](#), [ADS](#)
- Khaire, V., & Srianand, R. 2018, [ArXiv e-prints](#), [ADS](#)
- Khrykin, I. S., Hennawi, J. F., McQuinn, M., & Worseck, G. 2016, *ApJ*, 824, 133, [doi](#), [ADS](#)

- Khrykin, I. S., Hennawi, J. F., & McQuinn, M. 2017, *ApJ*, 838, 96, doi, [ADS](#)
- Khrykin, I. S., Hennawi, J. F., & Worseck, G. 2018, [ArXiv e-prints](#), [ADS](#)
- Kirkman, D., Tytler, D., Lubin, D., & Charlton, J. 2007, *MNRAS*, 376, 1227, doi, [ADS](#)
- Kirkman, D., & Tytler, D. 2008, *MNRAS*, 391, 1457, doi, [ADS](#)
- Krolewski, A., Lee, K.-G., White, M., et al. 2018, *ApJ*, 861, 60, doi, [ADS](#)
- Kulkarni, G., Worseck, G., & Hennawi, J. F. 2018a, [ArXiv e-prints](#), [ADS](#)
- Kulkarni, G., Keating, L. C., Haehnelt, M. G., et al. 2018b, [ArXiv e-prints](#), [ADS](#)
- La Plante, P., & Trac, H. 2016, *ApJ*, 828, 90, doi, [ADS](#)
- Laor, A., & Netzer, H. 1989, *MNRAS*, 238, 897, doi, [ADS](#)
- Lau, M. W., Prochaska, J. X., & Hennawi, J. F. 2016, *ApJS*, 226, 25, doi, [ADS](#)
- Lawrence, A. 1991, *MNRAS*, 252, 586, doi, [ADS](#)
- Le Fèvre, O., Saisse, M., Mancini, D., et al. 2003, in *Proc. SPIE*, Vol. 4841, Instrument Design and Performance for Optical/Infrared Ground-based Telescopes, ed. M. Iye & A. F. M. Moorwood, 1670–1681, doi, [ADS](#)
- Lee, K.-G. 2012, *ApJ*, 753, 136, doi, [ADS](#)
- Lee, K.-G., Hennawi, J. F., White, M., Croft, R. A. C., & Ozbek, M. 2014a, *ApJ*, 788, 49, doi, [ADS](#)
- Lee, K.-G., Hennawi, J. F., Stark, C., et al. 2014b, *ApJ*, 795, L12, doi, [ADS](#)
- Lee, K.-G., Hennawi, J. F., White, M., et al. 2016, *ApJ*, 817, 160, doi, [ADS](#)
- Lee, K.-G., Krolewski, A., White, M., et al. 2018, *ApJS*, 237, 31, doi, [ADS](#)
- Lidz, A., Faucher-Giguère, C.-A., Dall’Aglio, A., et al. 2010, *ApJ*, 718, 199, doi, [ADS](#)
- Liske, J., & Williger, G. M. 2001, *MNRAS*, 328, 653, doi, [ADS](#)
- López, S., D’Odorico, V., Ellison, S. L., et al. 2016, *A&A*, 594, A91, doi, [ADS](#)
- Low, F. J., & Johnson, H. L. 1965, *ApJ*, 141, 336, doi, [ADS](#)
- Lukić, Z., Stark, C. W., Nugent, P., et al. 2015, *MNRAS*, 446, 3697, doi, [ADS](#)
- Lusso, E., Hennawi, J. F., Comastri, A., et al. 2013, *ApJ*, 777, 86, doi, [ADS](#)
- Lusso, E., Worseck, G., Hennawi, J. F., et al. 2015, *MNRAS*, 449, 4204, doi, [ADS](#)
- Lynden-Bell, D. 1969, *Nature*, 223, 690, doi, [ADS](#)
- MacLeod, C. L., Ivezić, Ž., Kochanek, C. S., et al. 2010, *ApJ*, 721, 1014, doi, [ADS](#)
- MacLeod, C. L., Ivezić, Ž., Sesar, B., et al. 2012, *ApJ*, 753, 106, doi, [ADS](#)
- Madau, P., & Meiksin, A. 1994, *ApJ*, 433, L53, doi, [ADS](#)
- Magnelli, B., Lutz, D., Santini, P., et al. 2012, *A&A*, 539, A155, doi, [ADS](#)
- Malkan, M. A. 1983, *ApJ*, 268, 582, doi, [ADS](#)
- Marchesi, S., Lanzuisi, G., Civano, F., et al. 2016, *ApJ*, 830, 100, doi, [ADS](#)
- Martini, P. 2004, *Coevolution of Black Holes and Galaxies*, 169, [ADS](#)
- Mason, C. A., Treu, T., Dijkstra, M., et al. 2018, *ApJ*, 856, 2, doi, [ADS](#)
- Mather, J. C., Cheng, E. S., Cottingham, D. A., et al. 1994, *ApJ*, 420, 439, doi, [ADS](#)
- Matthews, T. A., & Sandage, A. R. 1963, *ApJ*, 138, 30, doi, [ADS](#)
- McCarthy, J. K., Cohen, J. G., Butcher, B., et al. 1998, in *Proc. SPIE*, Vol. 3355, Optical Astronomical Instrumentation, ed. S. D’Odorico, 81–92, [ADS](#)
- McLeod, B., Geary, J., Conroy, M., et al. 2015, *PASP*, 127, 366, doi, [ADS](#)

BIBLIOGRAPHY

- McQuinn, M. 2009, *ApJ*, 704, L89, [doi](#), [ADS](#)
- McQuinn, M., & Worsack, G. 2014, *MNRAS*, 440, 2406, [doi](#), [ADS](#)
- McQuinn, M. 2016, *ARA&A*, 54, 313, [doi](#), [ADS](#)
- Meiksin, A., & White, M. 2004, *MNRAS*, 350, 1107, [doi](#), [ADS](#)
- Meiksin, A., Tittley, E. R., & Brown, C. K. 2010, *MNRAS*, 401, 77, [doi](#), [ADS](#)
- Meiksin, A., & Tittley, E. R. 2012, *MNRAS*, 423, 7, [doi](#), [ADS](#)
- Meiksin, A. A. 2009, *Reviews of Modern Physics*, 81, 1405, [doi](#), [ADS](#)
- Miller, J. S., Goodrich, R. W., & Mathews, W. G. 1991, *ApJ*, 378, 47, [doi](#), [ADS](#)
- Miralda-Escudé, J., Haehnelt, M., & Rees, M. J. 2000, *ApJ*, 530, 1, [doi](#), [ADS](#)
- Miralda-Escudé, J. 2003, *ApJ*, 597, 66, [doi](#), [ADS](#)
- Monet, D. G., Levine, S. E., Canzian, B., et al. 2003, *AJ*, 125, 984, [doi](#), [ADS](#)
- Muller, G. P., Reed, R., Armandroff, T., Boroson, T. A., & Jacoby, G. H. 1998, in *Proc. SPIE*, Vol. 3355, *Optical Astronomical Instrumentation*, ed. S. D’Odorico, 577–585, [ADS](#)
- Nenkova, M., Ivezić, Ž., & Elitzur, M. 2002, *ApJ*, 570, L9, [doi](#), [ADS](#)
- Netzer, H. 2015, *ARA&A*, 53, 365, [doi](#), [ADS](#)
- Novak, G. S., Ostriker, J. P., & Ciotti, L. 2011, *ApJ*, 737, 26, [doi](#), [ADS](#)
- Oñorbe, J., Hennawi, J. F., & Lukić, Z. 2017, *ApJ*, 837, 106, [doi](#), [ADS](#)
- Oñorbe, J., Davies, F. B., Lukić, Z., Hennawi, J. F., & Sorini, D. 2018, [ArXiv e-prints](#), [ADS](#)
- Oke, J. B. 1963, *Nature*, 197, 1040, [doi](#), [ADS](#)
- Oke, J. B., & Gunn, J. E. 1983, *ApJ*, 266, 713, [doi](#), [ADS](#)
- Oke, J. B., Cohen, J. G., Carr, M., et al. 1995, *PASP*, 107, 375, [doi](#), [ADS](#)
- O’Meara, J. M., Lehner, N., Howk, J. C., et al. 2015, *AJ*, 150, 111, [doi](#), [ADS](#)
- . 2017, *AJ*, 154, 114, [doi](#), [ADS](#)
- Oppenheimer, B. D., Segers, M., Schaye, J., Richings, A. J., & Crain, R. A. 2018, *MNRAS*, 474, 4740, [doi](#), [ADS](#)
- Padmanabhan, N., Schlegel, D. J., Finkbeiner, D. P., et al. 2008, *ApJ*, 674, 1217, [doi](#), [ADS](#)
- Padovani, P., Alexander, D. M., Assef, R. J., et al. 2017, *A&A Rev.*, 25, [doi](#), [ADS](#)
- Padovani, P. 2017, *Nature Astronomy*, 1, 0194, [doi](#), [ADS](#)
- Page, D. N., & Thorne, K. S. 1974, *ApJ*, 191, 499, [doi](#), [ADS](#)
- Palanque-Delabrouille, N., Yèche, C., Myers, A. D., et al. 2011, *A&A*, 530, A122, [doi](#), [ADS](#)
- Palanque-Delabrouille, N., Yèche, C., Borde, A., et al. 2013, *A&A*, 559, A85, [doi](#), [ADS](#)
- Pâris, I., Petitjean, P., Ross, N. P., et al. 2017, *A&A*, 597, A79, [doi](#), [ADS](#)
- Pâris, I., Petitjean, P., Aubourg, É., et al. 2018, *A&A*, 613, A51, [doi](#), [ADS](#)
- Pazder, J. S., Roberts, S., Abraham, R., et al. 2006, in *Proc. SPIE*, Vol. 6269, *Society of Photo-Optical Instrumentation Engineers (SPIE) Conference Series*, 62691X, [doi](#), [ADS](#)
- Peebles, P. J. E. 1980, *Physica Scripta*, 21, 720, [doi](#), [ADS](#)
- Penzias, A. A., & Wilson, R. W. 1965, *ApJ*, 142, 419, [doi](#), [ADS](#)
- Perlman, E. S., Mason, R. E., Packham, C., et al. 2007, *ApJ*, 663, 808, [doi](#), [ADS](#)
- Planck Collaboration, Aghanim, N., Akrami, Y., et al. 2018, [ArXiv e-prints](#), [ADS](#)
- Pogge, R. W. 1988, *ApJ*, 332, 702, [doi](#), [ADS](#)
- Press, W. H., & Schechter, P. 1974, *ApJ*, 187, 425, [doi](#), [ADS](#)

- Rahmati, A., Pawlik, A. H., Raičević, M., & Schaye, J. 2013, *MNRAS*, 430, 2427, doi, ADS
- Rauch, M. 1998, *ARA&A*, 36, 267, doi, ADS
- Reimers, D., Kohler, S., Wisotzki, L., et al. 1997, *A&A*, 327, 890, ADS
- Reimers, D., Fechner, C., Hagen, H.-J., et al. 2005, *A&A*, 442, 63, doi, ADS
- Richards, G. T., Fan, X., Newberg, H. J., et al. 2002a, *AJ*, 123, 2945, doi, ADS
- Richards, G. T., Vanden Berk, D. E., Reichard, T. A., et al. 2002b, *AJ*, 124, 1, doi, ADS
- Richards, G. T., Lacy, M., Storrie-Lombardi, L. J., et al. 2006, *ApJS*, 166, 470, doi, ADS
- Richards, G. T., Myers, A. D., Peters, C. M., et al. 2015, *ApJS*, 219, 39, doi, ADS
- Richardson, J., Zheng, Z., Chatterjee, S., Nagai, D., & Shen, Y. 2012, *ApJ*, 755, 30, doi, ADS
- Rieke, G. H. 1978, *ApJ*, 226, 550, doi, ADS
- Rorai, A., Becker, G. D., Haehnelt, M. G., et al. 2017a, *MNRAS*, 466, 2690, doi, ADS
- Rorai, A., Hennawi, J. F., Oñorbe, J., et al. 2017b, *Science*, 356, 418, doi, ADS
- Rorai, A., Carswell, R. F., Haehnelt, M. G., et al. 2018, *MNRAS*, 474, 2871, doi, ADS
- Salpeter, E. E. 1964, *ApJ*, 140, 796, doi, ADS
- Sandage, A., Véron, P., & Wyndham, J. D. 1965, *ApJ*, 142, 1307, doi, ADS
- Sargent, W. L. W., Young, P. J., Boksenberg, A., & Tytler, D. 1980, *ApJS*, 42, 41, doi, ADS
- Schawinski, K., Koss, M., Berney, S., & Sartori, L. F. 2015, *MNRAS*, 451, 2517, doi, ADS
- Schaye, J., Theuns, T., Rauch, M., Efstathiou, G., & Sargent, W. L. W. 2000, *MNRAS*, 318, 817, doi, ADS
- Schaye, J., Crain, R. A., Bower, R. G., et al. 2015, *MNRAS*, 446, 521, doi, ADS
- Scheuer, P. A. G. 1965, *Nature*, 207, 963, doi, ADS
- Schindler, J.-T., Fan, X., McGreer, I. D., et al. 2018, *ApJ*, 863, 144, doi, ADS
- Schirber, M., Miralda-Escudé, J., & McDonald, P. 2004, *ApJ*, 610, 105, doi, ADS
- Schlafly, E. F., & Finkbeiner, D. P. 2011, *ApJ*, 737, 103, doi, ADS
- Schlegel, D. J., Finkbeiner, D. P., & Davis, M. 1998, *ApJ*, 500, 525, doi, ADS
- Schmidt, M. 1963, *Nature*, 197, 1040, doi, ADS
- . 1965, *ApJ*, 141, 1295, doi, ADS
- Schmidt, M., & Green, R. F. 1983, *ApJ*, 269, 352, doi, ADS
- Schmidt, T. M., Worseck, G., Hennawi, J. F., Prochaska, J. X., & Crighton, N. H. M. 2017a, *ApJ*, 847, 81, doi, ADS
- Schmidt, T. M., Worseck, G., Hennawi, J. F., et al. 2017b, *Frontiers in Astronomy and Space Sciences*, 4, 23, doi, ADS
- Schmidt, T. M., Hennawi, J. F., Worseck, G., et al. 2018a, *ApJ*, 861, 122, doi, ADS
- Schmidt, T. M., Hennawi, J. F., Lee, K.-G., et al. 2018b, *ArXiv e-prints*, ADS
- Scott, J., Bechtold, J., Dobrzycki, A., & Kulkarni, V. P. 2000, *ApJS*, 130, 67, doi, ADS
- Segers, M. C., Oppenheimer, B. D., Schaye, J., & Richings, A. J. 2017, *MNRAS*, 471, 1026, doi, ADS
- Selsing, J., Fynbo, J. P. U., Christensen, L., & Krogager, J.-K. 2016, *A&A*, 585, A87, doi, ADS
- Sesar, B., Ivezić, Ž., Lupton, R. H., et al. 2007, *AJ*, 134, 2236, doi, ADS
- Seyfert, C. K. 1943, *ApJ*, 97, 28, doi, ADS

BIBLIOGRAPHY

- Shakura, N. I., & Sunyaev, R. A. 1973, *A&A*, 24, 337, [ADS](#)
- Shankar, F., Weinberg, D. H., & Miralda-Escudé, J. 2009, *ApJ*, 690, 20, [doi](#), [ADS](#)
- Shen, Y., Strauss, M. A., Oguri, M., et al. 2007, *AJ*, 133, 2222, [doi](#), [ADS](#)
- Shen, Y., Strauss, M. A., Ross, N. P., et al. 2009, *ApJ*, 697, 1656, [doi](#), [ADS](#)
- Shen, Y., Brandt, W. N., Richards, G. T., et al. 2016, *ApJ*, 831, 7, [doi](#), [ADS](#)
- Shields, G. A. 1978, *Nature*, 272, 706, [doi](#), [ADS](#)
- Shull, J. M., France, K., Danforth, C. W., Smith, B., & Tumlinson, J. 2010, *ApJ*, 722, 1312, [doi](#), [ADS](#)
- Shustov, B., Gómez de Castro, A. I., Sachkov, M., et al. 2018, *Ap&SS*, 363, 62, [doi](#), [ADS](#)
- Simpson, C. 1998, *MNRAS*, 297, L39, [doi](#), [ADS](#)
- . 2005, *MNRAS*, 360, 565, [doi](#), [ADS](#)
- Smette, A., Heap, S. R., Williger, G. M., et al. 2002, *ApJ*, 564, 542, [doi](#), [ADS](#)
- Smith, H. J., & Hoffleit, D. 1963, *Nature*, 198, 650, [doi](#), [ADS](#)
- Smoot, G. F., Bennett, C. L., Kogut, A., et al. 1992, *ApJ*, 396, L1, [doi](#), [ADS](#)
- Soltan, A. 1982, *MNRAS*, 200, 115, [doi](#), [ADS](#)
- Sorini, D., Oñorbe, J., Lukić, Z., & Hennawi, J. F. 2016, *ApJ*, 827, 97, [doi](#), [ADS](#)
- Sorini, D., Oñorbe, J., Hennawi, J. F., & Lukić, Z. 2018, *ApJ*, 859, 125, [doi](#), [ADS](#)
- Speziali, R., Di Paola, A., Giallongo, E., et al. 2008, in *Proc. SPIE*, Vol. 7014, Ground-based and Airborne Instrumentation for Astronomy II, 70144T, [doi](#), [ADS](#)
- Springel, V., White, S. D. M., Jenkins, A., et al. 2005a, *Nature*, 435, 629, [doi](#), [ADS](#)
- Springel, V., Di Matteo, T., & Hernquist, L. 2005b, *MNRAS*, 361, 776, [doi](#), [ADS](#)
- Springel, V., Frenk, C. S., & White, S. D. M. 2006, *Nature*, 440, 1137, [doi](#), [ADS](#)
- Stark, C. W., White, M., Lee, K.-G., & Hennawi, J. F. 2015a, *MNRAS*, 453, 311, [doi](#), [ADS](#)
- Stark, C. W., Font-Ribera, A., White, M., & Lee, K.-G. 2015b, *MNRAS*, 453, 4311, [doi](#), [ADS](#)
- Steidel, C. C., Adelberger, K. L., Shapley, A. E., et al. 2003, *ApJ*, 592, 728, [doi](#), [ADS](#)
- Stern, D., Eisenhardt, P., Gorjian, V., et al. 2005, *ApJ*, 631, 163, [doi](#), [ADS](#)
- Stern, D., Assef, R. J., Benford, D. J., et al. 2012, *ApJ*, 753, 30, [doi](#), [ADS](#)
- Stern, J., Hennawi, J. F., & Pott, J.-U. 2015, *ApJ*, 804, 57, [doi](#), [ADS](#)
- Stevans, M. L., Shull, J. M., Danforth, C. W., & Tilton, E. M. 2014, *ApJ*, 794, 75, [doi](#), [ADS](#)
- Storey, P. J., & Hummer, D. G. 1995, *MNRAS*, 272, 41, [doi](#), [ADS](#)
- Stoughton, C., Lupton, R. H., Bernardi, M., et al. 2002, *AJ*, 123, 485, [doi](#), [ADS](#)
- Syphers, D., Anderson, S. F., Zheng, W., et al. 2011, *ApJ*, 742, 99, [doi](#), [ADS](#)
- . 2012, *AJ*, 143, 100, [doi](#), [ADS](#)
- Syphers, D., & Shull, J. M. 2013, *ApJ*, 765, 119, [doi](#), [ADS](#)
- . 2014, *ApJ*, 784, 42, [doi](#), [ADS](#)
- Tadhunter, C., & Tsvetanov, Z. 1989, *Nature*, 341, 422, [doi](#), [ADS](#)
- Tamura, N., Takato, N., Shimono, A., et al. 2016, in *Proc. SPIE*, Vol. 9908, Ground-based and Airborne Instrumentation for Astronomy VI, 99081M, [doi](#), [ADS](#)
- The LUVOIR Team. 2018, [ArXiv e-prints](#), [ADS](#)
- Theuns, T., Leonard, A., Efstathiou, G., Pearce, F. R., & Thomas, P. A. 1998, *MNRAS*, 301, 478, [doi](#), [ADS](#)

- Thorne, K. S. 1974, *ApJ*, 191, 507, [doi](#), [ADS](#)
- Tilton, E. M., Stevans, M. L., Shull, J. M., & Danforth, C. W. 2016, *ApJ*, 817, 56, [doi](#), [ADS](#)
- Trainor, R., & Steidel, C. C. 2013, *ApJ*, 775, L3, [doi](#), [ADS](#)
- Tytler, D., & Fan, X.-M. 1992, *ApJS*, 79, 1, [doi](#), [ADS](#)
- Urry, C. M., & Padovani, P. 1995, *PASP*, 107, 803, [doi](#), [ADS](#)
- Vanden Berk, D. E., Richards, G. T., Bauer, A., et al. 2001, *AJ*, 122, 549, [doi](#), [ADS](#)
- Verner, D. A., Verner, E. M., & Ferland, G. J. 1996a, in eprint arXiv:atom-ph/9604003, [ADS](#)
- Verner, D. A., Ferland, G. J., Korista, K. T., & Yakovlev, D. G. 1996b, *ApJ*, 465, 487, [doi](#), [ADS](#)
- Véron-Cetty, M.-P., & Véron, P. 2010, *A&A*, 518, A10, [doi](#), [ADS](#)
- Viel, M., Becker, G. D., Bolton, J. S., & Haehnelt, M. G. 2013, *Phys. Rev. D*, 88, 043502, [doi](#), [ADS](#)
- Villarroel, B., Nyholm, A., Karlsson, T., et al. 2017, *ApJ*, 837, 110, [doi](#), [ADS](#)
- Visbal, E., & Croft, R. A. C. 2008, *ApJ*, 674, 660, [doi](#), [ADS](#)
- Vogelsberger, M., Genel, S., Springel, V., et al. 2014, *MNRAS*, 444, 1518, [doi](#), [ADS](#)
- Vogt, S. S., Allen, S. L., Bigelow, B. C., et al. 1994, in *Proc. SPIE*, Vol. 2198, Instrumentation in Astronomy VIII, ed. D. L. Crawford & E. R. Craine, 362, [doi](#), [ADS](#)
- Walther, M., Hennawi, J. F., Hiss, H., et al. 2018a, *ApJ*, 852, 22, [doi](#), [ADS](#)
- Walther, M., Oñorbe, J., Hennawi, J. F., & Lukić, Z. 2018b, [ArXiv e-prints](#), [ADS](#)
- Weymann, R. J., Carswell, R. F., & Smith, M. G. 1981, *ARA&A*, 19, 41, [doi](#), [ADS](#)
- White, M., Myers, A. D., Ross, N. P., et al. 2012, *MNRAS*, 424, 933, [doi](#), [ADS](#)
- White, M. 2014, *MNRAS*, 439, 3630, [doi](#), [ADS](#)
- White, S. D. M., & Rees, M. J. 1978, *MNRAS*, 183, 341, [doi](#), [ADS](#)
- Whysong, D., & Antonucci, R. 2004, *ApJ*, 602, 116, [doi](#), [ADS](#)
- Wilson, A. S., Braatz, J. A., Heckman, T. M., Krolik, J. H., & Miley, G. K. 1993, *ApJ*, 419, L61, [doi](#), [ADS](#)
- Woodgate, B. E., Kimble, R. A., Bowers, C. W., et al. 1998, *PASP*, 110, 1183, [doi](#), [ADS](#)
- Worseck, G., & Wisotzki, L. 2006, *A&A*, 450, 495, [doi](#), [ADS](#)
- Worseck, G., Fechner, C., Wisotzki, L., & Dall’Aglia, A. 2007, *A&A*, 473, 805, [doi](#), [ADS](#)
- Worseck, G., & Prochaska, J. X. 2011, *ApJ*, 728, 23, [doi](#), [ADS](#)
- Worseck, G., Prochaska, J. X., McQuinn, M., et al. 2011, *ApJ*, 733, L24, [doi](#), [ADS](#)
- Worseck, G., Prochaska, J. X., O’Meara, J. M., et al. 2014, *MNRAS*, 445, 1745, [doi](#), [ADS](#)
- Worseck, G., Prochaska, J. X., Hennawi, J. F., & McQuinn, M. 2016, *ApJ*, 825, 144, [doi](#), [ADS](#)
- Worseck, G., Davies, F. B., Hennawi, J. F., & Prochaska, J. X. 2018, [ArXiv e-prints](#), [ADS](#)
- Wright, E. L., Eisenhardt, P. R. M., Mainzer, A. K., et al. 2010, *AJ*, 140, 1868, [doi](#), [ADS](#)
- York, D. G., Adelman, J., Anderson, Jr., J. E., et al. 2000, *AJ*, 120, 1579, [doi](#), [ADS](#)
- Yu, Q., & Tremaine, S. 2002, *MNRAS*, 335, 965, [doi](#), [ADS](#)
- Zel’dovich, Y. B. 1964, *Soviet Physics Doklady*, 9, 195, [ADS](#)
- . 1970, *A&A*, 5, 84, [ADS](#)
- Zheng, W., Syphers, D., Meiksin, A., et al. 2015, *ApJ*, 806, 142, [doi](#), [ADS](#)

Acknowledgements

I would like to thank my supervisor Joe Hennawi for giving me the opportunity to conduct this project and for the support throughout the years, at Heidelberg as well as in Santa Barbara. I am grateful for the trust and confidence, for letting me follow my style of work and not at least for the great experience at the Paranal Observatory.

I also would like to thank Gábor Worsack who supervised me on a daily basis during the first project, always found time for me and helped wherever possible.

I would like to thank all members of the ENIGMA group at MPIA and UCSB for their support, lively discussions and open exchange of thoughts and ideas. I enjoyed the dynamic and stimulating environment in this group which let me gain detailed insights into many research projects and helped me to gain a thorough understanding of the field.

Special thank goes to Michael Walther for countless scientific and non-scientific discussions, help with numerous daily challenges and for sharing his insights into statistical methods.

I am particularly happy to have been a member of the Max Planck Institute for Astronomy and very much enjoyed the friendly and inspiring atmosphere at the Galaxy Department which gave me the feeling to be part of a community.

A great thanks goes to all students at MPIA and from our IMPRS generation who made my life a lot more enjoyable and with whom I had fun an joy, in particular on Thursdays.

I am thankful to Joe Hennawi and Kees Dullemond for agreeing to referee my thesis and Eva Grebel and Luca Amendola for being part of my thesis committee.

Last, but not least, I would like to express my deep gratitude and thankfulness to my parents who always supported me, promoted my interest in astronomy and encouraged me to follow my path.

Declaration of Authorship

I, Tobias Schmidt, declare that this thesis titled, 'Constraints on Quasar Emission Properties from the He II and H I Transverse Proximity Effect' and the work presented in it are my own.

I confirm that:

- This work was done wholly while in candidature for a research degree at the University of Heidelberg.
- Where any part of this thesis has previously been submitted for a degree or any other qualification at this University or any other institution, this has been clearly stated
- Where I have consulted the published work of others, this is always clearly attributed.
- Where I have quoted from the work of others, the source is always given. With the exception of such quotations, this thesis is entirely my own work.
- I have acknowledged all main sources of help.
- Where the thesis is based on work done by myself jointly with others, I have made clear exactly what was done by others and what I have contributed myself.

Signed: _____

Date: _____